Data assimilation

Geomechanical parameter estimation in the Groningen hydrocarbon reservoir from PS-InSAR measurements with a particle filter

K. Beers

Master Thesis
Geoscience and Remote Sensing

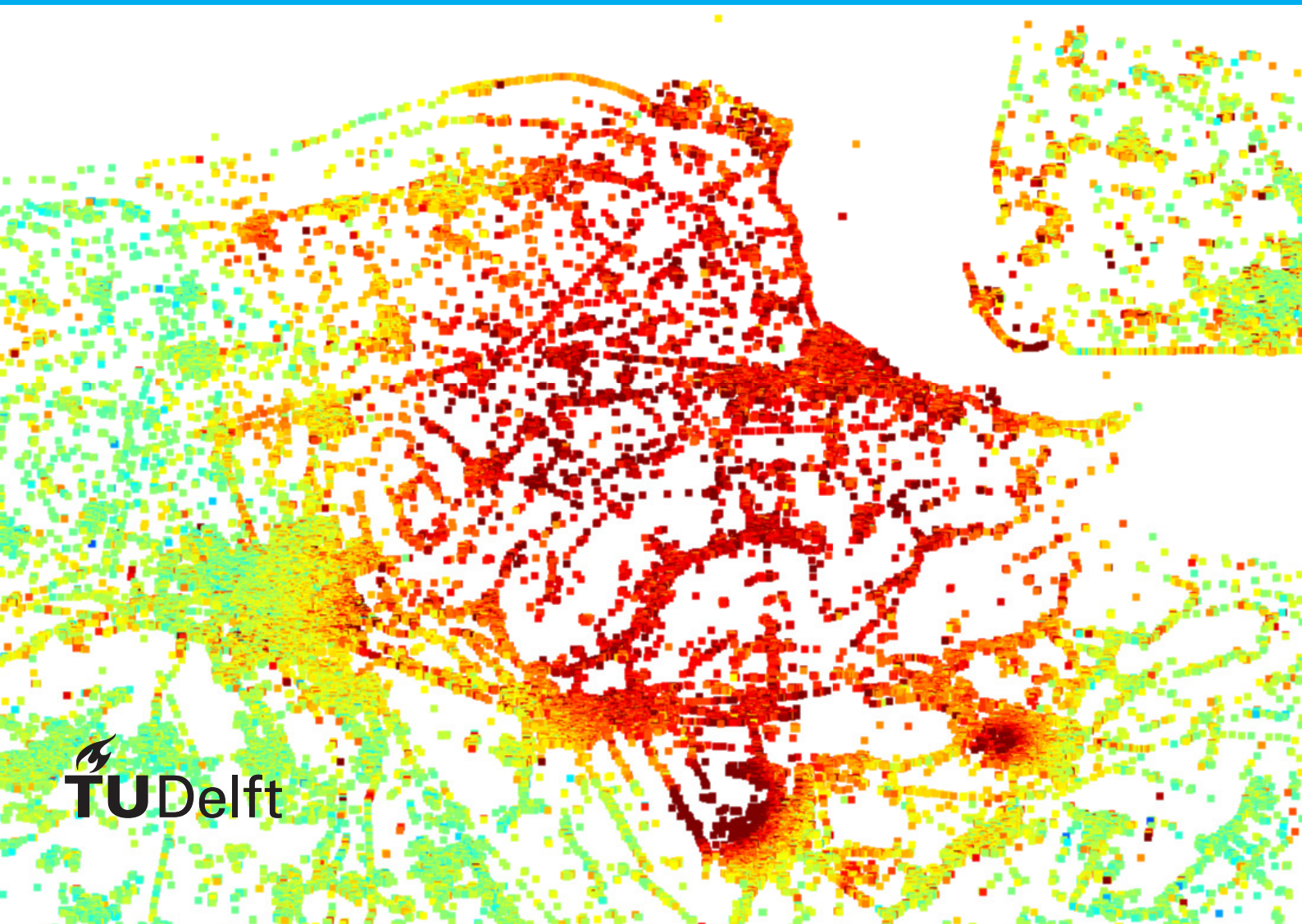

TU Delft

Data assimilation

Geomechanical parameter estimation in the Groningen hydrocarbon reservoir from PS-InSAR measurements with a particle filter

by

K. Beers

to obtain the degree of Master of Science in Applied Earth Sciences
specialised in Geoscience and Remote Sensing
at the Delft University of Technology,
to be defended publicly on Thursday June 21, 2018.

Student number:	4335546	
Thesis committee:	Prof.dr.ir. R.F. Hanssen,	TU Delft, supervisor
	Dr.ir. F.C. Vossepoel,	TU Delft, supervisor
	Dr. A. Barnhoorn,	TU Delft

An electronic version of this thesis is available at `http://repository.tudelft.nl/`.

TU Delft

Abstract

This thesis explores the usage of the particle filter as a data assimilation technique to estimate subsurface processes, such as reservoir volume change from space-geodetic PS-InSAR surface measurements. The specific research area is Groningen, where subsidence is induced by hydrocarbon and salt production.

The satellite radar PS-InSAR technique is used for observing subsidence values in the line-of-sight for a Radarsat-2 descending and a TerraSAR ascending set of measurements. A geomechanical model, the Mogi point source, translates subsurface volume changes to surface deformation. The geomechanical model parameters are estimated by the data assimilation technique particle filter from the observed surface measurements.

The particle filter is tested on synthetic data in a couple of test situations with an identical twin experiment. Synthetic data means that the date is simulated. The test situations are low dimensional in order to understand the results when using the particle filter and to get a grip on how the particle filter works, when the variables and parameters in the filter are changed. The experiment consists of two parts, one truth part and one estimated part. The truth part is to be recovered with the particle filter. The estimation part consists of a source strength and deformation part. The particle filter recovers the truth part, where the amount of recovery is a measure of how well the particle filter performs. This knowledge is used for interpreting the particle filter results of the real case, when applying the particle filter to PS-InSAR measurements of the Groningen region and estimating geomechanical parameters of the Mogi point source model.

Three different identical twin experiment test setups are tested, where the number of Mogi sources is varied; the distance between the Mogi sources; and the number of deformation locations. The test situations are kept low dimensional, which means that the number of Mogi sources varies from 1 to 16 and the number of deformation locations varies from 1 to 256. This is done in order to understand the results when applying the particle filter. The limitations are defined of the geomechanical model and the particle filter. Estimating a setting with a number of parameters > 1 than the source strength estimation benefits from the resampling.

The knowledge of the synthetic data experiments is used in the particle filter application on the PS-InSAR measurements of the Groningen gas field. A workflow is created in how to apply the steps of the particle filter on the PS-InSAR measurements in Groningen. Several solutions are developed for improving the fit between measurements and model. One of these solutions is localisation. Localisation means that the particle filter is applied locally, where the Mogi model parameters are estimated locally and taking in account only the local PS-InSAR measurements within a radius of 3000 m above each location of the Mogi sources. This localisation is done for each Mogi source location and provides a Mogi model parameter estimation that is not influenced by a fit far outside of the Mogi source influence area. The Mogi source influence sphere of deformation values at the surface depends on the depth of the Mogi sources. The Mogi source is placed at a depth of -3000 m and the influence radius at the surface above the Mogi source is 3000 to 4500 m.

The localisation solution has a deformation RMSE of 1.74 mm and a high percentage of fit, namely 97%, when using fitted PS-InSAR measurements. The RMSE is 6.00 mm and the fit is 59%, when using unfitted PS-InSAR measurements. Furthermore the localisation is applied on unfitted PS-InSAR measurements for the period 2010 to 2016 This resulted into yearly estimated source strength with a northwest to southeast trend. This trend might reflect the amount of subsidence at the surface and thus reservoir compaction. The reservoir is the thickest in the northwest part of the Groningen field and this fits to the PS-InSAR measurements and estimated source strengths.

Cover figure: Radarsat-2 PS-InSAR descending measurements of the Groningen region over the period 2009 to 2016. The deformation is in millimetres where the dark red colours represent a subsidence of -50 mm and the light green colour a change of 0 mm.

Acknowledgements

I would like to express my gratitude to my thesis committee during the realisation of this graduation project.

Firstly, I would like to acknowledge my main supervisor and graduation professor Ramon Hanssen for coming up with this project, as it is currently a topic of extensively research by many institutions and universities in the Netherlands. Also I thank him for his continuous ideas and insights.

Secondly I would like to thank my daily supervisor Femke Vossepoel for her large contribution to the project by the introduction of the used methodology. And further I would like to thank her for her steering guidance during this graduation project, the regular meetings and her endless enthusiasm for the topic.

Thirdly I would like to thank SkyGeo Delft for providing the PS-InSAR measurement sets of Groningen. Testing and applying my methodology on these real world measurements made this thesis so much more interesting. I am really thankful for this.

I would like to thank the master graduation students from the monthly subsidence meetings for their discussions, help and motivation. Also I would to thank Hans van der Marel for his help with the conversion of coordinates. Furthermore I would like to thank fellow Geoscience and Remote Sensing students for their encouragement during the whole studies. And especially I would like to thank Luciana for her positive attitude and the many inspirational coffee breaks we had during the study.

I would like to thank the fellow master graduation students at my TU Delft work place for the positive working environment that kept me motivated, especially during the last five months.

Last, but not least, I would like to thank my family for their support during my studies.

K. Beers
Delft, June 2018

Contents

List of Figures

List of Tables

List of Abbreviations

3D	three-dimensional
AHN	Algemeen Hoogtebestand Nederland
ALD	Azimuth Look Direction
AMR	Amsweer
BIR	Bierum
DA	Data Assimilation
DEM	Digital Elevation Model
EKL	Eemskanaal
EKR	De Eeker
EnKF	Ensemble Kalman Filter
ES-MDA	Ensemble Smoother with Multiple Data Assimilation
FRB	Froombosch
GNSS	Global Navigation Satellite System
GPS	Global Positioning System
GRO	Groningen
InSAR	Interferometric Synthetic Aperture Radar
KF	Kalman Filter
KNMI	Koninklijk Nederlands Meteorologisch Instituut
KPD	Kooipolder
Lat	Latitude
Lon	Longitude
LOS	Line-Of-Sight
LRM	Leermens
MWD	Midwolda
NAM	Nederlandse Aardolie Maatschappij
NAP	Normaal Amsterdams Peil
NBR	Noordbroek
NWS	Nieuw Scheemda
OVS	Overschild
OWG	Oudeweg
PAU	De Paauwen
PDF	Probability Density Function
PGA	Peak Ground Acceleration
POS	Ten Post
PSI	Persistent Scatterer Interferometry
PS-InSAR	Persistent Scatterer Interferometric Synthetic Aperture Radar
Radar	Radio Detection and Ranging
RD	Rijksdriehoek coordinates
RTCM	Rate Type Compaction Model
RTCiM	Rate Type Compaction isotach Model

SAP	Sappemeer
SAR	Synthetic Aperture Radar
SCB	Schaapbulten
SIR	Sequential Importance Resampling
SLO	Slochteren
SPI	Spitsbergen
SZW	Scheemderzwaag
SDB	Siddeburen
TJM	Tjuchem
TUS	Tusschenklappen
TVD	True Vertical Depth
UGS	Under Ground Storage
UTB	Uiterburen
VDM	Veendam
WSN	Winschoten
ZND	‘t Zandt
ZPD	Zuiderpolder
ZVN	Zuiderveen
ZWD	Zuidwending

List of Symbols

az	Azimuth
A	Event A in conditional probability
A	Pixel amplitude, when used in context of InSAR
B	Event B in conditional probability
B	Baseline, when used in context of InSAR
$B_{\parallel}$	Parallel baseline
$B_{\perp}$	Perpendicular baseline
C	Event C in conditional probability
d	Observations
d_e	East deformation, component of $D_{\text{LOS,R}}$
d_n	North deformation, component of $D_{\text{LOS,R}}$
d_u	Up deformation, component of $D_{\text{LOS,R}}$
D_{LOS}	Deformation in the line-of-sight
$D_{\text{LOS,R}}$	LOS component for a right-looking satellite
E	Young's modulus, ratio of stress and strain
F	Force
FWHM	Full width at half maximum
$\%g$	Percentage of acceleration, where $1g = 9.81$ [m/s^2]
H	Height
$H(\Psi_i)$	Model generated output at the same locations of observations d
H_{asc}	Ascending satellite track
H_{des}	Descending satellite track
HWHM	Half width at half maximum
i	Imaginary unit, when used in context of InSAR
inc	Incidence angle
I	Intensity of the radar reflection
$\text{Im}\{P\}$	Imaginary part of the phasor
k	Grid distance
mod_i	Estimated weighted deformation
$\vec{M}$	Master satellite position
M_L	Local magnitude
n	Number of observations
N	Number of ensemble members
N_{t_i}	Number of how many times the particles are duplicated
N_{t_t}	Total number of replicated particles
P	Complex phasor
$\vec{P}_0$	Point located on a reference surface height
$\vec{P}_H$	Point located on the surface height
p	Probability density function
p_d	Probability density function of the observations

p_m	Probability density function of the model
Pr	Probability
Q_n	Cumulative sum of the normalised weights
r	Surface distance
R	Error covariance of the observations, when used in a statistical context
R	Range to the master satellite acquisition, when used in context of InSAR
R	Radial distance, when used in context of the Mogi source model
$R*$	Radial distance of image source
R_t	Number of residuals
$\mathrm{Re}\{P\}$	Real part of the phasor
RMSE	Root mean square error
$\vec{S}$	Slave satellite position
u_x, u_y, u_z	Displacement in x-, y-, z-direction
u_m	Random numbers from an uniform distribution with zero mean
w_i	Normalised particle weight
$\hat{w}_i$	Weight residuals
W	Weights summed
x_1, y_1, z_1	Coordinates at the surface
x_{mogi}	Coordinates of the Mogi source in x-direction
X_{m}	Threshold for low and high points
y_{mogi}	Coordinates of the Mogi source in y-direction
Y_{m}	Threshold for low and high points
z	Depth
z_{mogi}	Coordinates of the Mogi source in z-direction
α	Radius
α	Heading (azimuth) of satellite, when used in context of InSAR
α_h	Heading (azimuth) of satellite with respect to the North
γ	Scale parameter used in half width at half maximum (HWHM)
δ	Dirac delta
Δ_{area}	Change in area
Δ_{volume}	Change in volume
ΔP	Change in pressure
$\Delta x, \Delta y, \Delta z$	Difference between the surface coordinates (x_1, y_1, z_1) and Mogi coordinates $(x_{\mathrm{mogi}}, y_{\mathrm{mogi}}, z_{\mathrm{mogi}})$
ϵ_{ij}	Strain in ij-direction
θ_{inc}	Incidence angle
λ	Wavelength of the radar, when used in context of InSAR
λ	Lamé first elastic constant
μ	Shear modulus of elasticity, Lamé second elastic constant
ν	Poisson's ratio, a measure of a material's compressibility perpendicular to an applied stress
π	Pi
σ	Standard deviation
σ^2	Variance
σ_{ij}	Stresses in ij-direction
φ	Phase difference
φ_{atmo}	Atmospheric part
φ_{defo}	Deformation part

φ_{flat}	Flat Earth part
φ_{noise}	Noise part
φ_{orb}	Orbital part
φ_{scat}	Scatter part
φ_{topo}	Topographic part
χ_i	Cumulative distribution of the particle weights
ψ	Phase
Ψ	Full state

1 Introduction

1.1. Motivation

The aim of this research is to explore how surface subsidence measurements can be used to derive information about subsurface processes, such as volume change, that is induced by hydrocarbon production. The estimated subsurface information could provide insights of the subsurface compaction behaviour. In addition this compaction behaviour could provide a future production prediction method, when linked to the gas production and reservoir pressure change. The specific research area is Groningen, where subsidence is induced by hydrocarbon production.

Subsidence of the surface can be caused by natural and anthropogenic factors. Anthropogenic factors that cause subsidence are drainage, mining, groundwater extraction and consolidation. The subsidence in Groningen is caused by hydrocarbon production.

The discovery of the giant Groningen hydrocarbon field in 1959 triggered the exploration and production of natural gas in the Netherlands (Breunese et al., 2005). There are now many hydrocarbon fields present onshore and offshore in the Netherlands (figure 1.1). The production of hydrocarbons causes a pressure decline in pores of the reservoir and leads to compaction of the porous reservoir rock due to the weight of the above lying layers, the overburden. The compaction manifests itself at the surface in the form of subsidence, as shown in figure 1.2 on the left and the pressure decline is shown on the right. The surface subsidence of the Groningen field has an oval shape with a diameter of several kilometres and a subsidence of 22-30 cm in the centre and north of the field, while the south experiences a subsidence of 10-18 cm. The change in pressure and volume in the subsurface could reactivate faults and cause earthquakes at reservoir level. Furthermore the induced subsidence and earthquakes lead to damages of buildings at the surface above the reservoir. This is the case for the Groningen region in the north of the Netherlands.

Seismicity induced by the production of gas is monitored and recorded by the KNMI. The induced seismicity started near Assen on 26th of December 1986 with a magnitude of M_L = 2.8. The limited magnitude of $M_L \leq 2.0$ in the Groningen region changed on 16th of August 2012, when there was an earthquake of magnitude M_L = 3.6 at Huizinge in the municipality of Loppersum. Several strong earthquakes followed with a magnitude around $M_L \geq 3.0$ (orange dots in left figure 1.2).

The hydrocarbon exploration plan of Groningen for the coming three years and the monitoring and precautions of possible future induced earthquakes and subsidence are summarized in the winningsplan of Groningen (NAM, 2016). Pressure maintenance is expected to reduce the seismic hazard and reservoir compaction, but to what extent is not established and understands yet, therefore further research is needed.

The total hydrocarbon production rate per year is now lowered to reduce the number and magnitude of the earthquake. The effect of this decreased production is monitored. Despite the reduction of hydrocarbon production in the Loppersum region, a major induced earthquake of magnitude M_L = 3.4 was registered on 8th of January 2018 in Zeerijp near cluster 't Zandt.

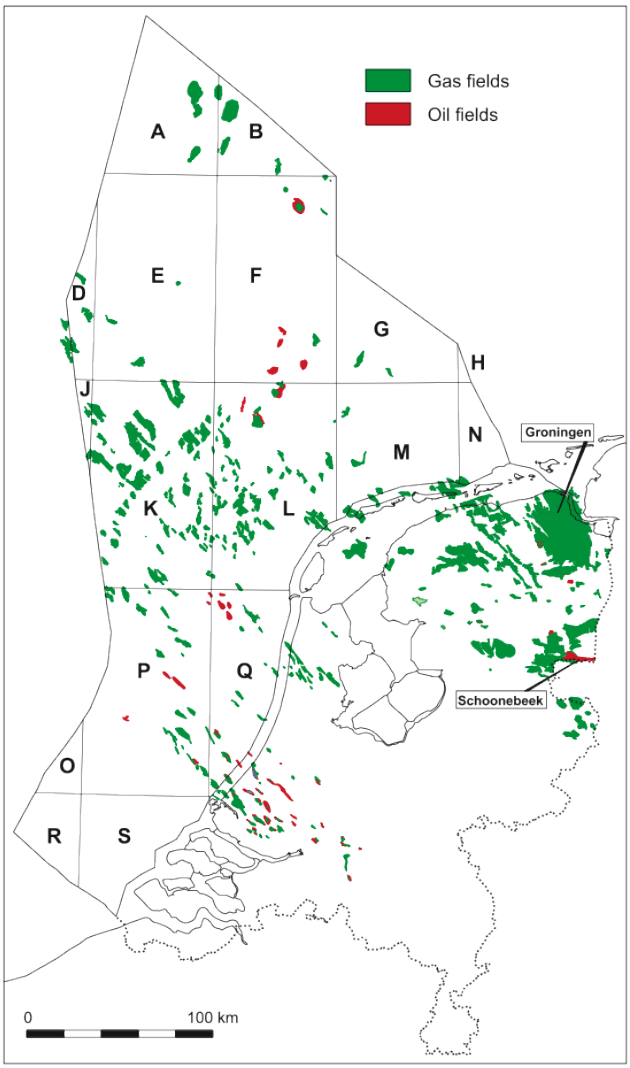

Figure 1.1: Gas and oil fields in the Netherlands onshore and offshore (source: De Jager and Geluk (2007))

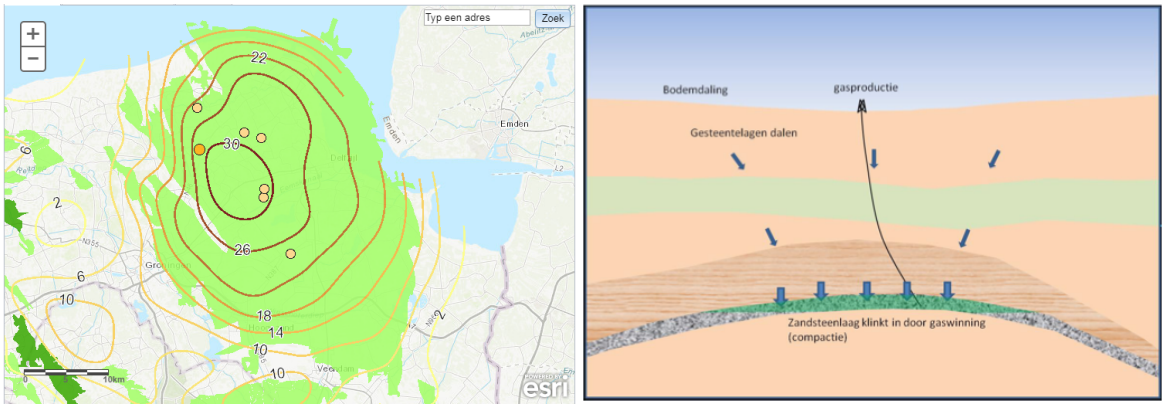

Figure 1.2: **Left**: The total surface subsidence in cm of the Groningen hydrocarbon field estimated using levelling campaigns for the period 1963 to 2013. The largest green outline is the Groningen gas field; the smaller green patches are smaller gas fields. The dark green areas are gas storage fields. The contour lines show the amount of subsidence that is larger in the centre and North of the field than in the south. The orange dot is the Huizinge earthquake and the light orange dots are earthquakes $M_L > 3.0$ between 2012 and present. (source: NAM (2017a)) **Right**: Subsidence illustration, where the reservoir (green part) experiences a decline in pressure. The reservoir compacts due to the weight of the overlying layers, the overburden (source: NAM (2016))

1.2. Space-geodetic PS-InSAR surface measurements

The satellite radar technique Persistant Scatterer Interferometric Synthetic Aperture Radar (PS-InSAR) provides deformation time series of the surface and can monitor surface deformation during the day and night. The spatial resolution of the PS-InSAR technique depends on the reflectivity of the ground objects (houses are good reflectors) and the temporal resolution depends on the repeat pass of the satellite, which is different for each satellite. The Groningen area is 30x40 km and the spatial resolution of the PS-InSAR technique provides coverage of this area. The technique is well suited for this thesis research, where a high spatial and temporal resolution will help to derive subsurface processes from the subsidence measurements.

1.3. Current methods on estimating subsurface processes from surface measurements

Previous studies of estimating subsurface processes from geodetic measurements in the Netherlands are for the locations Bergermeer gas field in North-Holland near the city of Alkmaar and the Groningen gas field. All studies use an inverse modelling method or data assimilation to estimate subsurface processes from observed levelling or PS-InSAR measurements. Data assimilation can be considered as an inverse modelling method, but does not involve inversion.

The Bergermeer location has studies done by Hanssen (2008) and Fokker et al. (2016), where the first one uses the analytical solution of Mogi (1958) for reservoir modelling and an inverse Bayesian model to estimate the parameters for the analytical solution. The subsidence observations are levelling and PS-InSAR measurements. Fokker et al. (2016) uses the semi-analytical forward model of Fokker (2002) and Fokker and Orlic (2006) to model surface movement. The study uses space-geodetic PS-InSAR measurements in order to estimate subsurface model parameters of the Bergermeer gas field. The goal is to match pressure and aquifer activity to surface movement. The inverse modelling method is an Ensemble Smoother with multiple data assimilation of Emerick and Reynolds (2013). This method can handle the non-linearity of the forward model and enables a future extension of parameters to be estimated. Both Bergermeer studies will be explained in detail further on in the thesis.

The Groningen location has studies done by Fokker and Van Thienen-Visser (2016); NAM (2016); Van Oeveren et al. (2017); Van Thienen-Visser et al. (2015), where analytical and finite element geomechanical models are used to translate reservoir compaction towards the surface. Furthermore estimation methods used in these studies are linear inversion and Bayesian methods.

An inverse modelling or data assimilation method is also required for this thesis in order to estimate subsurface information from subsidence values at the surface. A couple of data assimilation methods are already tested in previous studies, as described above. This thesis tests an upcoming reservoir history matching data assimilation method, the particle filter (Emerick and Reynolds, 2013; van Leeuwen, 2010), in combination with a simple subsurface volume change method of Mogi (1958). The Mogi volume change method is a point source. The choice for using the Mogi point sources is that this analytical method provides volume changes in the reservoir and the number of Mogi sources can be expanded easily in any desired number. This provides the user a lot of freedom in the number of Mogi sources placed at reservoir level. The computed surface deformation of each Mogi point source is summed into one surface field of subsidence values. The data assimilation method particle filter is able to extent the number of estimated parameters and therefore changing the number of Mogi sources is possible. Furthermore any other geomechanical model could be used in a future extension of the particle filter method.

1.4. Research objective

The main aim of this research is how to derive information about subsurface processes from subsidence measurements and can be formulated into a main research question as follows:

How can the particle filter, as a data assimilation technique, be used in order to estimate geomechanical parameters of subsurface processes, such as reservoir volume change, from space-geodetic PS-InSAR surface measurements?

The particle filter method is explored for the Groningen region. This method finds the best fit between observed subsidence values and modelled subsidence values. The observations are measured by the satellite radar technique PS-InSAR and a forward model, a geomechanical model, models the subsidence. The geomechanical model is the Mogi point sources model. This model translates the subsurface volume changes into subsidence values at the surface. If the estimated volume changes are linked to the hydrocarbon production or reservoir pressure change, then future predictions of the amount of subsidence can be made for a known production rate. The workflow scheme of this thesis is shown in figure 1.3 and provides an overview of the input / output of the particle filter and the corresponding chapters.

The main research question is broken up into sub-questions in order to reach the aim of this thesis, namely how to derive information about subsurface processes from subsidence measurements at the surface. The particle filter is first tested in an identical twin experiment with synthetic data (simulated data) that has a truth and an estimated part. The truth part is to be recovered with the particle filter. The amount of recovery is a measure of how well the particle filter performs. This knowledge is used for interpreting the particle filter results of the real case, when applying the particle filter to PS-InSAR measurements of the Groningen region and estimating geomechanical parameters of the Mogi point source model.

The sub-questions are divided in into two parts, namely the particle filter experiment and the particle filter applied to the real Groningen case. The sub-questions for the particle filter experiments part are:

1. What are the limitations of the geomechanical model when used in the particle filter?
2. How does the particle filter perform on synthetic data in an identical twin experiment?
3. Are there limitations of the particle filter?

The sub-questions for the second part, application of the particle filter to PS-InSAR measurements, are:

4. How does the particle filter perform on the PS-InSAR measurements?
5. Can a number of Mogi sources at well locations and at a reservoir depth of -3000 m adequately represent subsurface processes?
6. The hydrocarbon production is lowered in the Loppersum production region after the year 2013 in order to lower the number and magnitude of induced seismic events. Is this change in production visible in the PS-InSAR measurements, for example by showing a decrease in subsidence?
7. Is it possible to estimate geomechanical model parameters that model the observed surface deformation? Or is there a missing part in modelling the surface deformation signal?
8. Is there any link between the estimated Mogi source strengths and the hydrocarbon production and / or the change in reservoir pressure?

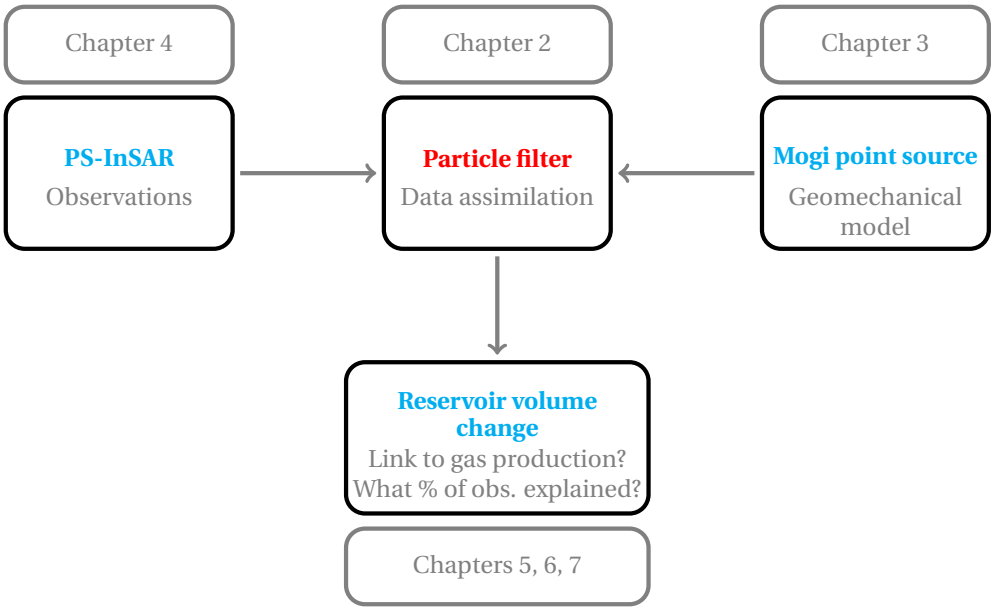

Figure 1.3: Workflow of this thesis, **red** = method, **blue** = input / output and obs.=observations.

1.5. Outline

The thesis is structured into eight chapters. Chapter 2 provides a theoretical background of the data assimilation method and in particular the particle filter technique. Furthermore previous studies of estimating geomechanic processes and parameters from surface measurements are described for two regions in the Netherlands, the Bergermeer gas field and the Groningen gas field.

Chapter 3 provides information of the hydrocarbon and salt production of the Groningen area. In addition the geomechanical model, the Mogi point source, is described. This model translates reservoir volume changes towards the surface into subsidence values.

Chapter 4 contains the observation technique that is used to observe surface deformation. This is the space-geodetic PS-InSAR technique.

Chapter 5 contains synthetic experiments of the particle filter. This is done to find out the performance and possible limitations of the particle filter. There are four experiments applied to three different setups.

Chapter 6 shows the results of the particle filter method applied to descending PS-InSAR measurements. In addition the particle filter method is applied to ascending PS-InSAR measurements and the preliminary results are shown in chapter 7. Furthermore chapter 8 provides a conclusion and recommendations.

2

Particle filter theoretical background

This chapter contains the theoretical background of a particle filter, a data assimilation technique. Section 2.1 explains the data assimilation technique, section 2.3 describes several data assimilation techniques and section 2.4 presents the particle filter method that is used in this thesis. In addition previous studies of estimating subsurface processes from PS-InSAR measurements are given in section 2.6.

2.1. Data assimilation

Data assimilation (DA) is the science where observational data of a system is fused with estimates of that system from a model, in order to obtain a new and more accurate description of the system (Vetra-Carvalho et al., 2018; Wikle and Berliner, 2007). Examples of a system are processes in meteorology e.g. cloud formation and precipitation; in oceanography e.g. ocean circulation; and in the petroleum industry for example reservoir history matching (Emerick and Reynolds, 2013).

Data assimilation can be considered as an inverse modelling method, but does not use inversion. An illustration of forward and inverse modelling is shown in figure 2.1 together with the mathematical notation. This figure helps to visualise the problem and method of this thesis. The forward model is the Mogi source model (Mogi, 1958) and this model is used for translating reservoir volume changes towards the surface. The data assimilation method particle filter is used to estimate the Mogi model parameters.

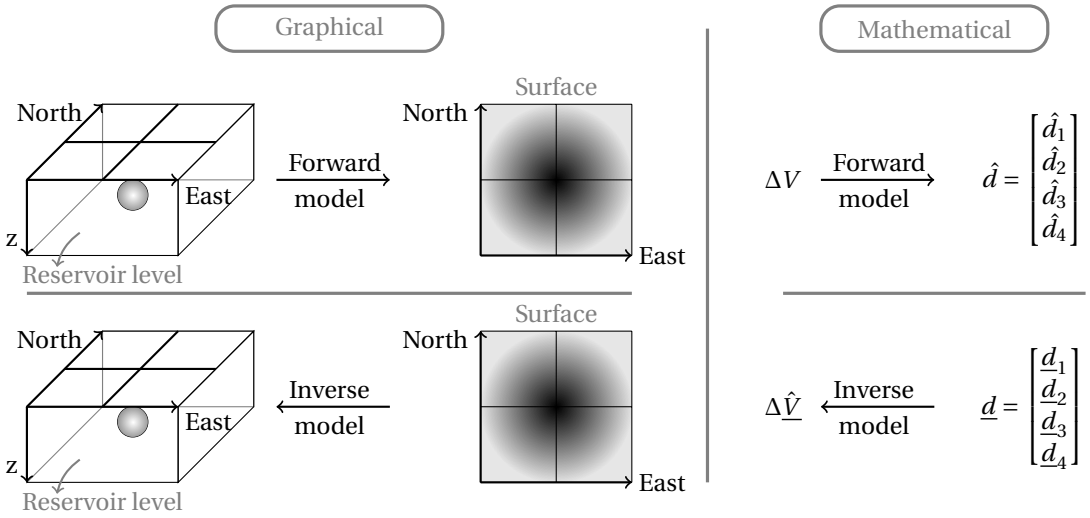

Figure 2.1: Graphical illustration and mathematical notation of a forward and inverse model for a subsidence bowl. The forward model in this thesis is the subsurface volume changes translated into surface deformation. The inverse model is where the observed surface deformation is translated into subsurface volume changes; this is the reverse of the forward model. •, ΔV=volume change and □, $\underline{d}$=observations (four)

In addition to the DA methods, this method requires observations and a *prior*, a model that models the

state of the system in order to obtain the *posterior*, i.e. the state of a system. This thesis uses the observations obtained by the PS-InSAR technique and the prior is a geomechanical reservoir model that translates reservoir volume changes into surface subsidence values. The used geomechanical model is the analytical solution of Mogi (1958). This model is explained in chapter 3 and the PS-InSAR technique is explained in chapter 4.

There are various types of data assimilation methods; two of them are mentioned in the introduction chapter, namely Ensemble Smoother with multiple data assimilation; and the particle filter. In addition data assimilation methods like the Kalman Filter (a.k.a. Least Squares Estimator) and Ensemble Kalman Filter are known and used. All these methods uses Bayes' theorem to obtain the posterior of the system, this theorem is explained in section 2.2.

2.2. Bayes' theorem

Bayes' theorem consists of two fundamental rules of probability theory, namely the sum rule and product rule. Probability theory provides a mathematical framework in how to quantify and manipulate uncertainty (Bishop, 2006). Probability is expressed in a number ranging from 0 - 1, where absolute certainty of an event is 0 or 1 and uncertainty any number in between 0 and 1 (Bishop, 2006; Davis, 2002). The sum and product rule of the probability theory is best explained by a simple example.

Figure 2.2: **a** A red box with a black and white coloured marble, as an illustration used in the **sum** rule of the probability theory. **b** A red box with a black and white coloured marble and a black cube, as an illustration used in the **product** rule of the probability theory.

The **sum rule**: a setting of a red box with two marbles. Collecting a marble from this red box will have the probability that it is black or white coloured (see figure 2.2 a).

This situation has only two possible outcomes. If the marble is black coloured, the marble cannot be white coloured, and vice versa. This example is mutually exclusive. The probability of collecting a black coloured marble is 0.5 and a white coloured marble is 0.5. The probability that one event happens or the other is the **sum** of their separate probabilities:

$$\Pr(\text{black } \textbf{or} \text{ white}) = \Pr(\text{black}) + \Pr(\text{white}) \tag{2.1}$$

where Pr is the probability. For the example is found:

$$\Pr(\text{black } \textbf{or} \text{ white}) = 0.5 + 0.5 = 1. \tag{2.2}$$

The **product rule**: an item is collected from a red box in anticipation of finding a black coloured marble, instead of a white coloured marble; or a black coloured cube (see figure 2.2 b).

The colouring of the marbles and cubes are at a later time than the shaping of these items. Both events, finding a black item and being a marble, can occur at the same time, but they are not related they are independent. The probability of collecting a marble is 0.5 and black coloured is 0.5. The *joint* probability of collecting a black coloured marble is the **product** of the probabilities:

$$\Pr(\text{marble } \textbf{and} \text{ black}) = \Pr(\text{marble}) \cdot \Pr(\text{black}). \tag{2.3}$$

For the given example the probability of collecting a black coloured marble:

$$\Pr(\text{marble } \textbf{and} \text{ black}) = 0.5 \cdot 0.5 = 0.25. \tag{2.4}$$

If two events are related and the outcomes are dependent on each other, than the joint probability of these events are conditional. *Conditional* probability is very useful, because an event can be observed, while the other related event is hidden.

For example collecting blind an item from the red box results in feeling the shape of the item, but not seeing the colour of the item yet. The marble shape can occur in both colours, while the cube shape can occur only in black. What is the probability that the black item is a marble? Event A is that the item is a marble and event B that the item is black. The conditional probability of this example is given as $\Pr(A|B)$. In order to compute this conditional probability Bayes' theorem is used and is written as follows (Bishop, 2006; Davis, 2002):

$$\Pr(A,B) = \Pr(A|B)\Pr(B) = \Pr(B|A)\Pr(A), \tag{2.5}$$

where $\Pr(A,B)$ is the *joint* probability and $\Pr(A|B)$ and $\Pr(B|A)$ the *conditional* probabilities. Equations of (2.5) combined gives Bayes' theorem:

$$\Pr(A|B) = \frac{\Pr(B|A)\Pr(A)}{\Pr(B)}. \tag{2.6}$$

Bayes' theorem can be applied to the marble being black coloured example, by defining the separate probabilities first, after Bishop (2006); Davis (2002):

- $\Pr(A)$, the probability that the item is a marble despite other information. This is 0.5.
- $\Pr(C)$, the probability that the item is not a marble shape, but a cube shape. This is 0.5.
- $\Pr(B|A)$, the probability that the item is black coloured given that the item is marble shaped. This is 0.5.
- $\Pr(B|C)$, the probability that the item is black coloured given that the item is cube shaped. This is 1.
- $\Pr(B)$, the probability that the item is black coloured, despite other information. This is $\Pr(B) = \Pr(B|A)\Pr(A) + \Pr(B|C)\Pr(C)$, when filling in $\Pr(B)=0.5 \cdot 0.5 + 1 \cdot 0.5 = 0.75$.

The above information is filled in Bayes' theorem eq. (2.6):

$$\Pr(A|B) = \frac{\Pr(B|A)\Pr(A)}{\Pr(B)} = \frac{0.5 \cdot 0.5}{0.75} = 0.33. \tag{2.7}$$

Bayes' theorem can also be applied on probability density functions (pdf).

2.3. Data assimilation methods

There are several types of data assimilation methods for example the Kalman filter, ensemble Kalman filter, particle filter and ensemble smoother. These examples are described below.

The Kalman Filter (KF) is a sequential data assimilation approach derived from Bayes' theorem by assuming a Gaussian prior and likelihood probability density function; linear model operators; and independent measurement and model noise processes. A sequential approach means that when new data becomes available the previous estimate of the system state is updated without starting the calculations from the beginning. The mean and the covariance of the Kalman filter are propagated between observations and model equations; this is the speciality of the filter. The model equations can be nonlinear, then the filter is used as the Extended Kalman Filter, where the model is linearized. The error covariance in this method can become unstable and too large to be stored. Therefore the Ensemble Kalman Filter (EnKF) is developed to overcome this problem (van Leeuwen et al., 2015; Vetra-Carvalho et al., 2018; Wikle and Berliner, 2007).

The ensemble Kalman filter is first introduced by e.g. Evensen (1994), and is a Monte Carlo approach, where the prior means and variance/covariance matrices are estimated by Monte Carlo samples. These samples are named ensembles. Monte Carlo methods are based on stochastic numerical sampling from distributions (Bishop, 2006). The EnKF was introduced in oceanographic problems and made the application of the Kalman filter possible for high-dimensional problems in oceanography, but also in meteorology. There are many variation of the EnKF and a review can be found in Vetra-Carvalho et al. (2018).

The Ensemble Smoother with multiple data assimilation (ES-MDA) uses a smoother. A smoother computes an update by assimilating all the available data (past and present), instead of the sequential in time approach of the ensemble EnKF method. This is the only difference with the EnKF method. The parameter state estimation problem becomes a parameter estimation problem. The EnKF is a parameter state estimation problem and observes inconsistency issues with state estimation. The multiple data assimilation in ES-MDA means that the ensemble smoother is applied multiple times. It is an iterative procedure where the output ensemble of the smoother is the input of the next ensemble smoother, while using the same observed data (Emerick and Reynolds, 2013; Fokker et al., 2016).

The particle filter is like the ensemble Kalman filter and uses ensembles (in this case named particles) sampled from a distribution and these samples are the prior pdf. However the particle filter is a fully nonlinear data assimilation technique and obtains the posterior using the prior and likelihood probability density function without the restriction of being Gaussian. These are the advantages of the particle filter over the ensemble Kalman filter and the main reasons to use and test the particle filter in this thesis. A Gaussian prior and likelihood results in a Gaussian posterior, but if the prior and likelihood are non-Gaussian then the posterior is also non-Gaussian. There are many variations of the particle filter and a review can be found in Vetra-Carvalho et al. (2018). The particle filter is explained in detail in section 2.4.

2.4. Particle filter

The particle filter is a non-linear data assimilation technique and uses a Monte Carlo methods where the probability distributions of the model state, given the observations, is approximated by a number of particles. The particles represent thus the model states. These particles are often called 'ensemble members'. This term is used further on in this thesis.

The model state (ensemble members) can be described by a probability density function. The parameters in a model are described each by a pdf and the joint probability density of all parameters is the full state. In particle filtering the full state Ψ is described by the model state pdf $p(\Psi)$. This pdf is combined with observations to obtain and estimate the posterior pdf. Bayes' theorem applies this and can be written as follows with model state Ψ and observations d:

$$p_m(\Psi|d) = \frac{p_d(d|\Psi)\,p_m(\Psi)}{p_d(d)}, \tag{2.8}$$

where $p()$ refers to a probability density function, subscript m refers to the model and subscript d refers to the observations. The denominator of eq. (2.8) is rewritten as:

$$p_d(d) = \int p(d,\Psi)\,d\Psi = \int p(d|\Psi)\,p_m(\Psi)\,d\Psi \tag{2.9}$$

which shows that the denominator is the normalising of the posterior distribution. The normalising constant is required to ensure that the sum=1 on the left-hand side of the equation. Illustration of probability density functions is shown in figure 2.3, where the prior and observation pdf results into the likelihood pdf, in between both pdf's. In addition the prior and likelihood pdf results into the posterior pdf.

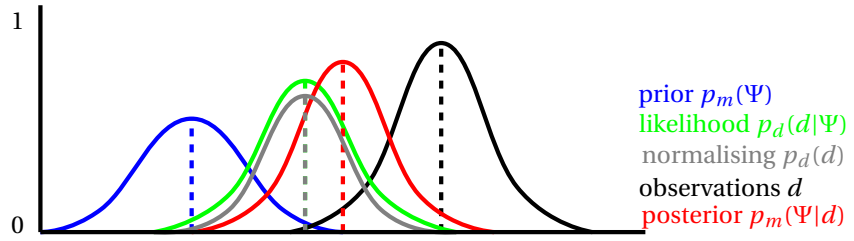

Figure 2.3: Probability density function illustration of observations, prior, likelihood, normalising and posterior distribution, as used in Bayes' theorem. The normalised likelihood pdf is a combination of the prior and observations pdf. The posterior is a combination of the prior and likelihood and then normalised.

The four distributions of Bayes' theorem are explained below, after Bishop (2006); Van Leeuwen (2009); Wikle and Berliner (2007):

- The data distribution $p_d(d|\Psi)$ refers to the probability density of the data given the model state. It represents the **likelihood** of the data, given the model state.
- The **prior** distribution $p_m(\Psi)$ is the prior pdf of the model state.
- The marginal distribution $p_d(d)$ also known as the prior predictive distribution. The distribution is the pdf of the observations and is not dependent on the model state. This marginal distribution is the **normalising** of the posterior distribution. It can be seen as a normalising constant.

- The **posterior** distribution $p_m(\Psi|d)$ is the distribution of the model state, given the data. The posterior distribution is an update of the prior knowledge $p_m(\Psi)$ given the observations $p_d(d)$: **posterior**= **likelihood** x **normalising constant** x **prior**. The posterior distribution is the one that is estimated in this thesis.

The probability density function of the model $p_m(\Psi)$ is not easy to represent, because it depends on many variables. The particle filter uses therefore the idea of representing the model pdf by a number of random draws from the model. The ensemble members are created by a Monte Carlo technique and the N ensemble members from model density $p_m(\Psi)$ can be seen as:

$$p_m(\Psi) = \frac{1}{N}\sum_{i=1}^{N}\delta(\Psi - \Psi_i), \tag{2.10}$$

where the randomly drawn particles are denoted with subscripts i and δ is the dirac delta function (Van Leeuwen, 2009; Vossepoel and van Leeuwen, 2007). An implementation of Bayes' theorem is importance sampling; this is a technique where a weight is assigned to a correct estimation (Bishop, 2006). Using eq. (2.10) in eq. (2.8):

$$p_m(\Psi|d) = \sum_{i=1}^{N} w_i\delta(\Psi - \Psi_i), \tag{2.11}$$

where weights w_i assigned to correct ensemble members are given by:

$$w_i = \frac{p_d(d|\Psi_i)}{\sum_{j=1}^{N} p_d(d|\Psi_j)}. \tag{2.12}$$

The probability density function of the observations $p_d(d|\Psi)$ are often taken as a Gaussian distribution:

$$p_d(d|\Psi_i) = \frac{1}{\sqrt{2\pi\sigma^2}}\exp\left\{-\frac{1}{2}[d - H(\Psi_i)]^T R^{-1}[d - H(\Psi_i)]\right\}, \tag{2.13}$$

where d is the observation, σ^2 the variance, $H(\Psi_i)$ the model generated output that is similar to the observations d and R the error covariance of the observations (Van Leeuwen, 2009).

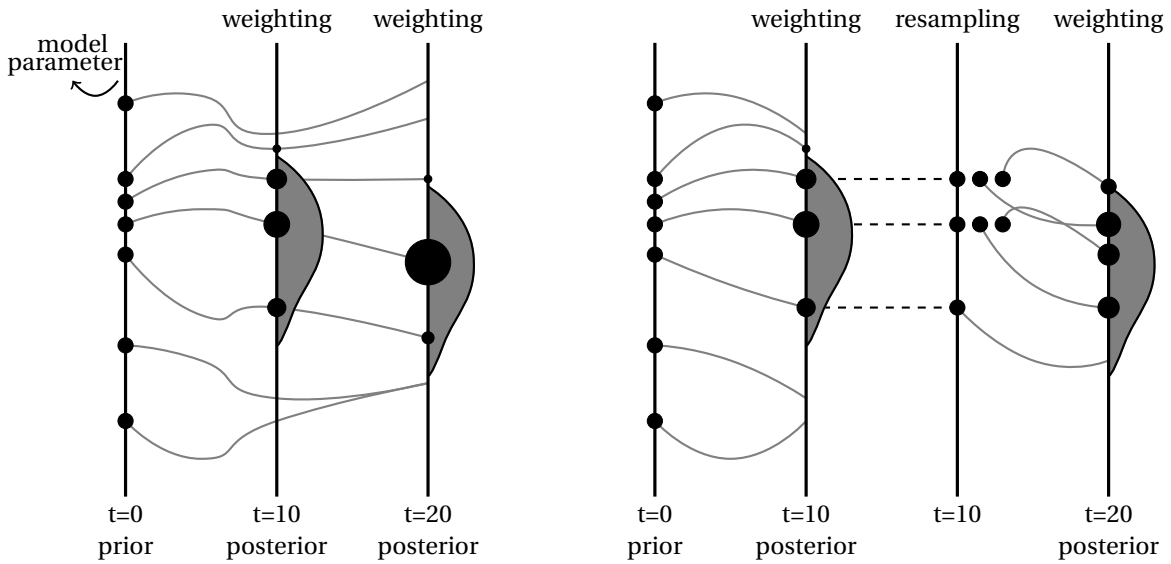

Figure 2.4: **Left**: Particle filter with importance sampling. The vertical axis represents the model variable, where the size of the bullets on the axis corresponds to the weight of each ensemble member (particle). The horizontal axis represents time. The ensemble members are equal sized at t=0, weighted at t=10 and at t=20 the filter is degenerated. **Right**: Particle filter with the resampling step, this example is the sequential importance resampling (SIR). The ensemble members are equal sized at t=0, weighted at t=10, resampled at t=10 and t=20 is the posterior. (after: Van Leeuwen (2009))

The steps of importance sampling are listed below together with the corresponding time steps in brackets referring to the left visualisation in figure 2.4.

1. N ensemble members Ψ are sampled from $p_m(\Psi)$ according to eq. (2.10), (t=0).

2. All ensemble members are generated forward in time, (t=0 to t=10).

3. The difference between observations and model output are multiplied with the observational density function $p_d(d|\Psi)$ in order to assign weights to correct ensemble members by eq. (2.12). These weights are normalised and this results in the posterior distribution $p_m(\Psi|d)$, (t=10).

4. Steps 2 and 3 are repeated until all ensemble members in time are processed, (t=20).

The advantage of importance sampling is that the ensemble members themselves stay the same and are not modified. However the disadvantage of importance sampling is that the ensemble members are not modified. When the ensemble members are weighted and move away from the observations, then the ensemble members are not directed back to the observations. A second disadvantage of importance sampling is that old weights are multiplied with new weights. After several runs one ensemble member will have all the weight and other ensemble members have low weights, this is called filter degeneracy. This filter degeneracy is not wanted, because the variation in the ensemble members is lost. Other definitions found in literature for filter degeneracy are 'filter divergence' or 'particle filter collapse' (Van Leeuwen, 2009; Vetra-Carvalho et al., 2018; Vossepoel and van Leeuwen, 2007) The problem of filter degeneracy can be solved by resampling and localisation. Localisation is using the particle filter local, this is a solution for the filter degeneracy in high-dimensional spaces with a large number of independent observations. The weights of ensemble members vary a lot and one ensemble member obtains a weight close to one, while the other ensemble members have weights close to zero. Applying resampling to this situation results into a variation loss of the ensemble members. The resampling technique is explained in section 2.5.

2.5. Resampling

Resampling is a method where the particles with low weights are abandoned and the particles with height weights are copied multiple times. An example of resampling is sequential importance resampling (SIR) (Van Leeuwen, 2009; Vossepoel and van Leeuwen, 2007). This method is shown in figure 2.4 (right) and explained in steps below.

1. N ensemble members Ψ are sampled from $p_m(\Psi)$ according to eq. (2.10), (t=0) .

2. All ensemble members are generated forward in time, (t=0 to first t=10).

3. The difference between observations and model output are multiplied with the observational density function $p_d(d|\Psi)$ in order to assign weights to correct ensemble members by eq. (2.12). These weights are normalised and this results in the posterior distribution $p_m(\Psi|d)$, (first t=10)

4. Resample the ensemble members with a high weight (when N times weight > 1) and the weights of the posterior ensemble members are equal again for the next step, (second t=10).

5. All ensemble members are generated forward in time, (second t=10 to t=20).

6. The weights are assigned to correct ensemble members by eq. (2.12), (second t=20).

7. Steps 2-6 are repeated until all ensemble members in time are processed.

The choice of resampling method is important, because also in the SIR method filter degeneracy can occur. Van Leeuwen (2009) discusses a couple of resampling techniques i.e., probabilistic resampling, residual sampling, stochastic universal sampling, Monte Carlo Metropolis-Hastings and regularization. The first one, probabilistic resampling, samples randomly from the weights density. The randomness of this method introduces sampling noise. This is unwanted noise. Residual sampling can be applied to reduce the sampling noise. The weights in this method are multiplied by the ensemble size N. A number of copies are taken of each ensemble member where the integer part of the weight is larger than 1. For example the ensemble member weight is 0.002 and N=1000, the integer part is then 0.002 x 1000 = 2. This value is larger then 1 and a copy is taken of the belonging ensemble member. The integer parts are subtracted from the weights. The resulting distribution is used to draw randomly the rest of particles. The residual resampling method is tested in this thesis and explained in section 2.5.1.

2.5.1. Residual resampling

The resampling technique in this study is used in an iterative way to obtain a better fit. This technique is similar to the nonlinear case of multiple data assimilation used in ES-MDA. This method perturbs the observation vector of each ensemble member for every iteration. This is done to keep variation (Emerick and Reynolds, 2013). The resampling technique in this study is thus an iterative way. There is no change in time; it is one set of observations. The best fit is obtained with a distribution created from the ensemble members with high weights. The ensemble members are randomly generated from this distribution. A problem that arises from resampling is that there are several identical ensemble members after the resampling step. If there is no model error, than the ensemble members remain the same during forward integration. This could lead to filter degeneracy. This can be avoided by adding noise (perturbation) or variation to the resampled ensemble members, this step is termed regularization or 'jitter'.

The residual resampling technique is used for this thesis, because it is a simple and easy-implemented method. This method is tested in chapter 5. Li et al. (2015) provide a qualitative comparison of resampling algorithms. This article is used to describe the resampling method below. The resampling techniques in this article are divided into sequential and distributed algorithms. The sequential algorithms use an approximating distribution of the latest weights. The residual resampling technique consists of two steps, namely a deterministic replication of the particles and sampling randomly from the remaining weights (residuals), this is the multinomial part. This multinomial part is also known as probabilistic resampling (Vetra-Carvalho et al., 2018). The deterministic replication of the ensemble members with a weight larger than $1/N$:

$$N_{t_i} = N w_i, \tag{2.14}$$

where N_{t_i}>1 represents the number of how many times the ensemble members Ψ_i are duplicated, for example an ensemble member with a high weight can be duplicated multiple times, while a lower weighted ensemble member is duplicated only once; N is the number of ensemble members and w_i is the normalised particle weight. The total number of ensemble members N_{t_t} that is replicated:

$$N_{t_t} = \sum_{i=1}^{N} N_{t_i}. \tag{2.15}$$

The number of rest places R_t that is needed to be filled: $R_t = N - N_{t_t}$. The second part is the multinomial part that is sampling randomly from the remaining ensemble member weights, the residuals. The weight residuals are computed as follows:

$$\hat{w}_i = w_i - \frac{N_{t_i}}{N}, \tag{2.16}$$

where $\hat{w}_i$ is the weight residual. These weights are normalised (sum=1) by multiplying it with a rest factor N/R_t. The number of rest places R_t to be filled is drawn from a uniform distribution u_m of interval (0,1). The random numbers, indices, are used to select weights from the cumulative sum of the normalised weights Q_n. The ensemble members are selected when the following condition is meet:

$$u_m < Q_n \tag{2.17}$$

with

$$Q_n = \sum_{k=1}^{n} \hat{w}_k, \tag{2.18}$$

where Q_n is the cumulative sum of the normalised weights with n the counter of ensemble members; u_m the number drawn from a uniform distribution with m the counter of rest places; and $\hat{w}_k$ is the normalised residual weight. The cumulative sum is used because it can detect a step change of the weights. For example if there are many low weights and these are summed cumulatively, than it results in small changes of the cumulative sum. One large weight between the low weights results in a major step change, when the weights are summed cumulatively. This large step spans a big interval of weights. This interval is more often true to meet the condition of eq. (2.17). And on average more index numbers are sampled near a large weight. This is wanted for this residual resampling method. The ensemble members are now duplicated and the total number N is achieved. The ensemble members need regularization or 'jitter' to prevent filter degeneracy. Randomly generated noise from a Gaussian distribution with a to be decided variance is generated to add to the Mogi source strength ensemble members after resampling is done.

2.6. Previous studies of estimating subsurface processes from geodesy measurements

This section describes studies that use inverse modelling in combination with geomechanical models in order to model surface deformation, caused by hydrocarbon or salt extraction in the subsurface in the Netherlands. The locations are the Bergermeer gas field in North-Holland near the city of Alkmaar and the Groningen gas field. The application of the deformation model is combined with InSAR and / or levelling measurements.

Levelling is a technique that measures height difference. The heights of a point relative to a reference frame can be computed when the height of a benchmark is known. The measured heights are typically measured relative to a model of the equipotential surface (geoid) (Verhagen, 2015). The levelling network of the Groningen field is shown in figure 2.5. In Groningen levelling campaign is done every 5 year.

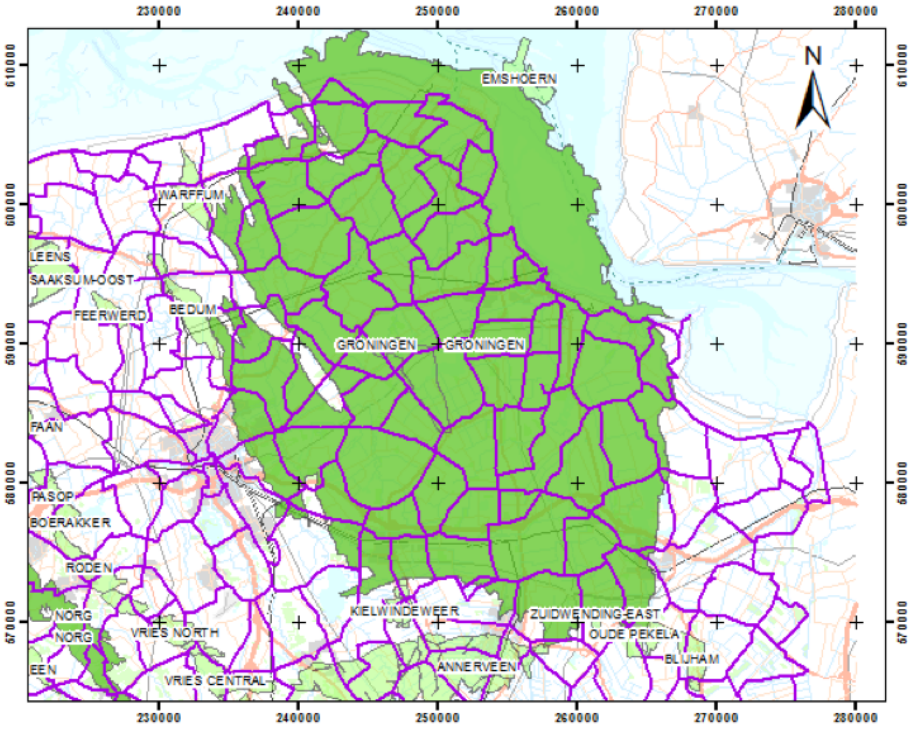

Figure 2.5: Levelling network (purple) of the Groningen field (green). (source: NAM (2013))

2.6.1. Bergermeer location

Hanssen (2008) uses the Mogi (1958) model for modelling the subsurface deformation of the Bergermeer gas field. The depth and position of the Mogi sources are kept fixed; therefore only the source strength of the Mogi sources is estimated. An inverse Bayesian model provides the volume changes of the correlated Mogi point sources. This inversion of estimating volume changes is done for levelling and PS-InSAR measurements. The study shows similar results of volume change for both measurement techniques. The Mogi sources are placed at the depth of the gas reservoir, around 2500 m. The Bergermeer location contains of five reservoirs. One of the reservoirs has a size of 1.0 x 3.6 km and 2 Mogi sources are placed in that reservoir. A second reservoir of size 2.0 x 6.0 km contains 5 Mogi sources. A source is placed every 1.5 x 1.5 km.

Fokker et al. (2016) uses the semi-analytical forward model of Fokker (2002) and (Fokker and Orlic, 2006) to compute surface movement. The study uses space-geodetic PS-InSAR measurements in order to estimate subsurface model parameters of the Bergermeer gas field. The goal of this study is to match pressure and aquifers activity to the surface movement. The inverse modelling method is an Ensemble Smoother with multiple data assimilation of Emerick and Reynolds (2013). The multiple data assimilation is applied in order to handle the non-linearity of the forward model. The Ensemble Smoother method is chosen over a least-squares regression method to enable a future extension of parameters to be estimated. The procedure of updating the model in a single step is called Ensemble Smoother and updating of the model for several time

steps is called a filter. The multiple data assimilation means that the Ensemble smoother is applied multiple times, the output of the first run is than used as input for the next run and so on. The method succeeded in estimating compaction coefficients for the Bergermeer gas field.

The above method is further illustrated by two case studies of Candela et al. (2017) to show the robustness of the above-described workflow. The first case study is a faulted and compartmentalized reservoir in the Netherlands, where undepleted gas compartments are identified. The second case shows variation in aquifer activity around a Dutch gas field, by using PS-InSAR data. The goal is to estimate model parameters such as compaction coefficient and elastic modulus of the under-overburden. The uncertainties of model parameters are disregarded. The authors propose to do a stochastic ensemble approach for each step in the workflow.

2.6.2. Groningen location

The geomechanical model of the winningsplan NAM (2016) computes the compaction due to depletion of gas at reservoir level. Two models are investigated that compute the reservoir level compaction, namely the time-decay and the isotach model. Both compaction models use reservoir pressure as input simulated by Shell's reservoir simulator MoReS. The reservoir compaction is translated to subsidence at the surface; this translation uses the semi-analytic approach of Geertsma (1973); Geertsma and van Opstal (1973). The above-described methodology is included in Shell's 'SubCal' software (NAM, 2016). The time decay compaction model is a model based on the observation of a delayed subsidence after pressure depletion. The subsidence continues after the depletion has ceased. The part in the system that governs the decay time scale is difficult to identify. It is likely that the pressure diffusion effects are not fully captured in the reservoir modelling step. Salt creep could also be a possible explanation. The time decay constant can capture the subsidence response to reservoir compaction. A first order diffusive time decay function is used to find the single time constant. There is a possibility that the time decay constant is not a material property of the reservoir rock, but can be due to reservoir geometry details like pore fluids (NAM, 2016).

The rate type compaction model (RTCiM) for sandstone is based on the isotach concept. The isotachs are constant loading rate lines in the stress-strain diagram. A unique isotach corresponds to every loading rate on a sample. The compaction of the reservoir rock depends on the loading rate as shown in laboratory experiments. A faster loading rate leads to a stiffer response, while a constant load leads to creep. The isotach Rate Type Compaction Model is represented by a set of three equations. The model is applicable to field situations where the reservoir compaction is considered one-dimensional (Pruiksma et al., 2015). The original rate type compaction model (RTCM) for sandstone was already developed in the 80's by De Waal (1986) and predicted a maximum subsidence between 60-70 cm at the end of the Groningen production period. The RTCiM model combines this RTCM model with the isotach concept (De Waal et al., 2015; NAM, 2016).

A numerical scheme (NAM, 2016) is used to calculate the compaction with the RTCiM model. A simulation computes the compaction.

Geomechanical models use subsidence measurements (levelling) for calibrating the model. Both models, the time decay and RTCiM, show good fit results with the observed subsidence values. The RTCiM is chosen as the base case for compaction models, because the fit is slightly better. Also this model reacts faster when changes in reservoir pressure occur. The maximum forecasted subsidence with this model is 50 cm in the centre after depletion of the gas reservoir.

Van Thienen-Visser et al. (2015) estimates and predicted subsidence by using the compaction models Rate Type isostach Compaction (RTiCM) and Time Decay. An insight in reservoir properties is provided by the resulting fit pattern between the estimated and measured subsidence. Both models model compaction. The compaction is dependent on rock type of the gas bearing reservoir layer, the Rotliegend sandstone for Groningen. The subsidence measurements consist of levelling and PS-InSAR data. A static geological model determines detailed information on porosity, reservoir thickness and depth of the reservoir. The porosity of the reservoir varies from 0.12 to 0.22. A 1D model is used to translate the compaction at reservoir level towards the surface subsidence. A Bayesian Red Flag procedure (Nepveu et al., 2010) is used to determine unknown parameters from the difference between modelled and measured subsidence. One of the unknown parameters that is estimated by the Red Flag procedure is the time decay in years of the time decay model. This parameter is around 4.8 years. The computed compaction by the RTiCM is shown in figure 2.6. The pattern of the difference (measured - modelled) is explained by differences in modelled porosity and aquifer pressure.

Fokker and Van Thienen-Visser (2016) use a linear inversion method to invert for compaction of the Groningen reservoir by using surface measurements of optical levelling of height differences. Double dif-

ferences are constructed between stable benchmarks of levelling campaigns. Compaction in the reservoir may affect the permeability and porosity. In this study the permeability changes are ignored, because of the small effect on reservoir pressure development. Furthermore the porosity changes have a small effect on reservoir pressure development as well, because of the compressibility of the gas. A linear elastic forward model is used to translate reservoir compaction to subsidence. The compaction results showed areas that compact more and less to what has been estimated with a prior compaction model.

Van Oeveren et al. (2017) history matches the Groningen filed dynamic model with pressure data and water influx data to subsidence data. Subsidence is modelled with a simplified geomechanical model and then matched to subsidence data. The goal of this study is to show how the subsidence data can be used to constrain dynamic reservoir models to pressure and water data and then used as a forecasting method. The reservoir pressure is measured at the production clusters and in observations wells. The subsidence data is a combination of satellite and levelling surveys. A specification of the satellite surveys is not mentioned in this paper, but I suspect it is GPS data.

The calculated reservoir compaction is translated to the surface by the equation of Geertsma and van Opstal (1973). The total surface subsidence is calculated as the sum of subsidence bowls for each grid cell (4 x 4 km). The method assumes a homogeneous half-space with a Poisson's ratio of 0.25. The root mean square error (RMSE) is calculated over the difference of modelled subsidence and measured subsidence. The study assumes that all the subsidence is caused by compaction of the Groningen reservoir. A set of 1000 different models is generated from a space-filling experimental design that is used to select settings for variable model parameters. Each model parameter is sampled within a uniform range.

The study concluded that a good match of subsidence data corresponds to a good match to pressure data at well locations. The subsidence data can be used to constrain the model outside of a well control. A depleting Carboniferous layer and residual gas in an aquifer can cause any residuals of the subsidence match.

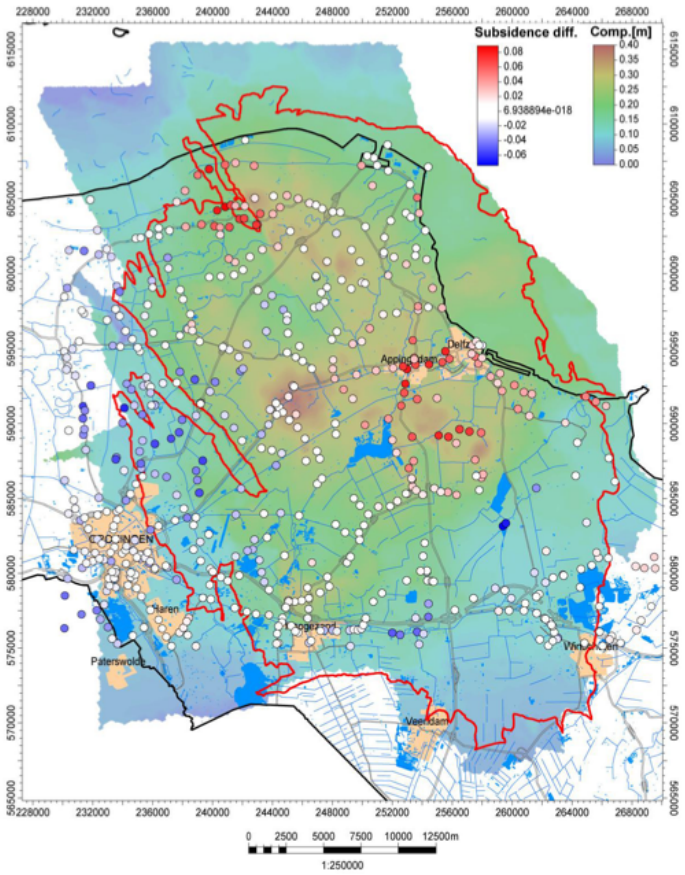

Figure 2.6: Groningen compaction [m] computed by the RTiCM model at January 2012. The difference (measured - modelled) is shown at levelling benchmarks in red/blue colours [m]. (source: Van Thienen-Visser et al. (2015))

3

Subsidence in Groningen

This chapter provides the geological background of the anthropogenic subsidence mechanisms for the Groningen location. These mechanisms are the hydrocarbon and salt production and explained in section 3.1. The background information provides the needed knowledge and understanding for interpreting the subsidence measurements and estimated geomechanical subsurface processes at different locations of the Groningen area. The geomechanical parameters are estimated in chapter 6 and 7. In addition the analytical solution of Mogi (1958), the geomechanical model, is described and translates reservoir volume changes to subsidence values. This solution is used in this thesis and described in section 3.4.

3.1. Groningen reservoir

The mining of salt and hydrocarbons causes a compaction of the reservoir layer, due to the change in pressure equilibrium. The overburden weight presses on the reservoir and causes compaction of the reservoir. The Groningen reservoir thickness varies from 140 m in the southeast to 300 m in the northwest. The reservoir can compact in the northwest more resulting in surface subsidence variation. Also the variable porosity of the reservoir layer and the presence of aquifers, water-bearing layers, that are connected to the depleting reservoir contributes to different surface subsidence measurements. The aquifer is located below the gas for the Groningen area, because the water is denser than the hydrocarbons (NAM, 2016). The geological southeast to northwest cross-section of figure 3.1 (left) shows the variable layer thickness of the gas-bearing Rotliegend sandstone. In addition reservoir compaction propagates not immediately towards the surface but

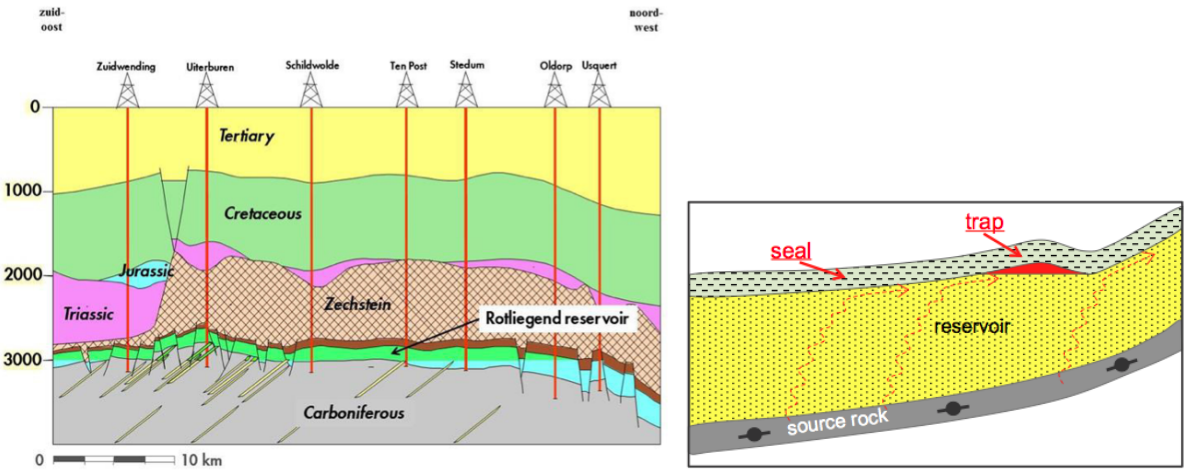

Figure 3.1: **Left**: Vertical schematic profile of the Groningen gas field from southeast to northwest. The Rotliegend reservoir (turquoise layer with green part is gas) is thicker in the northwest than in the south. The Zechstein on top of the Rotliegend is a salt layer and seals the gas-bearing layer. (source: NAM (2016)) **Right**: Vertical schematic profile of the four ingredients for a hydrocarbon field. The source rock charges the porous reservoir rock, under the influence of buoyancy. The gas is trapped in a structural anticline (red lens) and the impermeable seal layer seals the reservoir (source: De Jager (2014))

is subject to a delay in time (Ketelaar, 2009; NAM, 2016).

The top of the reservoir is located at a depth of 2750 m in the south to 2900 m in the north with the water zone at 3000 m (NAM, 2016). The four ingredients of a hydrocarbon field, source rock, reservoir, seal and trap, are illustrated in figure 3.1 (right). The reservoir rock is porous sandstone of the Permian Upper Rotliegend Group. The Groningen source rock is the Upper Carboniferous Westphalian that contains coal. The seal of the Groningen reservoir is Zechstein salt. The salt on top of the reservoir is produced at three locations in Groningen, Veendam, Winschoten and Zuidwending. The Groningen reservoir contains many traps, with variable thickness and depths.

3.2. Hydrocarbon production

The gas is extracted by the Nederlandse Aardolie Maatschappij (NAM) from 258 wells spread over 22 production locations of the Groningen gas field. The field has a size of 30 by 40 km. Furthermore there are 28 observation wells that are used for reservoir management. Figure 3.2 shows the 22 production clusters and the Groningen reservoir area (green). There are 4 production regions called 'Eemskanaal', 'Loppersum', 'Oost' and 'Zuidwest', respectively the coloured squares grey, orange, purple and blue. The gas production in the winter is higher than in the summer. The summer production is stored in empty gas fields; this is done to prevent major fluctuations in subsidence of the gas field.

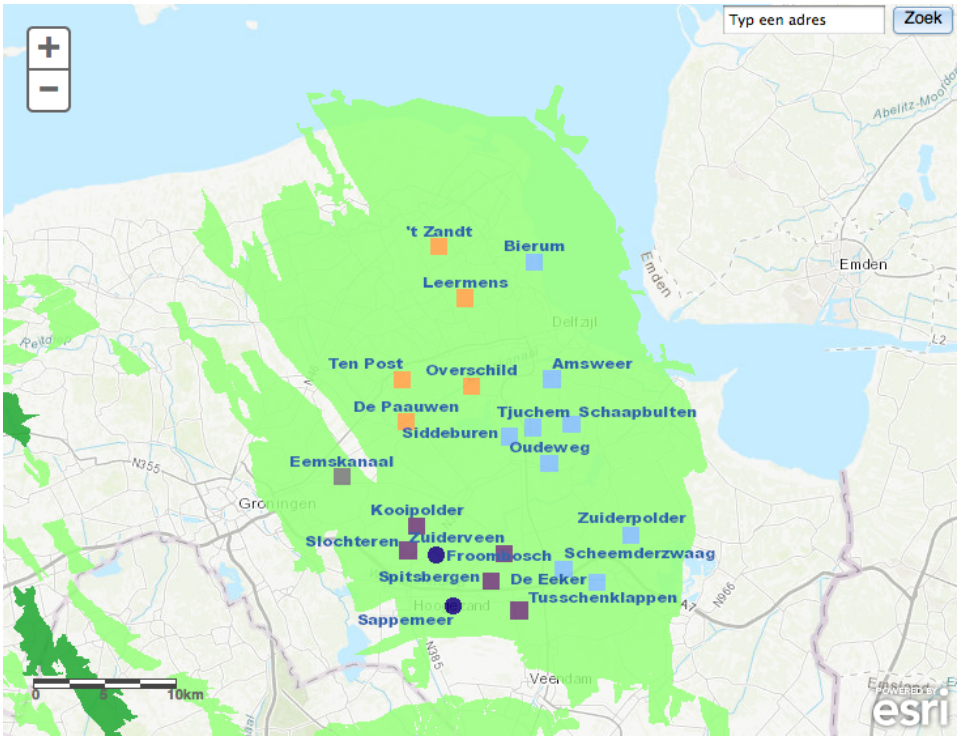

Figure 3.2: Groningen field with 22 production clusters and 4 production regions; orange=Loppersum, blue=Oost, grey=Eemskanaal and purple=Zuidwest. The two blue dots are called 'satellite of production location'; both are 2 production clusters and belong to the purple Zuidwest region, (source: NAM (2017b)).

The reservoir pressure declines over the years, due to the gas production as shown in figure 3.3. The reservoir pressure is used to produce the hydrocarbons from the production wells (NAM, 2016). The continuous production of the gas is done in a way to minimize pressure differences between north and south locations. Two Under Ground Storages (UGS) are developed to store the summer-produced gas and to have winter supplies. These are located in Grijpskerk and Norg and are the dark green areas of figure 3.2 (NAM, 2016). There is a decline in the total gas production, as shown in figure 3.4 in Nm^3 [1]. This decrease in production is after the year 2013, where the Dutch government decided to lower the production in order to lower the number and magnitude of the earthquakes.

[1] normal cubic meters Nm^3 for a temperature of 0°C and a pressure of 1.01325 bar

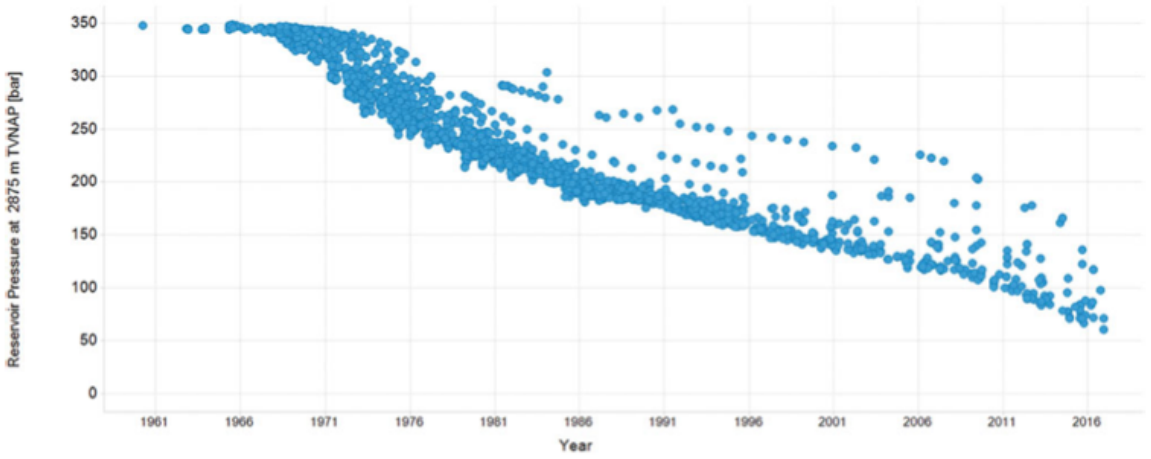

Figure 3.3: Down-hole pressure measurements of many wells in the Groningen field over the period 1959-2016 at 2875 m TVD NAP in the gas phase, TVD=true vertical depth as measured from the surface (source: Van Oeveren et al. (2017))

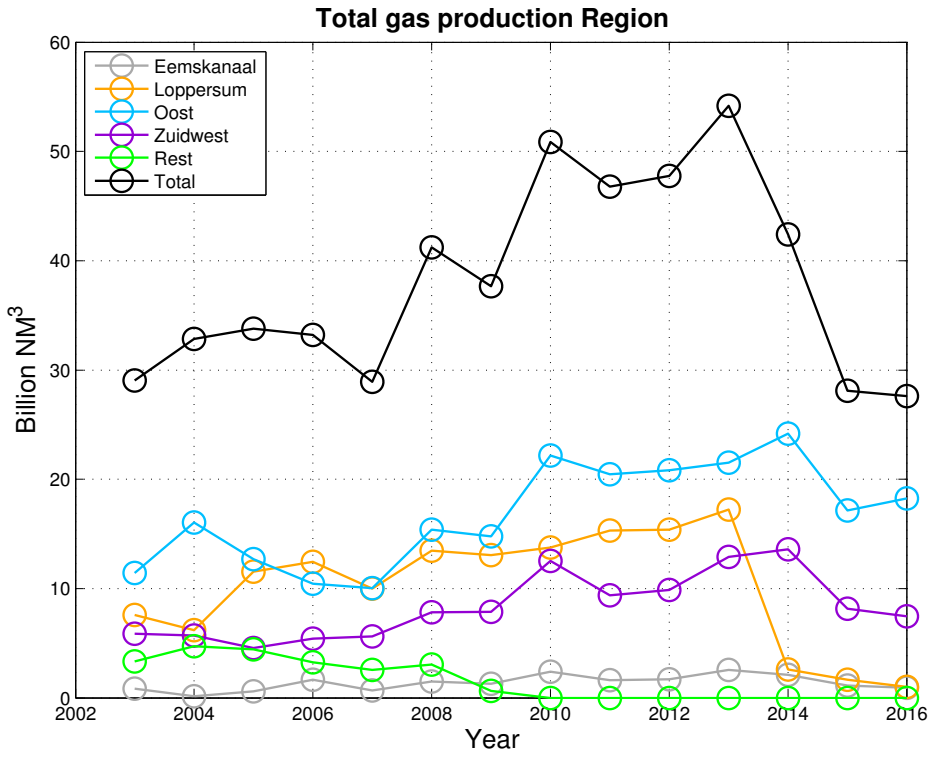

Figure 3.4: Total gas production and regional gas production for the period 2003-2016 in Billion Nm^3. The production is decreased in the Loppersum region after the year 2013, in order to reduce the number of induced earthquakes in that area. The rest region contains four wells that stopped producing after the year 2009. This region is shown, because it can possible influence the deformation rates for the years of 2010-2016. (data source: NLOG (2017b).)

3.3. Rock salt production

Three locations in the south of the Groningen gas field are rock salt production locations. Rock salt is produced from the subsurface by solution mining, where the hot water is injected into the salt. The salt dissolves and the saturated salt water is pumped to the surface. This kind of salt mining produces caverns that can close over time due to the plasticity of salt. When a thick layer of sediment lies on top of the salt than the buried salt can behave plastic due to pressure and temperature increases. The rock salt layers are the Zech-

stein Group and the Röt Formation (NLOG, 2017c). The salt can flow due to the weight of the rocks on top. This is how salt pillars and salt pillows are formed. Figure 3.5 shows a schematic of a salt pillar in the subsurface. The top of salt pillars is only 150-500 [m] below the surface. The locations are Veendam, Winschoten and Zuidwending (NLOG, 2017d). The yearly salt productions of the three locations are presented in figure 3.6 and show a stable production from 2006 to 2016.

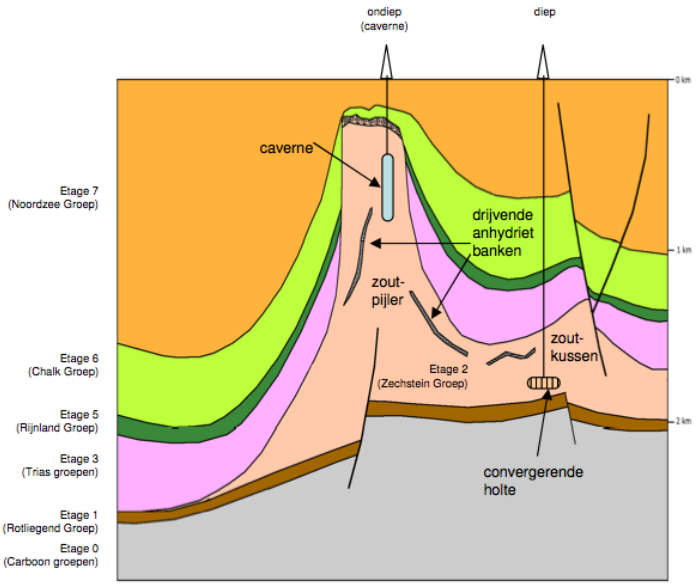

Figure 3.5: Vertical schematic profile of the rock salt production in a salt pillar. The top of the salt pillar is shallow, around 500 m depth in this figure. (source: NLOG (2017d)).

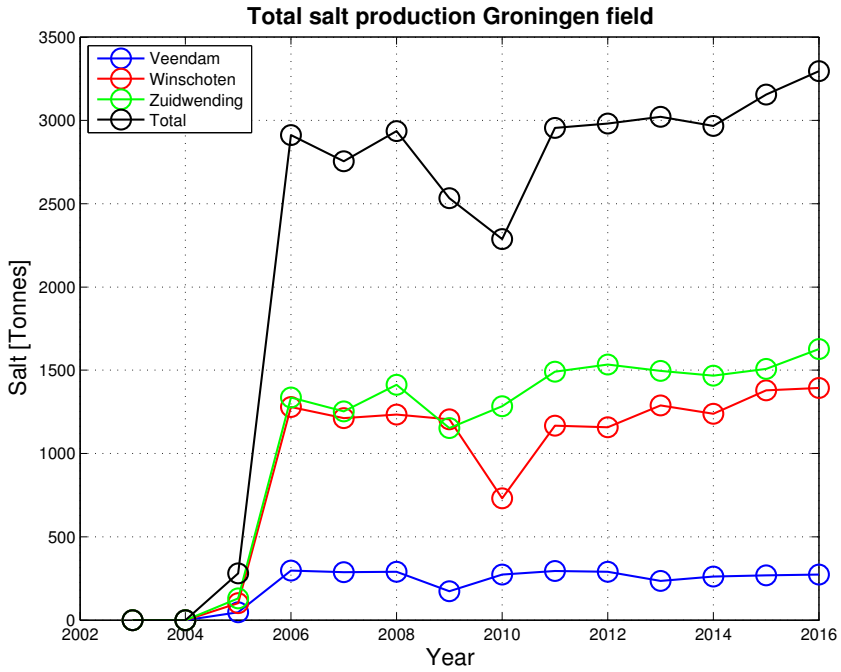

Figure 3.6: Total yearly salt production Tonnes for each cluster for the period 2003-2016. The salt production is quite stable over the years. (data source: NLOG (2017e).)

3.4. Geomechanics

Many research studies model surface deformation to understand the behaviour of the subsurface due to gas exploration. All studies use a subsurface model at reservoir level that models subsidence, caused by volume change. Examples of subsurface models are the analytical solution of Geertsma (1973); the semi-analytical solution of Fokker (2002); Fokker and Orlic (2006); and a numerical solution, such as finite element methods Geertsma and van Opstal (1973). The analytical solution of Geertsma (1973) is built on the knowledge of point source models of Anderson (1936) and Mogi (1958).

The Mogi (1958) point source model use an analytical solution and is used originally for volume changes of magma chambers in volcanoes. The Mogi analytical model is used in this thesis, because of the simplicity and the number of Mogi sources can be expanded in any desired number. A more detailed description of the model is presented in section 3.4.1.

The Geertsma (1973) analytical solution is a single-layer linear forward model that computes the displacement at the surface. The model uses the nucleus of strain that is a small finite volume under influence of a reduction in pore-pressure. The model is disc-shaped at reservoir depth with a thickness and radius with a homogeneous reservoir and surroundings. The nucleus solution is integrated over the reservoir volume to compute the subsidence above this disc-shaped reservoir.

The semi-analytical solution of Fokker (2002) and Fokker and Orlic (2006) combines analytical and numerical approaches into a forward model. The model uses a combination of analytic solutions to the elasticity equations that approximate predefined boundary conditions. A least squares method is used for this approximation. The study uses solutions originating from nuclei of strain; this can be a centre of compression or a finite force working on one point. The model is applicable to a multi-layer subsurface, where elasticity parameters can be changed per layer. The computational time is limited for this model.

The numerical solution, such as finite elements, simulates the complete relationship of the subsurface with flow models and the subsurface geometry and heterogeneity.

The Groningen winningsplan (NAM, 2016) investigated two reservoir compaction models for the Groningen subsidence calculation; these are the semi-analytic approach of Geertsma (1973) and a numerical approach of Geertsma and van Opstal (1973). Both models describe a non-linear relationship with pressure drop. The reservoir pressure is the input for both compaction models and comes from Shell's reservoir simulator MoReS. This reservoir simulator is a 3-dimensional gridded model with porosity and permeability information and solves the fluid flow and pressure changes in line with historic production. The model contains geological knowledge. The outcome of the compaction at reservoir level is propagated towards the surface and results in surface deformation. The semi-analytic and numerical approach does this propagation.

3.4.1. Mogi model

The simple analytical solution of Mogi (1958) is used in this thesis for translating the reservoir volume changes into subsidence values. The 'Mogi model' is a point pressure source model or nucleus of strain. The volume changes at reservoir level can be represented by one or multiple Mogi sources. The Mogi model is very easily adapted and can have multiple sources placed equally spaced in a grid or multiple sources placed at the well locations. First the subsidence values of each point source are computed and then all the separate subsidence values are summed.

The usage of the Mogi model simplifies the deformation problem, because the source model assumes the Earth's crust as an ideal semi-infinite elastic body, known as elastic half-space. The deformation at the surface is caused by a spherical source with hydrostatic pressure change. Hydrostatic pressure is a pressure present in a fluid at rest a (Allaby, 2008; Fossen, 2010). The change of the spherical Mogi source is equal in all directions. The half-space has a planar surface that bound a continuum extending infinitely in all directions. The half-space is mechanically isotropic and materially homogeneous. The Mogi model specifies a linear relation between applied forces (stresses, σ_{ij}) and displacements (strains, ϵ_{ij}) at any point in the body. These characteristics of a body are called isotropic linearly elastic (Lisowski, 2007). The relationship between stress and strain is described by two independent elastic constants. The Mogi model uses Poisson's ratio ν and the modulus of elasticity in shear μ.

Poisson's ratio ν is the ratio of lateral unit strain to longitudinal unit strain in a body, which is stressed in the longitudinal direction. This value of ν is determined in laboratory experiments, where a cylinder shape of different rock samples is pressurized at both ends of the cylinder. The cylinder sample will shorten in length (longitudinal axis) and expand in diameter (lateral axis).

The shear modulus μ relates strain to shear stress and provides stiffness to a material and is also known

as the second constant of Lamé (Lisowski, 2007). The shear modulus μ has units of pressure and has a typical value in the range of 10,000 MPa to 30,000 MPa for intact crustal rocks. Fractured rocks and sediments have values of 100 to 1,000 MPa. Poisson's ratio, ν, is the measure of a materials compressibility perpendicular to an applied stress (Fossen, 2010). The ν values ranges from 0.15 to 0.30, where ν=0.25 is most common used (Lisowski, 2007). According to Lele et al. (2015) the Poisson's ratio varies for each unit for the Groningen field. The Slochteren unit is porosity-dependent. The overburden units like the Zechstein salt have values of 0.25 - 0.35 and the units Triassic, Rijnland, Chalk and North Sea layers have values of 0.25 - 0.3.

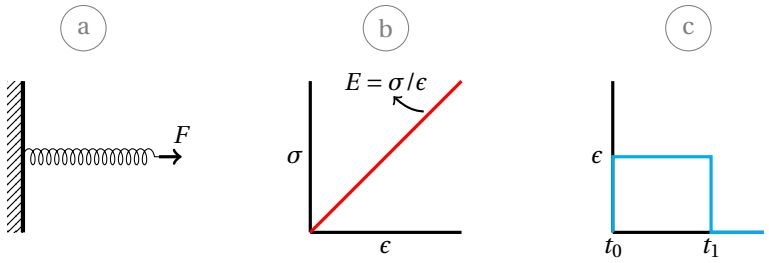

Figure 3.7: Linear stress-strain relationship, explained with a spring. **a**: shows a spring with force F acting on the spring. **b**: shows the linear elastic curve of strain $e = \epsilon$ versus stress σ, where E is the Young's modulus. **c**: shows a time plot with an instant response to stress (e), when a force is acting on the spring. The strain σ is non-permanent. (after: Fossen (2010))

The linear stress-strain relationship is often explained with a spring, as shown in figure 3.7a. The spring stretches under force F, when the force is zero again the spring returns to its old shape. Figure 3.7b shows the linear elastic relation between stress and strain when a force acts on the spring, where E is the Young's modulus, the stiffness of a material. This linear stress/strain relationship $E = \sigma/\epsilon$, can be rewritten and is known as Hooke's law:

$$\sigma = E\epsilon, \tag{3.1}$$

where σ is stress, E is Young's modulus and ϵ strain (Fossen, 2010). The nine stress components σ_{ij} are the following stress tensor:

$$\sigma_{ij} = \begin{pmatrix} \sigma_{xx} & \sigma_{xy} & \sigma_{xz} \\ \sigma_{yx} & \sigma_{yy} & \sigma_{yz} \\ \sigma_{zx} & \sigma_{zy} & \sigma_{zz} \end{pmatrix}, \tag{3.2}$$

where σ_{xx}, σ_{yy}, and σ_{zz} are normal stresses and $\sigma_{xy}, \sigma_{xz}, \sigma_{yx}, \sigma_{yz}, \sigma_{zx}$ and σ_{zy} are shear stresses. The (x, y, z) coordinate system is centred on a free surface ($z = 0$). The nine stress components are visualised in figure 3.8. Hooke's law for a homogeneous isotropic elastic material is as follows:

$$\sigma_{ij} = \lambda\epsilon_{\alpha\alpha}\delta_{ij} + 2\mu\epsilon_{ij}, \tag{3.3}$$

where λ is Lamé's first elastic constant, strain $\epsilon_{\alpha\alpha} = \epsilon_{xx} + \epsilon_{yy} + \epsilon_{zz}$, δ_{ij}=1 for i=j or 0 otherwise, μ=Lamé's second elastic constant, and $\sigma_{yx} = \sigma_{xy}$, $\sigma_{zx} = \sigma_{xz}$, $\sigma_{zy} = \sigma_{yz}$. The planar surface of the elastic half-space, an x-,y-plane at z=0, is free of stress, $\sigma_{xz} = \sigma_{yz} = \sigma_{zz} = 0$, the free surface. These surface stress conditions reduce the six independent strain components to three components. The change in area at the surface is $\Delta_{\text{area}} = \epsilon_{xx} + \epsilon_{yy}$ and the change in volume:

$$\Delta_{\text{volume}} = \epsilon_{xx} + \epsilon_{yy} + \epsilon_{zz} = \frac{1-2\nu}{1-\nu}(\epsilon_{xx} + \epsilon_{yy}) = \frac{1-2\nu}{1-\nu}\Delta_{\text{area}} \tag{3.4}$$

(Lisowski, 2007; Segall, 2010).

As described above, the Mogi analytical solution makes use of a half-space solution. This solution uses an image source opposite of the subsurface source. This is done to construct the free surface and to cancel out-of-plane shear stresses. Figure 3.9 shows the coordinate system and geometric relations of the Mogi source and its image source (Lisowski, 2007). Only four parameters are needed to derive the surface displacement by a hydrostatic pressure change in a spherical source in elastic half-space with a radius smaller than the depth, $\alpha \ll z$. These parameters are the source centre $x_{\text{mogi}}, y_{\text{mogi}}, z_{\text{mogi}}$ coordinates and the source strength (Mogi,

1958). The surface displacement is as follows:

$$\begin{pmatrix} u_x \\ u_y \\ u_z \end{pmatrix} = \alpha^3 \Delta P \frac{(1-\nu)}{\mu} \begin{pmatrix} \frac{\Delta x}{R^3} \\ \frac{\Delta y}{R^3} \\ \frac{\Delta z}{R^3} \end{pmatrix}, \tag{3.5}$$

where u_x, u_y, u_z are displacements at point (x_1, y_1, z_1), Δx, Δy, Δz is the difference between x_1, y_1, z_1 and x_{mogi}, y_{mogi}, z_{mogi}, ν is Poisson's ratio, μ is the shear modulus (Lamé's second elastic constant), α the radius, ΔP the pressure change and $R = \sqrt{\Delta x^2 + \Delta y^2 + \Delta z^2}$ is the radial distance from the center of the source to a point at the surface. The scaling factor or the source strength are ΔP, α, μ and ν together. These individual contributions cannot be separated, because a large pressure change in a small spherical source, will give the same deformation as a small pressure change in a large spherical source for the same radial distance R and when $\alpha \ll z$ (Lisowski, 2007).

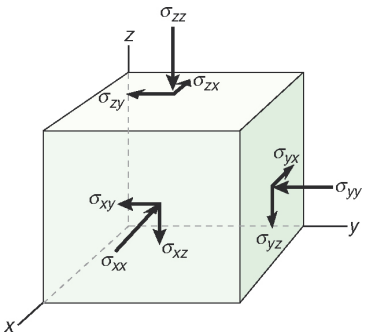

Figure 3.8: Positive stress components acting on faces of a small cube, $\sigma_{xx}, \sigma_{yy}, \sigma_{zz}$ are normal stresses, those are stresses perpendicular on a face. The other stresses are shear stresses and are parallel to the edges of the cube. (source: Fossen (2010))

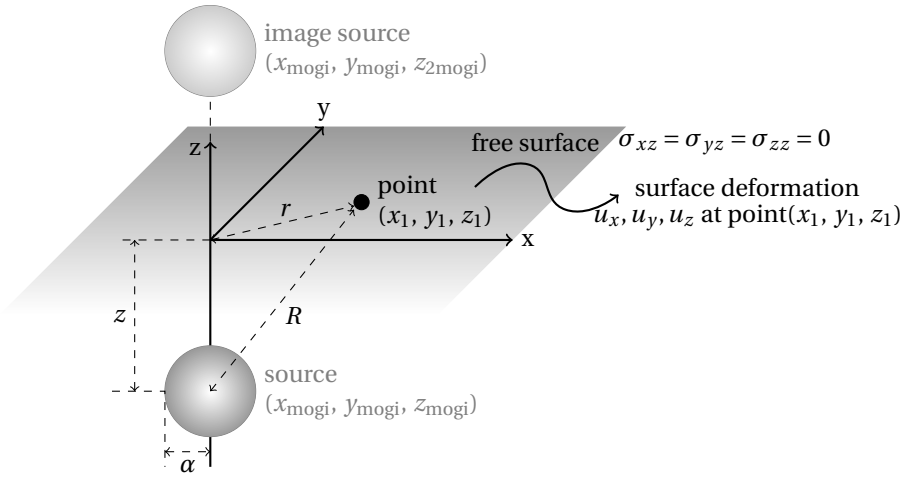

Figure 3.9: Coordinate system and geometric relations of a pressure source and the location of the image source that is used to derive surface deformation u_x, u_y, u_d at point (x_1,y_1,z_1), z=depth, R=radial distance, α=radius of source, r=surface distance; and stresses $\sigma_{xz} = \sigma_{yz} = \sigma_{zz} = 0$, (after: Lisowski (2007))

The half-space solution of Van Zwieten (2016) is used in this thesis. The model is written in the Python programming language for usage of coordinates in meters. This thesis uses the Matlab programming language therefore the model is rewritten into Matlab. The steps of the code itself can be found in Appendix B.1. This Mogi model derives surface deformation with a half-space solution. There are no outer boundaries sets for the model and therefore the computed Mogi source deformation at the surface can extent infinitely in all x-, y- and z-directions.

This thesis uses multiple Mogi sources placed at the hydrocarbon production well locations. The Mogi model is used multiple times, where the total displacement is a linear combination of the contributions of

each Mogi source. The model computes the displacement in the x-, y- and z-direction (or East, North and Up). The LOS vector is used to correct the deformation into the satellite direction.

4

PS-InSAR technique

The data assimilation method, particle filter is explained in chapter 2 and chapter 3 provides the subsidence mechanisms of the Groningen location. These are the production of hydrocarbons and salt. This chapter provides the space-geodetic PS-InSAR technique that is used to observe the subsidence in Groningen.

The Groningen surface is monitored by the following surveying techniques: levelling, InSAR and GNSS. All surveying techniques are relative, where the height differences are measured between different points. In Groningen the levelling geodetic technique is done every 5 years. The space-geodetic techniques are GPS stations and Interferometric Synthetic Aperture Radar (InSAR). The temporal resolution of these techniques are respectively continuously and ~16 days. The spatial resolution for GPS depends on the number and spread of GPS stations, while InSAR depends on the reflectivity of ground objects (houses for example are gsood reflectors). The GPS stations produce data for the period 2013 - present. The PS-InSAR has a much longer time period coverage. The gas production is lowered in 2014 and data before and after this year is available in PS-InSAR data. The lowered gas production is perhaps present in the time series of the PS-InSAR data, by showing a reduced subsidence signal.

Interferometric Synthetic Aperture Radar (InSAR) is a radar technique that is used to generate images of ground deformation and elevation by using two synthetic aperture radar (SAR) images. A phase difference of the returned radar signal is used to construct an interferogram that contains information about deformation and topography. This thesis uses only the end product of InSAR data. The InSAR technique is explained briefly in the following sections, an extended and detailed description of the processing of InSAR data can be found in Hanssen (2001).

4.1. Synthetic Aperture Radar

Radio detection and ranging (radar) is a technique and an instrument. The radar instrument emits electromagnetic pulses in the microwave to radio wave wavelength range and some of this energy is scattered back in its line-of-sight (LOS) to the instrument. The two-way travel time of the pulse is used to determine the range to a detected object. The range is expressed as phase [radians]. The returned radar signal depends on the slope, roughness and dielectric constant of the object. The transmitted radar pulses have known characteristics, namely amplitude, polarization, phase and time reference, and wavelength. An object alters these characteristics. An advantage of radar is that it can be used all day, it depends not on daylight and it can penetrate clouds.

The synthetic aperture radar (SAR) is an imaging radar class. The radar is fixed on an airplane or satellite and looks sideways towards the Earth; the look direction is perpendicular to the flight direction and can be used for ascending and descending orbits. The synthetic aperture is an artificially long antenna that is created synthetically by using a moving antenna that is sending and receiving continuously radar pulses, as shown in figure 4.1. The usage of this moving antenna increases the along-track resolution.

A SAR image consists of a regular grid where every pixel has a complex phasor P:

$$P = A \exp(i\psi), \tag{4.1}$$

where i is the imaginary unit, A is the pixel amplitude, the square-root of the intensity I of the radar reflection, and ψ is the fractional phase of the received radar signal. The real ($\mathrm{Re}\{P\}$) and imaginary ($\mathrm{Im}\{P\}$) part of the

phasor are related to amplitude A and the range dependent phase ψ:

$$\mathrm{Re}\{P\} = A\ \cos(\psi),\ \ \mathrm{Im}\{P\} = A\ \sin(\psi), \tag{4.2}$$

with

$$A = \sqrt{(\mathrm{Re}\{P\})^2 + \mathrm{Im}\{P\})^2},\ \ \psi = \arctan(\frac{\mathrm{Im}\{P\}}{\mathrm{Re}\{P\}}). \tag{4.3}$$

The complex value of a radar image pixel is formed by the summation of all reflections on the Earth's surface in the corresponding area. Two reflection cases can be determined, namely point scattering and distributed scattering. The point scattering uses a strong reflecting object that dominates the radar measurement. The distributed scattering uses many small objects that reflect the radar signal (Hanssen, 2001; Van Leijen, 2014).

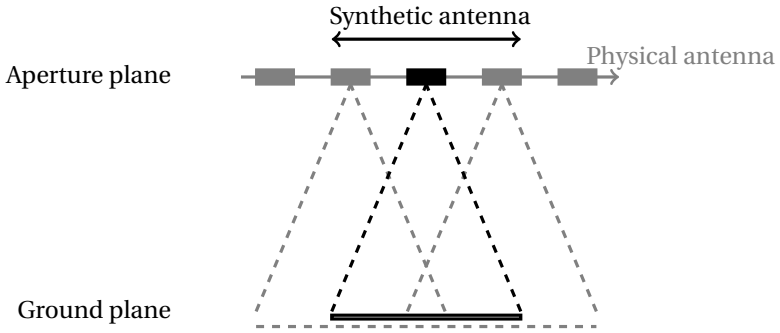

Figure 4.1: Graphical illustration of SAR, the synthetic antenna improves the along-track resolution by moving.

4.2. InSAR

Interferometric Synthetic Aperture Radar (InSAR) uses two SAR images to generate an interferogram. The two SAR images are acquired by repeated acquisitions in time or space. An interferogram can be created by multiplication of the complex conjugate of two SAR images (master and slave image). Figure 4.2 illustrates the geometry of repeat-pass InSAR. Angular measurements can be obtained as well. The differences in phase measurements of the returned signal are used to measure precisely the relative deformation of an object, with millimetre accuracy. The obtained phase difference φ for a single pixel is:

$$\varphi = -2\pi a + \varphi_{\mathrm{flat}} + \varphi_{\mathrm{topo}} + \varphi_{\mathrm{defo}} + \varphi_{\mathrm{atmo}} + \varphi_{\mathrm{orb}} + \varphi_{\mathrm{scat}} + \varphi_{\mathrm{noise}}, \tag{4.4}$$

where α is the heading of the satellite; the interferometric range is split into the flat Earth part φ_{flat}, topographic part φ_{topo} and deformation part φ_{defo} part, φ_{atmo} are errors due to atmospheric conditions, and φ_{orb} represents errors in the orbit parameters. The flat Earth and topographic phase are related to the baseline B, the difference in distance between the two satellite positions. The flat Earth phase is the effect of a reference surface on the interferometric phase and can be approximated as follows:

$$\varphi_{\mathrm{flat}} = \frac{4\pi}{\lambda} B_{\parallel}, \tag{4.5}$$

where λ is the wavelength of the radar and $B_{\parallel}$ the parallel baseline. The topographic phase is the influence of the topography above the reference surface and can be defined as follows:

$$\varphi_{\mathrm{topo}} = \frac{-4\pi}{\lambda} \frac{B_{\perp}}{R\ \sin(\theta_{\mathrm{inc}})} H, \tag{4.6}$$

where $B_{\perp}$ is the perpendicular baseline, R is the range to the master satellite acquisition and H is the height. The deformation phase is the actual displacement of a point on the surface. This can be defined as:

$$\varphi_{\mathrm{defo}} = \frac{-4\pi}{\lambda} D_{\mathrm{LOS}}, \tag{4.7}$$

where D_{LOS} is the deformation in the line-of-sight. The atmospheric phase φ_{atmo} is the difference between the atmospheric states of two SAR acquisitions. The scattering phase is the difference between scattering

characteristics of two SAR acquisitions. And the noise phase φ_{noise} term can be system noise or processing interferogram formation noise.

An interferogram contains information about deformation and topography in the form of fringes, 2π phase-cycles, when the baseline is larger than zero. The baseline is the distance between the location of the first and second pass of a satellite.

The topography is removed from the interferogram in order to obtain deformation information. The topography is obtained from a topographic interferogram or a digital elevation model (DEM). The topographic phase is insensitive to topography in case of a zero perpendicular baseline $B_\perp$, as shown in equation (4.6). Additional information is used when the baseline is not zero e.g. this can be another interferogram with conditions favourable for topography, for instance a large baseline $B_\perp$ and a limited deformation and atmospheric signal, or an existing DEM. The resulting interferogram is a differential interferogram (Van Leijen, 2014).

Topographic mapping of repeat-pass interferometry has problems as layover, foreshortening, shadow, surface decorrelation (decrease of coherence) and atmopheric error. The last two problems are reduced by using a long baseline. The coherence is the amount of similariy between the two images in an interferogram. A high coherence is when the scattering of objects remains the same (Hanssen, 2001; Samiei-Esfahany, 2017; Van Leijen, 2014).

4.3. Persistent Scatterer InSAR

The InSAR technique e.g.Van Leijen (2014), has three degrading factors atmospheric such as atmospheric noise that can superimposes an error signal that can be seen as a deformation signal; scattering within one resolution cell that changes over time; and differences in the satellite repeat orbit. Time series analysis of the same area by using a stack of radar acquisitions can overcome the above-described factors. One type of time series analysis is the Persistent Scatterer Interferometry (PSI), also known as Persistent Scatterer Interferometric Synthetic Aperture Radar (PS-InSAR). The PS-InSAR technique uses the scatterers that are constant in a time series; these scatteres are for example buildings and other man-made structures. The persistent scatterer does not have to be the dominant scatterer within a resolution cell. Distributed scatters are characterized by lower reflectivity values in a resolution cell, examples are rocks or land areas.

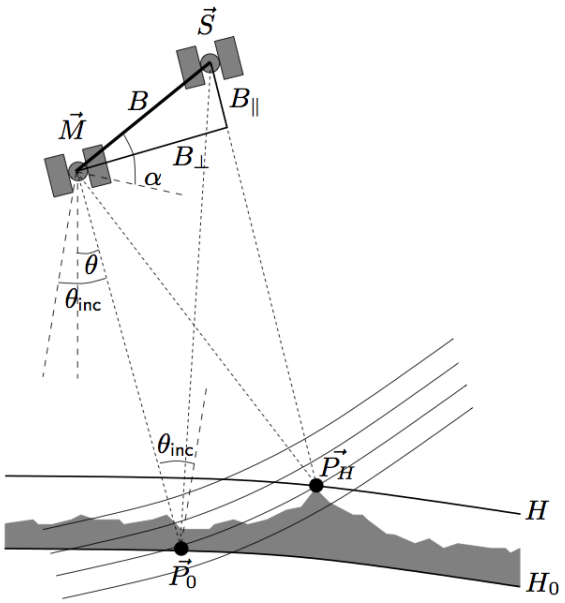

Figure 4.2: Repeat-pass InSAR geometry, where the satellite orbit trajectories are travelling into the paper. The $\vec{M}$ and $\vec{S}$ denotes the master and slave satellite position and baseline B the distance between both satellite positions. The baseline is decomposed in the parallel baseline $B_\parallel$ (range direction) and perpendicular baseline $B_\perp$ (perpendicular to the range direction). Point $\vec{P_0}$ is located on a reference surface height and point $\vec{P_H}$ on the surface height. (source: Van Leijen (2014))

4.4. Decomposition of the line-of-sight vector

The line-of-sight (LOS) vector is the three-dimensional deformation vector with three components denoted as d_e, d_n and d_u, East North and Up. The relation of these components with the LOS component D_{LOS} for a satellite orbit with heading (azimuth) α_h with respect to the North and incidence angle θ_{inc} is (Hanssen, 2001; Van Leijen, 2014):

$$\begin{aligned} D_{\text{LOS,R}} &= d_u \cos(\theta_{\text{inc}}) - \sin(\theta_{\text{inc}}) \, [d_n \cos(\alpha_h - 3\pi/2) + d_e \sin(\alpha_h - 3\pi/2)], \\ &= d_u \cos(\theta_{\text{inc}}) - \sin(\theta_{\text{inc}}) \, [-d_n \sin(\alpha_h) + d_e \cos(\alpha_h)], \\ &= d_u \cos(\theta_{\text{inc}}), -d_n \sin(\theta_{\text{inc}}) \sin(\alpha_h), d_e \sin(\theta_{\text{inc}}) \cos(\alpha_h), \end{aligned} \tag{4.8}$$

where $d_{\text{LOS,R}}$ is the LOS component for a right-looking satellite, θ_{inc} is the incidence local angle and α_h the heading. Figure 4.3 (left) shows a top view of ascending and descending heading of a right-looking satellite with respect to the North and on the right a 3D view with the incidence angle of the satellite.

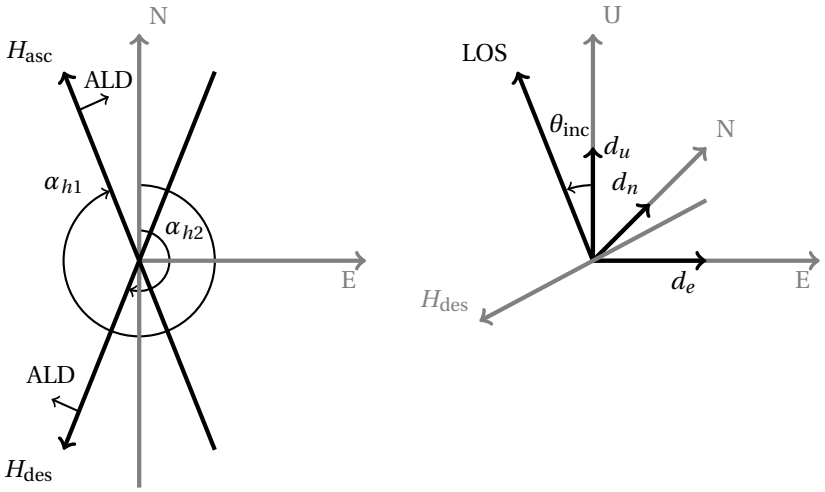

Figure 4.3: **Left**: top view of an ascending (H_{asc}) and descending (H_{des}) satellite track with heading angles, respectively α_{h1} and α_{h2}, ALD is the azimuth look direction, in this case a right-looking satellite. **Right**: 3D view of the incidence angle θ_{inc} of the line-of-sight with the three components d_u, d_n and d_e (after: Hanssen (2001))

The inverse of eq. 4.8 is used for estimating the three components (Van Leijen, 2014). Hanssen (2001) estimated a decomposition of $D_{\text{LOS,R}}$ [0.92, -0.07,0.38] $[d_u, d_n, d_e]$ for an incidence angle of θ_{inc}=23° and a heading of α_h=190°. The Up component depends only on the incidence angle and has the largest value. These numbers are computed again with a method of Wright (2009) found in a Matlab script that simulates interferograms and uses simple elastic sources for point pressure changes in magma chambers. The method is as follows:

$$\begin{aligned} \text{inc} &= 90^\circ - \theta_{\text{inc}}, \\ \text{az} &= 360^\circ - \alpha_h, \\ d_u &= \sin\left(\text{inc} \cdot \frac{\pi}{180^\circ}\right), \\ d_n &= -\sin\left(\text{az} \cdot \frac{\pi}{180^\circ}\right) \cdot \cos\left(\text{inc} \cdot \frac{\pi}{180^\circ}\right), \\ d_e &= -\cos\left(\text{az} \cdot \frac{\pi}{180^\circ}\right) \cdot \cos\left(\text{inc} \cdot \frac{\pi}{180^\circ}\right). \end{aligned} \tag{4.9}$$

This method is the same as the third line in eq. (4.8) and produces the same values as the Hanssen (2001) decomposition for a right-looking satellite. Both methods can be used to compute the descending LOS vectors of the Radarsat-2 dataset. The LOS vector is: [0.8281, -0.1070, 0.5503] $[d_u, d_n, d_e]$ for a descending satellite with heading 191° and incidence angle 34.1°.

5

Particle filter synthetic experiments

The particle filter is tested on synthetic data in a couple of test situations with an identical twin experiment. Synthetic data means that the data is simulated. The test situations are low dimensional in order to understand the results when using the particle filter and to get a grip on how the particle filter works, when the variables and parameters in the filter are changed. The methodology is explained in section 5.1, the results are shown in section 5.2 and the discussion and conclusion is presented in section 5.3.

The methodology consists of four subsections: section 5.1.1 explains the steps of the identical twin experiment; section 5.1.2 the experiments and goals; section 5.1.3 the experiment setups of the Mogi sources and deformation locations; and section 5.1.4 the experiment variables input. The result section consists also of four subsections: section 5.2.1 provides the particle filter and Mogi model experiment; section 5.2.2 the particle filter variability in variances experiment; section 5.2.3 the particle filter resampling experiment; and section 5.2.4 the particle filter variability in start value and 'jitter' variance experiment.

5.1. Methodology

The identical twin experiment is visualised in figure 5.1. The experiment consists of two parts, one 'truth' part and one estimated part. The truth part is to be recovered with the particle filter.

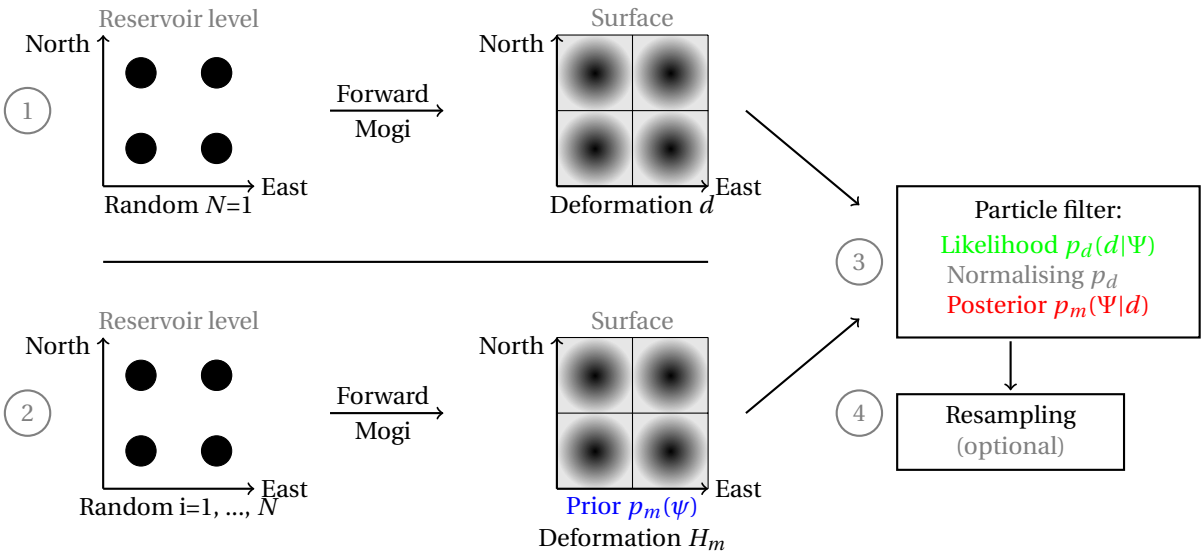

Figure 5.1: Graphical illustration of one of the identical twin experiments of this thesis. See section 5.1.1 for an explanation. •=Mogi source and □=deformation, where the grey colour represents deformation dark gray=strong deformation, N= 100, 1000, etc., colours corresponds to the colours of figure 2.3

This thesis uses the Mogi point source forward model and this model is explained in detail in section

3.4.1. Figure 5.1 visualise the Mogi source strengths (volume factors at reservoir level) with black dots and the Mogi model propagated deformation by squares with a gray coloured gradient. The dark gray colours represent large deformation. The truth part of the synthetic experiment is that the values are known. In this synthetic experiment the source strengths of the Mogi sources are known and thus also the model propagated deformation values. The estimation part consists of a source strength and deformation part as well. The particle filter recovers the truth part, where the amount of recovery is a measure of how well the particle filter performs.

The particle filter is explained in section 2.4. In this thesis a Gaussian probability density function (eq. (5.1)) is assumed for the observational probability density function. This is without applying the observational error-covariance matrix of eq. (2.13). The usage of that matrix is beyond the scope of this thesis. In addition a second observational probability density function is tested; this is the Lorentz probability density function (also known as the Cauchy density). The Lorentz pdf has a similar peak shape as the Gaussian pdf, but becomes broader to the sides. These broader sides will allow more particles to be correct and is robust to outliers (Vossepoel and van Leeuwen, 2007). The Gaussian probability density function is as follows:

$$p_d(d|\Psi) = \frac{1}{\sqrt{2\pi\sigma^2}} e^{-(\frac{d-H(\Psi_i)^2}{2\sigma^2})}, \tag{5.1}$$

where d is the deformation, σ^2 the variance, Ψ_i the full state that is the joint pdf of all parameters and $H(\Psi_i)$ the model state pdf, where the Mogi model generates the output at similar locations as the observed deformation d. In this synthetic experiment does the Mogi model generate the deformation d, but in the real Groningen case is the deformation measured by the PS-InSAR technique. The weight assigned to each correct ensemble member represents the observations probability density and is computed by

$$w_i = \frac{1}{W} \frac{1}{\sqrt{2\pi\sigma^2}} e^{-(\sum_{m=1}^{M} \frac{d_m - H_m(\Psi_i)^2}{2\sigma^2})}, \tag{5.2}$$

with W given by

$$W = \sum_{i=1}^{N} \frac{1}{\sqrt{2\pi\sigma^2}} e^{-(\sum_{m=1}^{M} \frac{d_m - H_m(\Psi_i)^2}{2\sigma^2})}, \tag{5.3}$$

where $m = 1,...,M$ represents the deformation and $i = 1,...,N$ the ensemble members. The Lorentz probability density function is as follows:

$$p_d(d|\Psi) = \frac{1}{\left[1 + \left(\frac{d - H(\Psi_i)}{\gamma}\right)^2\right]}, \tag{5.4}$$

where γ is a scale parameter, half width at half maximum (HWHM). The full width at half maximum (FWHM) is 2γ. The FWHM relationship with the standard deviation σ is FWHM $= 2\sqrt{2\ \ln(2)}\,\sigma$. The weight assigned to each correct ensemble member is computed for the Lorentz probability density function as follows:

$$w_i = \frac{1}{W} \prod_{m=1}^{M} \frac{1}{\left[1 + \left(\frac{d_m - H_m(\Psi_i)}{\gamma}\right)^2\right]}, \tag{5.5}$$

with W given by

$$W = \sum_{i=1}^{N} \prod_{m=1}^{M} \frac{1}{\left[1 + \left(\frac{d_m - H_m(\Psi_i)}{\gamma}\right)^2\right]}, \tag{5.6}$$

where $m = 1,...,M$ represents the deformation and $i = 1,...,N$ the ensemble members. The assigned weights to the ensemble member are normalised, sum=1 (Vossepoel and van Leeuwen, 2007). These normalised weights are used to calculate the posterior (the state of a system) and evaluates the performance of the particle filter. The prior is the ensemble members before the particle filter is applied. And the posterior = likelihood x normalising constant x prior. The prior ensemble members are weighted and the resulting posterior is the sum of the weighted ensemble members. This posterior is computed for both the source strengths and the model propagated surface deformation. The mean of the prior is computed as well in order to compare the

source strength and deformation results with the posterior source strength and deformation estimation. The comparison is done with the root mean square error (RMSE):

$$\text{RMSE} = \sqrt{\frac{\sum_{i=1}^{n}(d_i - \text{mod}_i)^2}{n}}, \tag{5.7}$$

where n= the number of observations, d_i the observed deformation and mod_i the weigthed estimated deformation, the posterior. A perfect twin experiment will have a zero RMSE.

5.1.1. Steps identical twin experiment

The four steps of the identical twin experiment are visualised above (figure 5.1) and described below:

1. **Truth part of the identical twin experiment**
   The truth part of the experiment is generated by sampling source strengths N=1 randomly from a Gaussian distribution, eq. (2.10). The example of figure 5.1 has four Mogi sources and thus four source strengths that are sampled from the Gaussian distribution. A start value (value close to the mean of the Gaussian distribution) and variance value σ^2 is needed to define a Gaussian distribution. The Mogi model computes surface deformation d, eq. (B.1) - (B.13) with the Gaussian random generated source strengths. The last step is to add noise to the deformation values in order to simulate measurement instrument errors. There is always a measurement instrument error in a real situation. This is done by sampling randomly from a Gaussian distribution with a zero mean and a to be decided variance value σ^2.

2. **Generating the prior** $p_m(\psi)$
   The model pdf is generated by sampling a large number of randomly Gaussian generated source strengths N=1, ...n with eq.(2.10). These are the ensemble members and for each realization a surface deformation H_m is computed using eq. (B.1) - (B.13). The model representation of surface deformation for each ensemble member is now generated.

3. **Particle filter**
   The difference between the observed deformation d and modelled surface deformations H_m are multiplied with the observational density function $p_d(d|\Psi)$ (Gaussian or Lorentz distribution eq. (5.2) or (5.4)). The likelihood is obtained, these are the particle filter weights. This distribution is multiplied with p_d for normalising and results into the posterior distribution $p_m(\Psi|d)$.

4. **Resampling** (optional step)
   The resampling step is applied when the results of the particle filter are not sufficient. The residual resampling technique, eq. (2.14) - (2.18), is used to resample the source strengths. Uncorrelated Gaussian noise is added to the resampled ensemble members, in order to vary the ensemble members. This noise or 'jitter' is generated with a zero mean value by eq. (2.10). The Mogi model computes surface deformation from the resampled source strengths.

The RMSE is used to compare the posterior results with the truth part of the identical twin experiment; this can be done for the source strengths and the deformation values.

5.1.2. Experiments and goals

There are four different identical twin experiments with the goal to find out if the source strength can be estimated, when variables are varied in the four steps of the identical twin experiment of section 5.1.1. The four experiments are tested for three different Mogi sources / observations setups, as explained in section 5.1.3. The four experiments are:

1a. **Mogi model experiment** (results in section 5.2.1)

- **What**: The first part is an experiment where the limitations of the geomechanical model is tested. The Mogi source depth, source strength and Poisson's ratio is varied.
- **Goal**: What are the surface deformation values when the depth of the source is varied. Is there a difference in surface deformation when changing the depth 1, 10 or 100 m?

- **How**: The first test setup of figure 5.3 is used where the observed deformation is at the centre above the Mogi source (1 Mogi source and 1 deformation). The settings of table 5.2 are used.

1b. **Particle filter** (results in section 5.2.1)

- **What**: The second part of the experiment is where the particle filter is applied on the 1 Mogi source and 1 deformation setup.
- **Goal**: How does the particle filter perform when a bias value (surface topography) is added to the deformation. Is there a difference in the estimated source strength values with the different bias values?
- **How**: The first test setup of figure 5.3 is used (1 Mogi source = 1 observation) with the settings of table 5.2. The test is done twice, once without and once with a bias value. The unbiased and biased situation is illustrated in figure 5.2. This bias value is added to the truth part, the observed deformations, one as: deformation + noise and one as: deformation + noise + bias.

2. **Particle filter variance variability, step 3 of the identical twin experiment** (results in section 5.2.2)

- **What**: This particle filter test is a broad experiment in order to find out how the particle filter works when only step 3 is varied (the variance of the observational probability density function) and whether there are any differences between the Gaussian and Lorentz density function.
- **Goal**: The main question of this experiment is how does the RMSE vary for the different setups with a number of Mogi sources varying from 1 to 16. Is there any difference in the RMSE and how does this RMSE vary with different observational probability density variances?

  This is important, because the number of Mogi sources is not known that are needed to estimate the real situation with the PS-InSAR measurements. And in the real situation there is no twin experiment so the truth is not known.

  What can the RMSE of the deformation say on how well the source strength is estimated? And what is the influence of the variation in distances between the Mogi sources and deformations on the RMSE value? The answer to these questions is found in the twin experiment and the RMSE values of the source strength. Furthermore does the number N of ensemble members matter? And how do the RMSE values differ, when running 5 different ensemble member sets.
- **How**: The test is applied to five different setup situations (figure 5.3) with a number of Mogi sources varying from 1 to 16. The distance between the Mogi sources and deformation values are varied three times, namely 1500, 3000 and 6000 m. The number of prior ensemble members N is 1000. The RMSE value is computed (eq. (5.7)) for each setup, this results into 12 subplots with each 10 RMSE values. This is a large amount of results to be analyzed.

  The number of N is varied from 10 - 10000 ensemble members for all the five setups of figure 5.3 with a distance of k=1500 m between the deformations and particle filter variance σ^2=25 mm. This is done to find out how the RMSE values vary for the deformations and source strengths.

  The RMSE values are computed for 5 different ensemble member sets and for all the five test setups of figure 5.3. The distances between the deformations are k=1500, 3000, 6000 m, Gaussian noise added to the observations of σ^2=25, 4 mm and the particle filter variance σ^2=25, 4 mm.

  The particle observational probability density function versus the deformation and source strength ensemble members is plotted for two setups, the 1 Mogi and 2 Mogi sources of figure 5.3.

3. **Particle filter resampling, step 4 of the identical twin experiment** (results in section 5.2.3)

- **What**: This test finds out if the resampling step in an iterative way improves the estimation of the deformation values and source strengths.
- **Goal**: Are the RMSE values lowered by the resampling step? Are there any differences when varying the distances between the Mogi sources / observations?
- **How**: The resampling step is done by selecting the ensemble members with the highest weights (highest value of the observational probability density function) and duplicate the ensemble members that belong to these high weights. The threshold value is the integer part of the weight larger than 1, for example the weight is 0.002 and N=1000, the integer part is then 0.002 x 1000 = 2. To

avoid filter degeneracy 'jitter' is added to the source strength ensemble members; this is Gaussian random uncorrelated noise with a variance of σ^2=0.25 [-]. Dividing the source strength variance by two chooses this value. It is assumed that the resampled ensemble members do not need as large a spread as in step 2, where the start value variance σ^2=0.5 [-]. The results of this experiment will show if this assumption was correct. The probability density functions of the prior and posterior deformation and source strength are plotted and the RMSE values are computed (eq. (5.7)). The test setups are figure 5.3 and 5.4 with the settings of table 5.4.

4. **Particle filter variability of the start value (step 2) and the resampling 'jitter' variance (step 4) of the identical twin experiment** (results in section 5.2.4)

   - **What**: The ensemble members of step 2 are generated with a start value different from the 'truth' in step 1. The resampling part, step 4, is done with two different variances for generating Gaussian noise or 'jitter'.
   - **Goal**: The goal is to find out if the particle filter can estimate the deformation and source strength when the variance and start value in step 2 are different from step 1, the first part of the identical twin experiment. And how the differences in variance of generating 'jitter' in the resampling step influences the estimation of the deformation and the source strength. This test is done in order to simulate a real world problem. A real world problem one does not know the source strength truth.
   - **How**: This experiment is applied to all three setups, as shown in the figures 5.3, 5.4 and 5.5 and with the settings of table 5.5.

All experiments are done with random uncorrelated Gaussian noise added to the deformations with a variance of σ^2=25 mm. The choice for this variance value is based on the fact that PS-InSAR individual measurements have a precision of 2-8 mm (SkyGeo, 2017). This is a-priori information that is used in the observational probability density function of the particle filter. The particle filter pdf with a variance of σ^2=25 mm (σ=5 mm) in step 3 and Gaussian noise added to the deformation with a variance of σ^2=25 mm is expected to show RMSE values around 4-5 mm, because this will indicate that the particle filter works well.

The posterior, used for computing the RMSE (5.7), is estimated by multiplying the prior x likelihood x normalising constant. The prior deformation has Gaussian noise added with a variance of σ^2=25 mm. Furthermore the likelihood are weights computed by the observational pdf with a variance of σ^2=25 mm. The RMSE is thus in the order of the σ=5 mm, because it is computed from prior and likelihood values with a standard deviation of σ=5 mm.

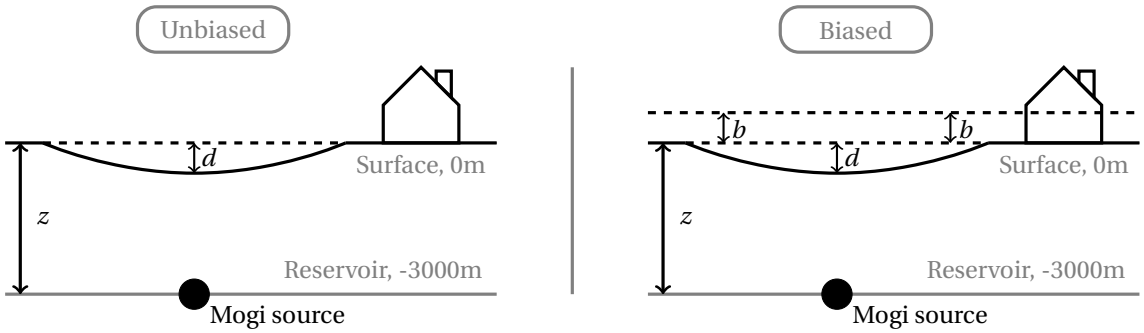

Figure 5.2: Setup of the Mogi model (not on scale) **left:** unbiased situation. **right:** biased situation, z=depth, d=deformation and b=bias.

5.1.3. Experiment setups of Mogi sources and deformation

The Mogi sources are placed at depths of the Groningen reservoir level of -3000 [m]. The Mogi source is sphere shaped, deformation at the surface above the source will be circular and bowl shaped. The deformation right above the Mogi source will be the largest and smaller further away from the centre. It is assumed that the deformation is easy to estimate when the Mogi source is located at the same location, because the circular shaped Mogi surface deformation has its centre located at the location of the Mogi source. This centre is where the deformation is located.

This is the choice for the first setup, as presented as a top view in figure 5.3. The **Mogi source location = at deformation location** setup, this is setup 1. There are five setups, where the number of Mogi sources and deformation locations are increased simultaneously. This result in a 1, 2, 4, 9 and 16 Mogi sources setups, where thus the number of source strengths to be estimated increases. The distance of k=1500, 3000 and 6000 m between the deformation is chosen this way to find out how the deformation of the Mogi sources interfere.

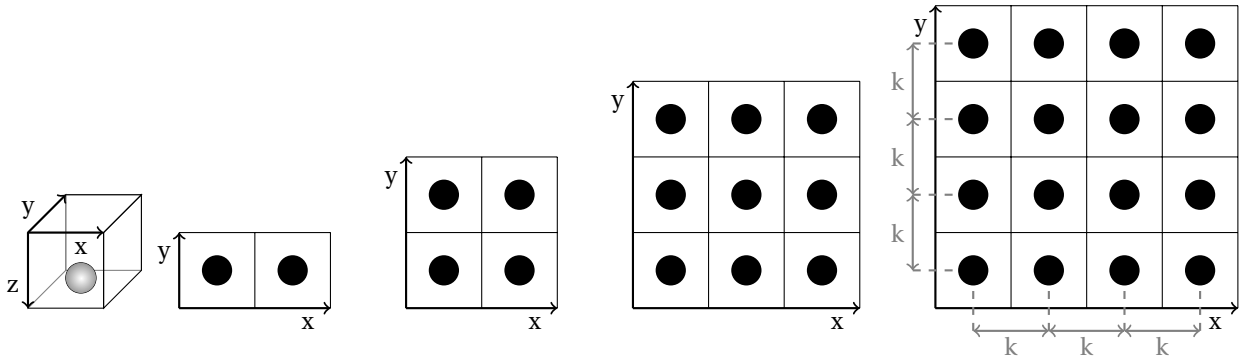

Figure 5.3: Setup 1: **Mogi source location = at deformation location.** Five synthetic test setups on a x-, y-grid respectively 1D, 2D and three 3D situations. The first one is a side view and the following four are top view illustrations. k = distance between deformation locations [m], • = Mogi source at reservoir level and □ = deformation at the surface

The second setup (figure 5.4 top view) is with 1 Mogi source 16 deformations and 1 Mogi source with 256 observations and thus 1 parameter to be estimated. The **1 Mogi source location ≠ at deformation location** setup, this is setup 2. This setup is a bowl shaped deformation. It is an easy test setup with one Mogi source strength needed to be estimated. The larger number of deformation locations will show if these extra deformations are needed to obtain a better source strength estimate or that the source strength can be estimated with a limited number of 16 deformation locations.

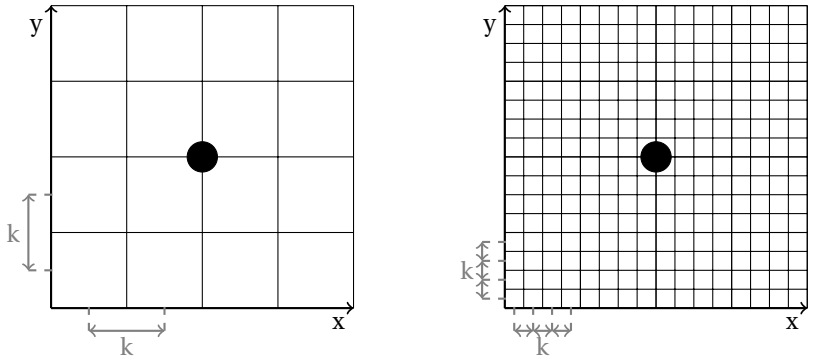

Figure 5.4: Setup 2: **1 Mogi source location ≠ at deformation location.** Two 3D synthetic test setups with 1 Mogi source and 16 and 256 deformations with grid distances of respectively 1500 and 300 m. • = Mogi source at reservoir level and □ = deformation at the surface

The third setup (figure 5.5 top view) has the same sumber of deformation locations as the second, but then with 4 Mogi sources and thus 4 parameters to be estimated. This is the **4 Mogi source locations ≠ at deformation location** setup, this is setup 3. The distance of these Mogi sources are chosen with the idea of a real-world scenario. The Groningen field contain wells that are closely grouped and have a distance between them in the order of 1800-4000 m, see figure A.1.

The four experiments of section 5.1.2 are applied on the three setups described above. Table 5.1 summarizes which experiment is applied to which setup. Each column in the table represent one of the three setups and each row then what number of Mogi sources and number of deformation locations. The settings of each experiment are summarized in the tables 5.2 to 5.5.

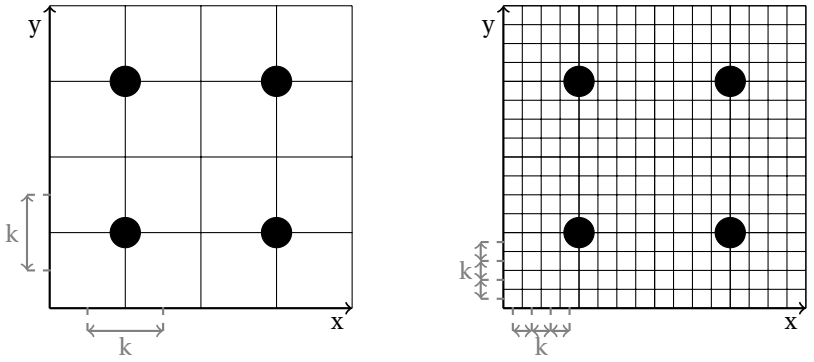

Figure 5.5: Setup 3: **4 Mogi sources locations ≠ at deformation location.** Two 3D synthetic test setups with 4 Mogi sources at a distance of 3000 m from each other in a 16 and 256 observations grid with respectively k=1500 and 300 m. • = Mogi source at reservoir level and □ = deformation at the surface

Table 5.1: The four identical twin experiments and the application to the different test setups, where each setup column represents the three setups described above. obs.=observed deformation, for example 16 obs. is 16 observed deformation locations.

Experiments		Setup 1	Setup 2	Setup 3	Settings
1a.	Testing the Mogi model	1 Mogi = 1 obs.			Table 5.2
1b.	Testing the particle filter	1 Mogi = 1 obs.			Table 5.2
2.	Testing particle filter variances	Mogi = obs.			Table 5.3
3.	Testing resampling step	16 Mogi = 16 obs.	1 Mogi ≠ obs.		Table 5.4
4.	Testing start value and 'jitter' variance	16 Mogi = 16 obs.	1 Mogi ≠ obs.	4 Mogi's ≠ obs.	Table 5.5

5.1.4. Experiment input

The parameters of each experiment are summarized in separate tables, table 5.2, 5.3, 5.4 and 5.5. Table 5.3 show the first three steps of the identical twin experiment (steps in section 5.1.1) and the parameters that are chosen for each step. The randomly generated source strength has a start value and a variance value, σ^2. Step 3 in the particle filter is where the observational probability density function is applied and four variance values are chosen that represent the observational error. The variance values are a small value of σ^2=1 mm to a large value of σ^2=100 mm. This variance will broaden the width of the Gaussian and Lorentz observational probability density functions (pdf) and increases the chance of ensemble members that will fall into this pdf. Furthermore a larger weight can be assigned to the ensemble members resulting in more ensemble members to be correct.

Table 5.2: **Testing the particle filter on the Mogi model**, for setup 1: **1 Mogi location = at 1 deformation location**. The number of ensemble members N is fixed and LOS vector [0 0 1]$[d_e d_n d_u]$.

Identical twin step:		1	2	3
Ensemble members variance:	σ^2 [-]	0.5	0.5	-
Ensemble members start value:	[-]	-1.0	-1.0	-
Ensemble members number:	N	1	1000	
Gaussian observation noise:	σ^2 [mm]	25	-	-
Particle filter Gaussian pdf:	σ^2 [mm]	-	-	25
Mogi source depth:	z [m]	-3000, -3001, -3010, -3100	-	-
Poisson's ratio:	ν	0.20, 0.25, 0.30	-	-
Bias value:	b [mm]	3, 30	-	-

Table 5.3: **Testing particle filter variances**, for setup 1: **Mogi source = at deformation location**. There are four observational pdf variances in the particle filter. The number of ensemble members N is fixed, the same for the Mogi source depth z=-3000 m, Poisson's ratio ν=0.25 and LOS vector [0 0 1][$d_e d_n d_u$].

Identical twin step:		1	2	3
Ensemble members variance:	σ^2 [-]	0.5	0.5	-
Ensemble members start value:	[-]	-1.0	-1.0	-
Ensemble members number:	N	1	10, 100, 1000, 10000	-
Distance between obs. location:	k [m]	1500, 3000, 6000	1500, 3000, 6000	-
Gaussian observation noise:	σ^2 [mm]	25, 4	-	-
Particle filter Gaussian pdf:	σ^2 [mm]	-	-	1, 10, 25, 100
Particle filter Lorentz pdf:	σ^2 [mm]	-	-	1, 10, 25, 100

Table 5.4: **Testing the resampling step.** The observational pdf variance of the particle filter is fixed, the same for the number of ensemble members N is fixed, the same for the Mogi source depth z=-3000 m, Poisson's ratio ν=0.25 and LOS vector [0 0 1][$d_e d_n d_u$].

		16 Mogi sources = at deformation location			
Identical twin step:		1	2	3	4
Ensemble members variance:	σ^2 [-]	0.5	0.5	-	-
Ensemble members start value:	[-]	-1.0	-1.0	-	-
Ensemble members number:	N	1	1000	-	-
Distance between obs. location:	k [m]	1500, 3000, 6000	1500, 3000, 6000	-	-
Gaussian observation noise:	σ^2 [mm]	25	-	-	-
Particle filter Gaussian pdf:	σ^2 [mm]	-	-	25	-
Gaussian resample 'jitter':	σ^2[-]	-	-	-	0.25
		Mogi sources ≠ deformation location			
Ensemble members variance:	σ^2 [-]	0.5	0.5	-	-
Ensemble members start value:	[-]	-1.0	-1.0	-	-
Ensemble members number:	N	1	1000	-	-
Distance between obs. location:	k [m]	-	1500, 300	-	-
Gaussian observation noise:	σ^2 [mm]	25	-	-	-
Particle filter Gaussian pdf:	σ^2 [mm]	-	-	25	-
Gaussian resample 'jitter':	σ^2[-]	-	-	-	0.25

Table 5.5: **Testing the start value and 'jitter' (noise).** The number of ensemble members N is fixed, the same for the Mogi source depth z=-3000 m, Poisson's ratio ν=0.25 and LOS vector [0 0 1]$[d_e d_n d_u]$.

		16 Mogi sources = at deformation location			
Identical twin step:		1	2	3	4
Ensemble members variance:	σ^2 [-]	0.5	1.0	-	-
Ensemble members start value:	[-]	-1.0	-2.0	-	-
Ensemble members number:	N	1	1000	-	-
Distance between obs. location:	k [m]	1500, 3000, 6000	1500, 3000, 6000	-	-
Gaussian observation noise:	σ^2 [mm]	25	-	-	-
Particle filter Gaussian pdf:	σ^2 [mm]	-	-	25	-
Gaussian resample 'jitter':	σ^2[-]	-	-	-	0.25, 0.5
		1 Mogi source ≠ deformation location			
Ensemble members vatiance:	σ^2 [-]	0.5	1.0	-	-
Ensemble members start value:	[-]	-1.0	-2.0	-	-
Ensemble members number:	N	1	1000	-	-
Distance between obs. location:	k [m]	-	1500, 300	-	-
Gaussian observation noise:	σ^2 [mm]	25	-	-	
Particle filter Gaussian pdf:	σ^2 [mm]	-	-	25	-
Gaussian resample 'jitter':	σ^2[-]	-	-	-	0.25, 0.5
		4 Mogi sources ≠ deformation location			
Ensemble members vatiance:	σ^2 [-]	0.5	1.0	-	-
Ensemble members start value:	[-]	-1.0	-2.0	-	-
Ensemble members number:	N	1	1000	-	-
Distance between obs. location:	k [m]	3000	1500, 300	-	-
Gaussian observation noise:	σ^2 [mm]	25	-	-	-
Particle filter Gaussian pdf:	σ^2 [mm]	-	-	25	-
Gaussian resample 'jitter':	σ^2[-]	-	-	-	0.25, 0.5

5.2. Results identical twin experiment

The results of the identical twin experiments are presented in the following subsections. Each experiment shows a selection of results, the rest of the results are placed in appendix D.

5.2.1. Particle filter and Mogi model experiment

The Mogi geomechanical model is tested with variable source depths, source strenghts and different Poisson's ratios. This is experiment 1a. The particle filter with a Gaussian observational pdf is tested on the Mogi model with noisy and biased deformations (input parameters: table 5.2). This is experiment 1b. The results of these experiments are presented in table 5.6.

The Mogi source depth is varied from -3000 to -3100 m. The choice for these depths is based on the approximate well depths of the production wells in Groningen. These well depths vary from -2800 to -3000 m (see table A.3 in the appendix). The result of varying the depth from -3000 to -3100 leads to a surface deformation difference of millimetres between the four depths. The Mogi sources are placed at a constant depth for the remaining experiments, because a change depth does not influence the surface deformation much, only by 0.2 mm.

Poisson's ratio ν is varied by 0.05 and results in two values, namely 0.20 and 0.30. This is done for a fixed depth of -3000 m and source strength of -0.4871 [-]. The choice for a ratio of ν=0.20 and 0.30 is based on the values of Lele et al. (2015), where Poisson's ratio varies for the different stratigraphical units of the Groningen subsurface. The results show a deformation value of -3.24 and -2.16 mm for respectively ν=0.20 and 0.30. Changing the ratio by 0.05 resulted in a deformation change of 0.50 mm. Poisson's ratio change has a small influence on the deformation values.

The Mogi source strength is varied by adding -0.10 and -1.00 [-] to the source strength of the previous experiment (-0.4871 [-]). The resulting surface deformation difference with the previous experiment is respectively 0.55 and 5.56 mm. This is a linear relationship. A surface deformation difference of 5.56 mm is caused by a source strength difference of 1.00 [-]. This is an important fact for future estimated surface differences, especially when the Mogi model is applied on a real situation, where the source strength is not known and needs to be estimated. A difference of ±5.56 mm between the observed deformation and estimated surface deformation, will have a source strength offset of ±1.00 [-], when there is no noise or bias present in the surface deformation values. A bias and noise free surface deformation is not a realistic situation, therefore particle filter experiments are done with noisy observations.

Table 5.6: Mogi model experiment. The highlighted values show parameters that are varied. The particle filter results are the last three rows, where deformation + noise and deformation + noise + bias. P.=particle, S.=source, Res.=residual and obs.=observed deformation.

Depth z [m]	Poisson's ratio ν	Bias b [mm]	Noise σ^2 [mm]	P. filter σ^2 [mm]	S. strength 'truth' [-]	Res. source strength [-]	Observation [mm]	Res. obs. [mm]
-3000	0.25	-	-	-	-0.4871	-	-2.70	-
-3001	0.25	-	-	-	-0.4871	-	-2.70	-
-3010	0.25	-	-	-	-0.4871	-	-2.68	-
-3100	0.25	-	-	-	-0.4871	-	-2.53	-
-3000	**0.20**	-	-	-	-0.4871	-	-3.24	-
-3000	**0.30**	-	-	-	-0.4871	-	-2.16	-
-3000	0.25	-	-	-	**-0.5871**	-	-3.26	-
-3000	0.25	-	-	-	**-1.4871**	-	-8.26	-
-3000	0.25	**-**	25	25	-0.4871	0.0538	1.60	4.60
-3000	0.25	**3**	25	25	-0.4871	0.1625	4.60	6.40
-3000	0.25	**30**	25	25	-0.4871	1.7732	31.60	24.46

The particle filter estimates the posterior source strength and surface deformation. The residual results are presented in the last three rows of table 5.6. Three cases are conducted with the particle filter one where only Gaussian generated noise is added and two where different bias values are added.

The experiment with only added noise shows the lowest residuals on both parts (source strength and deformation), compared to the other two experiments. This seems logic, because the resulting model deformation value is closer to the noisy deformation and source strength truth and is not influenced by the bias values as in the other two experiments. The deformation residual of 4.60 mm does not result in a source strength residual of ±1.00 [-], as found out above in the Mogi model, where the particle filter is not applied. The particle filter is able to estimate the real source strength truth by 0.05 [-], even with noisy observations.

The experiment with the added bias values shows large residuals. The bias of 3 millimetre results in a residual value that is 1/3 of the source strength truth and 1.4 times larger than the deformation truth. The 30 millimetre bias value added to the observed deformation results in a residual source strength value of 1.70 [-] and a residual deformation of 24.50 mm. The particle filter is able to estimate a source strength value within 1.70 [-] from the truth, despite the deformation difference of 24.50 mm. It can be concluded that the particle filter estimates the source strengths 1.70 [-] from the truth value, by a deformation residual of 24.50 mm. The following experiments test the particle filter in different settings with multiple Mogi sources and variable distances between the observed deformations.

5.2.2. Particle filter variance variability experiment

Figure 5.6 shows the RMSE of the identical twin experiment for 1,2,4,9 and 16 Mogi sources at the same deformation locations. The particle filter is applied with four different variance values of the Gaussian and Lorentz observational pdf (input: table 5.3). The RMSE varies between 3 to 5 mm. They are expected if the particle filter is effectively finding the minimum between observed deformation and modelled deformation. The RMSE and the variance value of the Gaussian noise added to the observed deformation values are both in the same order of 5 mm. The difference between the experiments with the Gaussian pdf (black dots) for the observations and the Lorentz pdf (black circles) for the observations is small for large variances and large for small variances. The setup with 1 and 2 Mogi sources show lower RMSE values than the setups of 4, 9 and 16 Mogi sources. The setups with more Mogi sources have their deformations interfering each other from all directions.

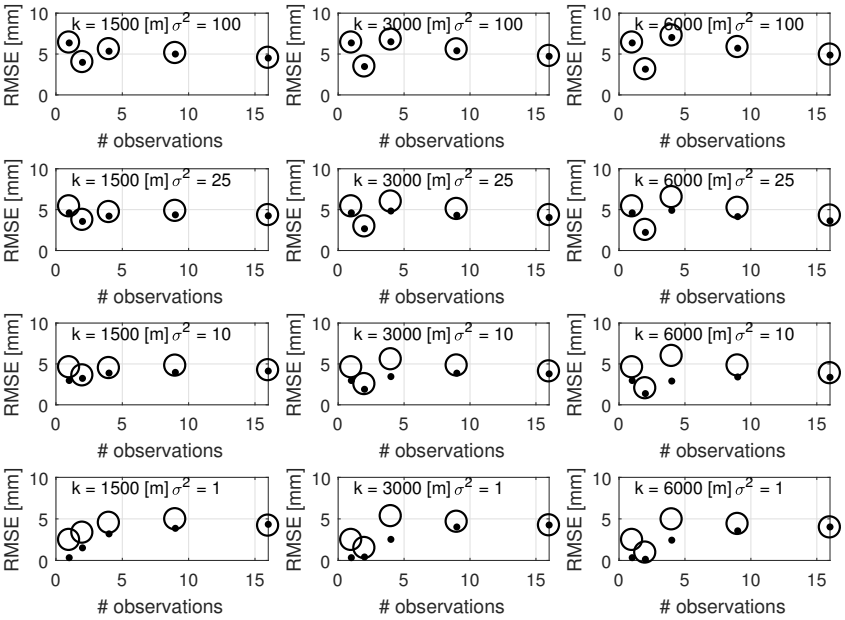

Figure 5.6: RMSE values (y-axis) of the observed deformation [mm] for the five test setups (x-axis). Top row - bottom row have observational pdf variances of σ^2=100 - 1 mm. Each column shows the three different distances k between the deformations. The number of ensemble members of each Mogi source strength N=1000. • = results generated by the observational Gaussian pdf, ◯ = Lorentz pdf

Figure 5.7 shows the RMSE values of the identical twin experiment for the estimated source strengths. This is the interesting part of the twin experiment, because the objective of the particle filter is to estimate these source strengths. The high and low RMSE values pattern for the observed deformations are also present

in the subplots for the source strengths (red dots and circles). The RMSE values of the 16 Mogi sources at the same deformation locations are lower than the RMSE values of the 9 Mogi sources at the same deformation locations. This holds for all 16 subplots. There is almost no difference between the RMSE subplots of σ^2=25 and 100 mm for the distances k=3000 and 6000 m between the deformation locations. The Mogi sources interfere less for these large distances k. As a result the estimated Mogi source strengths are unique.

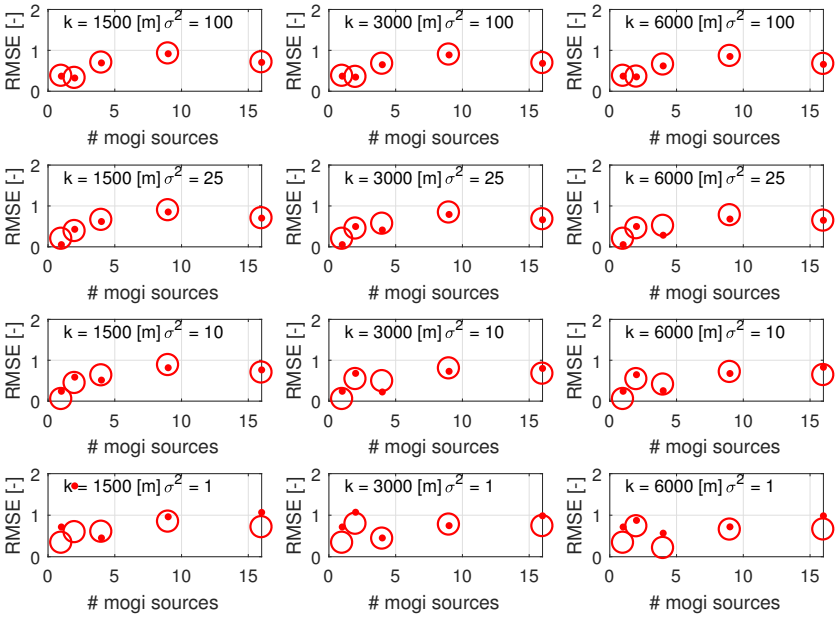

Figure 5.7: RMSE values (y-axis) of the source strengths [-] for the five test situations (x-axis). Top row - bottom row have observational pdf variances of σ^2=100 - 1 mm. Each column shows the three different distance k between the deformations. The number of ensemble members of each Mogi source strength N=1000. The particle filter uses an observational, • = Gaussian pdf, ◯ = Lorentz pdf

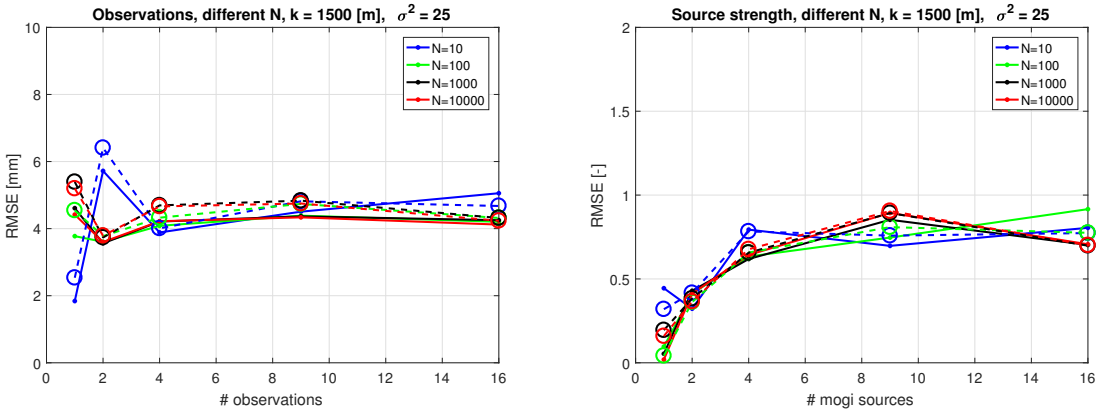

Figure 5.8: RMSE values for different numbers of ensemble members N=10, 100, 1000 and 10000 for grid space k=1500 m and particle filter variance σ^2=25 mm. **Left**: RMSE values [mm] of the deformation for the five test situations (x-axis). **Right**: RMSE values [-] of the source strengths for the five test situations (x-axis). • = Gaussian observational pdf, ◯ = Lorentz observational pdf

The number of ensemble members N is varied for the five test situations for distance k=1500 m between the deformation. The particle filter is applied with the observational Gaussian and Lorentz pdf with variance σ^2=25 mm. The results are shown in figure 5.8. The RMSE of the deformation show similar results for the different N values and similar results for the Gaussian and Lorentz observational pdf. The source strength RMSE values are similar as well for different sizes of N. The number N does not matter for this setting. For this number of Mogi sources at the same deformation locations, the particle filter is able to estimate the

source strengths with a small number of ensemble members.

The previous figures are generated from one set of ensemble members. Step 2 of the identical twin experiment (steps in section 5.1.1) is repeated 5 times in order to find out if the RMSE values are robust. The RMSE values of the five experiments are plotted in figure 5.9 top row for the five test situations with a particle filter with an observational Gaussian pdf of variance σ^2=25 mm. The average standard deviation of the deformation RMSE values is 0.10 mm and 0.02 [-] for the source strengths. The standard deviation is low for both parts, and it can be concluded that using one set of ensemble members in step 2 is representative for the simulation results.

Figure 5.9 bottom row shows the RMSE values of the particle filter with the Gaussian observational pdf variance of σ^2=4 mm and added Gaussian noise to the observed deformation with a variance of σ^2=4 mm. The source strength RMSE values show almost the same results as the top row plot. There is no difference between the source strength RMSE values, when using different variances values for generating noise and applying the particle filter with a Gaussian pdf. So the particle filter performance is comparable to the above situation of using a variance of σ^2=25 mm for the Gaussian noise and Gaussian observational pdf.

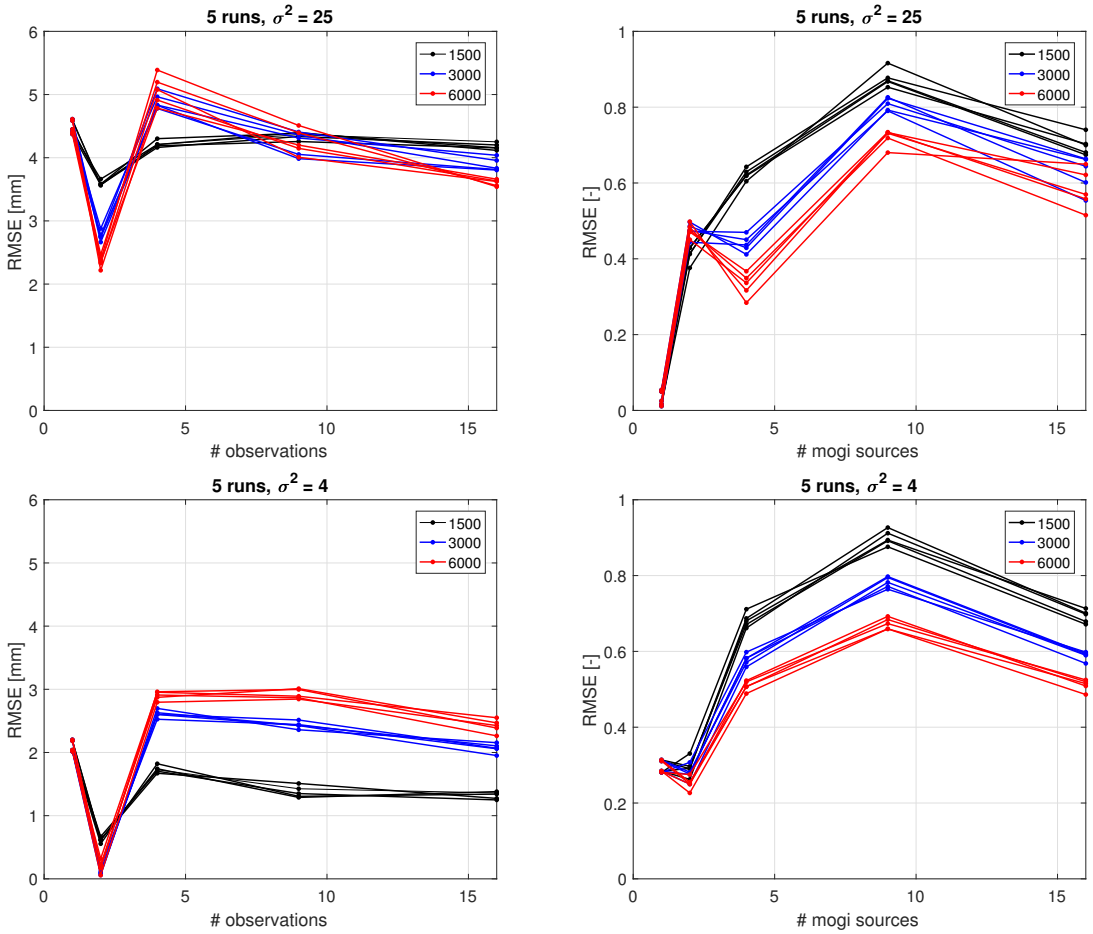

Figure 5.9: RMSE values of 5 experiments for the five test situations (x-axis), N=1000, distance k=1500, 3000 and 6000 m between the deformation locations and particle filter with a Gaussian observational pdf variance σ^2=25 and 4 mm and Gaussian noise added of variance σ^2=25 and 4 mm. **Left column**: RMSE values [mm] of the deformation for the five experiments, situations (x-axis). **Right column**: RMSE values [-] of the source strengths for the five experiments, situations (x-axis).

The particle filter weights representing the observational pdf are plotted for the 1 Mogi source and 2 Mogi sources setting (of figure 5.3) in figure 5.10. This figure shows on the left the result of particle filter observational pdf (Gaussian and Lorentz) plotted versus the deformation and on the right the observational pdf plotted versus the source strength. The particle filter variance σ^2=25 mm is used. The results with the Gaussian pdf for observations are the black dots and the red dots are the results of the Lorentz pdf for observations. The Lorentz pdf is wider at the bottom compared with the Gaussian pdf, because the pdf is computed differently. The estimated deformation with the Gaussian pdf is close to the truth value of the deformation (green

dot), while the estimation of the Lorentz pdf is further from the truth value and from the noisy deformation (blue dot). The estimated source strength shows the same behaviour, namely the source strength estimation of the Gaussian pdf is closer to the truth than the source strength estimation of the Lorentz pdf (red diamond). The particle filter is able to estimate the posterior deformation and source strength value correctly, despite the noisy deformation.

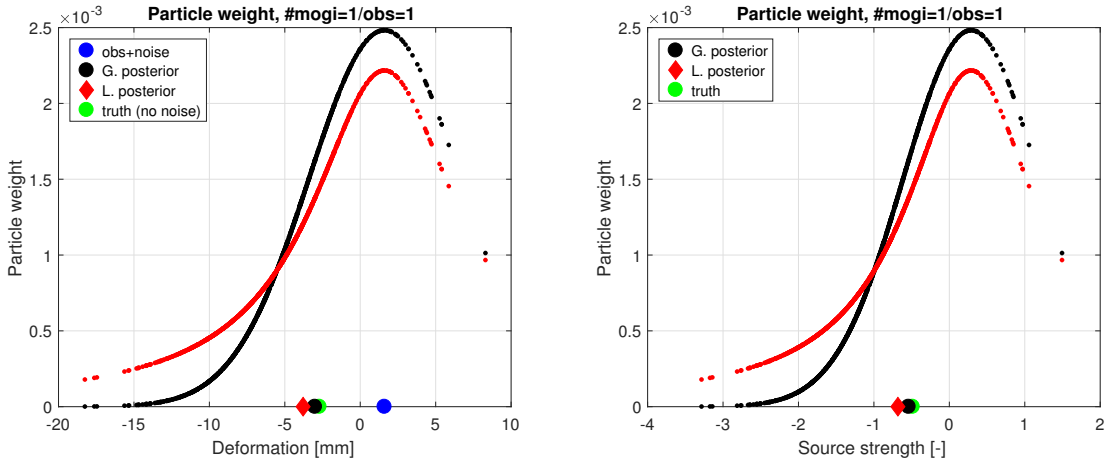

Figure 5.10: Particle filter observational pdf vs. ensemble members for a 1 Mogi setting, **black** = Gaussian pdf and **red** = Lorentz pdf. Both pdf's with variance σ^2=25 and Gaussian noise added of variance σ^2=25 mm. **Left**: deformation **Right**: source strength.

Figure 5.11 shows the result of the 2 Mogi sources at the same deformation location. 2. The curve is not as distinct as the Gaussian pdf in the 1 Mogi setting; this is caused by the proximity of the two Mogi sources located at a distance of 1500 m from each other. The sources their displacements interfere at this distance, when placed at a reservoir level depth of -3000 m. The particle filter observational pdf results in this kind of behaviour, the non-distinct Gaussian curve shape.

One point is highlighted in pink that shows an observational pdf value of 2.9e-04. This point is close to the truth for the first deformation point, while for the second deformation point this is not the case. This results in estimated source strength values far away from the truth source strength for both Mogi sources. The estimate of the ensemble member with the highest weight have a deformation close to the noisy truth deformation, but their source strength is not close to the source strength truth. Therefore this result shows that taking only the estimate of the ensemble member with the highest weight of the particle filter is not enough to estimate the source strength correctly. The proximity of the two Mogi sources causes a non-distinct Gaussian curve. The Gaussian curve is almost filled; this is caused by a difference in estimated deformation for the first and second point. The estimated posterior deformation value (black dot and red diamond) is close to the truth (green dot). This accounts for the deformation and source strength part of the identical twin experiment. There is for this setting no difference between the Gaussian and Lorentz observational pdf.

5.2.3. Particle filter resampling experiment

The resampling experiment is done for setup 1: 16 Mogi sources = at deformation locations and setup 2: 1 Mogi source ≠ at 16-256 deformation locations.

Setup 1: 16 Mogi sources = at deformation locations

Figure 5.12 presents a deformation map of the observed deformation, the source strength values and four residual maps for a distance of k=1500 m between the deformation locations. The title of the four bottom plots contains the RMSE. The resampling step of the particle filter is tested. The residual maps of the deformation (left column) show a small change in residual values. The resampled map is lighter in colour, which corresponds to a value closer to zero. In other words the estimated deformation is close to the observed deformation. The change in residual values is expressed in the RMSE value as well. The RMSE is changed from 4.25 to 3.96 mm. The resampling step lowers the RMSE value of the deformation estimate.

The residual map of the source strengths (right column) is changed as well after resampling. The source estimates in the subplot (title: residuals, posterior) have larger errors. The residual values are increased instead of decreased, while the errors in the deformation subplot has decreased in that corner. The RMSE value

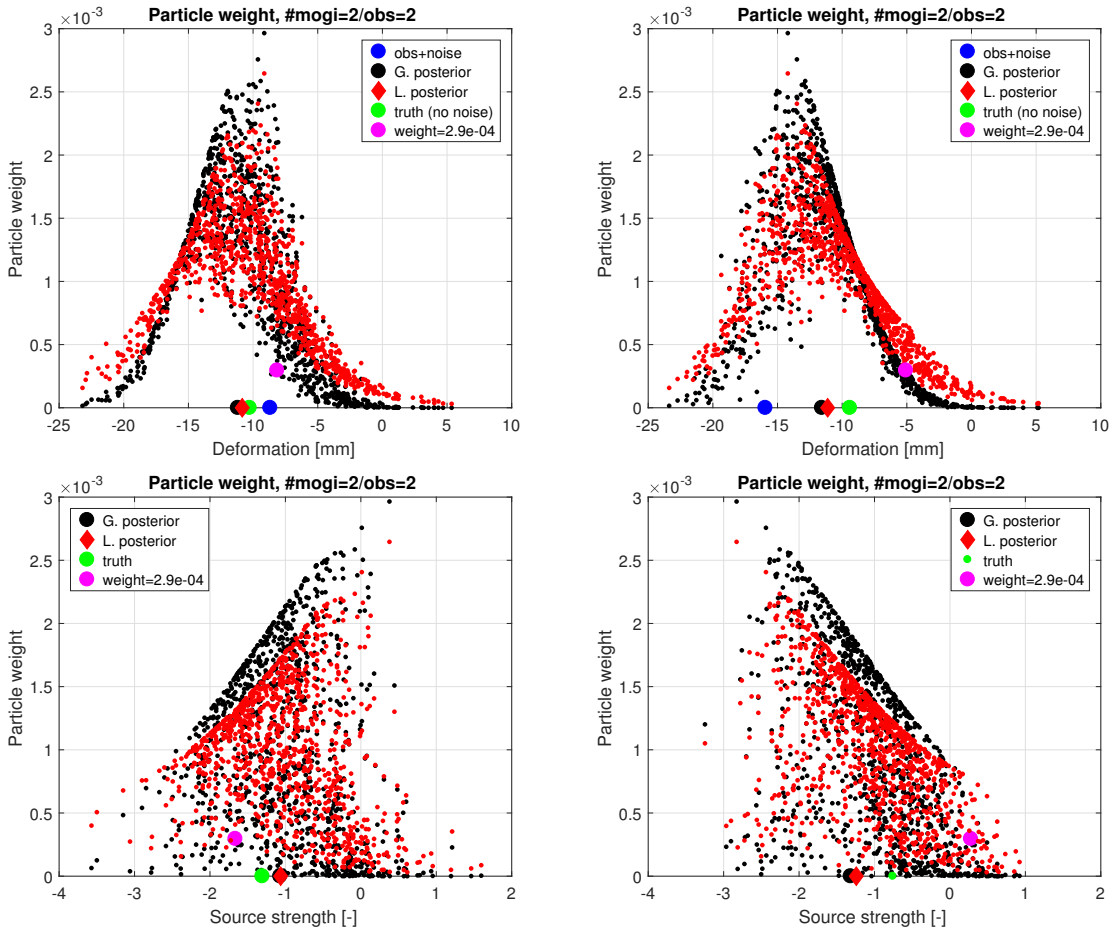

Figure 5.11: Particle filter observational pdf vs. ensemble members for a 2 Mogi setting, **black** = Gaussian pdf and **red** = Lorentz pdf. Both pdf's with variance σ^2=25 and Gaussian noise added of variance σ^2=25 mm. **Top row**: deformations **Bottom row**: source strengths

of the source strengths before resampling is lower than the RMSE value after resampling. This is the other way around for the deformation RMSE values. The RMSE has changed from 0.703 [-] to 0.742 [-].

The same behaviour of the RMSE values of the deformation and source strengths is present for the test setups with distances k=3000 and 6000 m between the deformation locations. The RMSE values of deformation and source strength with larger distances between them are lower compared to k=1500 m. The deformations of these Mogi sources interfere more at a distance k=1500 m. This results in more correct ensemble members where weight is assigned to. This higher number of weighted ensemble member combinations lead apparently to a higher RMSE value. The larger distances will have a better chance on an unique solution, because the Mogi sources their deformations influence each other less. This results in more correct ensemble members that are the same, leading to a unique solution.

The resampling step uses for the added 'jitter' (noise) to the resampled ensemble members a small variance value. This small value is enough to reproduce new ensemble members and lowering the RMSE value and residuals for the estimated deformation. This is the goal of the resampling step.

The probability density functions of deformation and source strengths are plotted in figure 5.13. These are the pdf's of the case with 16 deformation locations. The coming sections will show the distribution of each location separately. The left figure shows an offset in the prior pdf (blue) compared to the posterior curve, this is expected, because the observed deformations are not taken into account. The particle filter is applied and this result in the posterior curve (red). The posterior curve is aligned with the observation curve (black). This is the goal of the particle filter. The use of the particle filter is a better estimate, than the prior guess of the deformation. The maximum weighted curve (green) shows the estimated deformation when using only the highest weighted ensemble member. This shows a good fit with the observations in this experiment setup of distance k=1500 m. The fit is less good when using distances of k=3000 and 6000 m (figures D.4 and D.7). In these cases the posterior curve is the better option to use.

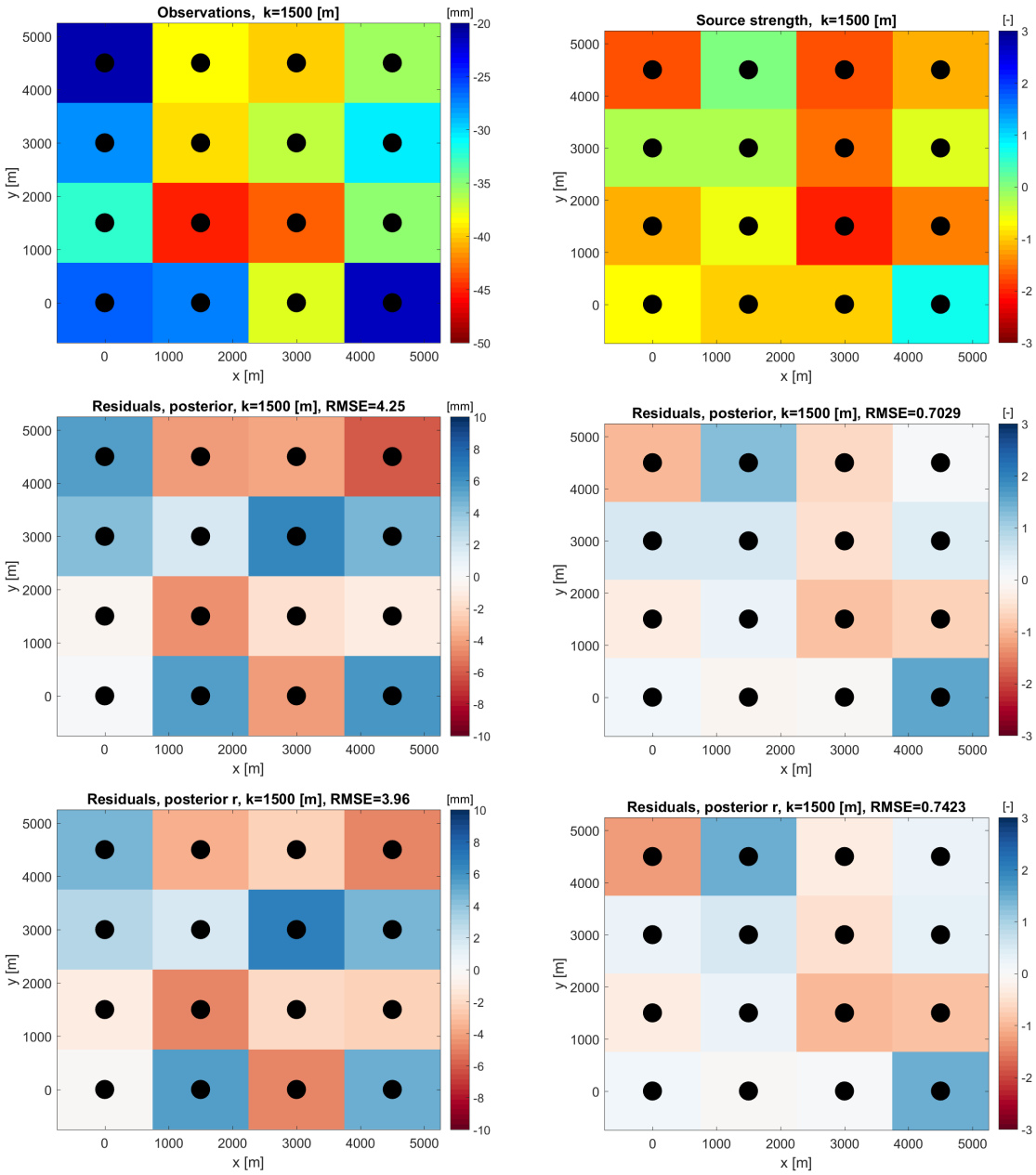

Figure 5.12: Deformation map and residuals maps (observed deformation minus estimated deformation, blue/red coloured) for k=1500 m, Gaussian pdf σ^2=25 mm. **Left column**: observed deformation map [mm], posterior deformation, posterior resampled **Right column**: source strength truth map [-], posterior source strengths, posterior resampled. Residual map colours generated by: Cobeldick (2017).

The posterior curve (red) of the source strength shows a better fit with the source strength 'truth' curve (black), than the prior curve (blue) with the source strength 'truth'. The resampled posterior curve (grey) shows an even better fit with the source strength 'truth'. All curves have similar mean values. The maximum weighted curve (green) shows an almost perfect fit, but the residual height map has at some point's very large residuals (figure D.1). The distribution of the source strength estimates is good, but the deformation estimates are not. The posterior estimation is the better option, than using only the maximum weighted ensemble member. This is also concluded in section 5.2.2 for the figure 5.11.

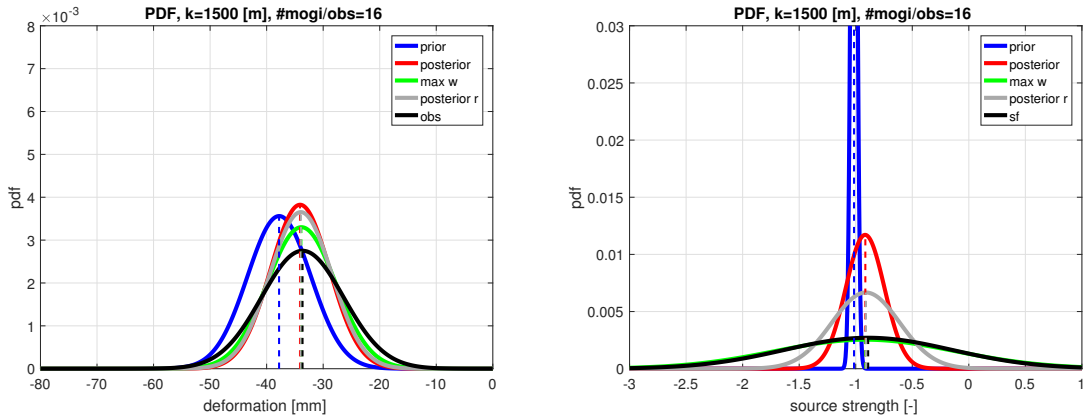

Figure 5.13: **Left**: the probability density functions of the observed deformation (black), prior deformation (blue), posterior (red), posterior resampled (grey) and maximum weighted (green). **Right**: source strength pdf's.

Setup 2: 1 Mogi ≠ at deformation locations

The resampling step is also tested on the setup with one Mogi source and a varying number of deformation locations and distances between the locations. The pdf's of the deformation for these one Mogi source setups are presented in figure 5.14. The left figure shows the pdf's of the 1 Mogi source with 16 deformation locations. The mean value of the resampled curve (grey) is aligned with the mean value of the observed deformation (black curve). The RMSE values are 4.33 and 4.30 mm respectively before and after resampling. The deformations RMSE value indicate that the first attempt of estimating the Mogi source strength is already sufficient, because the RMSE value change is almost zero.

The right figure shows the pdf's of the experiment setup with a higher number of deformation locations (256 instead of 16). There is no difference between the posterior and resampled posterior curve, this is also expressed in the RMSE value of respectively 5.03 and 5.03 mm. The RMSE value of these 256 deformation locations setup is 0.50 mm larger than the RMSE value of 16 observations setup. The denser and higher number of noisy deformations results in a higher RMSE value.

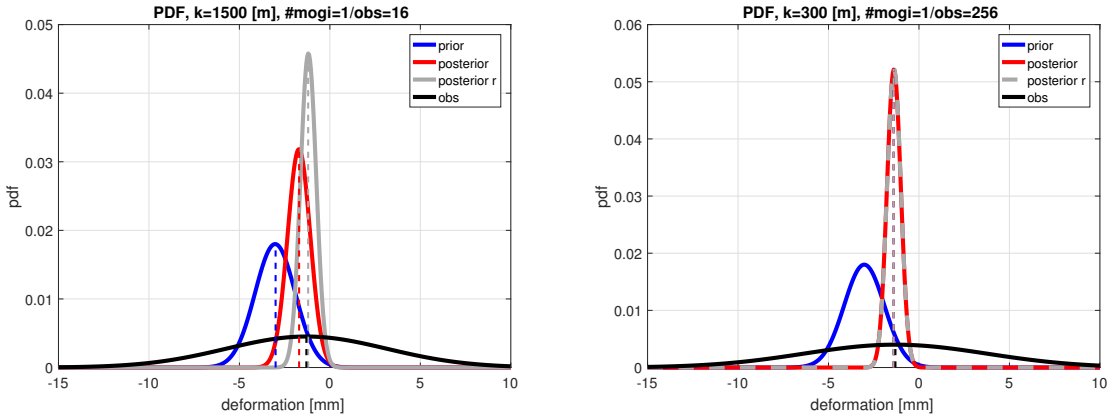

Figure 5.14: **Left**: the probability density functions of the 1 Mogi source setup for k=1500 m. Observed deformation (black), prior deformation (blue), posterior (red) and posterior resampled (grey). **Right**: the probability density functions of the 1 Mogi source setup for k=300 m.

The results of the estimated source strengths are presented in table 5.7. The first test situation with distance k=1500 m and 16 deformation locations show a posterior source strength value that differs only 0.09 [-] from the truth. The resampling step improves the estimation of the source strength. This is also seen for the deformation values. This seems a logic result, because there is only one Mogi source to be estimated. There are no other sources with their deformations that interfering the estimate.

The second test with 256 deformation locations show also a low posterior value, the same as the experiment of 16 deformation locations. The resampled source strength residual value is larger than the residual prior value. The resampling step shows not an improvement for this case. The high number of deformation

locations and 1 Mogi source do not need a resampling step. Many ensemble members are given a high weight and the resampling step has duplicated many of these ensemble members. This results in a source strength value that does not match with the 'truth' value. A solution could be adding a larger 'jitter' (noise) variance to vary the new ensemble members more or not performing the resampling step at all.

Table 5.7: Resampling step experiment estimated source strength results of the particle filter. The last three columns show the residual values of the prior, posterior and resampled posterior source strength with the source strength truth

Grid k [m]	Particle filter σ^2 [mm]	Jitter σ^2 [-]	Source strength 'truth' [-]	Prior residual [-]	Posterior residual [-]	Posterior r residual [-]
1500	25	0.25	-0.4871	-0.537	0.091	-0.084
300	25	0.25	-0.4871	-0.537	-0.089	0.585

5.2.4. Particle filter variability in start value and 'jitter' variance experiment

The difference in start value between generating the 'truth' and source strength ensemble members and the different 'jitter' variances added in the resampling step is done for three setups. Setup 1: 16 Mogi sources = at deformation locations, setup 2: 1 Mogi source ≠ at 16/256 deformation locations and setup 3: 4 Mogi sources ≠ at 16/256 deformation locations. The results are presented below.

Setup 1: 16 Mogi sources = at deformation locations

Figure 5.15 shows the residual deformation and source strength maps for a distance of k=1500 m between the deformation locations. The start value for generating the ensemble members is different from the start value that is used for generating the 'truth'. Furthermore two different 'jittter' (noise) variances are tested, namely σ^2=0.25 and 0.5 [-]. All residual maps have the same colour scale, this is done for an easy compare between the maps (also the extra ones in appendix D).

The left side of the figure shows the deformation results. The posterior map shows residual values between 10 and -10 mm. The RMSE value is 6.31 mm. The particle filter gives a good deformation estimate. The second and third row contains the resampled residual maps. The map with the added 'jitter' (noise) variance of σ^2=0.5 [-] has a RMSE value of 4.25 mm compared to the 4.40 mm of the 'jitter' (noise) variance of σ^2=0.25 [-] The difference in deformation RMSE values between these two maps is not large.

The right side of the figure shows the source strength results. The posterior residual map shows residual values of ±0.5 [-] and a RMSE value of 0.593 [-]. This value is lower than the RMSE value of the posterior map in figure 5.12, where the start value for generating the ensemble members is the same as for generating the truth value. The resampled residual maps show as well values around ±0.5 [-]. The resampling step with the jitter variance of 0.5 [-] has a lower RMSE value, than the resampling step of jitter variance 0.25 [-]. This is also seen in the resampling results of the deformation part. It can be concluded that the added jitter variance of 0.5 [-] results in a lower RMSE value for a setting where the variance is large for generating the source strength ensemble members.

This experiment is also performed for distances of k=3000 and 6000 m between the deformation locations. Similar trends in RMSE values for both deformation and source strengths are observed for these grid distances.

The pdf's of the 16 deformation locations and source strengths are plotted in figure 5.16. The left plot shows a big change from the prior distribution (blue curve) to the posterior distribution (red). The mean value (dashed line) from the posterior distribution is not fully aligned with the observations (black). Both resampling curves (grey and cyan) have a mean value that is perfectly aligned with the deformation mean value. The resampling step performs as expected. There is no difference between the two different jitter variances curve.

The right plot shows the pdf distribution of the truth source strength (black). This is a broad distribution. The prior distribution (blue) is far off, due to the different start values used for generating the ensemble members. The posterior distribution (red) shows a mean value (dashed line) that is already closer to the mean values of the truth source strength. The resampling step results in similar mean values as the source strength, which is also shown in the RMSE values of the previous figure. The pdf plots of the two other distances between the deformation locations, show similar results (Appendix D.2).

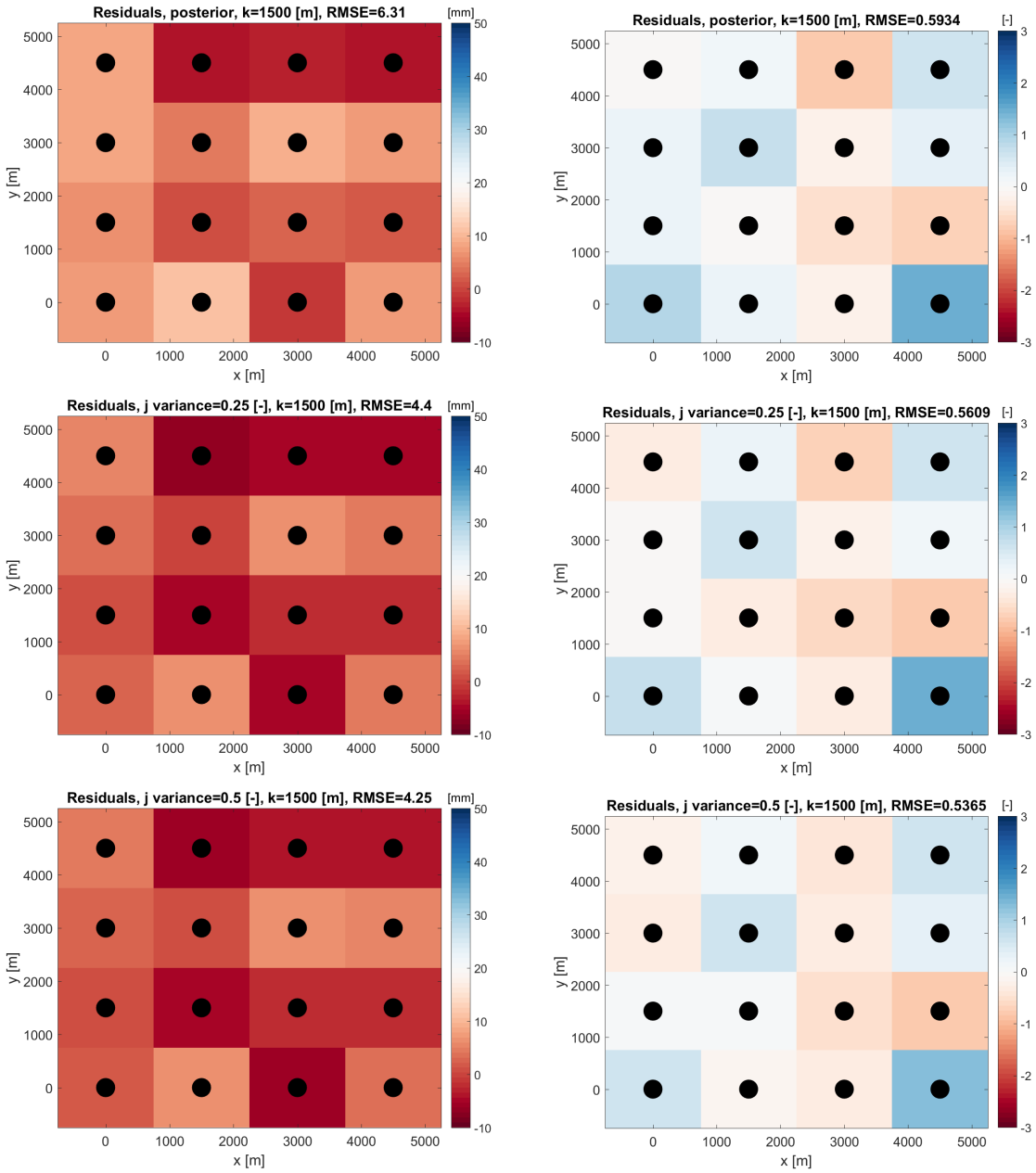

Figure 5.15: Deformation / source strength residuals maps (observed deformation minus estimated deformation) for k=1500 m, Gaussian pdf σ^2=25 mm. **Left column**: posterior deformation map, resampled posterior with 'jitter' σ^2=0.25 and 0.5 [-]. **Right column**: source strength results

Setup 2: 1 Mogi source ≠ at deformation locations

The experiment is applied as well on setup 2 with 1 Mogi source and 16 and 256 at deformation locations. The RMSE values of the deformation show an improvement after the resampling step. There is no difference between the results of the two different jitter variance values. The residual values of the source strength show an improvement after the resampling step. The pdf plot of the deformation is similar to figure 5.16.

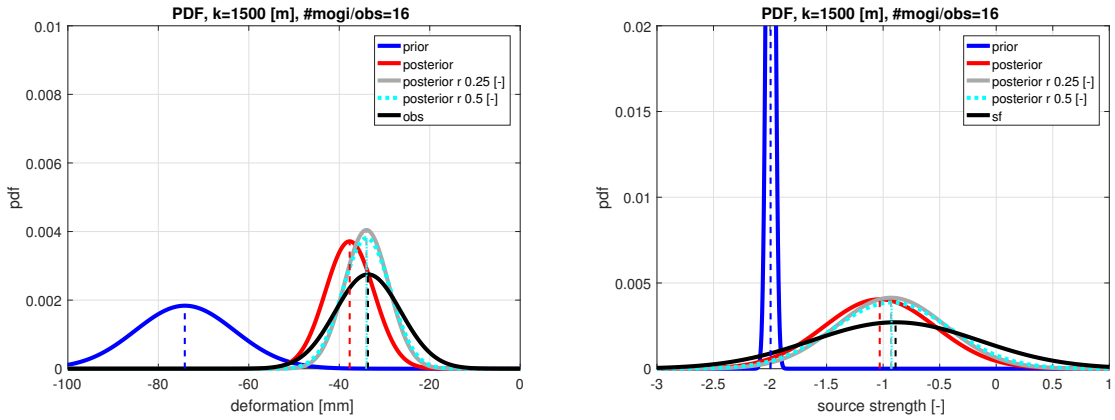

Figure 5.16: **Left**: the probability density functions of the observed deformation (black), prior deformation (blue), posterior (red) and posterior resampled (grey). **Right**: source strength pdf's. All distance k=1500 m.

Setup 3: 4 Mogi source ≠ at deformation locations

The results of setup 3 with 4 Mogi sources ≠ at 16 / 256 deformation locations are presented in the following figures below. Figure 5.17 shows the 16 deformations 'truth' (green dots), posterior estimated deformation, the ensemble members (red dots) and resampled ensemble members for a jitter variance 0.5 [-] versus the particle filter weight. The particle filter weight (observational pdf) is the same for all the 16 deformation locations, but it is interesting to see how the 'truth' value (green dot) and estimated deformation (black dot) varies from one deformation locations to another.

The bottom plot of 5.17 shows the resampled ensemble members where the y-axis scale is changed for a better view compared to the top plot. The bottom plot shows the highest weights assigned to the ensemble members near the estimated deformation (black). The particle filter and the number of N=1000 ensemble members results in 7 ensemble members with a high weight and many ensembles with a low weight.

The 4 Mogi source strengths of the 16 deformation locations are plotted as well versus the particle filter weight. These four subplots are presented in figure 5.18. The top plot in this figure shows the highest weights assigned to the ensemble members near the true source strength (green). The bottom plot shows the resampled ensemble members, where the high weights are located near the true source strength (green). The particle filter estimates the source strength well, because the estimated posterior source strength (black) and the true source strength (green dot) are almost aligned.

The results of the 4 Mogi source strengths versus particle filter weight of the 256 deformation locations show 2 high weights assigned to ensemble members (figure D.23 in the appendix). The resampling step assigns more high weights to ensemble members. The experiment setup, with a large number of deformations for estimating the 4 source strengths, benefits from the resampling step. The number of N=1000 ensembles seems not to be sufficient in the first run of the particle filter. The second run of the particle filter have only 5 ensemble members with a weight higher than 0.05 (value of a Gaussian observational pdf).

Table 5.8 shows the deformation and source strength truth values together with two different ensemble members of equal particle filter weight. This is done to illustrate how two equally weighted ensemble members can have different estimated deformation and source strength values. The deformation is different for a couple of locations, namely location 1, 2 and 6. The difference is larger than 1.0 mm. The estimated source strength values are different compared to the truth for three source locations. The largest difference is 0.55 [-]. This is a large difference compared to the other estimated source strength values. The problem is probably caused by the positive source strength truth value of 0.15 [-] for source number 2. This resulted in positive deformation values. In addition the distance of k=3000 m between the sources causes interference of the deformation of the sources.

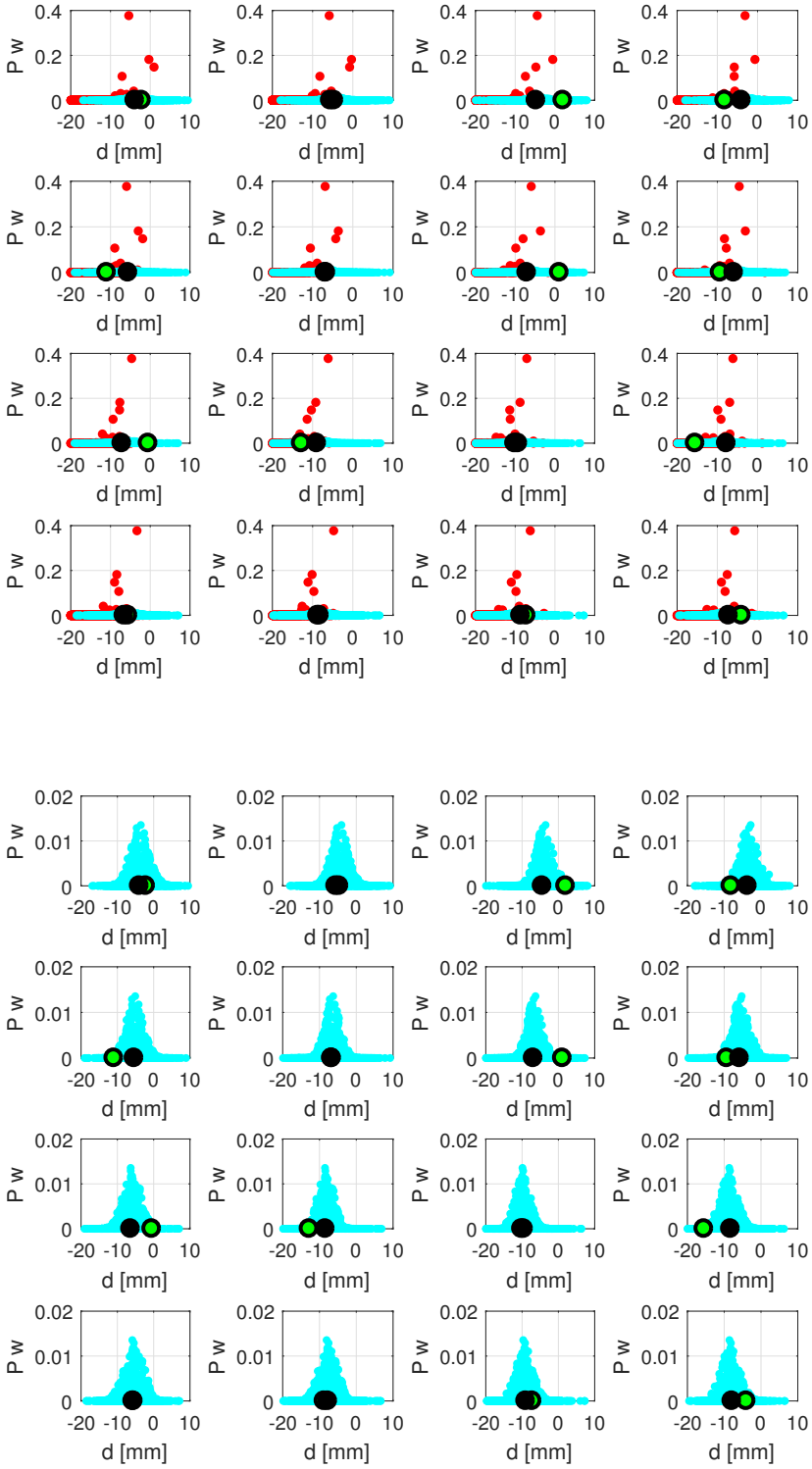

Figure 5.17: Deformation vs. particle filter weight, Gaussian pdf with σ^2=25 mm. The subplots are ordered the same as in figure D.16, where the top left subplot is the top left point in that figure. **Top**: red= ensemble members, cyan= resampled ensemble members with a jitter variance of σ^2=0.5 [-], black dot= estimated deformation and green dot=true deformation **Bottom**: cyan= resampled ensemble members with a jitter variance of σ^2=0.5 [-], black dot= estimated resampled deformation and green dot=true deformation, (different y-axis scale for a better view)

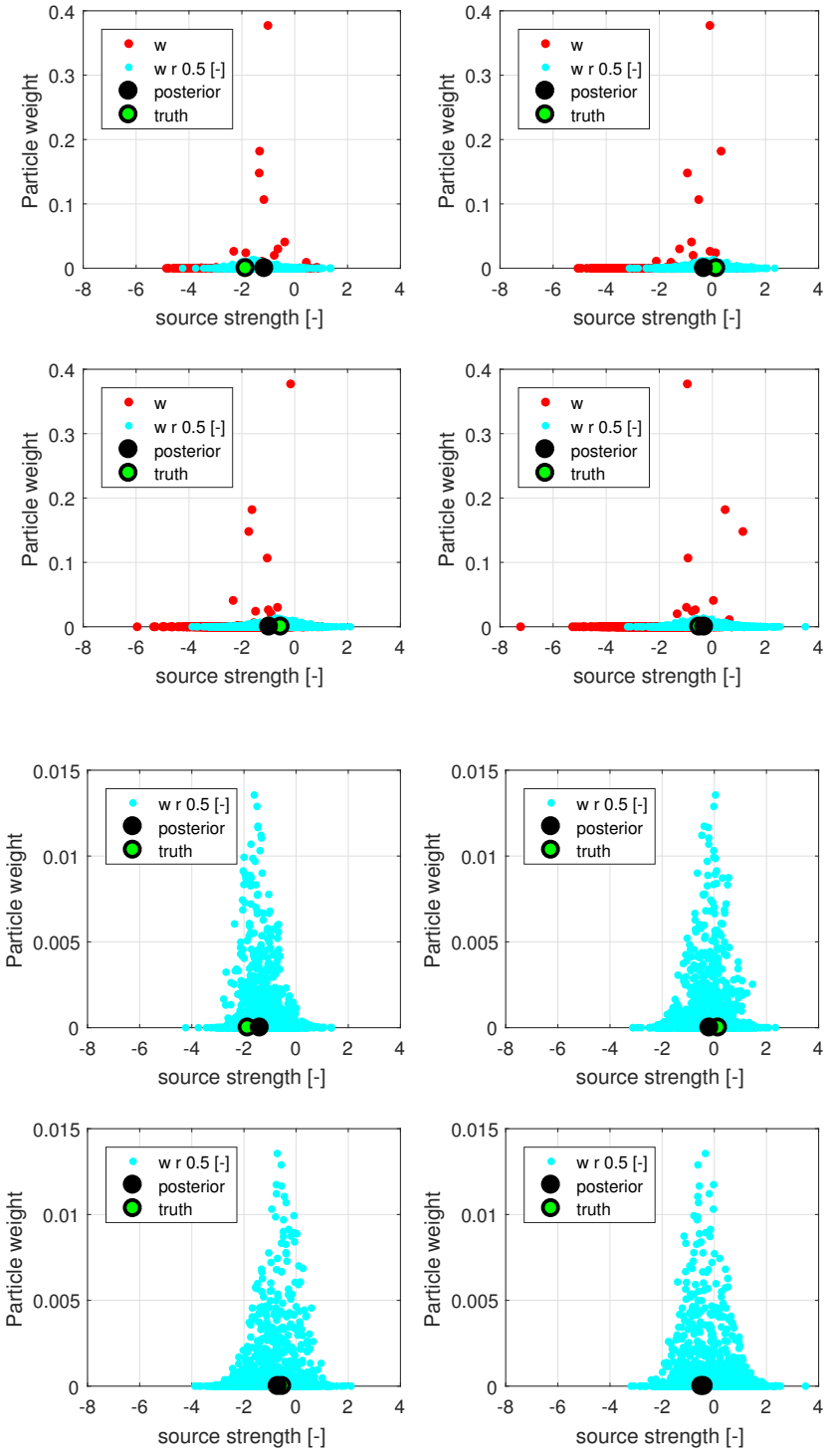

Figure 5.18: Source strength (16 obs.) vs. particle filter weight, Gaussian pdf with σ^2=25 mm. The subplots are ordered the same as in figure D.18, where the top left subplot is the top left point in that figure. **Top**: red= ensemble members, cyan= resampled ensemble members with a jitter variance of σ^2=0.5 [-], black dot=estimated source strength and green dot= source strength truth. **Bottom**: cyan= resampled ensemble members with a jitter variance of σ^2=0.5 [-], black dot=source strength truth, (different y-scale)

Table 5.8: **Testing start value and 'jitter' (noise).** Results of the Mogi sources ≠ at 16 deformation locations and two ensemble members with the same weight of 0.0117. The numbers of the locations correspond with the plot in figures 5.17 and 5.18, where number 1 is top left and 16, bottom right; and 1 top left and 4 bottom right. P.=particle

No.	Deformation [mm]	P. weight 0.0117	P. weight 0.0117	Source strength truth [-]	P. weight 0.0117	P. weight 0.0117
1	-2.15	-2.59	-4.69	-1.85	-1.46	-1.46
2	-5.56	-3.62	-5.51	0.15	-0.38	-0.23
3	2.02	-4.55	-5.11	-0.52	-0.76	-0.55
4	-8.14	-4.25	-4.12	-0.49	-0.02	-0.57
5	-10.93	-4.14	-5.96	-	-	-
6	-6.65	-5.82	-7.43	-	-	-
7	1.13	-7.16	-7.56	-	-	-
8	-9.28	-6.52	-6.33	-	-	-
9	-0.48	-5.91	-6.29	-	-	-
10	-12.78	-8.23	-8.49	-	-	-
11	-10.12	-9.94	-9.98	-	-	-
12	-15.47	-8.87	-8.75	-	-	-
13	-5.55	-5.74	-5.41	-	-	-
14	-8.73	-7.89	-7.51	-	-	-
15	-7.19	-9.38	-9.20	-	-	-
16	-3.97	-8.33	-8.23	-	-	-

5.3. Discussion and conclusion

This chapter describes the results of four synthetic experiments applied to three different setups. Each experiment has a goal with questions to answer by the results of the experiments. The answers and findings of each experiment are summarized below.

1a. **Mogi model experiment**

The first experiment is an experiment to test the limitations of the Mogi model, where the depth, source strength and Poisson's ratio is varied separately from each other. This is done for setup 1: 1 Mogi source = at deformation location. The deformation is located right above the Mogi sources in the centre of the spherical shaped surface deformation.

- The depth of the source strength is varied from -3000 to -3100 m. These depths are based on the approximate well depths of the production wells in the Groningen reservoir, see table A.3. The variable depths result in a deformation difference of 0.20 mm. This is an almost zero change. The variation in Poisson's ratio ν=0.20 and 0.30 results in a difference of 0.50 mm compared to the deformation with a Poisson's ratio ν=0.25. The variation in source strength of 0.1 to 1.0 [-] resulted in a deformation difference of 0.55 to 5.56 mm. This is a linear relationship. The difference of 5.56 mm will have a source strength offset of ±1.00 [-], when there is no noise or bias added to the surface deformation. The variation in source strength has the largest influence on the surface deformation value, based on the above-described results.

1b. **Particle filter experiment**

- The particle filter is applied on noisy deformation values. The residual between the posterior deformation and the deformation truth is 4.60 mm and the source strength residual is 0.05 [-]. The particle filter is able to estimate the source strength within ±0.05 [-] from the truth, despite the large deformation residual. The particle filter is a method that estimate the source strenghts

almost correct in this 1 Mogi source = at deformation location test setting, even when the deformation residual is 4.60 mm.

- The particle filter is applied on noisy and biased deformation. The residuals ranged from 6.40 to 24.46 mm for the deformation values and from 0.1625 to 1.7732 [-] for the source strengths. The first bias is 3 millimetre and the second is 30 millimetre. The particle filter is able to estimate the source strengths within a residual value of ±1.7732 [-], despite the large deformation residual value.

It can be concluded that the particle filter estimates source strengths from noisy observations with a residual of 0.05 [-] for a 1 Mogi source at deformation location setup.

2. **Particle filter variance variability, step 3 of the identical twin experiment**

   The second experiment is an exploration experiment in order to find out how the particle filter performs with different variances of the observational pdf, distances between the deformation locations, number of ensemble members N values and sets of ensemble members. The goal is to find out how the RMSE vary for the different setups with a number of Mogi sources varying from 1 to 16. And if there are any differences in RMSE and how does this RMSE vary with different observational pdf's? This is important, because the numbers of Mogi sources are not known that are needed to estimate the real situation with PS-InSAR measurements. And in the real situation there is no twin experiment so the truth is not known. The second goal is to find out if the RMSE values change by a variable number of ensemble members N. And what is the standard deviation of the RMSE values when running the particle filter Gaussian pdf with 5 different sets of ensemble member? Also what is the influence of the variation in distances between the deformation locations on the RMSE value? And how are the particle filter weights distributed?

   The RMSE value is stable in all situations of the deformation and source strengths. The findings of the experiment with different particle filter variances are summarized below.

   - The RMSE values of the experiment in which a Gaussian function represents the pdf of the observations are slightly lower than the RMSE values resulting from the Lorentz function. Therefore the Gaussian function is used further on in the experiments and applied to the real PS-InSAR measurements setup in the next chapter.
   - The particle filter applied to different setups estimate the deformation and source strengths with an average RMSE value of respectively of 5.0 mm and 1.0 [-].
   - The three different distances (k=1500, 3000 and 6000 m) between the deformation locations show similar RMSE values for both the deformation and source strengths.
   - The different number of particles N (10 to 10000) provide similar RMSE values, both for the deformation and the source strengths. The number of ensemble members N=10 provide a source strength estimate with a RMSE value of 0.7 [-] for the setting of 16 Mogi sources = at deformation locations. This is a good result.
   - The standard deviation of the RMSE values, computed over 5 different experiments is 0.10 mm for the deformations and 0.02 [-] for the source strengths.
   - The particle filter weights plotted versus the ensemble members of the 1 Mogi source = at deformation location show a clear Gaussian and Lorentz distribution. The 2 Mogi sources = at deformation locations setup show a non-distinct Gaussian curve shape, caused by the proximity of the two Mogi sources. Their deformation interfere each other, when the deformation location is a distance of 1500 m. The posterior source strengths are still close to the true source strength for this setting.

   The RMSE values of the source strength varies from 0.0 to 1.0 [-] for each different particle filter variance; Gaussian noise variances; and different numbers of ensemble members N. It can be concluded that the particle filter produces the same RMSE values, despite the different used noise variances in the deformations.

3. **Particle filter resampling, step 4 of the identical twin experiment**

The third experiment is an experiment where iterative resampling is tested. The main goal is to find out, in different setups, if the RMSE is lowered and if the estimation of the deformation and source strength is improved.

The findings of the experiment setup 1: **16 Mogi sources = at deformation locations** are summarized below.

- The resampling lowers the RMSE value of the deformation by 0.30 mm and increases the RMSE value of the source strength by 0.04 [-] for a distance of k=1500 m between the deformation locations. This is the same for larger distances k. The resampling step does not improve the source strength estimation.
- The deformations of the Mogi sources interfere at a distance k=1500 m between the deformation locations. This results in a larger number of correct ensemble members where weight is assigned. The higher number of weighted ensemble member combinations leads to a higher RMSE value. The larger distances will have a better chance for a unique solution, because the Mogi sources their deformations interfere each other less.
- The small variance value of the added 'jitter' (noise) to the resampled ensemble members improves the deformation estimation, but not the source strength estimation.

The findings of the experiment setup 2: **1 Mogi source $\neq$ at deformation locations** are summarized below.

- The resampling step improves the deformation and source strength RMSE values for the setup with 16 deformations. The resampling improves not the higher number of 256 deformation locations.
- The source strength resampled posterior residual value is larger than the posterior value. The larger number of deformation locations bring a larger amount of noise in the experiment and this results in a less correct estimated source strength value.

There is a difference between the experiment setups. The setup with 1 Mogi source and 16 / 256 deformations does not need resampling, while the experiment with multiple Mogi sources at the deformation locations benefits from the resampling. This is a caused by the number of parameters, source strengths that are estimated. The first estimate of these 16 source strengths is good and the resampling estimate is even better.

4. **Particle filter variability of the start value (step 2) and the resampling 'jitter' variance (step 4) of the identical twin experiment**

The ensemble members of step 2 in the identical twin experiment are generated with a start value (initial value) different form the 'truth' in step 1. Furthermore the resampling, step 4, is done with two different variances for generating Gaussian noise or 'jitter'. This noise is added to the resampled ensemble members. The first goal is to find out if the particle filter can estimate the deformation and source strength with the above-described variability. The second goal is to find out how the different jitter variances influences the estimation of both deformation and source strengths in different setups. The findings of the experiment are summarized below.

The findings of the experiment setup 1: **16 Mogi = at deformation locations** are summarized below.

- The particle filter is able to estimate the deformation and source strength, because the RMSE values are respectively around 4.30 mm and 0.50 [-]. These values are in the same order as the RMSE values in the previous experiment with the same start values.
- The number of N=1000 ensemble members is enough to estimate the deformation and source strengths, based on the results of the RMSE values.
- A larger jitter variance works better for the distances of 1500 and 3000 m between the deformation locations, because the mean values of the pdf's are more aligned. In addition the corresponding deformation RMSE values are lower for a jitter variance of 0.5 [-].

The findings of the experiment setup 2: **1 Mogi source ≠ at deformation locations** are summarized below.

- The particle filter is able to estimate the deformation and source strength values. The resampling improves the RMSE values.
- There is no difference in estimating the source strengths when using two different added jitter (noise) variance values.

The findings of the experiment setup 3: **4 Mogi sources ≠ at deformation locations** are summarized below.

- The number of N=1000 ensemble members is sufficient to estimate the deformation and source strength values of the experiment with 16 deformation locations. The resampling is not needed.
- The number of N=1000 ensemble members is not sufficient for estimating the deformation and source strength values of the experiment with 256 deformation locations. The resampling is needed for this setting with a large number of deformation locations.
- The jitter variance of 0.5 [-] is large enough for both settings.

The particle filter is able to estimate the source strengths for all the three experiment setups, even with a difference in start value. The number of N ensemble members has enough variability in order to estimate the source strengths, despite the difference in start The variance of the added jitter, noise, to the resampled ensemble members is large enough to provide variability in the ensemble members and thus to estimate the source strengths.

Overview table of the RMSE values of the particle filter experiments (table 5.9). The particle filter estimation is always better than the prior guess for estimating the source strengths.

Table 5.9: Overview of RMSE values of the identical twin experiments. Prior= mean ensemble members, posterior= weigthed mean ensemble members. The rows starting with obs show the RMSE results in [mm] and the rows starting with Mogi's are RMSE results in [-].

		Start value same as 'truth'			Start value different from 'truth'			
No. Mogi's deformations	Distance k [m]	Prior	Posterior	Resampling σ^2=0.25 [-]	Prior	Posterior	Resampling σ^2=0.25 [-]	Resampling σ^2=0.5 [-]
16 obs/	1500	6.33	4.25	3.96	41.10	6.31	4.40	4.25
	3000	5.46	4.04	3.01	19.10	5.51	4.33	4.21
	6000	5.59	3.63	2.55	10.40	5.50	4.28	3.89
16 Mogi's	1500	0.762	0.70	0.74	1.32	0.593	0.561	0.537
	3000	0.762	0.66	0.85	1.32	0.593	0.504	0.460
	6000	0.762	0.65	0.75	1.32	0.592	0.480	0.476
16 obs/	1500	4.71	4.33	4.30	6.52	4.35	4.03	4.03
1 Mogi	1500	-0.537	0.091	-0.084	1.486	-0.131	-0.029	-0.036
256 obs/	300	5.52	5.03	5.03	7.60	5.03	5.03	5.03
1 Mogi	300	-0.537	-0.089	0.585	1.486	-0.085	1.586	-0.084
16 obs/	1500	-	-	-	13.90	4.38	4.33	4.32
4 Mogi's	1500	-	-	-	1.51	0.488	0.319	0.305
256 obs/	300	-	-	-	15.40	5.42	5.03	5.01
4 Mogi's	300	-	-	-	1.51	0.511	0.176	0.184

6

Particle filter applied to descending Persistent Scatterer InSAR measurements

This chapter presents the results of the particle filter applied on real Persistent Scatterer InSAR (PS-InSAR) measurements in order to estimate reservoir volume changes. The obtained knowledge of the theoretical background of the particle filter of chapter 2, the subsidence knowledge of chapter 3, the described PS-InSAR technique of chapter 4 and the results of the particle filter applied to synthetic data of chapter 5 are all applied in this chapter. The methodology is explained in section 6.1, the results in section 6.2 and the discussion and conclusion in section 6.3.

6.1. Methodology

The methodology to estimate Mogi source strengths in a model of the Groningen field, from PS-InSAR surface measurements uses the particle filter. The details of the used PS-InSAR measurements are shown in section 6.1.1. Also the selection of PS-InSAR points based on point heights are explained in this section. Furthermore time series are plotted of a couple of well locations together with the gas or salt production at those locations. This is done to get familiar with the behaviour of the PS-InSAR measurements over time. The methodology is shown in section 6.1.2. In addition the application workflow of the particle filter is explained in section 6.1.3. The workflow is adapted based on the results of the applied particle filter. This section will form a connection between the methodology and the result sections.

6.1.1. PS-InSAR measurements: high and low point selection

The PS-InSAR measurements set of Groningen for this study is kindly provided by SkyGeo Delft. The set contains Radarsat-2 satellite measurements from a descending satellite track over the period 2009/09/12 - 2016/11/10. Table 6.1 shows the details of the data set. The set has for each PS point the point identification number; latitude/longitude; point height; the digital elevation model (DEM) height; quality of the points; slope of the fitted linear model and the most important one, the change over time relative to 2009/09/12. The Algemeen Hoogtebestand Nederland (AHN) is used as a DEM. The AHN heights are the heights relative to the Normaal Amsterdams Peil (NAP) (Amsterdam Ordnance Datum). This is the reference height used in the Netherlands.

The line-of-sight surface deformation of the Groningen region over the complete data set period is shown in figure 6.1. The figure shows the contour of the Groningen reservoir in black. The large densities of points are locations of cities and villages. These cities contain many buildings or other man-made structures that have a constant scatterer over time. A part of Germany is shown in the Northeast of the figure. The location Lat/Lon 53.2°/6.55° is the Groningen city and Lat/Lon 53.2°/6.55° is Delfzijl. There are three locations where the subsidence is caused by salt production. These locations are called Veendam at Lat/Lon 53.12°/6.85°, Winschoten at Lat/Lon 53.15°/7.0° and Zuidwending at Lat/Lon 53.2°/6.55°. The salt is produced from salt domes in the subsurface, as explained in section 3.3. The deformation is circular shaped at the surface above these domes.

The coordinates of the PS-InSAR measurements are converted into Rijksdriehoek (RD) coordinates. These coordinates are in meters and thus easier in use in the Mogi model, which are also meters. The coordinate

conversion is done with Matlab conversion scripts (named: 'crsutil, 'itrf' and 'rdnaptrans') kindly provided by Van der Marel (2018). The rest of this chapter will have the coordinates in RD.

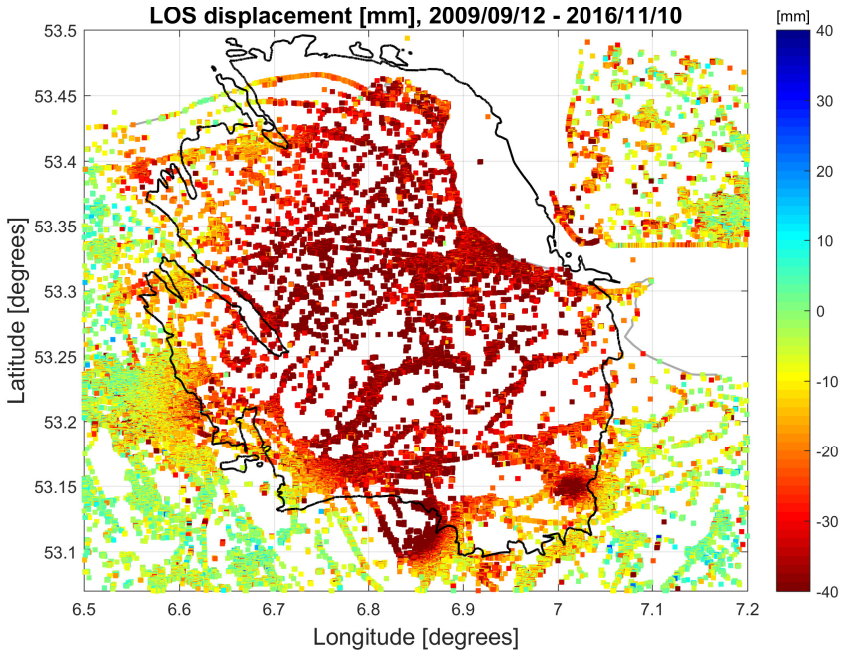

Figure 6.1: PS-InSAR line-of-sight displacement of Groningen in millimetres for the period 2009/09/12 - 2016/11/10 with the outline of the Groningen reservoir (black line) and the coast (grey line). The measurements show subsidence values above the reservoir. There are three locations where subsidence is caused by salt production. The locations are Lat/Lon 53.12°/6.85°; 53.15°/7.0°; and 53.2°/6.55°.

Table 6.1: Details of the PS-InSAR measurements of Radarsat-2, descending, right-looking, line-of-sight deformation

Heading angle	Incidence angle	Period	Repeat pass [days]	No. of epochs	No. of PS points	Point location precision [m]	Measurement precision [mm]
191°	34.1°	2009/09/12 2016/11/10	24	98	371892	X,Y : 2-3 Z : 2-2.5	6-8

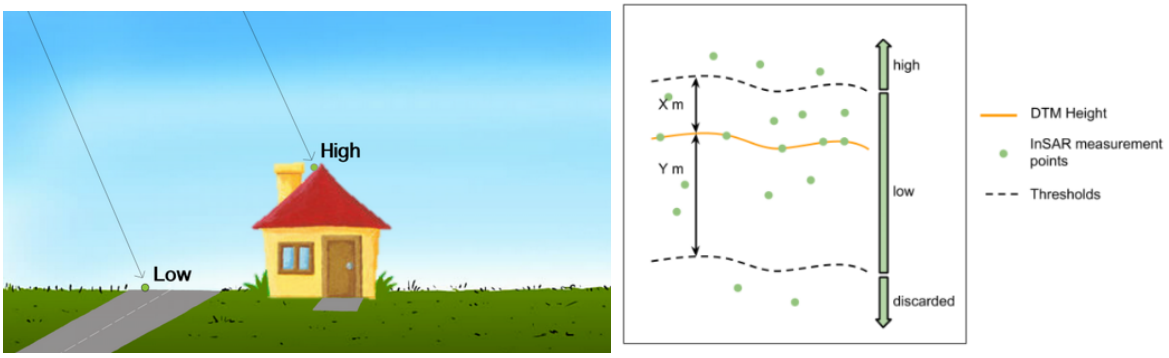

Figure 6.2: **Left**: illustration of high and low points. The high points are mainly houses that are assumed to be stable over a long period of time, generally built on poles resting on a stable Pleistocene sand layer (figure taken from SkyGeo (2017)). **Right**: determining high and low points by using the point height and DEM height. A second boundary of X_m is used, this boundary will be placed above the upper dashed line in the figure (figure taken from SkyGeo (2018)).

The point quality has a value ranging from 0 to 1 and is a relative measure of the quality of the point. A lower value indicates more noise in the time series. The point quality is a value computed by fitting an expected deformation model to the measurements in time. This model can have linear and seasonal components in it. The measurements are compared with the model and the difference determines the quality of the points, where a higher value represents a better match. The fit of the deformation model over time can be better or worse than the point quality value (SkyGeo, 2017). The PS-InSAR measurements are cropped to the boundaries of the Groningen reservoir in order to have only points that are assumed to be a result of the Groningen reservoir compaction.

Figure 6.2 (left) shows the difference in low and high points. Where the high points are stable man-made houses, generally built on poles that rests on an assumed stable Pleistocene sand layer 12 m in the underground. The rooftop of the houses is in the order of 7-12 m high. There are also houses built on plates, 'op staal', this is a shallow foundation on clay. The PS-InSAR points for these houses could reflect shallow compaction, due to foundation instabilities (Ketelaar, 2009). There are also houses built on, in Dutch, 'wierden' (named 'terpen' in Friesland). These are man-made hills. Houses were built on these hills in order to protect the inhabitants and cattle from high tides of the sea. There are many wierden and remnants of wierden left in Groningen. The Groningen wierden are brought to notice by Herber (2018). Points located on the wierden are removed from the data set, because it is not clear if deformation detected on these wierden represent shallow or deep compaction values.

The low points are points on the surface like roads. These roads are sometimes built on peat dikes. Peat dikes can alter over the years and show subsidence values. This subsidence has nothing to do with the volume change in the deep underground. The height information in the data set can be used to select those high points that reflect a possible subsidence signal that is linked to hydrocarbon production. Both point quality and height are used to determine a set of PS-InSAR points that can be used in the particle filter method.

Figure 6.2 (right) shows how high and low points and are determined according to SkyGeo (2018). The following rules are applied:

$$\begin{aligned} &\text{point height} - \text{DEM height} > X_\text{m} = \textbf{high} \text{ points}, \\ &\\ &\text{point height} - \text{DEM height} < X_\text{m} \ \textit{and} \\ &\text{point height} - \text{DEM height} > Y_\text{m} = \textbf{low} \text{ points}, \end{aligned} \tag{6.1}$$

where X_m= 3 m and Y_m= -10 m (SkyGeo, 2018). The result of the high and low points is shown in section 6.2.1. Two extra steps are applied for the high points, all points above the point height − DEM height > 13 m are discarded, this will be a second boundary, $X_{\text{m}2}$. This is done in order to remove points of electricity poles that are assumed to reflect thermal expansion behaviour instead of surface deformation. The second step is the removal of points located on wierden. It is assumed by the author of this thesis that points on houses on these man-made structures do not reflect deep surface deformation, but possible ground consolidation in or under the wierden. A wierden location data set of NGR (2018b) is used for PS-InSAR removal. This data set contains locations of polygons that are drawn around the wierden locations in .xml format. The wierden locations are mainly circular shaped. The script of Falkena (2012) is used in order to extract data from this xml file. A summary of the PS-InSAR point selection is presented in table 6.2 and in figure 6.7.

Table 6.2: Summary of the values used for PS-InSAR point selection of high points

Point quality	X_m [m]	Y_m [m]	$X_{\text{m}2}$ [m]	No. of wierden points	No. points left
0.7	3	-10	13	148	5101

6.1.2. Time series locations

There are four production regions. The time series are plotted for one well of each production region, in order to show the PS-InSAR measurements behaviour over time together with the cumulative monthly gas production. The average deformation value of each cluster is computed over from high PS-InSAR points within a radius of 1500 m of the wells. The number of PS-InSAR points is around 16 - 100.

The four clusters Eemskanaal, Overschild, Zuiderpolder and Slochteren are plotted; locations are respectively at coordinates X/Y 241/584; X/Y 250/590; X/Y 261/580 and X/Y 246/579 km. The choice for the Eemskanaal cluster is straightforward; this is the only well in the Eemskanaal region. The Overschild cluster choice

is based on the location, because this well is the centre well of the Loppersum production region. The choice for the Slochteren cluster is from a historic perspective. This is the best-known well and area of the Groningen reservoir, because of the hydrocarbon field discovery in 1959 at a Slochteren well (there are 12 wells that form the Slochteren cluster). The Zuiderpolder cluster choice is based on the location, this well is located in the southeast of the Groningen field. All time series present a total coverage of the whole Groningen field.

The time series of the complete region of Loppersum is plotted in section 6.2.2. This is the only region with a major drop in gas production after the year 2013. Therefore the subsidence of the other four remaining well clusters in that region is plotted against the gas production. A second degree polynomial fit is applied to the data, to have a more smoothly behaviour of the deformation over time when computing the surface deformation over one year. This is further explained in the result section 6.2.2 of the time series.

The time series for the three salt locations are plotted as well together with the salt production. The salt wells are located in the south of the Groningen field.

6.1.3. Particle filter steps applied to PS-InSAR measurements

The particle filter applied on PS-InSAR measurements is a process of trial and error. The particle filter is tested in the previous chapter with the maximum number of 256 deformation locations. The high points PS-InSAR measurements contain only data that is assumed to reflect the deep subsidence signal, caused by hydrocarbon production.

The particle filter is applied on each year separately in order to obtain a yearly reservoir volume change that can be possible linked to the yearly gas production. An estimation over a 5 year period or a monthly estimation could have been chosen as well, but I choose for a yearly estimation to start with. Future use of this method could explore other time periods to estimate the reservoir volume change. The years 2010 - 2015 are complete while in 2009 and 2016 some months are missing. The deformation over a year is computed by subtracting the deformation of the previous year, so for example for 2010 the deformation of December 2010 minus deformation of December 2009. This is done for the high points data set (5101 points as shown at the bottom of figure 6.7), for the second polynomial fitted data, and for the unfitted data. The difference in fit and unfit of the LOS deformation in 2010 is shown in figure 6.3. The fitted LOS deformation shows a smooth deformation instead of the non-smooth deformation of the unfitted LOS deformation.Both fit and unfit deformation is used as input to the particle filter and based on the results, a decision is made which input is used further on in the analysis.

The chronological workflow order of the PS-InSAR measurements selection is shown in figure 6.4. The grey circles are the input / output of the workflow and the black rectangles the steps that are done for example a point is removed or coordinates are converted into Rijksdriehoek coordinates.

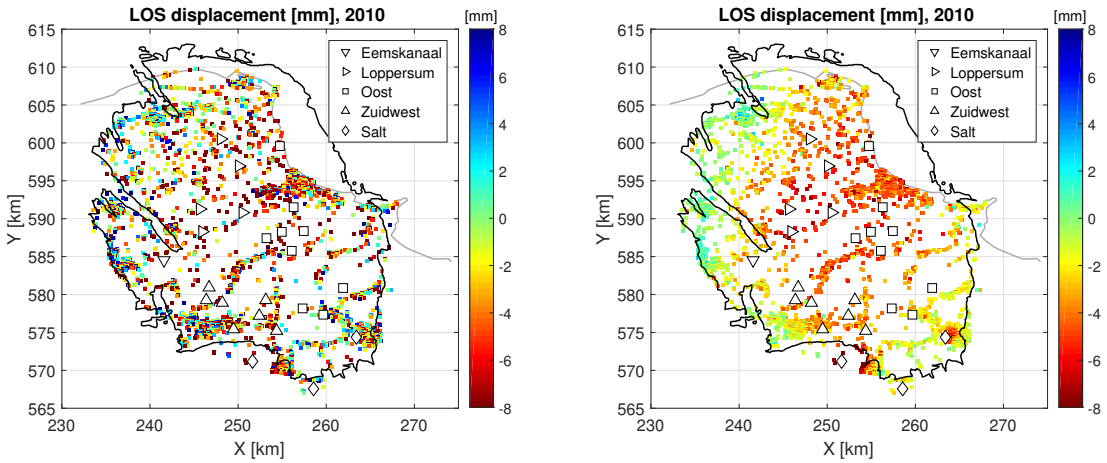

Figure 6.3: PS-InSAR deformation of 2010. **Left**: no fitted data, **Right**: the second degree polynomial fitted time series data.

The PS-InSAR measurements (5101) that are selected by the workflow (figure 6.4) are used in the following three steps of the particle filter:

1. **Generating the prior** $p_m(\psi)$
   The model pdf is generated by sampling a large number of randomly Gaussian generated source strengths

N=1, ...n with eq.(2.10). These are the ensemble members and for each realization a surface deformation H_m is computed using eq. (B.1) - (B.13). The model representation of surface deformation for each ensemble member is now generated.

2. **Particle filter**
   The difference between the PS-InSAR measurements d and modelled surface deformations H_m are multiplied with the observational density function $p_d(d|\Psi)$ (Gaussian distribution eq. (5.2)). The likelihood is obtained, these are the particle filter weights. This distribution is multiplied with p_d for normalising and results into the posterior distribution $p_m(\Psi|d)$. The RMSE values are computed with eq. (5.7) once for the whole field and once for only the influence area of the Mogi sources, as shown in figure 6.5.

3. **Resampling**
   The residual resampling technique, eq. (2.14) - (2.18), is used to resample the source strengths. Uncorrelated Gaussian noise is added to the resampled ensemble members, in order to vary the ensemble members. This noise or 'jitter' is generated with a zero mean value by eq. (2.10). The resampling is done twice with different variances of the observational pdf.

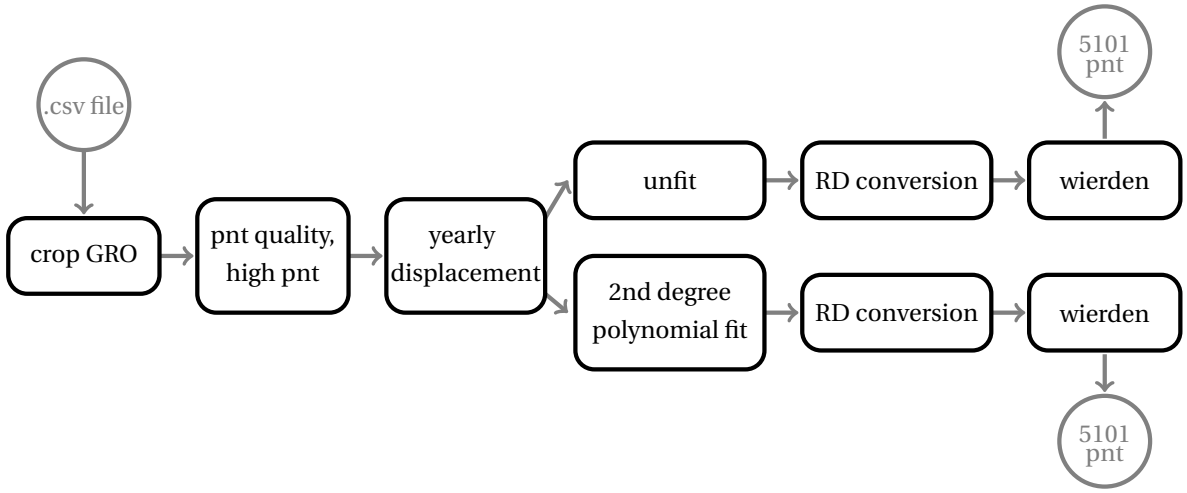

Figure 6.4: Workflow to select PS-InSAR measurements from the Radarsat-2 .csv file. The steps are described in the above sections. GRO=Groningen reservoir outline, pnt=point / points, RD=Rijksdriehoek

Table 6.3: Particle filter input for the situation with 25 Mogi sources, 5101 high PS-InSAR points. The 22 Mogi sources for gas have the same ensemble members settings, while the 3 salt sources have different settings per source, VDM = Veendam, WSN = Winschoten and ZWD = Zuidwending. Poisson's ratio ν=0.25 and the LOS vector [0.5503 -0.1070 0.8281]$[d_u, d_n, d_e]$. The years 2009 and 2016 are not complete, only a couple of months define these years, namely September - December for 2009 and January - November for 2016.

Step:		2 (gas)	2 (VDM)	2 (WSN)	2 (ZWD)	3
Ensemble members variance:	σ^2 [-]	0.25	0.125	0.125	0.125	-
Ensemble members start value:	[-]	-1	-0.5	-0.33	-0.33	-
Ensemble members number:	N	5000	5000	5000	5000	-
Mogi source depth:	z [m]	-3000	-1800	-1600	-1500	-
Particle filter Gaussian pdf 1st run:	σ^2 [mm]	144	144	144	144	-
Particle filter Gaussian pdf 2nd run:	σ^2 [mm]	-	-	-	-	100
Particle filter Gaussian pdf 3rd run:	σ^2 [mm]	-	-	-	-	64
Gaussian resample 'jitter variance':	σ^2 [-]	-	-	-	-	0.0156

Table 6.3 shows the final settings of the ensemble member variance, start value, number of ensemble members, the variances of the Gaussian observational pdf and the jitter variance added to the ensemble

members after resampling, which are used in the particle filter applied on the PS-InSAR measurements for each year. The result of the particle filter is presented in section 6.2.3. A trial and error process is performed of creating a set of ensemble member settings that fit the PS-InSAR measurements. A couple of particle filter runs are done, where the start value and variance are varied for to create randomly ensemble members of Gaussian source strengths. The variance of the observational pdf in the particle filter is varied from 144 to 64 mm. A start value of -1.0 [-] for generating the ensemble members for the gas source locations works well. A small variance of 0.25 [-] for generating the ensemble members works better than a large variance of 2.0 [-]. The smaller Gaussian distribution, where the ensemble members are drawn from, works thus well. This means that the observed deformations are in the same order and ensemble members are needed in the same order. This order is found with a variance value of 0.25 [-]. The large variance causes positive source strength values in the ensemble members and this results also in positive source strength values of the particle filter output. A positive source strength value result ns uplift; this is unwanted, because there is only subsidence in the Groningen field. The start value and variance of the gas wells are divided by 2 for the salt well Veendam and divided by 3 for the other two salt wells, because the depth of the Mogi sources are placed not at -3000 m as for the gas wells, but at a depth halfway, namely at -1800 and -1500 m. The shallower depths of the Mogi sources with the same deformations above the salt wells and gas wells need a smaller source strength value to compute the deformation that fits the PS-InSAR measurements.

The RMSE is computed for the whole field and for the influence area of the Mogi sources. A buffer of radius 4500 m is applied to each well in order to crop out the Mogi source their deformation influence area. The radius size is based on the result in figure 6.5. This figure shows the posterior model results of the fitted data (same as figure 6.11 top right) where the pink outline is the buffer around the wells. A percentage of fit is computed in order to show how well the posterior estimated deformation explains the measurement signal. A threshold of 2, 4, 8 and 12 mm is used. The source strengths is expected to be negative, because the Groningen area experiences subsidence and not uplift. Source strength estimation solutions with a positive strength are looked into to explain what causes this result.

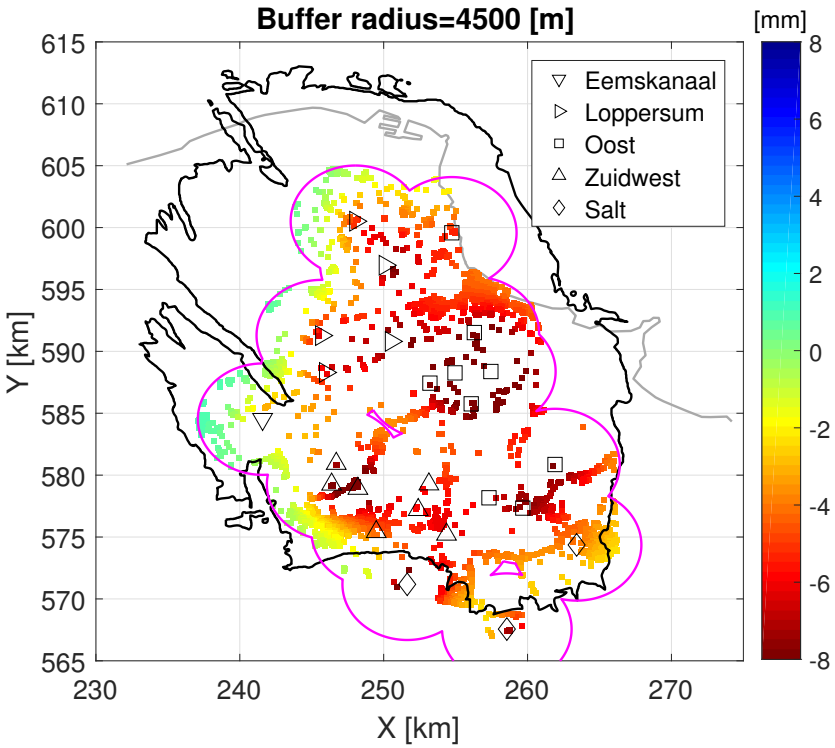

Figure 6.5: Buffer (pink outline) around the Mogi source locations with a radius of 4500 m. The deformation is the posterior result of the fitted data in 2010.

6.1.4. Particle filter applied to PS-InSAR measurement subsets

The particle filter is applied on two subsets of the fitted PS-InSAR measurements. The reason for taking subsets is to show if the same source strengths can be estimated as the estimation of section 6.1.3. Both subsets are created by taking only the even or uneven rows of the dataset of 5101 points. The results are presented in section 6.2.4.

6.1.5. Particle filter solution I for improving the source strength estimation: resampling

Three approaches are taken to improve the source strength estimation, described in section 6.1.5, 6.1.6 and 6.1.7. The particle filter experiments in chapter 5 shows that performing resampling improves the RMSE of the deformations and the source strengths. An improved RMSE value in this chapter will improve the estimation of the Mogi source strengths.

Using resampling in the particle filter is one of the possible solutions to improve the estimation of the overestimated areas at coordinates X/Y 255/588, X/Y 247/580 and X/Y 260/578 km. This is step 3 in section 6.1.3. The resampling uses the posterior source strengths and duplicates the largest weighted ensemble members. A small amount of noise, variance σ^2=0.0156 [-], is added to these source strength ensemble members in order to prevent filter degeneracy (see section 2.5). The generated ensemble members are used in the particle filter and the observational pdf is computed. This resampling is done twice with an observational pdf variance of σ^2=100 mm for the first resampling and a second observational pdf variance of σ^2=64 mm. The results are presented in section 6.2.5.

6.1.6. Particle filter solution II for improving the source strength estimation: guiding the initial source strength

A second solution of improving the overestimated areas is to use the posterior estimated source strengths as a start value in step 1 of the particle filter. These source strengths are used to guide the initial source strength. This step generates a number of randomly Gaussian source strengths around the start values with a source strength variance of σ^2=0.25 [-] for the gas producing wells and σ^2=0.125 [-] for the salt producing wells. The particle filter with a variance of σ^2=100 mm for the Gaussian observational pdf in step 2 are done and the results are shown in section 6.2.6. A second particle filter run is done with the estimated source strengths, this time with a observational pdf variance of σ^2=64 mm.

6.1.7. Particle filter solution III for improving the source strength estimation: localisation

A third solution for improving the three overestimated areas is to use localisation. Localisation is using the particle filter local, this is a solution for the filter degeneracy in high-dimensional spaces with a large number of independent observations. Local in this thesis depends on how many geomechanical models, in this case the Mogi sources placed at reservoir level.

The fit of the model is computed each time for a small area within a certain radius around the well locations. The model itself is still the summed contribution of all the Mogi source wells. Each well is now weighted separately (25 wells) and eq. (5.2) becomes:

$$w_i = \frac{1}{W(x,y)} \frac{1}{\sqrt{2\pi\sigma^2}} e^{-(\sum_{m=1}^{M} \frac{d_m - H_m(\Psi_i)^2}{2\sigma^2})}, \tag{6.2}$$

with W given by

$$W(x,y) = \sum_{i=1}^{N} \frac{1}{\sqrt{2\pi\sigma^2}} e^{-(\sum_{m=1}^{M} \frac{d_m - H_m(\Psi_i)^2}{2\sigma^2})}, \tag{6.3}$$

where $m = 1,...,M$ represents the observations within a radius of Mogi source point (x,y) and $i = 1,...,N$ the ensemble members. The size of the radius is varied four times, namely 1500, 3000, 4500 and 6000 m. The particle filter with an observational pdf variance of σ^2=100 mm is used. The particle filter variance is varied for radius =1500, namely 64, 49 and 36 mm. The results of the localisation are presented in section 6.2.7.

6.1.8. Estimated source strengths vs. deformation for 2010

The estimated source strengths of the fitted and unfitted PS-InSAR measurements are plotted versus the average deformation within a radius of 1500 m of the source. Solution III, the localisation, shows the best results, therefore the source strengths results are plotted against the average deformation as well both for fitted and unfitted measurements The results are presented in section 6.2.8.

6.1.9. Particle filter localisation for the period 2010 to 2016

The localisation with a radius of 3000 m is applied to all the wells. This is done both for the fitted and unfitted measurements of 2010 to 2016. The results are shown in section 6.2.9.

6.2. Results

The results of the PS-InSAR high point selection is shown in section 6.2.1. The time series of the production clusters are shown in section 6.2.2. The results of the particle filter for the well locations are presented in section 6.2.3 and 6.2.4. And solutions for improved source strength estimations are shown in section 6.2.5, 6.2.6 and 6.2.7.

6.2.1. High and low PS-InSAR points

The methodology section describes the usage of point heights and DEM heights to determine high and low points. The high points are mainly houses and the low points are roads. The PS-InSAR data set is cropped to the Groningen reservoir boundaries. Figure 6.6 shows the point heights [m], DEM heights [m] and the point quality. The point heights has values of -4 to 40 m, the scale bar is set to maximum 15 and minimum -15 m. The region in the centre shows mainly values below 0 m. The blue straight lines are electricity poles that are removed from the data set. The DEM height (top right) shows height values below 0 m in the centre of the plot. The point quality (bottom plot) ranges from 0.7 - 1.0. There is no trend or pattern present in similar point qualities for a certain region.

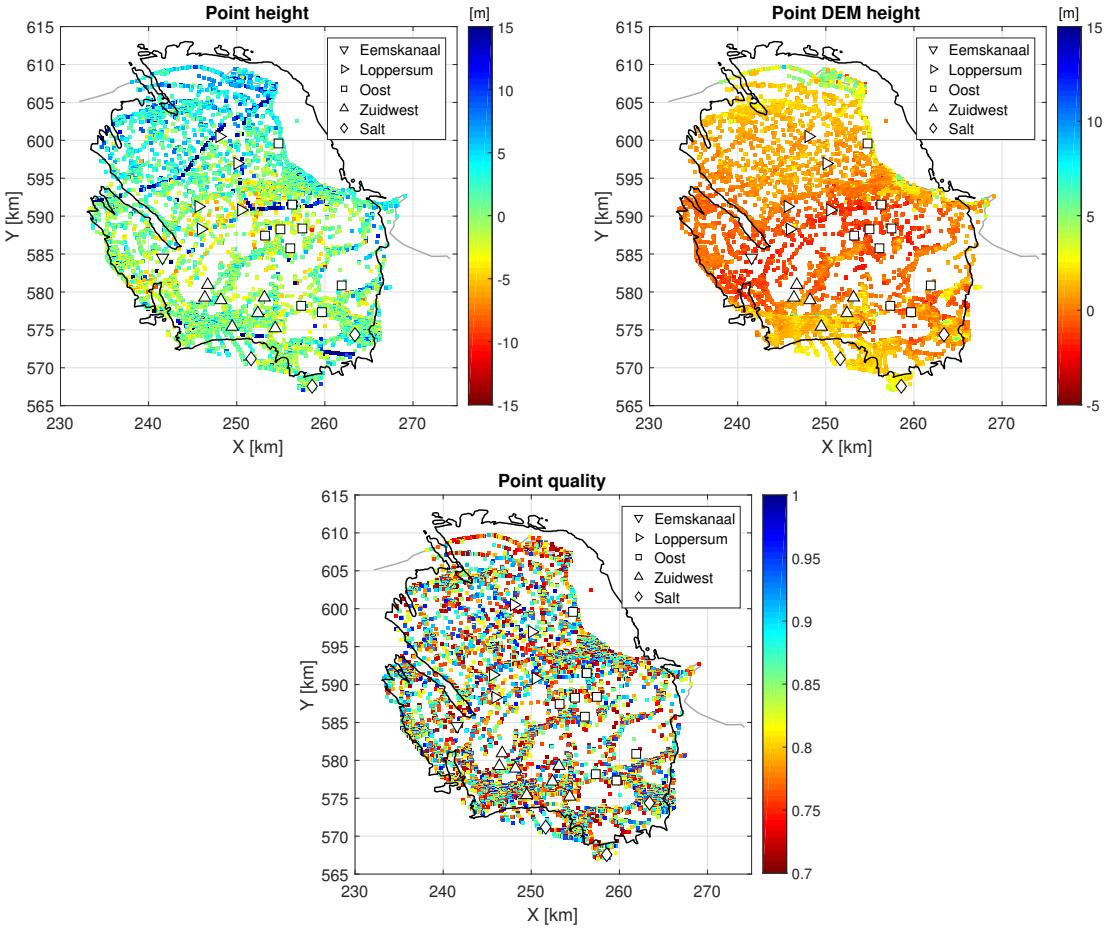

Figure 6.6: PS-InSAR cropped set, the Groningen reservoir (black line) and the well clusters are plotted for orientation. **Top left**: point height in [m], the dark blue points, points > 15 m, are identified as electricity poles. **Top right**: DEM height, many points in the centre are below 0 m, **Bottom**: point quality, only points ranging from 0.7-1.0. No. of points = 34982.

The high and low points are determined by using eq. (6.1). The selected points are presented in figure 6.7 by showing the point height [m]. The first high point selection (top left) shows a large decrease in point density compared to the plots in figure 6.6. The electricity poles are still present in the high point selection; these are removed in the second high point selection (bottom right). The low point selection (top right) have more points than the high point selection. The wierden locations (bottom left) are polygons that are drawn around the wierden are only present in the northern part of the Groningen reservoir (black outline). The

bottom plot on the right shows the second high point selection, where the wierden and points of electricity poles are removed; the number of points is now 5101.

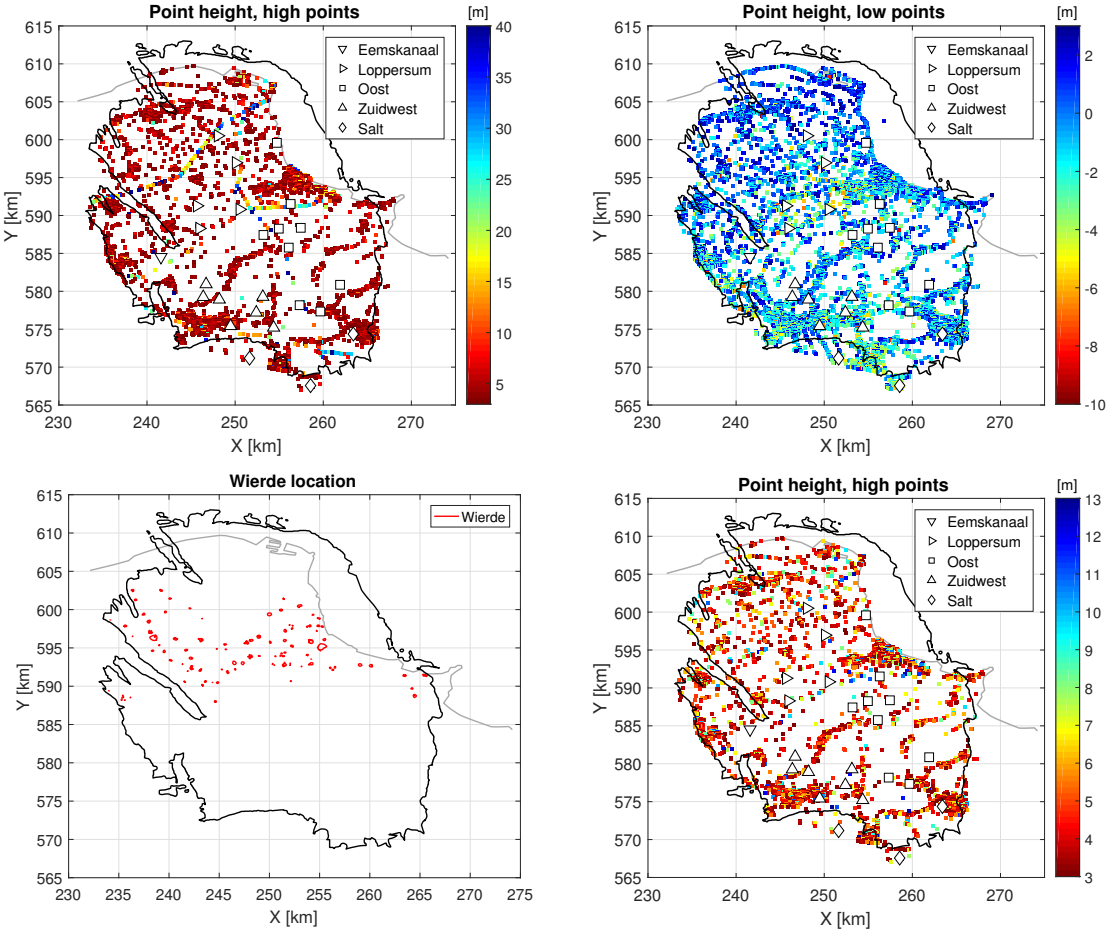

Figure 6.7: PS-InSAR cropped set, the Groningen reservoir (black line) and the well clusters are plotted for orientation. **Top left**: high points , No. of points = 5675. **Top right**: low points , No. of points = 29398. **Bottom left**: polygons of wierden. **Bottom right**: high points, removal of electricity poles and wierden, No. of points = 5101.

6.2.2. Time series

Figure 6.8 presents the time series of surface deformation for one production cluster of each production region and the remaining four production clusters of the Loppersum region together with the cumulative gas production (note: the gas production y-axis is reversed). The colours of the four clusters correspond to the colours of figure 3.2 and 3.4. Figure 6.9 presents the time series of surface deformation for the salt locations.

The Eemskanaal region has a stable gas production over the whole period and shows increased deformation values at the end of 2016. The Overschild cluster in the Loppersum region is located in the centre of the Groningen field. The deformation value is stable over the time period, while the gas production is decreased from the years 2014 to 2016. These are the years where the total gas production of the Groningen field is lowered, especially in the Loppersum region. The Zuiderpolder cluster shows increased deformation values with a stable gas production. The Slochteren cluster in the Zuidwest region shows deformation values similar to the Overschild cluster. The gas production is lower for the Slochteren cluster and not changed after 2013.

The time series of surface deformation of the Loppersum region, Leermens, Ten Post and 't Zandt cluster show all seasonal trends as in the Overschild cluster. There is no reduction in deformation. The cluster De Paauwen shows the largest deformation value of 50 mm compared to the other clusters in the Loppersum region.

The time series of the three salt producing locations are shown in figure 6.9. The Veendam cluster shows the largest deformation value of 58 mm compared to the other salt locations and gas clusters. The largest salt production is the Zuidwending cluster. All three the locations show a surface subsidence.

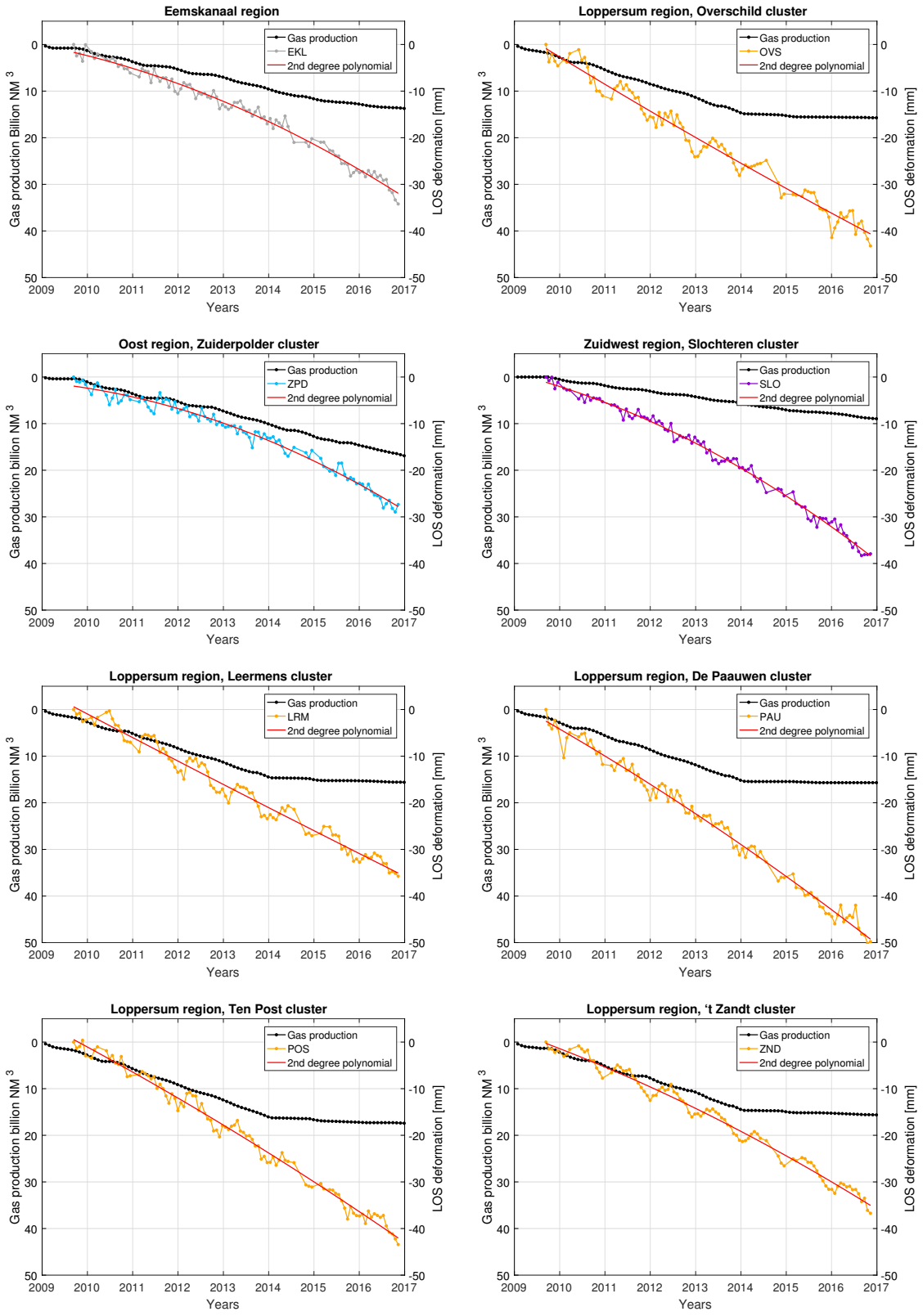

Figure 6.8: Time series (note: the gas production y-axis is reversed). **Top row**: Eemskanaal region (X/Y 241/584 km). Loppersum region, cluster Overschild (X/Y 250/590 km). **Second row**: Oost region (X/Y 261/580 km). Zuidwest region, Slochteren cluster (X/Y 245/579 km). **Third row**: Leermens cluster (X/Y 250/596 km). De Paauwen cluster (X/Y 246/588 km). **Bottom row**: Ten Post cluster (X/Y 245/591 km). 't Zandt cluster (X/Y 248/600 km).

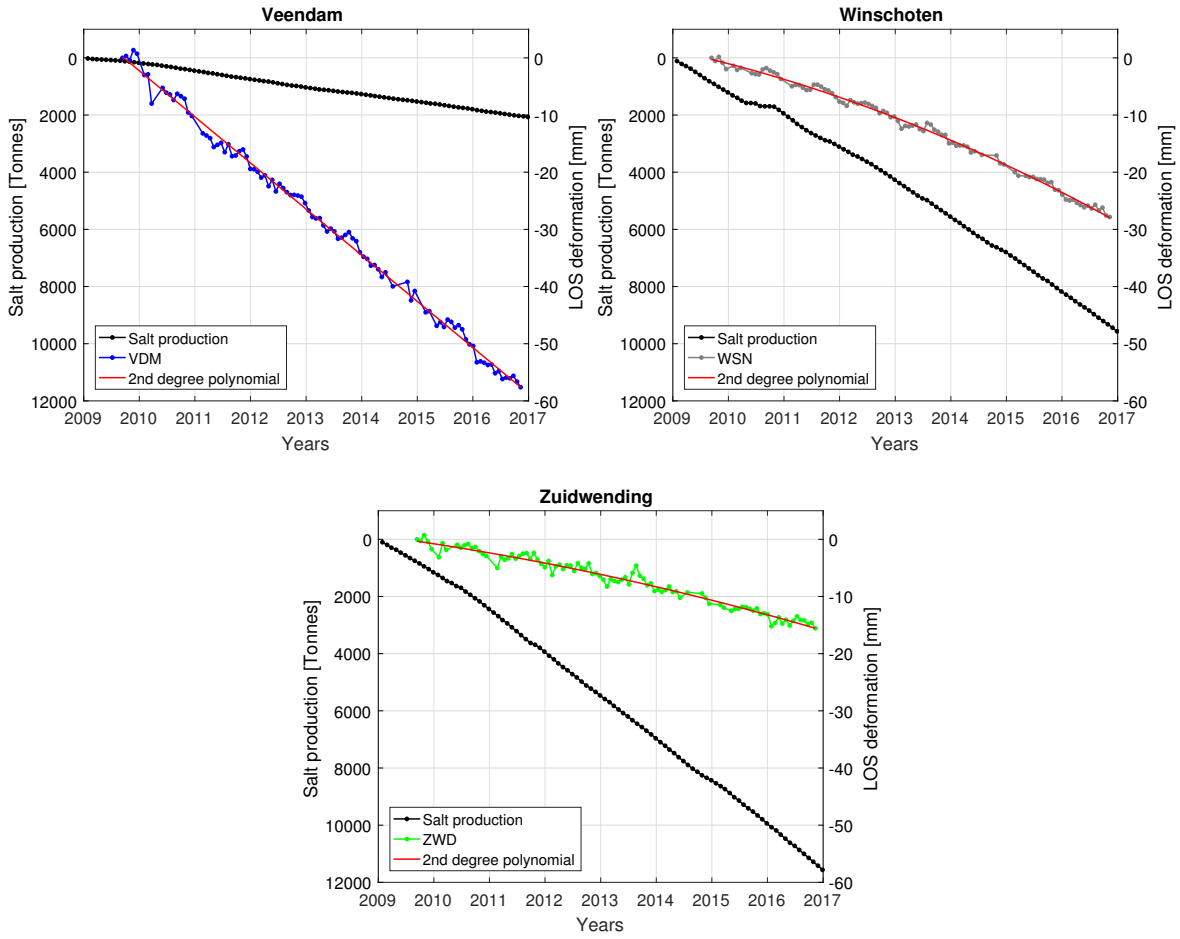

Figure 6.9: Time series of the salt locations (average within a radius of 1500 m) with a 2nd degree polynomial fit (red line) and cumulative monthly salt production (black line) for the specified cluster (note: the salt production y-axis is reversed). **Top left**: Veendam (X/Y 251/571 km). **Top right**: Winschoten (X/Y 263/574 km). **Bottom**: Zuidwending (X/Y 258/567 km).

6.2.3. Particle filter step 1 and 2 applied to unfitted and fitted PS-InSAR measurements

Figure 6.10 shows the particle filter result of the unfitted PS-InSAR measurements of 2010. A particle filter observational pdf variance of σ^2=144 mm is used. The PS-InSAR measurements (top left plot) vary and there is not a clear uniform deformation signal. The posterior deformation plot (top right) shows deformation values where the Mogi sources are placed. The residual plot (bottom left) shows an underestimation in the northwest of the figure and an overestimation around the Mogi source locations. Many deformation locations have a strong deformation (dark blue and dark red coloured). There are almost no areas with zero residuals. This is also expressed in the RMSE of 6.0 mm. The fit is 57% for a 4 mm threshold. The RMSE for the buffer area with a radius of 4500 m is 6.01 mm and fit is 58%. The source strength plot shows a northwest to southeast trend of Mogi source sizes. The sizes of the sources are larger in the northwest than in the southeast. All sources have a negative strength that is a good result, because this is one of the criteria of the particle filter estimation performance.

Figure 6.11 shows the result of the particle filter for one run with a particle filter Gaussian observational pdf variance of σ^2=144 mm for the year 2010 of the fitted PS-InSAR measurements. The RMSE is 2.18 mm and the fit is 93% for a 4 mm threshold. The RMSE for the buffer area with a radius of 4500 m is 2.24 mm and the fit is 92%. The PS-InSAR measurements show subsidence values in the centre of the Groningen reservoir, just like the unfitted PS-InSAR measurements only the fitted observations are smoother. These smoother observed deformations are easier to work with, when tuning the particle filter method. For example the residuals plot of figure 6.11 shows immediately which areas have a good fit or not, while figure 6.10 does not show these areas. There is no subsidence present in the northwest of the reservoir. The posterior deformation shows mainly large deformatioin values close to the well locations. The residual plot shows areas where

the estimated deformation fits the observations (white and light colours), underestimated (blue) areas and overestimated (red) areas. The underestimated part is the northwest region and the overestimated parts are three areas. These areas are located at coordinates X/Y 255/588, X/Y 247/580 and X/Y 260/578 km. All these three areas are at locations with multiple well clusters.

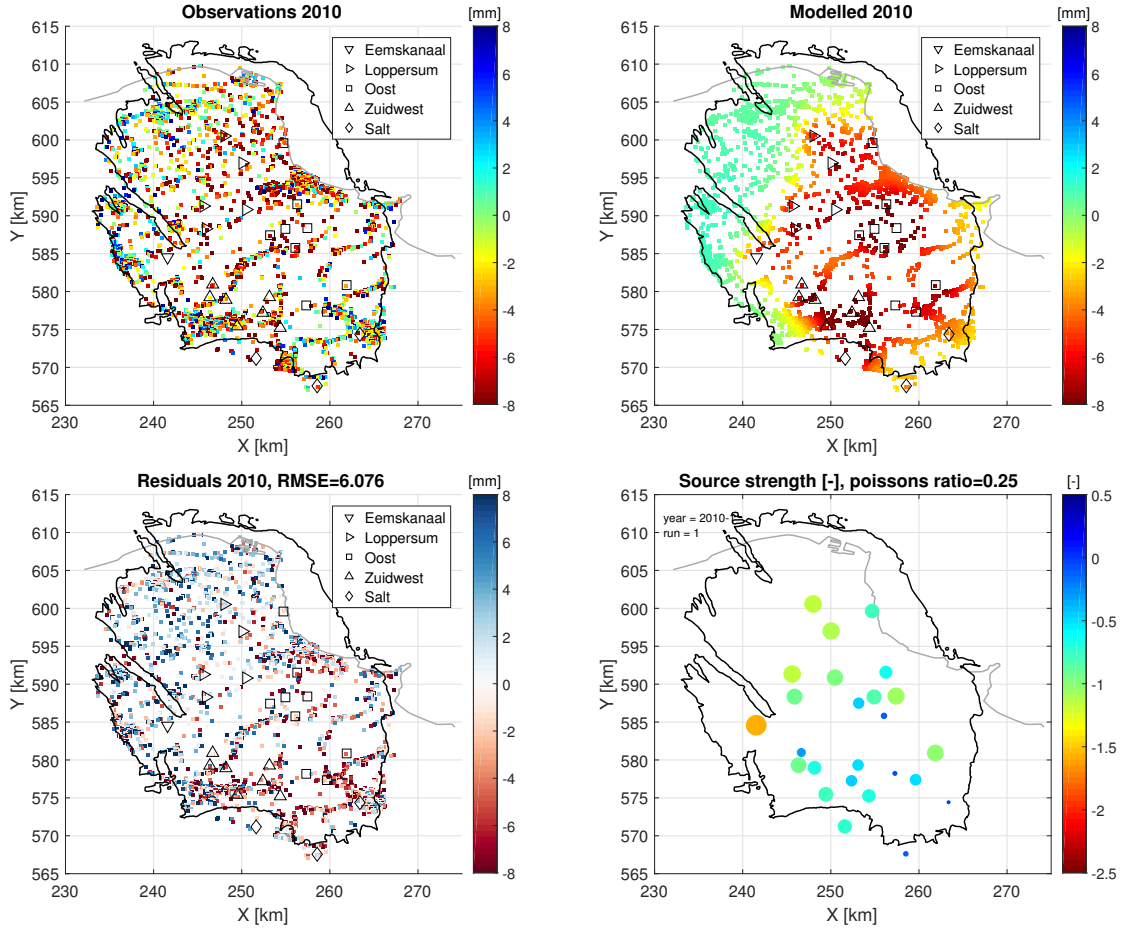

Figure 6.10: Particle filter results of unfitted data for one run and with an observational pdf variance of σ^2=144 [mm]. **Top left**: PS-InSAR measurements of 2010 (unfitted). **Top right**: Posterior deformation. **Bottom left**: Residuals = model - deformation **Bottom right**: Posterior source strength [-] of one run. The symbols represent the location of the wells and the gas production region as defined by the NAM. The symbols are transparent and do not block the results underneath. Fit is 57% for 4 mm threshold and 84% for 8 mm.

The source strength plots (bottom right) of figure 6.10 and 6.11 show similar results. For example the Slochteren source strength (X/Y 246/579) is the largest source strength of the three well clusters at coordinates X/Y 246/580 km. The source strength of the Eemskanaal well (X/Y 241/585 km) is for the unfitted data (figure 6.10) larger than the fitted data. The source strength estimation is related to the subsidence measurements. Furthermore many Mogi sources that estimate the subsidence measurements are located at distances of 3000 m from each other. Their deformation interfere, as found out in section 5.2.2 for a distance of 1500 to 3000 m between the Mogi sources and thus deformations. One of the criteria of the particle filter estimation performance is that all sources should be negative source strengths, because this results in subsidence. The source strength estimation of the above wells have negative source strengths that is a good results.

The particle filter observational pdf against the source strength ensemble members are plotted for well Ten Post (X/Y 246/591 km) in figure 6.12 for the unfit and fitted data of 2010. This is done in order to show how many of the ensemble members have obtained a high weight (> 0). Only two ensemble members have a large weight, this is for both plots. This is not much for N=5000 ensemble members.

Therefore three solutions are designed to improve the estimation of the three overestimated areas and to have more ensemble members obtained a weight. The first solution is to use step 3 of the particle filter this is resampling. The second solution is to use the estimated source strengths of this section as a guidence of the initial start values in step 1 to generate randomly Gaussian source strengths. The third solution is to use

localisation, where the particle filter is applied locally for each Mogi source well location. The methodology of these solutions are explained in sections 6.1.5, 6.1.6 and 6.1.7. The results of these solutions are presented in section 6.2.5, 6.2.6 and 6.2.7.

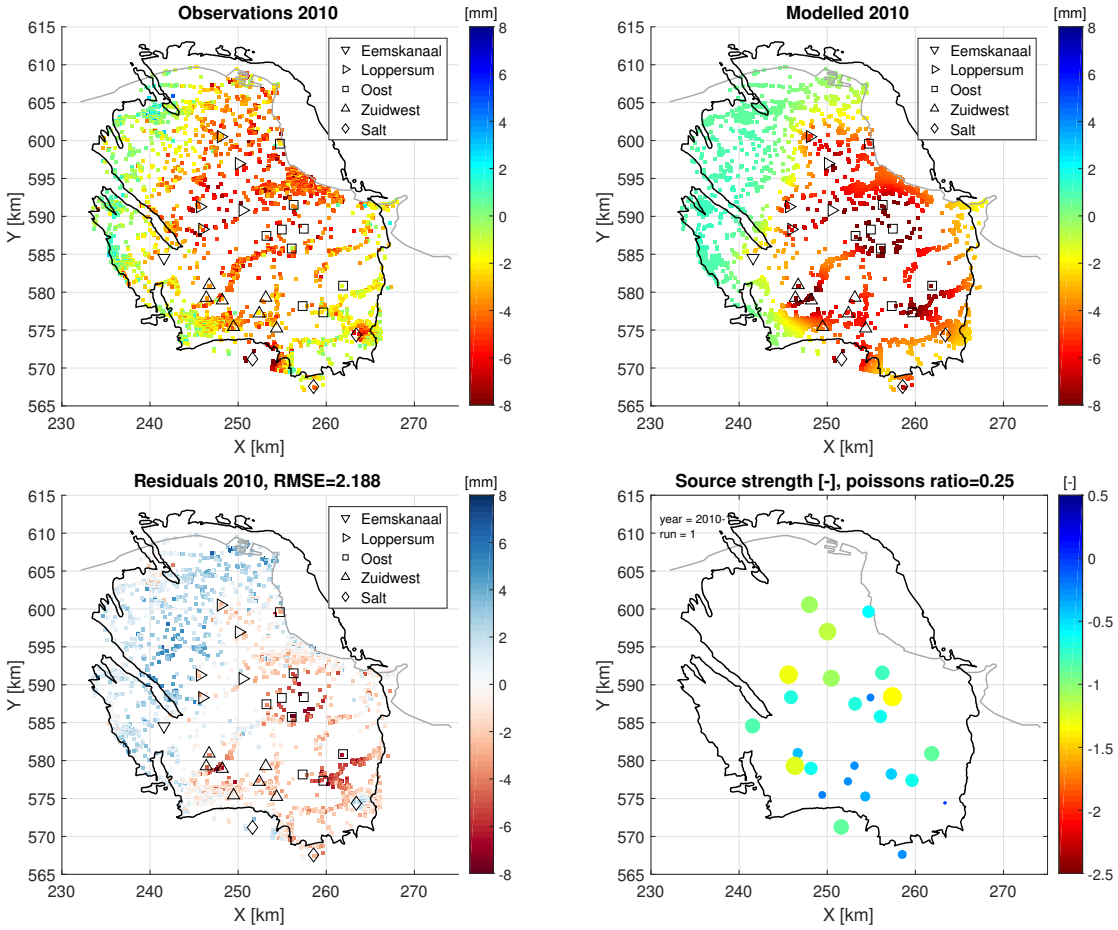

Figure 6.11: Particle filter results of fitted data for one run and with an observational pdf variance of σ^2=144 mm. **Top left**: PS-InSAR measurements of 2010 (fitted). **Top right**: Posterior deformation result. **Bottom left**: Residuals = model - deformation **Bottom right**: Posterior source strength [-] of one run. Fit is 93% for 4 mm threshold and 99.7% for 8 mm.

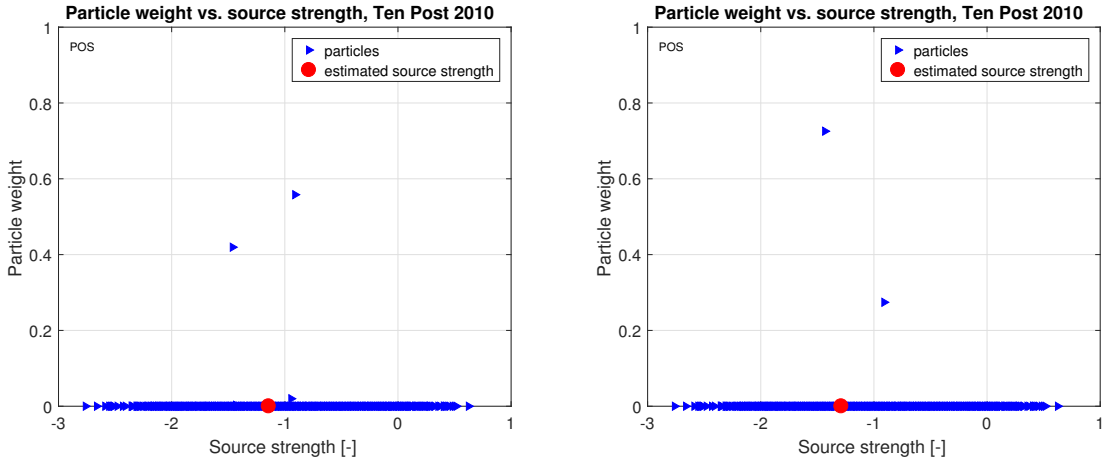

Figure 6.12: Source strengths vs. particle filter observational pdf for well Ten Post, X/Y 246/591 km, particle filter variance σ^2=144 mm. Blue=prior particles and red = estimated posterior source strength. **Left**: results for unfitted data 2010. **Right**: results for fitted data 2010.

6.2.4. Particle filter step 1 and 2 applied to a subset of fitted PS-InSAR measurements

Figure 6.13 presents both subset residuals and estimated source strength results. The RMSE values are the same compared to the RMSE value of figure 6.11 where the particle filter is applied to the whole set of PS-InSAR measurements. The fit for subset 1 is 93% for 4 mm threshold and 93% for subset 2. The fit is the same as for the whole set of PS-InSAR measurements as in the previous section. This holds also for the source strengths. The particle filter estimation performance criteria of having negative source strengths holds also for this estimation, because all estimated source strengths are negative that means subsidence. The same results for both subsets can be a result of the subsets containing still the same surface deformation signal. A second explanation can be that the posterior is the same as in the previous section, there are only two ensemble members weighted. The particle filter observational pdf is plotted against the source strength ensemble member of well Ten Post (X/Y 246/591 km) in figure 6.14. This plot shows only 2 ensemble members with a high weight for both subsets. The right plot is subset 2 and shows exactly the same results as in figure 6.12 on the right. The results of the other wells are not plotted, but most likely the results of the subsets are similar to the whole set.

An improvement of the particle filter could be a larger set of ensemble members, thus varying value N from 5000 to 6000 or even 10000 ensemble members. The particle filter observational pdf variance of σ^2=144 mm is already large (compared to the synthetic experiments of chapter 5); changing this value is not the solution. The methodology of section 6.1.5 to 6.1.7 describes three solutions to improve the source strength estimation. Perhaps one of these solutions provides an improvement of the source strength estimation. The results are presented in the following three sections (section 6.2.5, 6.2.6 and 6.2.7).

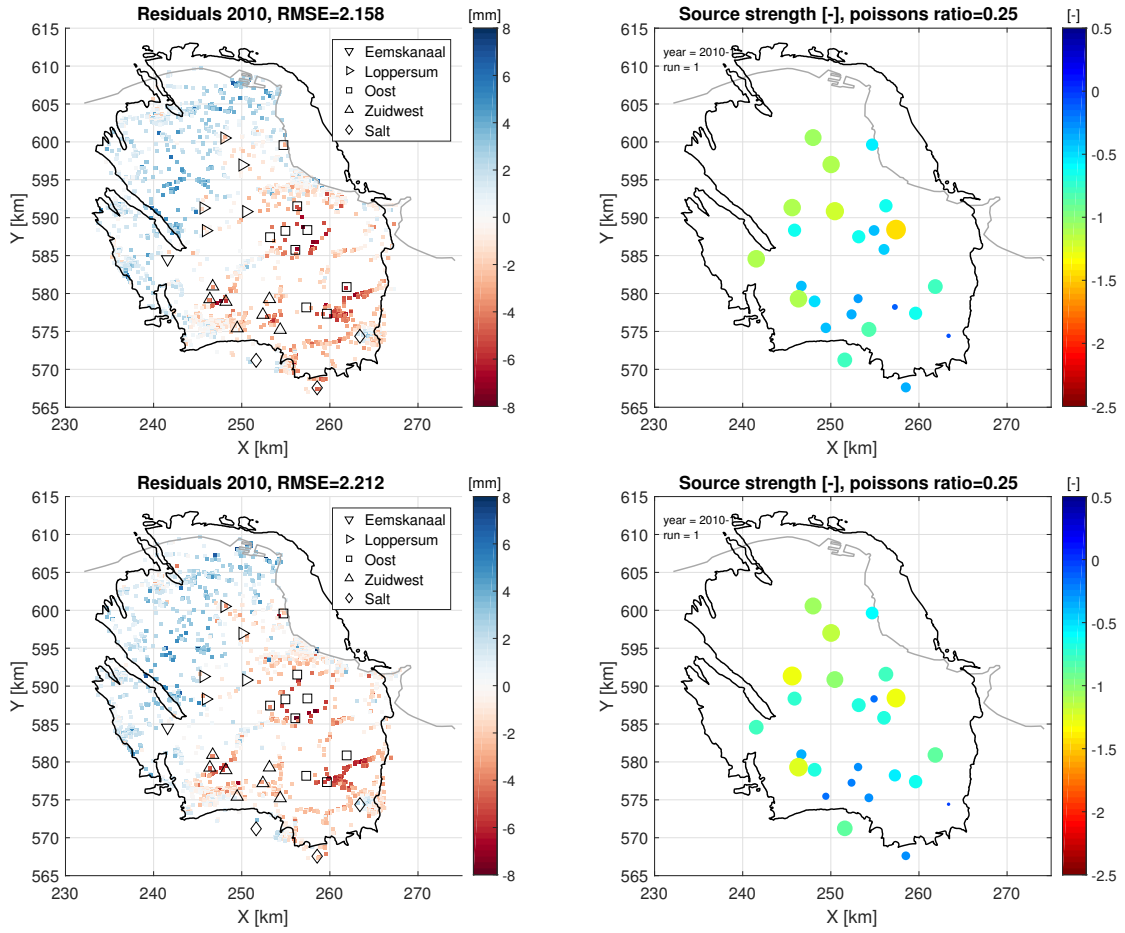

Figure 6.13: Particle filter results of fitted subset data for one run and with an observational pdf variance of σ^2=144 mm. **Top left**: Residuals = model - deformation, subset 1 **Top right**: Posterior source strength [-] of one run, subset 1 **Bottom left**: Residuals = model - deformation, subset 2 **Bottom right**: Posterior source strength [-] of one run. subset 2. Fit is 93% for 4 mm threshold and 99.8% for 8 mm for subset 1 and 93% for 4 mm threshold and 99.6% for 8 mm for subset 2.

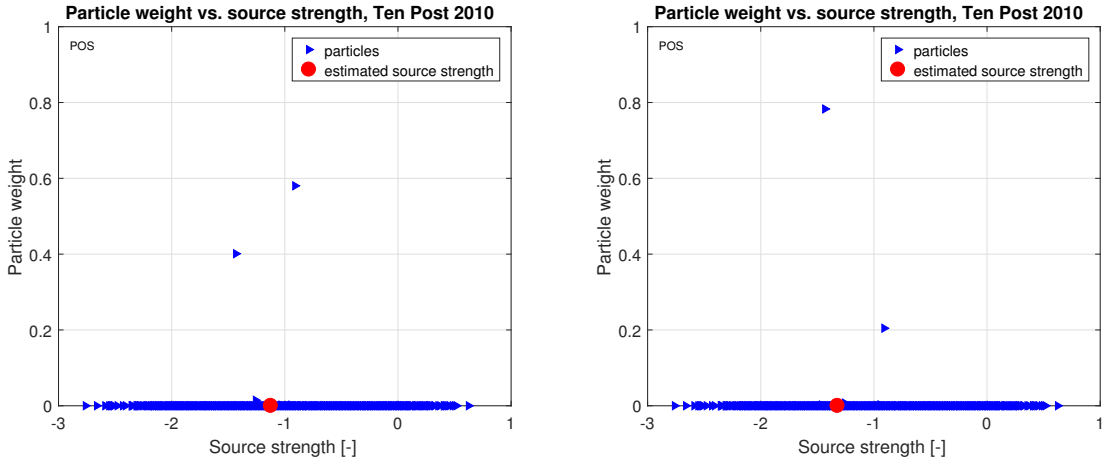

Figure 6.14: Source strengths vs. particle filter observational pdf for well Ten Post, X/Y 246/591 km, particle filter variance σ^2=144 mm. Blue=prior particles and red = estimated posterior source strength. **Left**: subset 1. **Right**: subset 2.

6.2.5. Solution I, particle filter resampling applied to fitted PS-InSAR measurements

Resampling of the particle filter is applied to the fitted PS-InSAR measurements as explained in the methodology of section 6.1.5. Figure 6.15 shows the results of residuals and the estimated source strengths. The residuals are lowered for the overestimated area near coordinates X/Y 260/578 km. The other two overestimated areas do not show any improvement after applying resampling. Furthermore the area around the three production clusters at coordinates X/Y 253/576 km shows a decrease in residual values that means an improved fit between deformations and modelled deformations. The source strengths of the three clusters in that area is lowered for cluster Zuiderveen (X/Y 253/579) and increased for cluster Tusschenklappen (X/Y 254/575). The resampling solution results in a better fit for this area. The source strengths of the three clusters in the overestimated area of X/Y 260/578 km show a decrease in strength for the west located cluster; this is De Eeker (X/Y 259/577). The other two overestimated areas (location X/Y 255/588 and X/Y 247/580) show small changes in source strength. The RMSE is 1.90 mm, this is an improvement of 0.2 mm compared to the old value, this 0.2 mm improvement is small. The fit is improved by 3% and is now 96% for a 4 mm threshold. The buffer area RMSE value is improved by 0.3 mm and is 1.89 mm. The fit is improved from 91.8% to 96.3% for a 4 mm threshold.

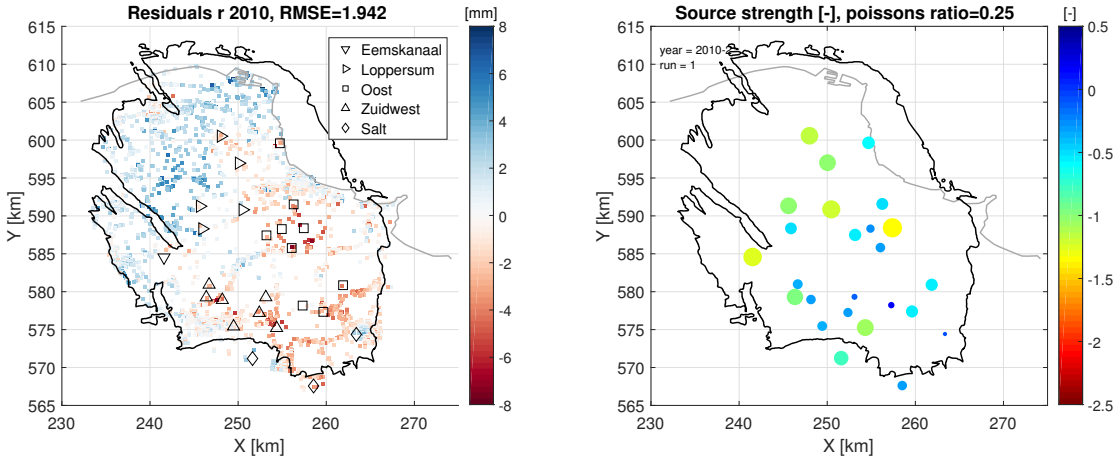

Figure 6.15: Resampling particle filter result of fitted data for one run and with an observational pdf variance of σ^2=100 mm. **Left**: Residuals = model - deformation **Right**: Posterior resampled source strength [-] of one run. Fit is 93% for 4 mm threshold and 99.7% for 8 mm.

The resampling improves the deformation estimation RMSE and percentage of the deformation, but not of source strength. One of the sources has a positive source strength value at location X/Y 257/578 km; this is cluster Scheemderzwaag. The point density is almost zero in this area; this causes probably the positive value,

because there is not enough deformation locations. In addition the source at location X/Y 259/577 km, cluster De Eeker, influences the estimation, because the source is only 2.5 km away and their deformations interfere the deformation of cluster Scheemderzwaag. The source strength estimation of this resampling solution is not the wanted outcome, because there are positive source strengths that mean uplift. The particle filter criteria of estimating only negative source strengths is not met for this solution.

Figure 6.16 shows the particle filter observational pdf plotted against the source strength ensemble members for cluster Ten Post. There are now 5 ensemble members with a large weight (for this plot > 0.25) instead of the 2 ensemble members of the first particle filter run in figure 6.12. The plot shows the variation of source strength is reduced compared to figure 6.12 on the right. That plot shows a variation of -3 to 0.5 and this plot shows a variation of -1.8 to -0.5. The plot shows a degeneracy in the ensemble members that means variation loss.

A second resampling is performed with a particle filter observational pdf variance of σ^2=64 mm. The RMSE for the complete field is 1.80 mm and the fit is 97% for a threshold of 4 mm. This second time of applying the resampling improves the estimation of the deformation, but still one of the source strengths have a positive value.

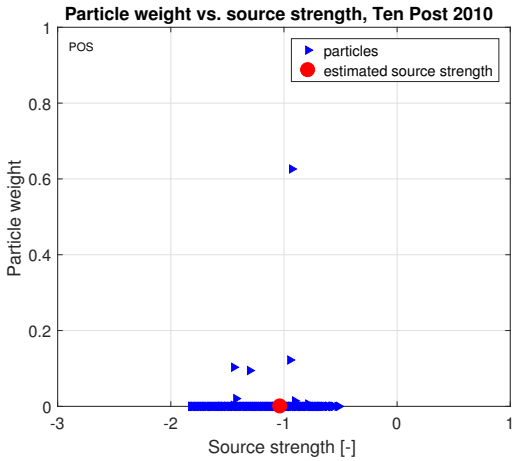

Figure 6.16: Source strengths vs. particle filter observational pdf for cluster Ten Post, X/Y 246/591 km. Blue=prior ensemble members and red=estimated posterior source strength. Resampling with an observational pdf variance of σ^2=100 mm.

6.2.6. Solution II, particle filter with guiding start values applied to fitted PS-InSAR measurements

The estimated source strengths of section 6.2.3 are used as guide for the initial value (start values) to generate randomly Gaussian source strengths. The particle filter prior generating and calculating the posterior (step 1 and 2) is applied to the fitted PS-InSAR measurements. Figure 6.17 shows the residuals and the estimated source strengths. The residuals of the observed deformation and modelled deformation are lowered for all the measurement points around the Mogi sources, compared to the results in section 6.2.3. The RMSE is 1.76 mm; this is an improvement of 0.4 mm compared to step 1 and 2 of the particle filter in section 6.2.3. The fit is improved by 4% and is now 97% for a 4 mm threshold.

The buffer area RMSE is improved by 0.6 mm and is now 1.58 mm and the fit is improved as well from 92% to 98% for a 4 mm threshold. The solution II improves the deformation estimation slightly better than solution I for the RMSE and percentage of fit of the deformations. One of the sources has a positive source strength value at location X/Y 259/577 km, cluster De Eeker. This is a different source than the positive valued source in section 6.2.5 that was cluster Scheemderzwaag. The area is the same, the low point density and the distance of 2.5 km between the sources probably causes the postive estimated source strength. The positive value means that uplift is modelled instead of subsidence. This is an unwanted result, despite solution II shows an improvement in the RMSE and percentage of fit compared to the estimation of section 6.2.4.

The overestimated areas at coordinates X/Y 255/588, X/Y 247/580 and X/Y 260/578 km show an improved estimation. This is also reflected in the RMSE value of 1.76 mm compared to the 2.18 mm RMSE value of section 6.2.3. The source strength figure 6.17 on the right show an increase of the Mogi source strengths at the locations Eemskanaal (X/Y 241/585), Ten Post (X/Y 245/591) and ‘t Zandt (X/Y 248/600) compared to

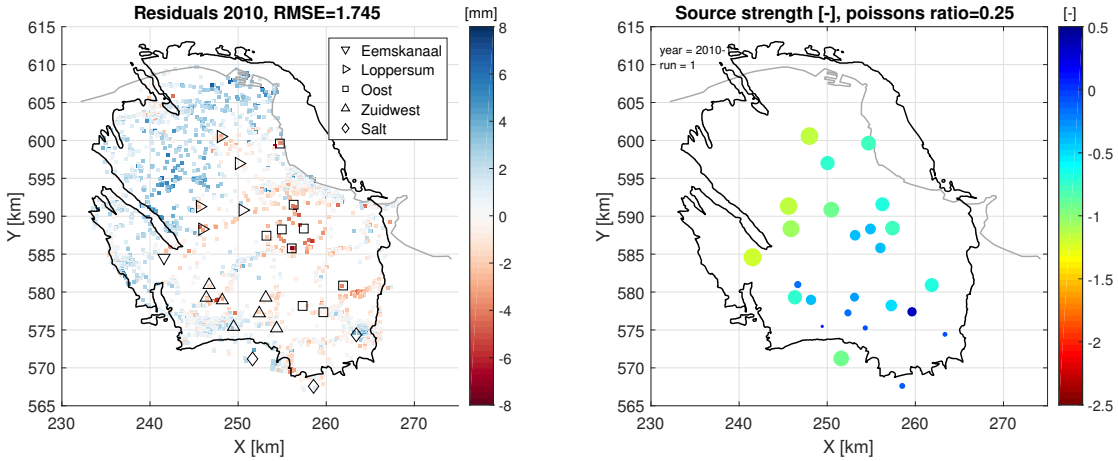

Figure 6.17: Particle filter result of fitted data for one run and with an observational pdf variance of σ^2=100 mm and with source strength ensemble members based on the posterior source strength of figure 6.11 bottom right. **Left**: Residuals = model - deformation **Right**: Posterior source strength [-] of one run. Fit is 97% for 4 mm threshold and 99.8% for 8 mm.

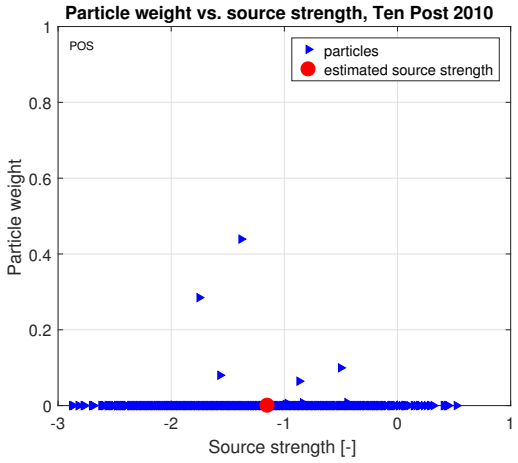

Figure 6.18: Source strengths vs. particle filter observational pdf for cluster Ten Post, X/Y 246/591 km. Blue=prior ensemble members and red=estimated posterior source strength.

figure 6.17 bottom right. The overestimated areas show a decrease in source strengths.

Figure 6.18 presents the source strengths ensemble members against the particle filter observational pdf for the well Ten Post (X/Y 246/591 km). There is clearly an improvement in the number of weighted particles compared to figure 6.12. The posterior source strengths are now based on the weighted mean results of 5 ensemble members instead of the 2 ensemble members in section 6.2.3.

A second run is performed with a particle filter observational pdf variance of σ^2=64 mm. The RMSE value for the complete field is 1.7 mm and the fit is 97%. This second iteration of using the estimated source strengths as guiding the initial value (start values) in generating ensemble members improves the estimation of the deformation, RMSE and percentage of fit. An improvement of the particle filter could be increasing the number of ensemble members N from 5000 to 6000 or 10000 in this solution of guiding the initial start value.

One of the sources has still positive source strengths. This solution II does not meet the particle filter estimation criteria of having all negative source strengths that mean subsidence. A solution to this is perhaps find in the localisation solution of section 6.2.7.

6.2.7. Solution III, particle filter localisation applied to fitted PS-InSAR measurements

The localisation methodology of section 6.1.7 is applied to the fitted PS-InSAR measurements. The RMSE and percentage of fit for the four different radius values are presented in table C.1 and C.2. This table shows the best values for a localisation with radius=4500 m. This is not my expectation for this method. I thought

the radius=1500 m would perform better. The deformation at a radius larger than 1500 m is still needed for estimating a good fit based on the overall RMSE values. The observational pdf variance σ^2 of the localisation with radius=1500 m is varied, namely 36, 49 and 64 mm in order to find out if the source strength estimation and RMSE is lowered and percentage of fit improved. The results are in the same order as the estimation with an observational pdf variance σ^2=100 mm. The percentage of fit is slightly increased with 2% for a threshold of 4 mm and for an observational pdf variance σ^2=49 mm.

The localisation is local, therefore the local RMSE for areas within 1500 m of the wells are plotted in figure 6.19. This plot shows the localisation of 1500 and 3000 m. The localisation of 1500 m performs indeed well for some of the wells, but the localisation of 3000 m performs best for all wells, based on this local RMSE value. Especially the Mogi source locations with their deformations interfere each other.

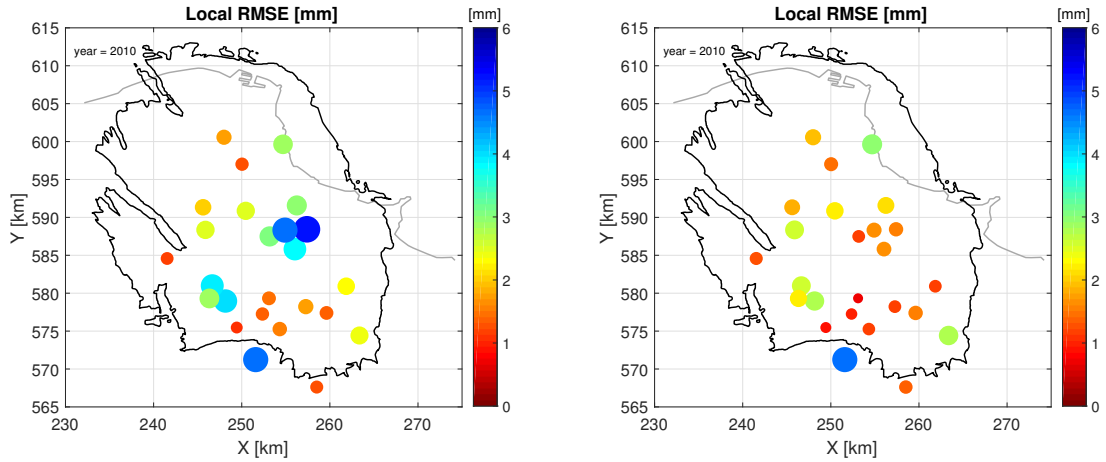

Figure 6.19: Local RMSE computed over an area of radius=1500 m. **Left**: localisation 1500 m. Fit is 96.5% for 4 mm threshold and and 99.7% for 8 mm. **Right**: localisation 3000 m. Fit is 97.3% for 4 mm threshold and and 99.8% for 8 mm.

The result of the residuals and the estimated posterior source strengths of radius=3000 m is shown in figure 6.20. There is one positive source strength present and located at X/Y 259/577 km, this is cluster De Eeker. The same location as the source in section 6.2.6. Four different radius values of the localisation are tested and all show positive source strength at De Eeker cluster location. The three overestimated areas at coordinates X/Y 255/588, X/Y 247/580 and X/Y 260/578 km show low residuals. This is also expressed in the RMSE value of 1.74 mm and the percentage of fit of 97.3% for a 4 mm threshold. The localisation works as expected, namely lowering the residuals and thus obtaining a good fit between measured and modelled deformation. The source strengths of the three overestimated areas are all similar in these three areas. There is no large source strength in the overestimated areas. All source strengths are now more or less the same. There is a southeast to northwest trend of source strength values. This is further discussed in the discussion section.

Figures 6.21 and 6.22 presents the source strength ensemble members against the particle filter observational pdf for cluster Ten Post (X/Y 246/591 km), for localisation radius=3000 and 4500 m, and for all the 25 wells for localisation radius=3000. The results of the particles versus the particle filter weights for a radius= 1500, 4500 and 6000 m are presented in figures C.1 to C.3.

There is clearly an improvement in the number of weighted ensemble members compared to the Ten Post cluster figure 6.12. The posterior source strengths are now based on the weighted mean results of many ensemble members, instead of the 2 weighted ensemble members in section 6.2.3. The shape of both plots differs from each other. The radius=3000 m particle weight plot shows a double well particle weight curve as shown and described in figure 5.11 of section 5.2.2. The RMSE value of the synthetic experiment **2 Mogi sources = at deformation locations** is 4.0 mm for the deformation and 0.4 [-] for the source strength for a double well situation (see figure 5.9). The RMSE value of the localisation 1500 m is 1.89 mm; this is slightly lower than the synthetic experiment. The synthetic experiment showed also that there is not much difference between the source strength RMSE values, when the deformation RMSE values differ. The estimated source strengths have a value of ±0.4 added to the estimation. The radius=4500 m particle filter observational pdf plot shows a curve that is not similar to a single or double well setup of section 5.2.2. The sources are influenced by more sources. The synthetic experiment RMSE value is 0.5 to 0.9 [-] for four sources or a larger number.

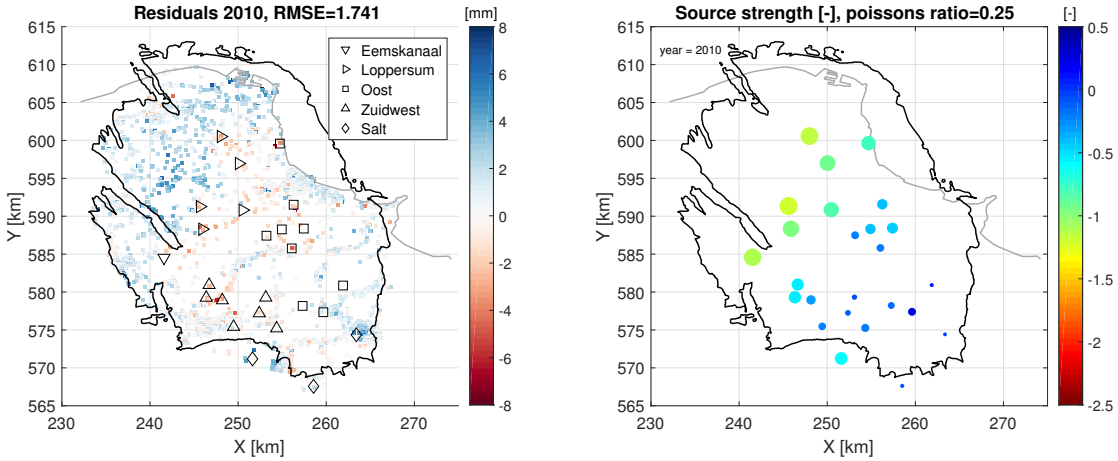

Figure 6.20: Particle filter result of localisation with radius=3000 m and with a particle filter variance of σ^2=100 mm. **Left**: Residuals = model - deformation **Right**: Posterior resampled source strength [-] of one run. Fit is 97.3% for 4 mm threshold and and 99.8% for 8 mm.

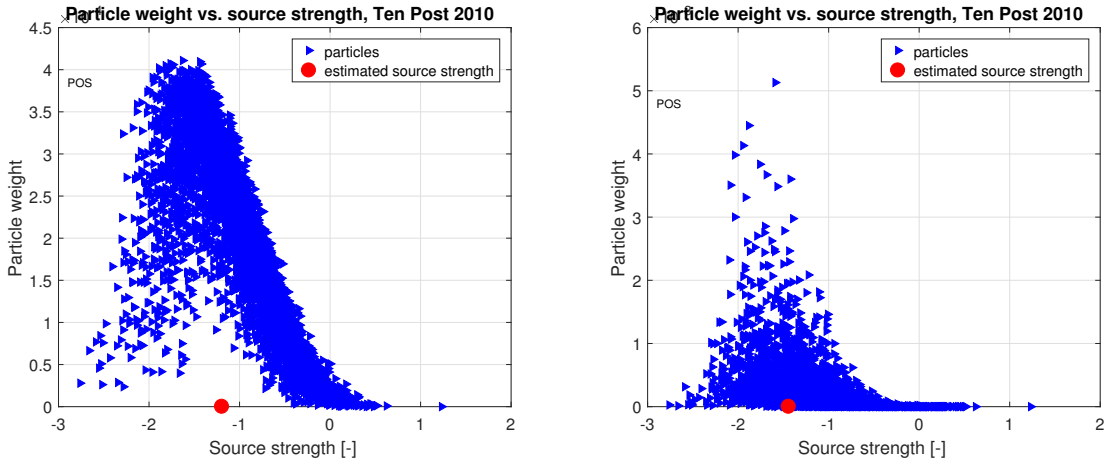

Figure 6.21: Source strengths vs. particle filter observational pdf for cluster Ten Post, X/Y 246/591 km and with a particle filter variance of σ^2=100 mm. **Left**: localisation of radius=3000 m. **right**: localisation of radius=4500 m. Blue=prior ensemble members and red=estimated posterior source strength.

The localisation estimated source strengths are thus ±0.5 to 0.9 [-]. It can be concluded that the localisation estimation of radius=3000 m performs better for the single and double well situations and also for the three and more sources surrounding each other. This is also shown in the local RMSE plot of figure 6.19 on the right.

The particle filter observational pdf plots of the 25 wells show for all wells many ensemble members with non-zero weight. The particle filter observational pdf shaped as a Gaussian curve indicates a Mogi source deformation that is not influenced by many surrounding wells, as shown and described in figures 5.10 and 5.11 of section 5.2.2. The noisier the plots are and the bell shaped curve disappears, the more a close-by Mogi source deformation influences the estimation. The wells BIR, EKL, LRM, OVS, PAU, POS, ZND and the three salt wells VDM, WSN and ZWD show all the shape of a single or double Mogi source well. These wells have a RMSE value of ±0.2 to 0.9 [-] as based on the synthetic experiments of section 5.2.2 in chapter 5. It can be concluded that the localisation of radius 3000 m is best based on the local RMSE values. The RMSE of the complete field differs not much from the other three localisations.

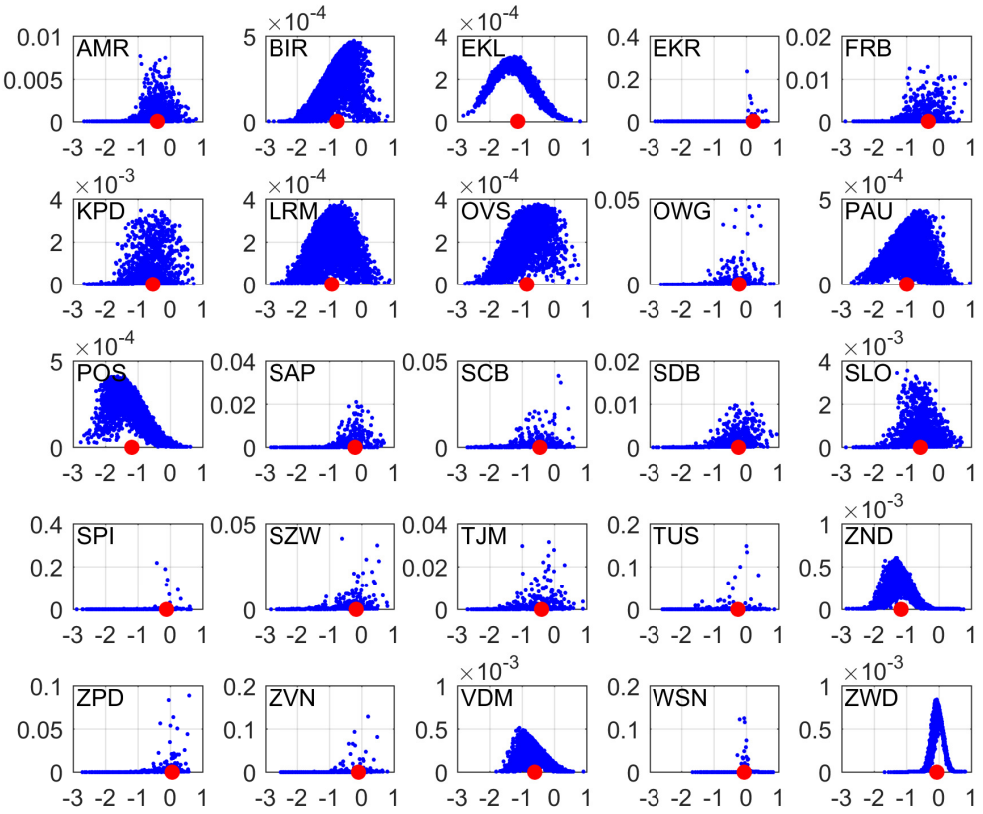

Figure 6.22: Source strengths vs. particle filter observational pdf for well each well (names in the upper left corner) and with a particle filter observational variance of σ^2=100 mm, localisation of radius=3000 m. Blue=prior particles and red=estimated posterior source strength.

6.2.8. Particle filter source strength vs. deformation for 2010

The sections 6.2.5 to 6.2.7 show three solutions for improving the estimating of the source strengths. These solutions use the fitted data, because this fit show a smooth deformation signal, which is perfect to tune the particle filter method to this real Groningen case. Solution III, the localisation shows the best estimation of the source strengths. This solution is used further on in this chapter and applied to unfitted data, since the particle filter is supposed to fit and find the best estimation.

Figure 6.23 shows the estimated source strength values versus the deformation. This deformation is an average value over an area of radius=1500 m around the Mogi source well. This is the same radius value as for the time series in section 6.2.2. The left plot are the estimated source strengths as a result applying the first two steps of the particle filter on the unfitted measurements. The right plot shows estimated source strengths as a result of solution III, a localisation with radius =3000 m applied to unfitted measurements.

The left plot shows that the sources in the Oost region (blue) are scattered over the whole plot, while the Zuidwest region (purple) and Loppersum region (orange) are grouped together. The deformation values of the Zuidwest area are similar, while the source strengths vary from -0.5 to -0.9 [-]. The Loppersum area shows similar source strengths for different deformations.

The Eemskanaal well shows a large deformation value with a large source strength. This behaviour is as expected. The deformation at the well is clearly not influenced by deformations from other wells. The result is similar to the **1 Mogi source = at deformation location** synthetic experiment in section 5.2.1. This synthetic experiment of section 5.2.1 has a deformation of -8.25 mm with a source strength truth of -1.48 [-]. Almost the same as the Eemskanaal well. The same synthetic experiment shows as well a deformation of -2.70 mm with a source strength truth of -0.48 [-]. The dashed line drawn in the plot is the result of that synthetic experiment. Many of the estimated source strengths in the centre are located on or near this line. The source strengths

show an expected result for the observed deformation.

The unfitted localisation result (right) show four positive source strength wells, two salt wells and two wells in the Oost production region. These wells are located on the dashed line linear relationship of the synthetic experiment in section 5.2.1. The sources are, according to the dashed line, a single source that is not influenced by deformations from surrounding sources. The Eemskanaal source shows a larger value of -2.0 compared to the -1.5 [-] of the top plot. The four production region wells are grouped together. The Zuidwest region shows only values nearby each other. These production regions contain only wells that are closely located and deformations of the Mogi sources interfere each other.

The positive source values are caused by the low number of PS-InSAR measurements within the localisation radius selection and/or the small deformation values and/or the short distances between the Mogi sources. Short distances between Mogi sources results into one source with a large negative strength and one source with a low positive strength. The synthetic experiment in section 5.2.3 shows in figure 5.12 a source with a positive source strength (lower right source) and a negative deformation for a test setup with distances of 1500 m between the Mogi sources. The negative source strength value of the surrounding sources clearly influence the deformation above the positive Mogi source. The presence of positive estimated source strength is thus not an exception and can be estimated by the particle filter due to a large source strength of one of the surrounded Mogi sources.

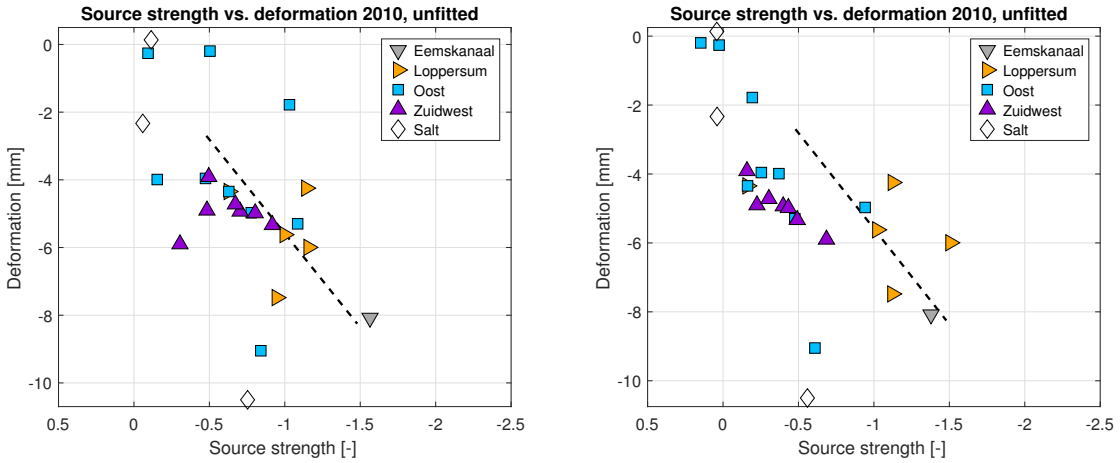

Figure 6.23: Source strength vs. deformation, deformation is average of points within radius=1500 m. **Left**: unfitted with estimated source strengths of particle filter step 1 and 2. **Right**: unfitted with estimated source strengths of localisation (radius=3000 m) particle filter. Dashed line: synthetic experiment linear relationship result of section 5.2.1. Note: the salt wells are at different depths, 1500 to 1800 m.

6.2.9. Particle filter localisation radius=3000 m applied to PS-InSAR measurements for the period 2010-2016

The localisation of radius 3000 m of the previous section is applied to the unfitted PS-InSAR measurements for the period 2010-2016. The estimated source strengths are shown in figure 6.24 for the unfitted PS-InSAR measurements (fitted see C.4).

The figure (unfitted) shows a source strength increase at the northwest locations from 2010 to 2016. This is a result of increasing deformation values in that area. Furthermore the other source strenghts are quite similar over the years. The deformations is a result of gas production leading to reservoir compaction.

The same wells of the time series, Eemskanaal, Overschild, Zuiderpolder and Slochteren, are plotted against the years. These are presented in figure 6.25 The Eemskanaal cluster estimated source strengths follows the deformation differences. A stop in deformation resulted in an decrease of source strength. The Overschild cluster shows a decreasing deformation value from -6.0 to -5.0 mm. The source strength follows this decreasing trend by decreasing source strengths. The Zuiderpolder cluster shows an increasing deformation from -1.8 to -5.0 mm. This increasing trend is not directly clear in the source strength values. This location shows some difficulty in estimating the source strength, because of the low number of PS-InSAR measurements. The Slochteren cluster shows an increasing deformation of -3.5 to -7.0 mm. This clear increasing deformation trend is not very clear in the estimated source strength values (bottom plot). This plot

shows variable source strength with ups and down. Clearly caused by the location of the source, because this source is surrounded by other Mogi sources that their deformations influence the estimation.

The gas production is plotted versus the estimated source strengths; these are shown in figure C.5. There is no clear correlation between them, also not when the time delay of 4.8 years (section 2.6.2 (Van Thienen-Visser et al., 2015)) is subtracted from the period of estimated source strengths. The RMSE value of the estimation of the source strengths in the synthetic experiments of chapter 5 show each time a RMSE value of 0.5 to 1.0 [-]. The estimated source strengths in this section could have source strength RMSE value of 1.0 [-]. This means that the estimation as shown in figure C.5 can vary and resulting in a different trend with high and low peaks differently that can linked to the gas production data, when taking the time delay factor in account.

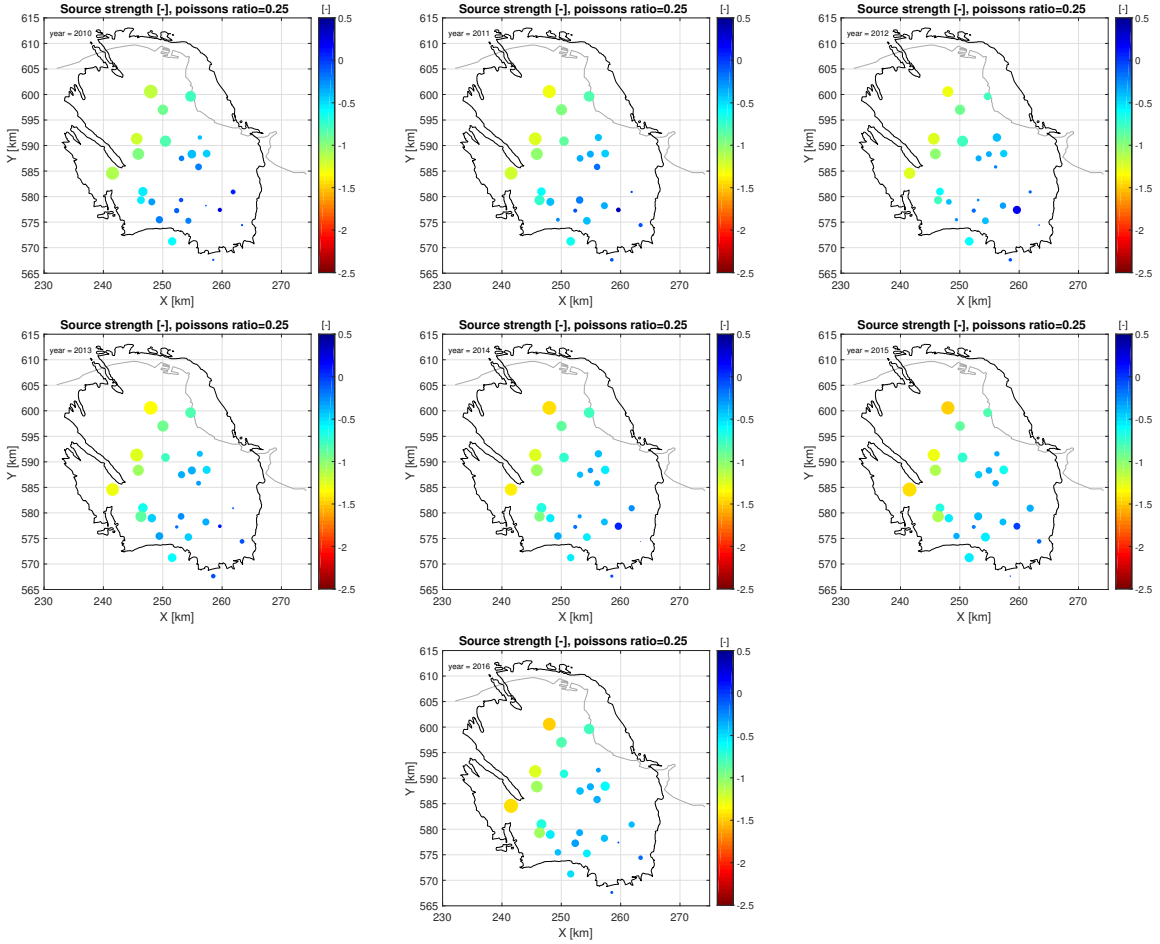

Figure 6.24: Estimated source strengths of 2010 to 2016 for a particle filter localisation radius=3000 m. **Top** : unfitted PS-InSAR measurments estimated source strengths of years 2010, 2011 and 2012. **Middle**: unfitted PS-InSAR measurments estimated source strengths of years 2013, 2014 and 2015. **Bottom**: unfitted PS-InSAR measurments estimated source strengths of year 2016. Note: the salt wells are at different depths, 1500 to 1800 m.

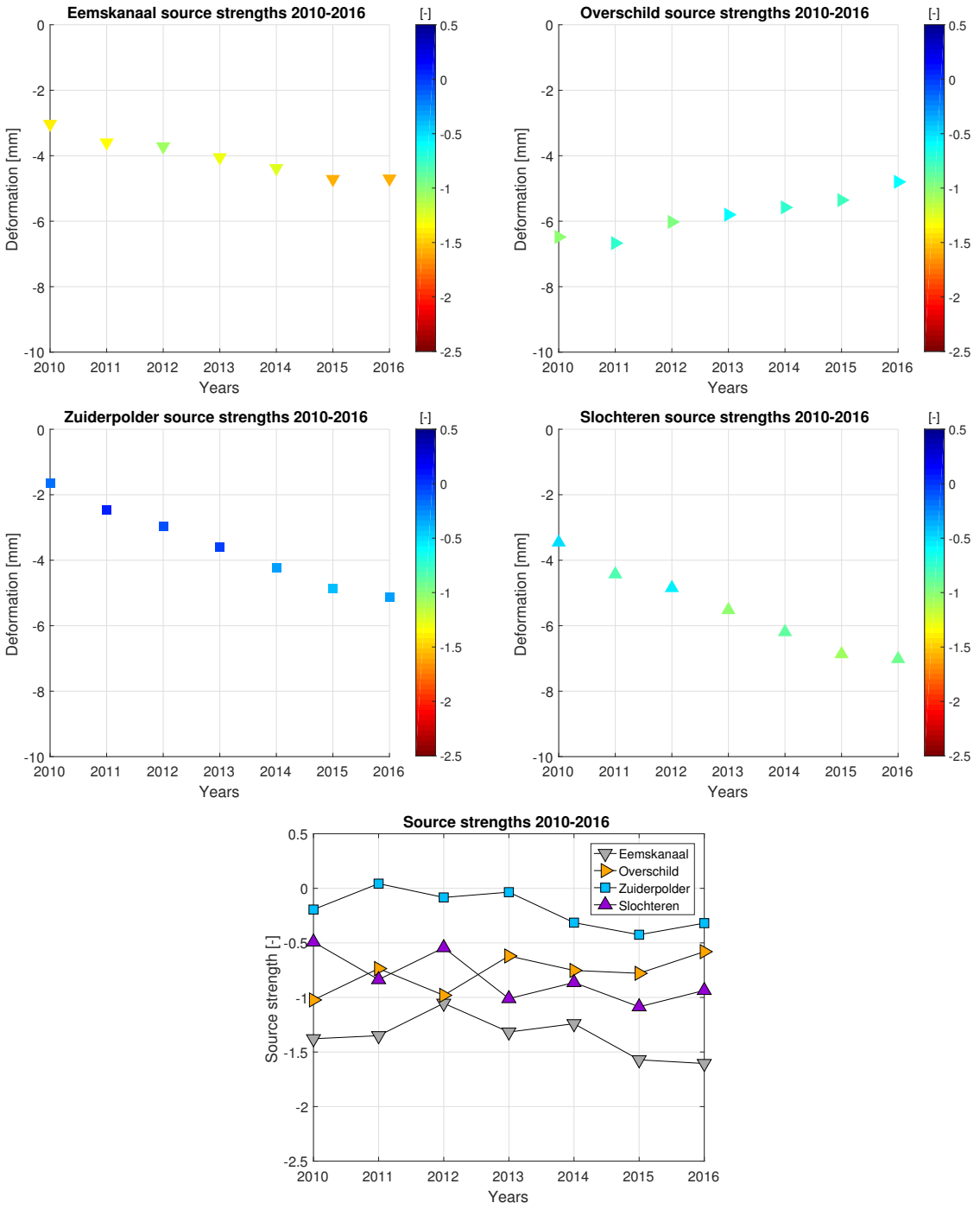

Figure 6.25: Source strength in colour and deformation over the period 2010-2016. **Top**: Eemskanaal and Overschild **Middle**: Zuiderpolder and Slochteren **Bottom**: estimated source strengths plotted together. The colour corresponds to the region colours that are also used in the time series of section 6.2.2.

6.3. Discussion and conclusion

This chapter describes the steps of the particle filter applied to the PS-InSAR measurements of Groningen. Time series are shown for a selection of production clusters in order to explore the deformation behaviour in the four production clusters. The time series deformation plot provide a first look on the deformation measurements over the period 2009 to 2016. Furthermore the particle filter and three solutions of improving the source strength estimation from PS-InSAR measurements are tested.

Time series of deformation

The Loppersum region time series shows a seasonal trend with large deformation values in January and December and lower deformation values in between these months. January and December are the months of the largest gas production and could cause the large surface deformation. This fit of deformation and gas production seems perfect, despite the presence of a time delay factor. This time delay causes a delay in how reservoir compaction is translated to the surface (NAM, 2016). For example a lowered gas production is shown many years later at the surface, as is mentioned in section 2.6.2 and modelled in a time decay model (exponential model) by the NAM (2016). Van Thienen-Visser et al. (2015) estimated a time decay constant of 4.8 years. The time series shown in section 6.2.2 will be the years 2004-2011 after subtracting the time decay parameter of 4.8 years. The decrease in gas production in the Loppersum region in the years 2014-2016 is perhaps visible in the deformation signal year 2019. This is for future research.

The gas production causes reservoir pressure depletion from 300 bar to 80 bar from the start of production till present (NAM, 2016). Only reservoir pressure measurements once every 2-3 years are available for the public. The reservoir pressure of the four wells, Eemskanaal, Overschild, Zuiderpolder and Slochteren are shown in figure 6.26. The average reservoir pressure declined from ±100 to 70 bar over the period 2010-2016 and results in surface subsidence. This is also present in the time series deformation there is a continuous subsidence. The reservoir pressure is not the same throughout the year and can vary perhaps from month to month. The seasonal deformation signal of the time series reflects the reservoir pressure depletion.

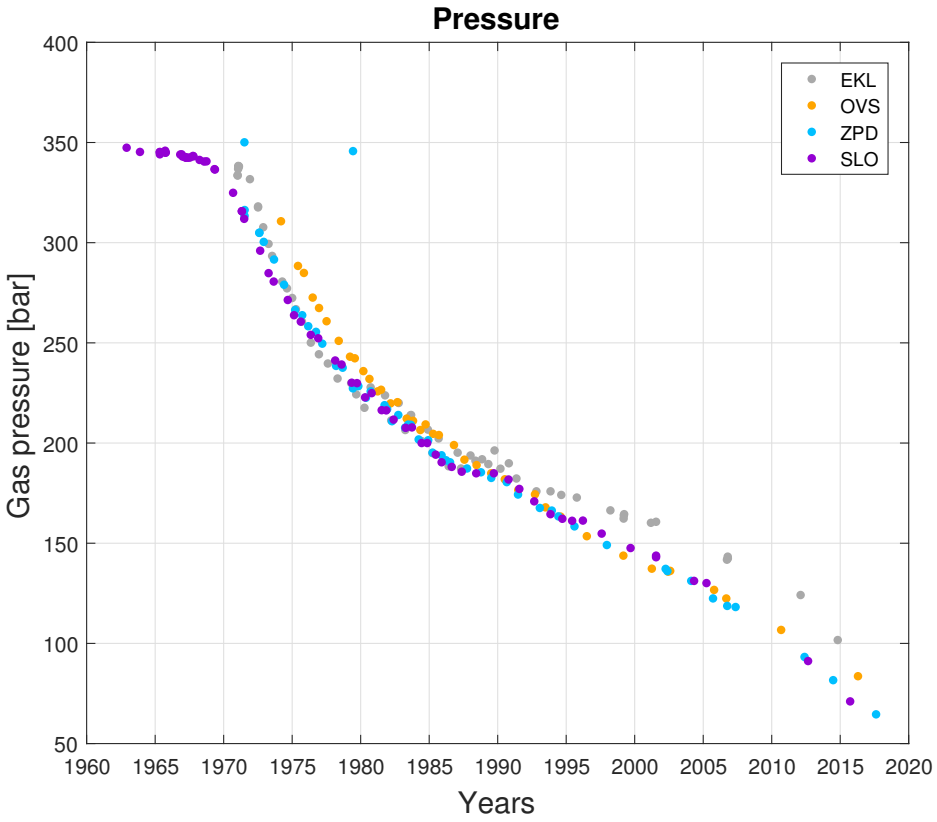

Figure 6.26: Reservoir pressure of four production clusters, namely Eemskanaal, Overschild, Zuiderpolder and Slochteren (data source: (NLOG, 2017a) and updated version obtained by Shell).

The Eemskanaal region and Slochteren cluster show a seasonal signal in the time series deformation, but the large deformation values are not precisely around the months of January and December. The Zuiderpolder cluster shows no seasonal signal. All four clusters are subsiding.

The Veendam salt location has a deformation of -60 mm over the period 2009 to 2016. This is the largest subsidence location of the three salt locations and the one with the lowest salt production over the period 2009 to 2016. This large deformation value may be related to the long history of salt production in this area. The salt production started in 1954 (NLOG, 2018).

Particle filter

The particle filter step 1 and 2 assimilating both fitted and unfitted PS-InSAR measurements resulted into a distribution of weights, where only 2 ensemble members obtain a high weight (>0.1). The resulting deformations RMSE values are low, namely 6.0 mm, which is a good result, because this RMSE is the same as the RMSE in all the synthetic experiments of chapter 5. Based on this it can be concluded that the source strength RMSE could be in the order of 0.5 to 1.0 [-], when taking into account the synthetic experiment results. Furthermore the residual plots show three overestimated areas, all with multiple well clusters. The deformations of the different Mogi source interfere and the particle filter is not able to find a unique solution.

The area at the three well clusters at coordinates X/Y 260/578 km is not represented by the Mogi sources very well (residual -8 mm). This can be caused by the fact that there was an extra well producing till the year 2009. That well, Midwolda, is now closed-in. The appendix figure A.2 show the producing well locations for the period 2003-2016. As mentioned in section 2.6.2 there is a delay in subsidence after pressure depletion. The observed subsidence in the mentioned area of the Midwolda cluster could be caused by gas production from that cluster. There are three other wells in that area that are closed-in as well and the modelled overestimation can be caused by a combination of all the closed-in wells.

Figure 6.22 shows that in case of localisation for most wells many ensemble members obtain a weight. Based on the local RMSE the localisation with radius 3000 m is the best for using the particle filter localisation method. This is actually not what I expected. The radius of 3000 m is quite large and covers a large amount of the Groningen field when drawn around the 25 wells. I expected the radius of 1500 m perform better, because the largest amount of deformation value is near the centre of the Mogi source and that would lead to a good fit with the measurements. Although the differences in RMSE is only 0.06 mm and the percentage difference is 1%. The localisation of radius 1500 m performs well for the Mogi sources that are single located which means not in a group. On the other hand the localisation of radius 3000 m performs well for both cases, thus single located Mogi sources and grouped located Mogi sources. The deformations for these grouped Mogi sources interfere and by applying a localisation of radius 3000 m a larger area of deformations is captured in the particle filter estimation, leading to a better source strength estimation.

In all the three solution parts at the same location positive source strength is present, namely cluster De Eeker. A positive source strength means normally uplift instead of subsidence, but in this case the number of PS-InSAR measurements are very low and there is a Mogi source located nearby that has a negative source strength estimated. This nearby Mogi source results in a negative deformation that influences the estimation of the positive source strength. The positive source strength is close to zero, thus could have been also a negative estimated strength, when more PS-InSAR measurements are present.

The estimated source strengths show for the whole period of 2010 to 2016 a southeast to northwest trend. This trend is related to the amount of deformation. It could possibly linked to the Groningen reservoir thickness that varies from 140 m in the southeast to 300 m in the northwest, as described in section 3.1. The reservoir can compact in the northwest more resulting in surface subsidence variation. Also the variable porosity of the reservoir layer and the presence of aquifers, water-bearing layers, that are connected to the depleting reservoir contributes to different surface subsidence measurements. The source strengths southeast to northwest trend could be related to this reservoir trend, but the groups of Mogi sources their deformations interfere and resulting in lower source strengths can also be the reason for the southeast to northwest trend.

Solution III applied to 2010-2016

The estimated source strengths for the whole period follows more or less the deformation increase or decrease trend. The Mogi sources that are located in groups show variable behaviour, the particle filter has some difficulty in estimating a unique source strength.

7

Particle filter applied to ascending Persistant Scatterer InSAR measurements

This chapter presents the preliminary results of the particle filter applied on real ascending Persistent Scatterer InSAR (PS-InSAR) measurements to estimate reservoir volume changes. The chapter is a first look of the particle filter results applied to a subset of ascending PS-InSAR measurements. Ascending measurements are chosen to find out if there is a difference or similarities in source strength estimation with the descending PS-InSAR estimation of chapter 6.

The methodology is explained in section 7.1, the results in section 7.2 and the discussion and conclusion in section 7.3.

7.1. Methodology

The high point selection workflow is explained in section 7.1.1. The time series in section 7.1.2 and the particle filter localisation of radius 3000 m in section 7.1.3.

7.1.1. PS-InSAR measurements: high point selection

A second set of PS-InSAR measurements of Groningen is kindly provided by SkyGeo Delft. The set contains TerraSAR-X measurements from an ascending satellite track over the period 2013/06/25 to 2017/06/27. Table 7.1 shows the details of the data set. The set has for each PS point the point identification number; latitude/longitude; RDX/RDY; point height; DEM height; quality of the points; slope of the fitted linear model; and the change over time relative to 2013/06/25. The workflow of figure 6.4 to select high PS-InSAR measurements from the .csv file is changed into the workflow of figure 7.1. The Rijksdriehoek coordinate conversion is not needed, because the data set contains these coordinates. The point quality and high point selection is done by using the values of table 6.2 in eqrefeq:highlow. The points of electricity poles are removed from the data set by using an electricity poles location data set of (NGR, 2018a). The wierden locations are removed as well by using the wierden data set of NGR (2018b).

Table 7.1: Details of the PS-InSAR measurements of TerraSAR-X, ascending, right-looking, line-of-sight deformation

Heading	Incidence angle	Period	Repeat pass [days]	No. of epochs	No. of PS points	Point location precision [m]	Measurement precision [mm]
349°	31.1°	2013/06/25 2017/06/27	11	117	1021207	X,Y : 2-3 Z : 2-2.5	6-8

The amount of PS-InSAR measurements are still very high after the removal of the above described points, namely 500,000. This amount of points will make the particle filter very slow. Therefor a subset is taken of these points. A grid of 1x1 km is laid over the point locations and each point is added to one of the grid locations. The number of points in each grid location are counted. A random number is taken from these grid counts and the belonging point is taken to represent the specific grid. This is done for the whole grid.

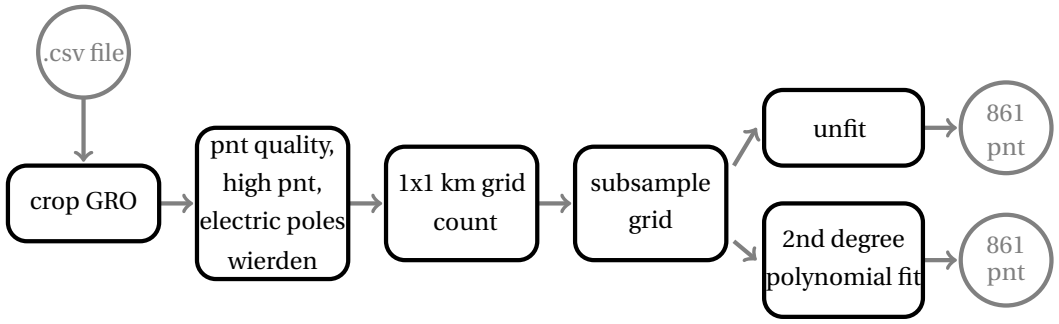

Figure 7.1: Workflow to select PS-InSAR measurements from the TerraSAR-X .csv file. The steps are described in the above sections. GRO=Groningen reservoir outline, pnt=point / points

7.1.2. Time series locations

The time series localations are the four production cluster in the production regions. These are Eemskanaal, Overschild, Zuiderpolder and Slochteren locations are respectively at coordinates X/Y 241/584; X/Y 250/590; X/Y 261/580 and X/Y 246/579 km. These are the same as in section 6.1.2 for the descending data set.

7.1.3. Particle filter localisation applied to the period 2014 to 2016

The particle filter localisation of radius=3000 m is the one applied to the period of 2010 to 2016 in the previous chapter. The method is applied as described in section 6.1.7 with (6.2) and (6.3). The results of 2014 to 2016 of the descending data set overlap with the results for this chapter with the ascending data set. The settings of the particle filter are shown in table 7.2 and are the same as in the previous chapter of the descending data set.

Table 7.2: Particle filter input for the situation with 25 Mogi sources, 861 high PS-InSAR points. The 22 Mogi's for gas have the same ensemble members settings, while the 3 salt sources have different settings per source, VDM = Veendam, WSN = Winschoten and ZWD = Zuidwending. Poisson's ratio ν=0.25 and the LOS vector [0.5503 -0.1070 0.8281]$[d_u, d_n, d_e]$. The years 2013 and 2017 are not complete, only a couple of months define these years, namely July to December for 2013 and January to June for 2017.

Step:		2 (gas)	2 (VDM)	2 (WSN)	2 (ZWD)	3
Ensemble members variance:	σ^2 [-]	0.25	0.125	0.125	0.125	-
Ensemble members start value:	[-]	-1	-0.5	-0.33	-0.33	-
Ensemble members number:	N	5000	5000	5000	5000	-
Mogi source depth:	z [m]	-3000	-1800	-1600	-1500	-
Particle filter Gaussian pdf 1st run:	σ^2 [mm]	144	144	144	144	-
Particle filter Gaussian pdf 2nd run:	σ^2 [mm]	-	-	-	-	100
Gaussian resample 'jitter' variance:	σ^2 [-]	-	-	-	-	0.0156

7.2. Preliminary results

The high points and gridded points are shown in section 7.2.1. The results of the time series of the production clusters are presented in section 7.2.2. The results of the particle filter localisation in section 7.2.3.

7.2.1. High points

The gridded PS-InSAR points of the 1x1 km grid are shown in figure 7.2 on the left. The highest number of points are counted in areas of cities and villages where many buildings are stable PS-InSAR points. The subsampled set is shown in figure 7.2 on the right, where the red circles are the subsampled points and the blue dots the original PS-InSAR points. The number of 500,000 points is reduced to 861 points. This is perfectly suited for a first look of applying the particle filter localisation with radius 3000 mon the PS-InSAR measurements.

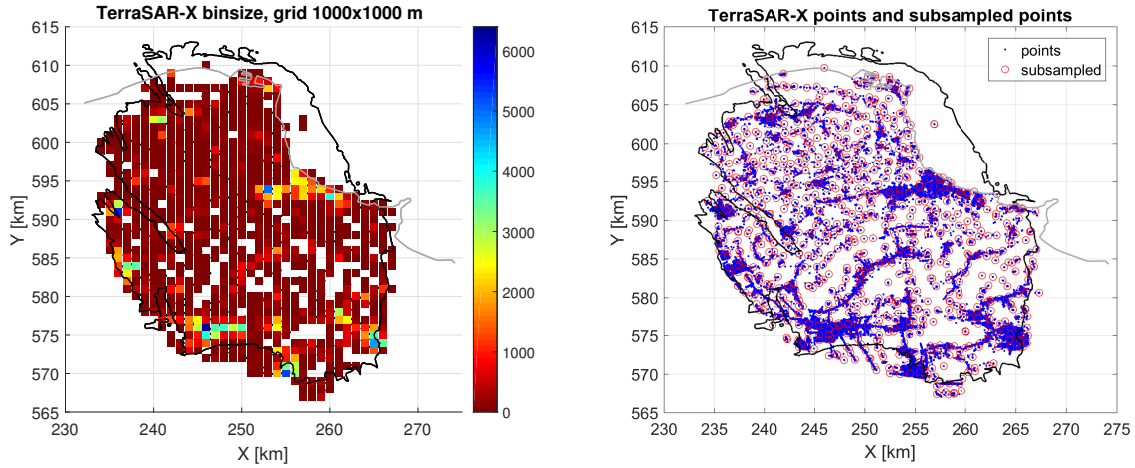

Figure 7.2: TerraSAR PS-InSAR points selection. **Left**: binsize of each grid, **Right**: subsampled points (red circle) and blue high points

7.2.2. Time series

Figure 7.3 presents the time series deformations of the four production clusters Eemskanaal, Overschild, Zuiderpolder and Slochteren. The time series deformations are the same location as the time series deformations of figure 6.8 and the overlapping period is 2014 to 2016.

The Eemskanaal region shows a stable gas production and a stable deformation rate. The deformation is 4 mm for the year 2014 . The descending set in the previous chapter shows a value of 5 mm for the year 2014. The Overschild cluster in the Loppersum region shows a deformation of 3 mm for the year 2014 and the descending set in the previous chapter a value of 4 mm for the year 2014.

The Zuiderpolder cluster shows a value of 2 mm for 2014 and the descending set a value of 4 mm for 2014. The Slochteren cluster shows a value of 5 mm for the year 2014 and the other data set a value of 6 mm.

All the four clusters show a difference in subsidence values of 2014. These values will affect probably the particle filter results and the source strength estimation. The seasonal trend shown in the descending set of the previous chapter is not present for the ascending set. The deformation is quite stable of the period.

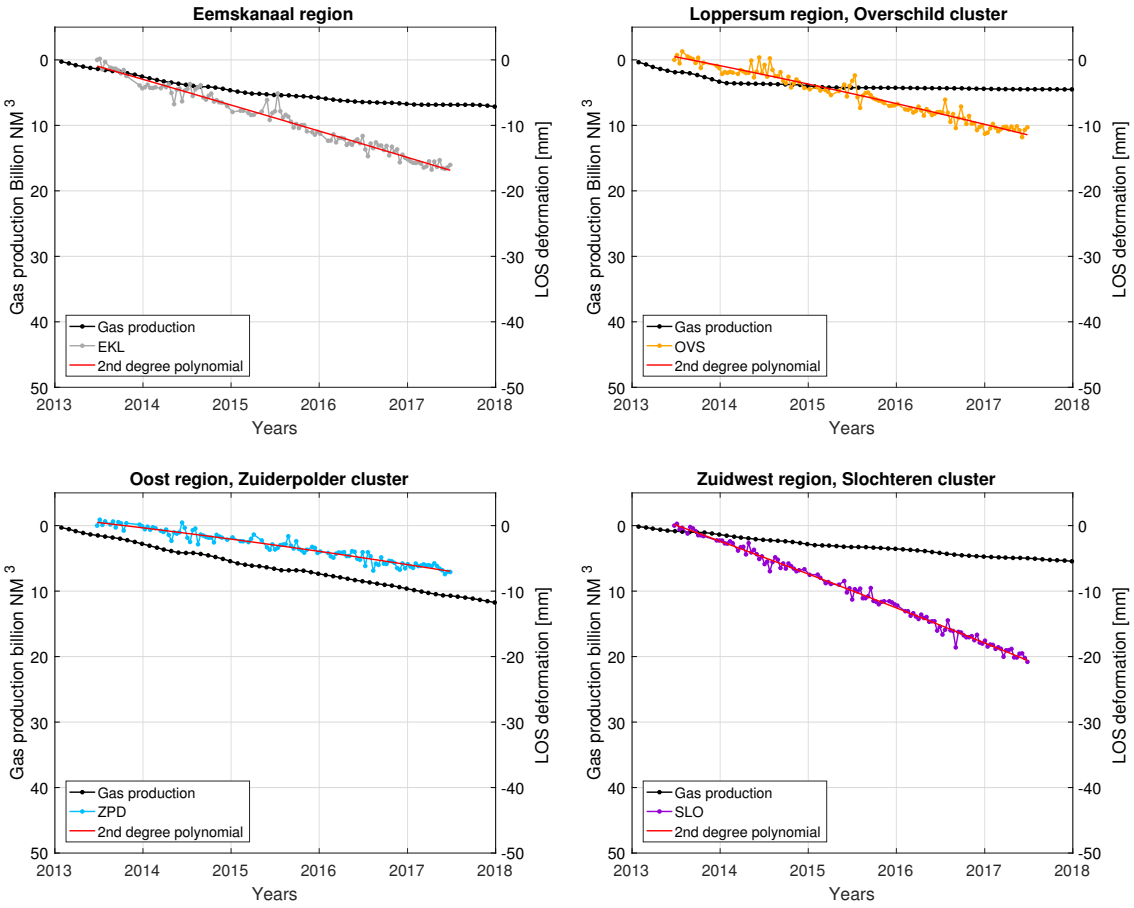

Figure 7.3: Time series (note: the gas production y-axis is reversed). **First row**: Eemskanaal region (X/Y 241/584 km). Loppersum region, cluster Overschild (X/Y 250/590 km). **Second row**: Oost region (X/Y 261/580 km). Zuidwest region, Slochteren cluster (X/Y 245/579 km).

7.2.3. Particle filter localisation radius=3000 m applied to PS-InSAR measurements of 2014

Figure 7.4 shows the particle filter localisation applied to PS-InSAR measurements of 2014. This year is the first year of the ascending PS-InSAR measurements that are complete, thus all the 12 months. The observed measurements (top left) show deformations in the whole reservoir of Groningen, except the southeast area. The residuals (bottom left) show an underestimation in the north part of the reservoir. This is the same as for the residual results of chapter 6.

The source strength estimation (bottom right plot) shows equal sized sources. There are two sources that are large, these are the cluster Bierum (X/Y 254/599 km) and Zuiderpolder (X/Y 261/580 km). The southeast to northwest trend of the estimated source strengths of chapter 6 is not present for this first source strength estimation. This difference is caused by different deformations and probably the number of deformations. This estimation uses only 861 deformation points, while chapter 6 uses 5101 deformation points.

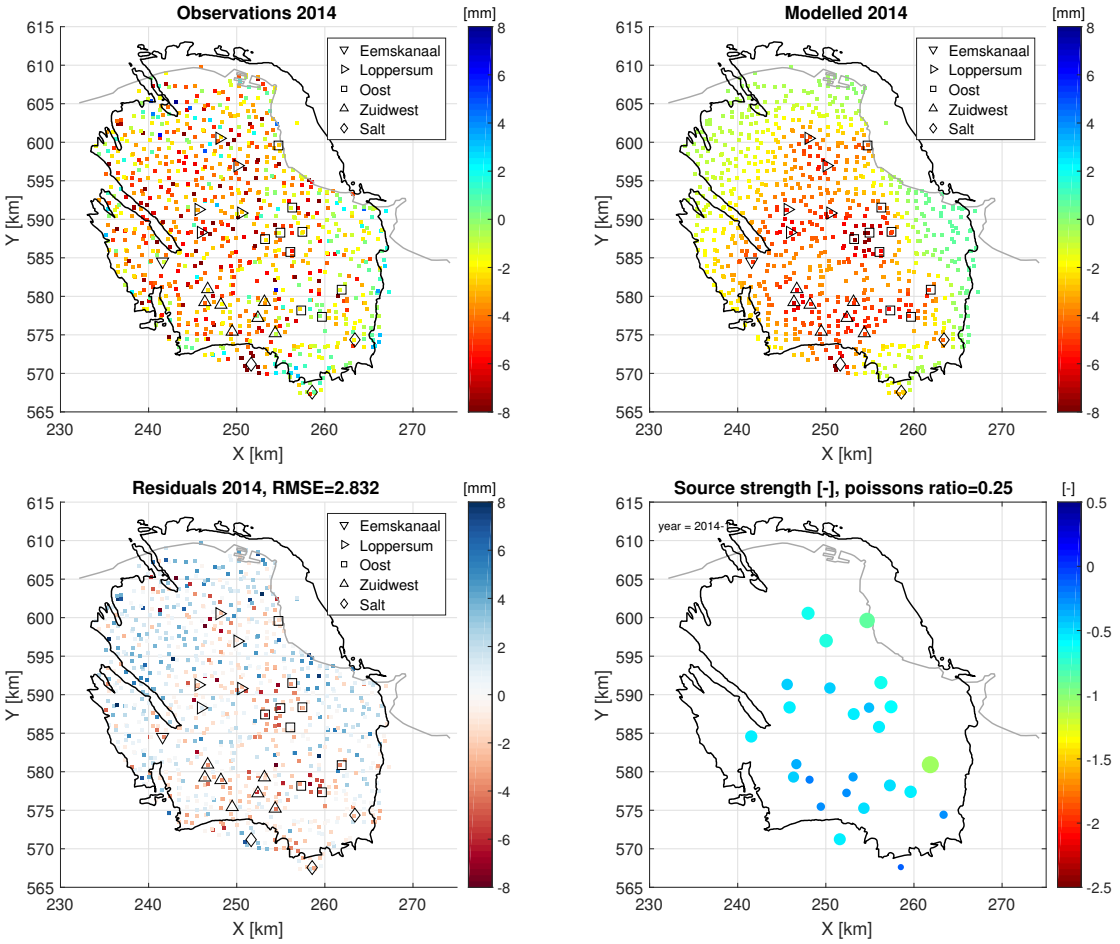

Figure 7.4: Particle filter localisation radius 3000 m results of unfitted data for one run and with a variance of σ^2=144 mm. **Top left**: PS-InSAR measurements of 2014 (unfitted). **Top right**: Posterior deformation result. **Bottom left**: Residuals = model - observation **Bottom right**: Posterior source strength [-] of one run. Fit is 87% for 4 mm threshold and 99.3% for 8 mm.

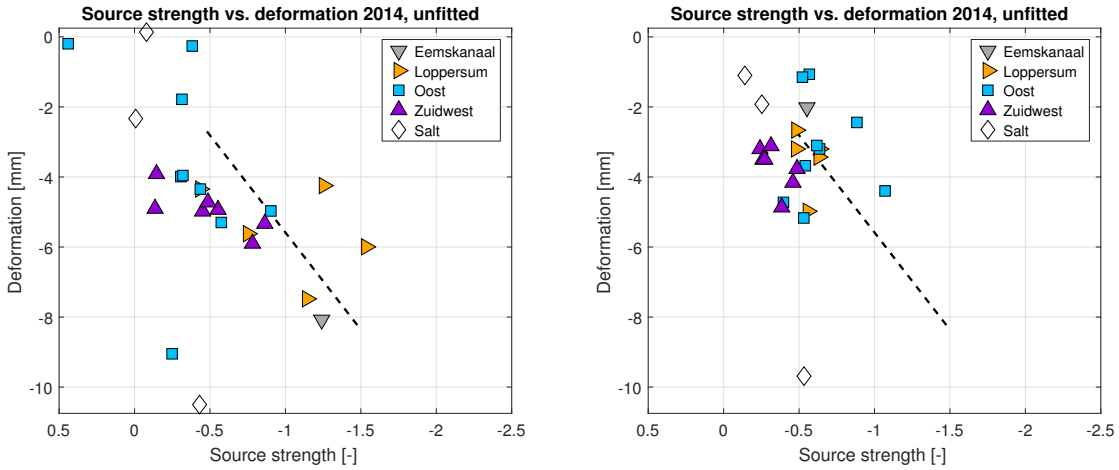

Figure 7.5: Source strength vs. deformation, deformation is average of points within radius=1500 m. **Left**: descending, unfitted with estimated source strengths of localisation radius=3000 m, same as figure 6.23. **Right**: ascending, unfitted with estimated source strengths of localisation radius=3000 m. Dashed line: synthetic experiment linear relationship result of section 5.2.1. Note: the salt wells are at different depths, 1500 to 1800 m.

7.3. Discussion and conclusion

The preliminary results of applying the particle filter localisation method on the ascending PS-InSAR measurements show different amount of deformation values compared to chapter 6. This can be a result of the different radar satellites and that the PS-InSAR measurements are from an ascending satellite orbit. This difference contributes to differences in measurements and in processing them into deformations.

Time series

The time series deformations show a difference in subsidence values of 2014 compared to the time series deformations of chapter 6 for all four clusters. These values affect the particle filter results and the source strength estimation. The seasonal trend shown in the descending set of chapter 6 is not present for the ascending set. The deformation of the ascending PS-InSAR measurements is quite stable over the period 2013 to 2017.

Particle filter localisation radius 3000 m

The estimated source strength against the deformation is plotted for the descending PS-InSAR measurements (same as figure 6.23) and the ascending PS-InSAR measurements for the year 2014. All the estimated source strengths of the ascending set is negative that means subsidence. This is a good result, because the particle filter criteria of estimating only negative source strengths is met for the year 2014.

It can be concluded that applying the particle filter on other PS-InSAR measurements sets needs further analysis, but the preliminary results are promising for future research.

8

Conclusions and recommendations

In this thesis the particle filter is used as a data assimilation technique to derive subsurface volume changes from PS-InSAR measurements. The particle filter is first tested on synthetic data with an identical twin experiment. This is done derive possible limitations of the geomechanical model. The main research question is:

How can the particle filter, as a data assimilation technique, be used in order to estimate geomechanical parameters of subsurface processes, such as reservoir volume change, from space-geodetic PS-InSAR surface measurements?

The main question is broken up into sub-questions in order to reach the aim of this thesis. The sub-questions are divided into two parts, namely the particle filter synthetic experiments and the particle filter applied to the real Groningen case. The sub-questions of the particle filter experiments are:

1. What are the limitations of the geomechanical model when used in the particle filter?

   The Mogi source model is first tested separately from the particle filter. The Mogi source depth, source strength and Poisson's ratio is varied. This is done in a setup with 1 Mogi source and 1 deformation location at the centre above the Mogi source. The Mogi source is sphere shaped, deformation at the surface above the source will be circular and bowl shaped. The deformation right above the Mogi source will be the largest and smaller further away from the centre.

   The depth is varied to four different values, namely -3000, -3001, -3010 and -3100 m. The Mogi source depth is based on the approximate well depths of the production well in Groningen. These well depths vary from -2800 to -3000 m. The varying depths resulted in similar deformation values with only a difference of 0.2 mm between the deformations. It can be concluded that the Mogi model depth variations from -3000 to -3100 m do not have a big influence on the deformations, when the source strength and Poisson's ratio are kept fixed.

   Poisson's ratio ν is varied three times, namely 0.20, 0.25 and 0.30 by a fixed depth of -3000 m and fixed source strength of -0.4871 [-]. The choice for these ratios is based on the values of Lele et al. (2015), where Poisson's ratio varies for the different stratigraphical units of the Groningen subsurface. The results show a deformation value of -3.24, -2.70 and -2.16 mm for respectively ν=0.20, 0.25 and 0.30. Changing the ratio by 0.05 resulted in a deformation change of 0.55 mm. It can be concluded that Poisson's ratio change has a small contribution to the deformation values.

   The Mogi source strength varies by adding -0.10 and -1.00 [-] to the source strength of -0.4871 [-]. The resulting surface deformation difference with the previous experiment is respectively 0.55 and 5.56 mm. This is a linear relationship. A value of -10.0 [-] added to the source strength of -0.4871 [-] results in a deformation difference of 55.6 mm. A surface deformation difference of 5.50 mm is caused by a source strength difference of 1.00 [-], when the model is noise and bias-free and not used in the particle filter. It can be concluded that the source strength has the largest contribution to the deformations.

   The particle filter with a Gaussian observational pdf is tested and estimates the posterior source strength and deformation. Three cases are conducted with the particle filter: one where only Gaussian generated noise is added and two where different bias values are added. The experiment with only added

noise shows the lowest residuals on both parts (source strength and deformation), compared to the other two experiments. The particle filter is able to estimate the real source strength truth by 0.05 [-], even with noisy observations.

The experiment with the added bias values shows large residuals. The bias of 3 millimetre results in a residual value that is 1/3 of the source strength truth and 1.4 times larger than the deformation truth. The 30 millimetre bias value added to the observed deformation results in a residual source strength value of 1.70 [-] and a residual deformation of 24.50 mm. The particle filter is able to estimate a source strength value within 1.70 [-] from the truth, despite the deformation difference of 24.50 mm. It can be concluded that the particle filter estimates the source strengths 1.70 [-] from the true value, by a deformation residual of 24.50 mm. This holds for this particular setting of 1 Mogi source and 1 deformation location with a Poisson value ν=0.25 and a noisy deformation. Results may differ for different settings of Mogi sources and deformation locations.

The rest of the identical twin experiments in chapter 5 show each time a RMSE value between 4-6 mm for the deformation part and 0.5 to 1.0 [-] for the source strength part. There is no noticeable difference between the particle filter with a Gaussian observational pdf or a Lorentz observational pdf.

It can be summarized that the limitation of the geomechanical model used in this synthetic experiment of the particle filter has always source strength RMSE in the range of 0.5 to 1.0 [-].

2. How does the particle filter perform on synthetic data in an identical twin experiment?

   The particle filter is able to estimate the deformation and source strength values of the three setups of section 5.1.3. This is concluded from the RMSE values of the deformation and source strength and these are around respectively 5.00 mm and 1.0 [-]. The RMSE of 5.00 mm is expected if the particle filter is effectively finding the minimum between observed deformation and modelled deformation. The RMSE and the variance value of the Gaussian noise added to the observed deformation values are both in the same order of 5 mm.

   The amount of ensemble members N is varied for the five test situations that has the Mogi sources at the deformation location with a distance k=1500 m between the deformation locations. The RMSE of the deformation and source strength show similar results for the different N values. The amount of N does not matter for this setting. For this number of Mogi sources at the same deformation locations, the particle filter is able to estimate the source strengths with a small number of ensemble members.

   The particle filter weights plotted versus the ensemble members of the **1 Mogi source = at deformation location** show a clear Gaussian and Lorentz distribution. The **2 Mogi sources = at deformation locations** setup show a non-distinct Gaussian curve shape, caused by the proximity of the two Mogi sources. Their deformations interfere with each other, when the deformation location is at a distance of 1500 m. The posterior source strengths are still close to the true source strength for this setting.

   The usage of N=1000 ensemble members during all the synthetic experiments is sufficient to produce a low RMSE for both parts of the particle filter, the deformation and source strength part. The number of ensemble members, variance of the particle filter and variance of the noise has no influence on the estimated source strength RMSE range of 0.5 to 1.0 [-].

   The iterative resampling experiments results in lowering of the RMSE value and thus a better estimation. The setup with 1 Mogi source and 16 / 256 deformations does not need resampling, while the experiment with multiple Mogi sources at the deformation locations benefits from the resampling. This is caused by the number of parameters (source strengths) that are estimated. A number of parameters > 1 that is estimated benefits from the resampling. This is an important conclusion from the synthetic experiments and this knowledge can be applied to the real Groningen case.

3. Are there limitations of the particle filter?

   The limitation of the particle filter is the number of parameters that needs to be estimated. The larger this number, the more ensemble members are needed for a good estimate, where not one ensemble member obtains all the weight, the highest value of the observational pdf. The choice of the initial start value and variance for generating the ensemble members is important, because it defines the spread of source strength values in the ensemble members. Furthermore, the choice of variance of the observational probability density function in the particle filter is important, since the variance defines the width of the observational pdf. A careful selection of this variance is needed; this will be a process of trial and error taking into account what is known about the actual observational errors.

The sub-questions of the particle filter applied to the real Groningen case with PS-InSAR measurements are:

4. How does the particle filter perform on the PS-InSAR measurements?

   The particle filter performance is only described for the results of the PS-InSAR descending measurements. The particle filter with a Gaussian observational probability density function variance σ^2=144 mm performs well on the PS-InSAR measurements (number of points: 5101). The RMSE of the deformations is 6.0 mm, which is a good result, because this RMSE is the same as the RMSE in all the synthetic experiments of chapter 5. Based on this it can be concluded that the source strength RMSE could be in the order of 0.5 to 1.0 [-], when taking into account the synthetic experiment results.

   The number of ensemble members that obtained a weight (>0) is 2 for a number of N=5000 ensemble members. This number is low; therefore three solutions are designed to improve the estimation of the source strengths, where more ensemble members obtain a weight. A larger number of weighted ensemble members results in better estimation of the source strengths.

   The particle filter with a Gaussian observational probability density function variance σ^2=144 mm is applied as well on second degree polynomial fitted PS-InSAR measurements (number of points: 5101). The RMSE of the deformations is 2.0 mm, which is a good result. The fitted measurements show a smoother deformation that is easier to work with, when tuning the particle filter method to the PS-InSAR measurements. The smooth deformations show easier the regions of overestimation and underestimation in the residual plots of model - observation.

   The particle filter with Gaussian observational pdf is applied on two subsets of the fitted measurements and the same source strengths are estimated as for the whole set of measurements. The number of 2550 points of these subsets are sufficient for estimating the source strengths, although the number of weighted ensemble members with a weight > 0.1 is only 2.

   Three solutions are tested to improve the estimation of the source strengths; these are tested on the fitted PS-InSAR measurements, because the residuals plots are visually better than the unfitted residual plots.

   The first solution is resampling. This resampling improves the deformation estimation RMSE and percentage of the deformation, but not of source strength. The RMSE is 1.90 mm that is an improvement of 0.3 mm and the fit is 96% for a 4 mm threshold. One of the sources has a positive source strength value at location X/Y 257/578 km; this is cluster Scheemderzwaag. The point density is almost zero in this area; this causes probably the positive value, because there are not enough deformation locations. In addition the source at location X/Y 259/577 km, cluster De Eeker, influences the estimation, because the source is only 2.5 km away and their deformations interfere the deformation of cluster Scheemderzwaag. The source strength estimation of this resampling solution is not the wanted outcome, because there are positive source strengths that mean uplift. The particle filter criteria of estimating only negative source strengths is not met for this solution.

   The second solution uses the particle filter estimation of the first run, the particle filter with a Gaussian observational pdf variance σ^2=144 mm, as guiding the start value for generating the prior ensemble members. The RMSE is 1.76 mm; this is an improvement of 0.4 mm compared to the first particle filter run and the fit is improved by 4% and is now 97% for a 4 mm threshold. One of the sources has a positive source strength value at location X/Y 259/577 km, cluster De Eeker. This is a different source than the positive valued source in section 6.2.5 that was cluster Scheemderzwaag. The area is the same, the low point density and the distance of 2.5 km between the sources probably causes the positive estimated source strength. The positive value means that uplift is modelled instead of subsidence. This is an unwanted result. The number of high weighted (>0.1) ensemble members is increased from 2 to 5. This is still a low number.

   The third solution is localisation. The localisation of radius 3000 m is the best estimation compared to the other radius values of 1500, 4500 and 6000 m. This is based on the local computed RMSE values of deformations for each source strength location. The RMSE is 1.74 mm and the fit is 97.3% for a 4 mm threshold. Further more the localisation estimation of radius=3000 m performs better for the single and double well situations and also for the three and more sources surrounding each other. The ensemble members show no longer 1 or 2 ensemble members with a high weight (>0.1). The ensemble members have now obtained equal weights.

The localisation of radius 3000 m is the best estimation and applied to the years 2010 to 2016. The estimated Mogi source strengths show a southeast to northwest trend. This trend could be related to the reservoir thickness variation, but also the groups of Mogi sources their deformations interfere and therefore results in lower source strengths, than the single located Mogi sources.

5. Can a number of Mogi sources at well locations and at a reservoir depth of -3000 m adequately represent subsurface processes?

   The Mogi sources located at a depth of -3000 m have only a limited influence sphere of deformation values at the surface. The number of 25 Mogi sources, where 22 are placed at gas well locations, is enough to represent the subsurface processes. This is based on the deformations RMSE value of 6.0 mm. This RMSE is for the unfitted PS-InSAR measurements. The benefit of placing the Mogi sources at the well locations is that local deformation change can be estimated, which is assumed taking place around the wells during gas production. The Mogi sources placed at the well locations are a physically realistic placement. Although deformations are not modelled, when the radius at the surface around the well locations is larger than 4500 m. A part of the Groningen reservoir in the north is not covered by Mogi sources, as shown in figure 6.5.

6. The hydrocarbon production is lowered in the Loppersum production region after the year 2013 in order to lower the number and magnitude of induced seismic events. Is this change in production visible in the PS-InSAR measurements, for example by showing a decrease in subsidence?

   This change is not visible in the time series deformations of the Loppersum region. There is a continuous subsidence. The deformation over the 2009-2016 period reflects more the reservoir pressure drop of figure 6.26.

7. Is it possible to estimate geomechanical model parameters that model the observed surface deformation? Or is there a missing part in modelling the surface deformation signal?

   It is possible to estimate geomechanical model parameters such as Mogi source strengths from PS-InSAR measurements. The missing part is that there is a limitation of the deformations influence sphrere of the Mogi sources, when placed at a depth of -3000 m. A larger depth of Mogi sources results in a larger the influence sphere, when the source strength is kept the same as for the -3000 m depth.

8. Is there any link between the estimated Mogi source strengths and the hydrocarbon production and / or the change in reservoir pressure?

   There is no link between the estimated Mogi source strengths and the gas production. The Mogi sources show at many wells an increase of source strength that is related to an increase of surface deformation. However there is a link between the estimated Mogi source strengths and the reservoir pressure change of the period 2010 to 2016. The Mogi source strengths increases and the reservoir pressure change increases over the period of 2010 to 2016 compared to the period of 2000 to 2010.

It can be concluded that the particle filter localisation method with radius 3000 m is the best one to estimate a Mogi model setup, when the number of parameters is larger than one and when placed at the well locations in the Groningen reservoir. The number of PS-InSAR measurements dictates the number of ensemble members. Therefore a particle filter applied locally results in lowering the number of observations and thus the number of ensemble members. The lower number of ensemble members decreases the computational time of the particle filter that is a good thing. The preliminary results of applying the particle filter localisation of radius 3000 to the ascending PS-InSAR measurements look promising. In addition it can be concluded that applying the particle filter on other PS-InSAR measurements sets, like the ascending PS-InSAR measurements of chapter 7, needs further analysis, but the preliminary results are promising for future research.

8.1. Recommendations

In future research of applying the particle filter on the Groningen case I have a couple of recommendations for the three main parts: particle filter, geomechanical model and PS-InSAR measurements.

For the particle filter I would recommend to try out the particle filter of eq. (2.13) with the error covariance of the measurements, because the used deformation measurements are now assumed to be uncorrelated.

And those measurements are not uncorrelated, but correlated. Furthermore a recommendation of linking the estimated strengths to the reservoir pressure change can be done. And perhaps a link to gas production can be made.

The Mogi geomechanical model is now applied by using 25 Mogi sources. Future research could increase the amount of Mogi sources, for example at the closed-in well locations of Midwolda, Noordbroek, Nieuw Scheemda and Uiterburen. Also other geomechanical models could be implemented as well, like the Geertsma (1973) model. This model is used by the NAM (2016) and perhaps a comparison can be made with the results of the Mogi model.

Recommendations regarding the PS-InSAR measurements are point selection and other PS-InSAR data sets of different radar satellites. At the moment the high points are used and the assumption is made that the high points are stable man-made structures, built on poles and representing movement of the deep subsurface. The houses in Groningen are not all built on poles, many houses are built on plates. These plates are only three meters deep and move possible along with changes in the groundwater level. An improved selection of points can be done. In addition other PS-InSAR measurement sets could be used for the Mogi source estimation. The preliminary particle filter results on the ascending PS-InSAR measurements in chapter 7 look promising. Further analysis is needed of the estimated source strengths of the subset, for example different subsets could be analysed.

The last recommendation considers the research of Jurjen Kamphuis. This master thesis explores the combination of a GPS station with a corner reflector attached to it. This corner reflector will be detected by the InSAR satellites and will have then a GPS location of that point. The whole set of PS-InSAR measurements can then be made absolute instead of relative. The PS-InSAR measurements used in this thesis are like a blanket of points located above the Groningen region. A GPS location helps the PS-InSAR measurements to be ‘attached’ to the surface, thus absolute.

Bibliography

Allaby, M., editor. 2008. *A Dictionary of Earth Sciences, Third Edition*. Oxford University Press.

Anderson, E.M. The dynamics of the formation of cone-sheets, ring-dykes, and caldron subsidence. *Proceedings of the Royal Society of Edinburgh*, 56:128–157, 1936.

Bishop, C.M. 2006. *Pattern Recognition and Machine Learning*. Springer Science+Business Media, LLC.

Bonafede, M. and Ferrari, C. Analytical models of deformation and residual gravity changes due to a mogi source in a viscoelastic mdedium. *Tectonophysics*, 471:4–13, 2009.

Breunese, J., Mijnlief, H., and Lutgert, J. The life cycle of the Netherlands' natural gas exploration: 40 years after Groningen, where are we now? *Dore, A.G. and Vining, B. A. (eds) Petroleum Geology: North-West Europe and Global Perspectives–Proceedings of the 6th Petroleum Geology Conference*, pages 69–75, 2005.

Candela, T., Osinge, S., van der Veer, E.F., ter Heege, J.H., and Fokker, P.A. Improving reservoir exploitation using fast geomechanical modelling coupled with surface displacement data assimilation. In *SPE Reservoir Characterisation and Simulation Conference and Exhibition*. Society of Petroleum Engineers, 2017.

Cobeldick, S. Colorbrewer: Attractive and distinctive colormaps, 2017. `https://www.mathworks.com/matlabcentral/fileexchange/45208-colorbrewer--attractive-and-distinctive-colormaps?,Accessed:11-04-2017`.

Davis, J.C. 2002. *Statistics and Data Analysis in Geology, Third Edition*. John Wiley and Sons.

De Jager, J. Lecture sheets. In *AES1800 Exploration Geology*. TU Delft, 2014.

De Jager, J. and Geluk, M.C. Petroleum geology. In Wong, Th.E., Batjes, D.A.J., and de Jager, J., editors, *Geology of the Netherlands*. KNAW, 2007.

De Waal, J.A. *On the rate type compaction behaviour of sandstone reservoir rock*. PhD thesis, Technische Hogeschool Delft, 1986.

De Waal, J.A., van Thienen-Visser, K., and Pruiksma, J.P. Rate type isotach compaction of consolidated sandstone. In *49th US Rock Mechanics / Geomechanics Symposium*. American Rock Mechanics Association, 2015.

Emerick, A.A. and Reynolds, A.C. Ensemble smoother with multiple data assimilation. *Computers and Geosciences*, 55:3–15, 2013.

Evensen, G. Sequential data assimilation with a nonlinear quasi-geostropic model using monte-carlo methods to forecast error statistics. *Journal of Geophysical Research*, 99:10143–10162, 1994.

Falkena, W. xml2struct, convert an xml file into matlab structure, 2012. `https://www.mathworks.com/matlabcentral/fileexchange/28518-xml2struct,Accessed:07-03-2018`.

Fokker, P.A. Subsidence prediction and inversion of subsidence data. *SPE/ISRM 78227, SPE/ISRM Rock Mechanics Conference, Irving, Texas*, 2002.

Fokker, P.A. and Orlic, B. Semi-analytic modelling of subsidence. *Mathematical Geology*, 38(5):565–589, 2006.

Fokker, P.A. and Van Thienen-Visser, K. Inversion of double-difference measurements from optical leveling for the groningen gas field. *International Journal of Applied Earth Observation and Geoinformation*, 49: 1–9, 2016.

Fokker, P.A., Wassing, B.B.T., van Leijen, F.J., Hanssen, R.F., and Nieuwland, D.A. Application of an ensemble smoother with multiple data assimilation to the Bergermeer gas field, using PS-InSAR. *Geomechanics for Energy and the Environment*, 5:16–28, 2016. doi: http://dx.doi.org/10.1016/j.gete.2015.11.003.

Fossen, H. 2010. *Structural Geology*. Cambridge University Press.

Geertsma, J. Land Subsidence Above Compacting Oil and Gas Reservoirs. *Journal of Petroleum Technology*, pages 734–744, 1973.

Geertsma, J. and van Opstal, G. A Numerical Technique for Predicting Subsidence Above Compacting Reservoirs, Based on the Nucleus of Strain Concept. *Verh. Koningklijke Nederlandse Geologische Mijnbouwkunding Genootschap*, 28:63–78, 1973.

Hanssen, R.F. 2001. *Radar Interferometry: Data Interpretation and Error Analysis*. Kluwer Academic Publishers, Dordrecht.

Hanssen, R.F. Bodemdaling kennemerland waargenomen met satellietradarinterferometrie. In Barends, F.B.J., Dillingh, D., Hanssen, R.F., and van Onselen, K.I., editors, *Bodemdaling langs de Nederlandse kust, Case Hondsbossche en Pettemer zeewering*. IOS Press, 2008.

Herber, R. Geology of the groningen field. In *The Science behind the Groningen Gas Field, Symposium on seismicitiy induced by gas production from the Groningen Field*, 2018. http://www.kngmg.nl/2018/02/presentaties-van-het-symposium-over-de-wetenschap-van-het-groningen-gasveld/-zijn-beschikbaar/,Accessed:06-03-2018.

Ketelaar, V.B.H. 2009. *Satellite Radar Interferometry, Subsidence Monitoring Techniques*, volume 14 of *Remote Sensing and Digital Image Processing*. Springer Science+Business Media B.V.

Lele, S.P., Garzon, J.L., Hsu, S-Y., Dedontney, N.L., Searles, K.H., and Sanz, P.F. (ExxonMobil Upstream Research Company Spring TX). 2015. Groningen 2015 geomechanical analysis. Technical report, Nederlandse Aardolie Maatschappij B.V.

Li, T., Bolic, M., and Djuric, P.M. Resampling methods for particle filtering, classifictation, implementation, and strategies. *IEEE Signal Processing Magazine*, 32(3):70 – 86, 2015.

Lisowski, M. Analytical volcano deformation source models. In Dzurisin, D., editor, *Volcano Deformation, Geodetic Monitoring Techniques*. Springer-Praxis Books in Geophysical Sciences, 2007.

McTigue, D.F. Elastic stress and deformation near a finite spherical magma body: Resolution of the point source paradox. *Journal of Geophysical Research*, 92(B12):12931–12940, 1987.

Mogi, K. Relations between eruptions of various volcanoes and the deformations of the ground surfaces around them. *Bulletin of the Earthquake Research Institute*, 36:99–134, 1958.

NAM. 2013. Gewijzigd winningsplan groningen. Technical report, Nederlandse Aardolie Maatschappij B.V.

NAM. 2016. Winningsplan Groningen Gasveld 2016. Technical report, Nederlandse Aardolie Maatschappij B.V.

NAM, 2017a. https://nam-feitenencijfers.data-app.nl/geotool/nam.html?layer=bodemdaling,Accessed:13-07-2017.

NAM, 2017b. https://nam-feitenencijfers.data-app.nl/geotool/nam.html?layer=beving,velden,Accessed:25-07-2017.

Nepveu, M., Kroon, I.C., and Fokker, P.A. Hoisting a red flag: An early warning system for exceeding subsidence limits. *Math Geosci*, 42:187–198, 2010.

NGR. Nationaal georegister, hoogspanning bovengronds in nederland, 2018a. http://nationaalgeoregister.nl/geonetwork/srv/dut/catalog.search#/metadata/849bbd25-cd5a-475d-a739-3f9244f26c43?tab=general,Accessed09-05-2018.

NGR. Nationaal georegister, wierden in provincie groningen, 2018b. http://www.nationaalgeoregister.nl/geonetwork/srv/dut/catalog.search#/metadata/435523de-be3b-48e4-8cb7-262c5571819c?tab=relations,Accessed:07-03-2018.

NLOG. Well locations, shapefile: Nlog boorgaten ed 1950 utm 31n 20160130, 2016. http://nlog.nl/bestanden-interactieve-kaart,Accessed:30-01-2016.

NLOG. Pressure data, updated version obtained by shell, 2017a. http://www.nlog.nl/drukgegevens, Accessed:19-04-2017.

NLOG. Gas production data per well, excel file: wellgasproduced 2003 - 2016, 2017b. http://nlog.nl/selectiescherm-productie,Accessed:05-05-2017.

NLOG. Rock salt, 2017c. http://www.nlog.nl/steenzout,Accessed:11-11-2017.

NLOG. Basic information sheets on rock salt (in dutch), 2017d. http://www.nlog.nl/steenzout, Accessed:11-11-2017.

NLOG. Salt production data per well, excel file: wellsaltproduced 2003 - 2016, 2017e. http://nlog.nl/selectiescherm-productie,Accessed:26-10-2017.

NLOG. Zout historie, 2018. http://www.nlog.nl/zout,Accessed:03-05-2018.

Pruiksma, J.P., Bruenese, J.N., van Thienen-Visser, K., and de Waal, J.A. Isotach formulation of the rate type compaction model for sandstone. *International Journal of Rock Mechanics and Mining Sciences*, 78:127–132, 2015.

Samiei-Esfahany, S. *Exploitation of Distributed Scatterers in Synthetic Aperture Radar Interferometry*. PhD thesis, TU Delft, 2017.

Segall, P. 2010. *Earthquake and Volcano Deformation*. Princeton University Press.

SkyGeo. Insar technical background, 2017. https://skygeo.com/insar-technical-background/,Accessed:30-11-2017.

SkyGeo. Insar technical background, 2018. https://skygeo.com/insar-technical-background/,Accessed:11-01-2018.

Van der Marel, H. Conversion of coordinates, rdnaptrans. 2018.

Van Leeuwen, P.J. Review particle filtering in geophysical systems. *Monthly Weather Review*, 137:4089 –4114, 2009.

van Leeuwen, P.J., Cheng, Y., and Reich, S. 2015. *Nonlinear Data Assimilation*, volume 2. Springer.

van Leeuwen, P.J. and. Nonlinear data assimilation in geosciences: an extremely efficient particle filter. *Quaterly Journal of the Royal Meteorological Society*, 136:1991–1999, 2010.

Van Leijen, F.J. 2014. *Persistent Scatterer Interferometry based on geodetic estimation theory*. Publications on Geodesy, Nederlands Centrum voor Geodesie en Geo-informatie.

Van Oeveren, H., Valvatne, P., Geurtsen, L., and van Elk, J. History match of the groningen field dynamic reservoir model to subsidence data and conventional subsurface data. *Netherlands Journal of Geosciences — Geologie en Mijnbouw*, 96(5):47–54, 2017.

Van Thienen-Visser, K., Pruiksma, J.P., and Breunese, J.N. Compaction and subsidence of the groningen gas field in the netherlands. *Proc. IAHS*, 372:367–373, 2015.

Van Zwieten, G.J., 2016. https://github.com/gertjanvanzwieten/halfspace,Accessed:01-10-2016.

Verhagen, A.A. Cie4614 land surveying and civil infrastructure, lecture sheets. TU Delft, 2015.

Vetra-Carvalho, S., van Leeuwen, P.J., Nerger, L., Barth, A., Altaf, U., Brasseur, P., Kirchgessner, P., and Beckers, J-M. State-of-the-art stochastic data assimilation methods for high-dimensional non-gaussian problems. *Tellus: A Dynamic Meteorology and Oceanography*, 70(1), 2018.

Vossepoel, F.C. and van Leeuwen, P.J. Parameter estimation using a particle method: Inferring mixing coefficients from sea level observations. *Monthly Weather Review*, 135, 2007.

Wikle, C.K. and Berliner, L.M. A bayesian tutorial for data assimilation. *Physica B: 230*, pages 1–16, 2007.

Wright, T. Interpreting and modelling interferograms, script to produce simulated interferograms using simple elastic sources for eartquakes, dykes, sills and point pressure changes at magma, 2009.

A

Groningen gas field

A.1. Wells

Table A.1: Groningen producing gas wells 2003-2016, data from NLOG (2016)

Cluster location	Layer	Wellname	Status
Amsweer	Rotliegend	AMR-1,-2,-3,-4,-5-S2,-6,-7,-8,-9,-10,-11,-12-S1	Production well
Bierum	Rotliegend	BIR-1,-2-S1,-3,-4,-5,-6,-7,-8,-9,-10,-11,-12,-13-S2	Production well
Eemskanaal	Rotliegend	EKL-1,-2,-3,-4,-5,-6,-7,-8,-9,-10,-11,-12,-13	Production well
De Eeker 1	Rotliegend	EKR1-1,-2,-3,-4-S1,-5,-6-S1,-7,-8,-9,-10-S1,-11,-12	Production well
De Eeker 2	Rotliegend	EKR2-1,-2,-3,-4,-5,-6,-7,-8,-9,-10	Production well
Froombosch	Rotliegend	FRB-1,-2,-3,-4,-5,-6,-7,-8	Production well
Kooipolder	Rotliegend	KPD-1,-2,-3,-4,-5,-6,-7,-8,-9,-10-S1,-11,-12	Production well
Leermens	Rotliegend	LRM-1,-2,-3,-4,-5,-6,-7,-8,-9,-10,-11	Production well
Overschild	Rotliegend	OVS-1,-2,-3,-4,-5-S1,-6,-7,-8,-9,-10,-11	Production well
Oudeweg	Rotliegend	OWG-1,-2,-3,-4,-5,-6,-7,-8,-9,-10,-11	Production well
De Paauwen	Rotliegend	PAU-2,-3,-4,-5,-6	Production well
Ten Post	Rotliegend	POS-1,-2,-3,-4,-5,-6,-7,-8,-9,-10,-11	Production well
Sappemeer	Rotliegend	SAP-6-S1,-7,-8,-9,-10,-11,-12,-13,-15-S1	Production well
Schaapbulten	Rotliegend	SCB-1,-2,-3,-4,-5,-6,-7,-8,-9,-10,-11	Production well
Siddeburen	Rotliegend	SDB-1,-2,-3,-4,-5,-6,-7,-8-S1,-9,-10,-11	Production well
Slochteren	Rotliegend	SLO-1,-2,-3,-4,-5,-6-S3,-7,-8,-9	Production well
Spitsbergen 1	Rotliegend	SPI1-1,-2,-3,-4,-5,-6,-7,-8,-9,-10	Production well
Spitsbergen 2	Rotliegend	SPI2-1,-2,-3,-4,-5,-6,-7,-8,-9	Production well
Scheemderzwaag 1	Rotliegend	SZW1-1,-2,-3-S1,-4,-5-S2,-6,-7,-8,-9,-10	Production well
Scheemderzwaag 1	Rotliegend	SZW2-1,-2,-3,-4-S3,-5,-6,-7,-8,-9,-10,-11	Production well
Tjuchem	Rotliegend	TJM-1,-2-S2,-3,-4,-5,-6,-7,-8,-9,-10,-11	Production well
Tusschenklappen	Rotliegend	TUS-1,-2,-3,-4-S1,-5,-6,-7,-8,-9,-10	Production well
‘t Zandt	Rotliegend	ZND-1,-2-S1,-3,-4,-5,-6-S1,-7,-8-S2,-9-S1,-10,-11-S2,-12-S2	Production well
Zuiderpolder	Rotliegend	ZPD-1,-2,-3-S3,-4,-5,-6,-7,-8,-9,-10,-11,-12-S1	Production well
Zuiderveen	Rotliegend	ZVN-1,-2,-3-S1,-4,-5,-6,-7,-8,-9,-10,-11,-12,-13	Production well

Table A.2: Groningen closed-in gas wells 2003-2016, data from NLOG (2016)

Cluster location	Layer	Wellname	Status
Midwolda	Rotliegend	MWD-1,-2,-3,-4,-5,-6,-7,-8,-9	Closed-in
Noordbroek	Rotliegend	NBR-1,-2,-3,-4,-5,-6,-7,-8,-9	Closed-in
Nieuw Scheemda	Rotliegend	NWS-1,-2,-3,-4,-5,-6,-7,-8,-9	Closed-in
Uiterburen	Rotliegend	UTB-1,-2,-3,-4,-5,-6,-7,-8,-9,-10	Closed-in

A.2. Gas production

Table A.3: Groningen total gas production per well clusters 2003-2007, data from NLOG (2017b)

Cluster	Region	X RD [m]	Y RD [m]	Depth [m]	2003 Billion [Nm^3]	2004 Billion [Nm^3]	2005 Billion [Nm^3]	2006 Billion [Nm^3]	2007 Billion [Nm^3]
Amsweer	Oost	256298	591517	2972	1.5346	0.8591	0.2204	0.5260	1.3173
Bierum	Oost	254735	599579	2985	2.1980	3.2008	2.7438	2.7184	1.9464
Eemskanaal	Eemskanaal	241584	584521	2934	0.8522	0.1270	0.5792	1.6742	0.6742
De Eeker 1&2	Oost	259669	577338	2813	0.4977	0.2342	0.7671	0.4819	0.6551
Froombosch	Zuidwest	248204	578911	2904	0.8074	0.7586	1.1433	0. 6997	0.5437
Kooipolder	Zuidwest	246704	580929	2910	1.2360	0.3475	0.5853	1.8635	1.3913
Leermens	Loppersum	250083	596956	2966	0.6609	1.0557	2.7686	2.3836	1.9186
Midwolda	Rest	264215	578572	2925	0.5052	0.5780	0.6657	0.5927	0.4145
Noordbroek	Rest	254894	579557	2887	1.1015	1.5185	1.4285	1.1143	0.7813
Nieuw Scheemda	Rest	258927	580067	2823	1.0727	1.9013	1.5912	0.8969	0.7983
Overschild	Loppersum	250508	590804	2975	1.0907	1.0873	2.3322	2.4874	1.9081
Oudeweg	Oost	256082	585760	2952	0.7948	2.6160	2.5528	1.8670	2.0113
De Paauwen	Loppersum	245933	588294	2986	2.6099	2.4078	2.6004	2.5834	2.3071
Ten Post	Loppersum	245664	591275	2973	0.9147	0.8188	2.9620	2.5685	2.1142
Sappemeer	Zuidwest	249482	575413	2936	1.0336	1.4852	1.0215	1.0383	0. 3914
Schaapbulten	Oost	257449	588371	2984	0.8315	2.1452	1.7360	1.0317	0.6472
Siddeburen	Oost	253213	587431	2871	2.2384	2.3835	1.4250	0.9213	0.8310
Slochteren	Zuidwest	246381	579259	2857	1.0916	1.2554	0.6227	0.5517	0.4549
Spitsbergen 1&2	Zuidwest	252398	577196	2811	1.0917	1.6303	1.0346	0.7447	1.5232
Scheemder-zwaag 1&2	Oost	257318	578169	2993	0.6491	1.7734	0.5027	0.6044	0.5537
Tjuchem	Oost	254955	588269	2958	2.1908	2.8526	2.2903	1.7411	1.4927
Tusschenklappen	Zuidwest	254366	575209	2877	0	0	0	0.0013	0.0001
Uiterburen	Rest	255173	577423	2620	0.6607	0.7390	0.7400	0.6385	0.5630
‘t Zandt	Loppersum	248035	600511	2954	2.3065	0.8379	0. 8641	2.4354	1.7646
Zuiderpolder	Oost	261906	580858	2927	0.4691	1.5902	0.4465	0.5311	0.5754
Zuiderveen	Zuidwest	253141	579267	2887	0.5996	0.2265	0.1575	0.5065	1.3246

Table A.4: Groningen total gas production per well cluster for 2008-2016, data from NLOG (2017b)

Cluster	2008 Billion [Nm^3]	2009 Billion [Nm^3]	2010 Billion [Nm^3]	2011 Billion [Nm^3]	2012 Billion [Nm^3]	2013 Billion [Nm^3]	2014 Billion [Nm^3]	2015 Billion [Nm^3]	2016 Billion [Nm^3]
Amsweer	1.8764	1.8184	2.5730	2.3611	1.8458	2.9766	3.0349	2.1622	2.4436
Bierum	2.9001	1.9979	3.2588	3.3059	3.0791	2.8582	4.0170	1.5087	2.2777
Eemskanaal	1.4843	1.2993	2.3876	1.6194	1.6927	2.5445	2.0922	1.1356	0.9002
De Eeker 1&2	0.8416	0.8597	1.2909	1.0475	0.9660	1.5047	1.7458	2.0094	1.7182
Froombosch	1.4753	0.6293	1.7223	1.3331	1.4567	1.4738	1.6790	0.9224	1.1178
Kooipolder	2.4002	2.2851	2.7393	2.0631	2.2542	2.8267	3.1717	2.2559	0.8976
Leermens	2.6584	2.6210	2.4940	3.1605	2.9931	3.1859	0.5716	0.2555	0.3084
Midwolda	0.6444	0.3164	0	0	0	0	0	0	0
Noordbroek	1.5003	0.3273	0	0	0	0	0	0	0
Nieuw Scheemda	0.4323	0	0	0	0	0	0	0	0
Overschild	2.8347	2.7458	2.6400	3.0854	2.8431	3.3278	0.6195	0.3153	0.1414
Oudeweg	2.3409	2.0584	2.9500	2.7443	2.8879	2.9150	2.7221	1.5945	2.2271
De Paauwen	2.2852	2.7759	2.7742	3.0329	3.2523	3.3351	0.2793	0.2327	0.0004
Ten Post	2.9985	2.7978	2.8820	3.4350	3.2810	3.6478	0.6035	0.5511	0.2010
Sappemeer	0	0.3542	1.7130	1.0463	0.9483	1.2405	1.5100	1.0762	0.9078
Schaapbulten	2.4311	2.1488	2.8410	2.7288	2.8420	1.2615	1.7034	1.6556	1.8519
Siddeburen	1.0735	2.1026	2.9040	2.8295	3.2374	3.0504	3.1801	2.3217	2.3069
Slochteren	0.2355	0.4902	1.3364	1.1933	1.2047	1.3611	1.4586	0.7215	1.1258
Spitsbergen 1&2	2.0767	1.6218	2.5312	1.7722	1.8602	2.8149	2.2857	1.6404	1.3305
Scheemder-zwaag 1&2	0.8051	0.7908	1.5083	1.0869	1.1093	1.4455	2.1160	1.9762	1.6889
Tjuchem	1.9372	1.9662	2.3328	2.6969	2.7831	2.7224	2.9849	2.0161	1.5756
Tusschenklappen	0.7311	1.3955	1.0443	0.9408	1.0595	1.2549	1.4297	0.8200	0.8730
Uiterburen	0.4585	0	0	0	0	0	0	0	0
‘t Zandt	2.6880	2.1364	2.9652	2.5870	3.0212	3.7224	0.5132	0.3043	0.3554
Zuiderpolder	0.5311	1.0276	2.5229	1.6691	2.05303	2.7797	2.6519	1.9142	2.1544
Zuiderveen	0.9024	1.1030	1.4468	1.0396	1.1017	1.9130	2.0376	0.7126	1.1887

Table A.5: Groningen total gas production per region for 2003-2008, data from NLOG (2017b)

Region	2003 Billion [Nm^3]	2004 Billion [Nm^3]	2005 Billion [Nm^3]	2006 Billion [Nm^3]	2007 Billion [Nm^3]	2008 Billion [Nm^3]
Eemskanaal	0.8522	0.1270	0.5792	1.6742	0.6742	1.4843
Loppersum	7.5829	6.2078	11.5276	12.4584	10.0128	13.4650
Oost	11.4045	16.0594	12.6848	10.4234	10.0305	15.3966
Zuidwest	5.8601	5.7038	4.5652	5.4060	5.6294	7.8214
Rest	3.3402	4.7369	4.4256	3.2427	2.5573	3.03570
Total	29.0401	32.8351	33.7826	33.2050	28.9043	41.2032

Table A.6: Groningen total gas production per region for 2009-2016, data from NLOG (2017b)

Region	2009 Billion [Nm^3]	2010 Billion [Nm^3]	2011 Billion [Nm^3]	2012 Billion [Nm^3]	2013 Billion [Nm^3]	2014 Billion [Nm^3]	2015 Billion [Nm^3]	2016 Billion [Nm^3]
Eemskanaal	1.2993	2.3876	1.6194	1.6927	2.5445	2.0922	1.1356	0.9002
Loppersum	13.0771	13.7556	15.3010	15.3909	17.2192	2.5874	1.6590	1.0063
Oost	14.7707	22.1821	20.4704	20.8041	21.5145	24.1566	17.1588	18.2447
Zuidwest	7.8794	12.5335	9.3887	9.8857	12.8852	13.5725	8.1493	7.4414
Rest	0.6437	0	0	0	0	0	0	0
Total	37.6705	50.8590	46.7796	47.7735	54.1636	42.4088	28.1028	27.5926

A.3. Salt production

Table A.7: Groningen total salt production per region for 2003-2008, data from NLOG (2017e)

Region	Lon RD [m]	Lat RD [m]	Depth [m]	2003 [Tonnes]	2004 [Tonnes]	2005 [Tonnes]	2006 [Tonnes]	2007 [Tonnes]	2008 [Tonnes]
Veendam	251633	571181	1833	0	0	47.1120	297.952	288.235	289.3727
Winschoten	263410	574362	1624	0	0	101.843	1279.4070	1213.428	1233.999
Zuidwending	258560	567561	1506	0	0	130.34	1336.06	1252.523	1411.800
Total	-	-	-	0	0	279.295	2913.425	2754.186	2935.171

Table A.8: Groningen total salt production per region for 2009-2016, data from NLOG (2017e)

Region	2009 [Tonnes]	2010 [Tonnes]	2011 [Tonnes]	2012 [Tonnes]	2013 [Tonnes]	2014 [Tonnes]	2015 [Tonnes]	2016 [Tonnes]
Veendam	172.986	273.7630	295.4420	289.5200	234.708	260.295	267.892	273.9420
Winschoten	1206.26	731.84	1166.91	1158.39	1289.770	1239.509	1379.578	1394.452
Zuidwending	1153.501	1282.944	1492.39	1534.219	1497.081	1467.83	1508.377	1626.59
Total	2532.74	2288.547	2954.747	2982.13	3021.566	2967.634	3155.84	3294.99

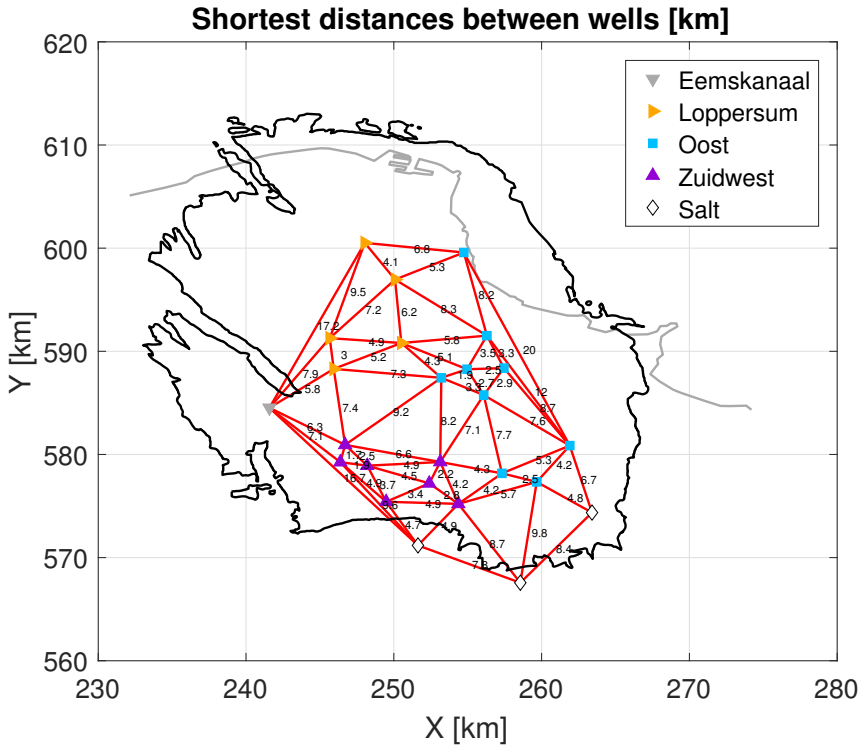

Figure A.1: Shortest distances [km] between the gas and salt wells. Black outline is the Groningen field and the grey line the coast.

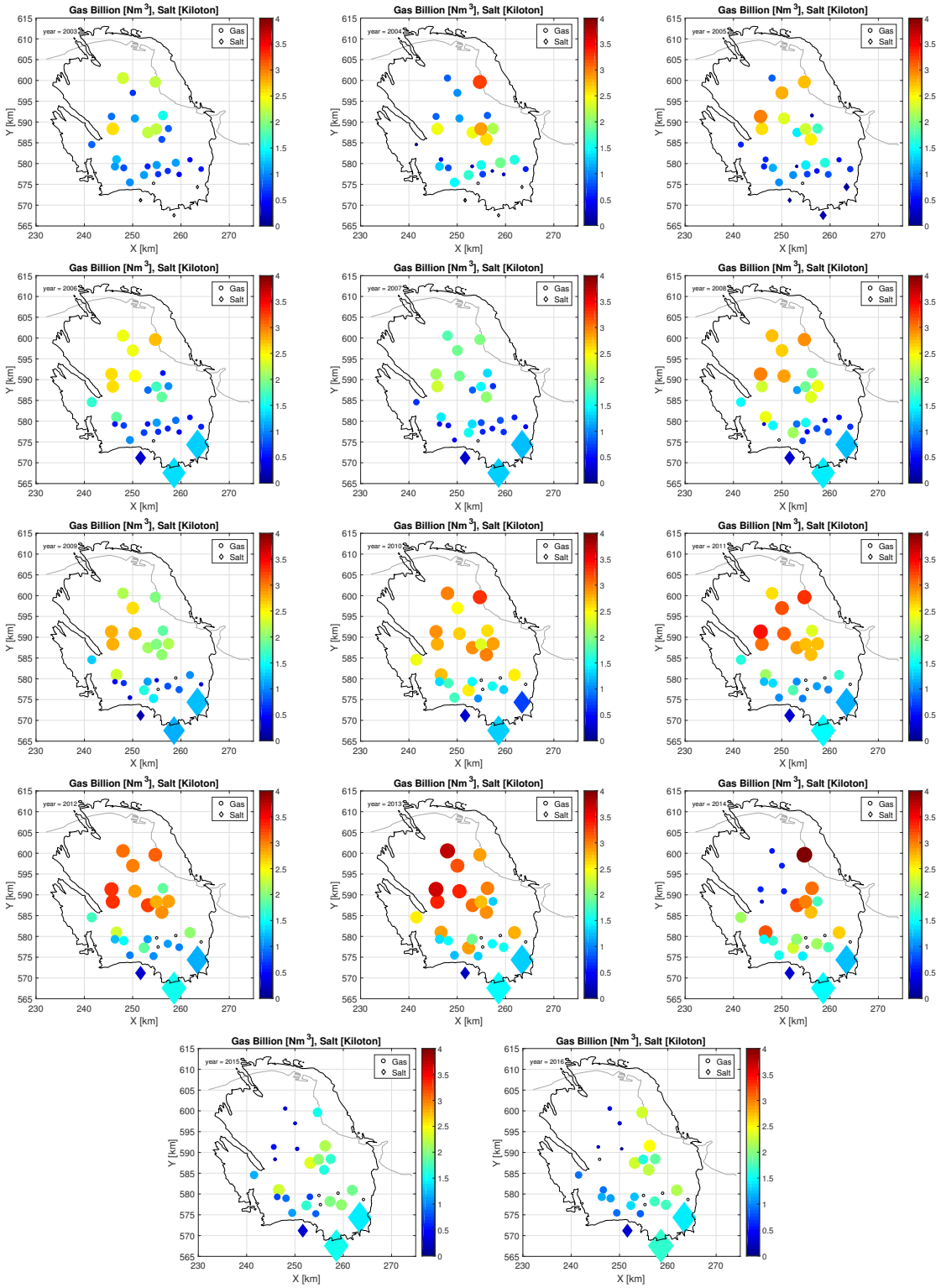

Figure A.2: Visualisation of gas data on the production locations, gas is in normal cubic meters Nm^3. Diamond square is the salt production (salt is in tonnes).

B

Subsurface model

B.1. Mogi, point source model

Mogi model of Van Zwieten (2016).
The input of the Mogi model are the coordinates of the Mogi source location and depth and coordinates of the surface grid and depth; Poisson's ratio v; LOS vector and source strength.

$$\begin{pmatrix} x_{\text{mogi}} \\ y_{\text{mogi}} \\ z_{\text{mogi}} \end{pmatrix}, \begin{pmatrix} x_1 \\ y_1 \\ z_1 \end{pmatrix}, v, \begin{pmatrix} d_e \\ d_n \\ d_u \end{pmatrix}, \text{source strength} \tag{B.1}$$

The difference in distance between the Mogi location and the surface grid location is computed:

$$\begin{pmatrix} \Delta x \\ \Delta y \\ \Delta z \end{pmatrix} = \begin{pmatrix} x_1 - x_{\text{mogi}} \\ y_1 - y_{\text{mogi}} \\ z_1 - z_{\text{mogi}} \end{pmatrix} \tag{B.2}$$

The radial distance R from the centre of the point source to a point at the surface is as follows:

$$R = \sqrt{\Delta x^2 + \Delta y^2 + \Delta z^2} \tag{B.3}$$

The radial distance divided by the surface coordinates:

$$\begin{pmatrix} \text{uA\_x} \\ \text{uA\_y} \\ \text{uA\_z} \end{pmatrix} = -\begin{pmatrix} \frac{\Delta x}{R^3} \\ \frac{\Delta y}{R^3} \\ \frac{\Delta z}{R^3} \end{pmatrix} \tag{B.4}$$

The difference of the image source:

$$\begin{pmatrix} \Delta x \\ \Delta y \\ \Delta z_2 \end{pmatrix} = \begin{pmatrix} x_1 - x_{\text{mogi}} \\ y_1 - y_{\text{mogi}} \\ \Delta z - 2z_1 \end{pmatrix} \tag{B.5}$$

The radial distance R^* from the image source:

$$R^* = \sqrt{\Delta x^2 + \Delta y^2 + \Delta z_2^2}, \tag{B.6}$$

where $d_2 = d - 2z$. The radial distance of the image source divided by the surface coordinates:

$$\begin{pmatrix} \text{uA}_x \\ \text{uA}_y \\ \text{uA}_z \end{pmatrix} = -\begin{pmatrix} \frac{\Delta x}{R^{*3}} \\ \frac{\Delta y}{R^{*3}} \\ \frac{\Delta z_2}{R^{*3}} \end{pmatrix} \tag{B.7}$$

The following steps are probably after Bonafede and Ferrari (2009); McTigue (1987); Segall (2010):

$$\begin{pmatrix} \text{uC}_x \\ \text{uC}_y \\ \text{uC}_z \end{pmatrix} = 6 \cdot \begin{pmatrix} \Delta x \\ \Delta y \\ \Delta z_2 \end{pmatrix} \frac{\Delta z_2}{R^{*5}} \tag{B.8}$$

$$\mathrm{uC}_z = \text{-}\mathrm{uC}_z + \frac{2}{R^{*3}} \tag{B.9}$$

$$\begin{pmatrix} u_x \\ u_y \\ u_z \end{pmatrix} = \begin{pmatrix} \mathrm{uA}_x \\ \mathrm{uA}_y \\ \mathrm{uA}_z \end{pmatrix} - \begin{pmatrix} \mathrm{uA}_{-x} \\ \mathrm{uA}_{-y} \\ \mathrm{uA}_{-z} \end{pmatrix} + z_1 \, \mathrm{uC} \frac{\nu}{1-\nu} \tag{B.10}$$

$$\begin{pmatrix} u_x \\ u_y \\ u_z \end{pmatrix} = \begin{pmatrix} u_x \\ u_y \\ u_z \end{pmatrix} - \begin{pmatrix} \mathrm{uA}_x \\ \mathrm{uA}_y \\ \mathrm{uA}_z \end{pmatrix} 1 - 2\nu \tag{B.11}$$

The displacement is in the x-, y-, and z-direction. The PS-InSAR values are displacements in the line-of-sight (LOS) of the satellite. The LOS vector is used to correct the height displacements with the dot product:

$$D_{\mathrm{LOS}} = \begin{pmatrix} u_x \\ u_y \\ u_z \end{pmatrix} \cdot \begin{pmatrix} d_e \\ d_n \\ d_u \end{pmatrix} \tag{B.12}$$

The source strength is used to scale the deformation D_{LOS}:

$$H = D_{\mathrm{LOS}} \cdot \text{source strength} \tag{B.13}$$

C

Particle filter PS-InSAR estimated source strength results

C.0.1. Overview particle filter results 2010

RMSE and percentage of fit of all the particle filter results.

Table C.1: RMSE of 2010, res.=residuals, SV=start value, loc.=localisation

Section		Particle filter σ^2 [mm]	RMSE [mm] Total field	RMSE [mm] Buffer radius=4500 [m]
6.2.3	Unfitted	144	6.07	6.01
6.2.3	Fitted	144	2.18	2.24
6.2.4	Fitted subet 1	144	2.15	2.21
6.2.4	Fitted subset 2	144	2.21	2.26
6.2.5	Fitted res.	100	1.94	1.89
6.2.5	Fitted res. res.	64	1.80	1.69
6.2.6	Fitted SV	100	1.74	1.58
6.2.6	Fitted SV SV	64	1.69	1.53
6.2.7	loc. 1500 m	100	1.82	1.70
-	loc. 1500 m	64	1.76	-
-	loc. 1500 m	49	1.76	-
-	loc. 1500 m	36	1.76	-
-	loc. 3000 m	100	1.74	1.59
6.2.7	loc. 4500 m	100	1.69	1.52
-	loc. 6000 m	100	1.71	1.56

Table C.2: Percentage of fit, for a couple of thresholds for 2010

Section			**Percentage % total field**				% **buffer radius=4500**			
		σ^2 [mm]	2mm	4mm	8mm	12mm	2mm	4mm	8mm	12mm
6.2.3	Unfitted	144	32.58	57.14	83.98	94.11	33.20	57.49	83.88	94.35
6.2.3	Fitted	144	66.04	93.02	99.72	99.98	66.58	91.85	99.81	100
6.2.4	Fitted subset 1	144	67.81	93.37	99.80	99.96	65.61	92.61	99.93	100
6.2.4	Fitted subset 2	144	67.72	93.09	99.64	100	66.64	91.75	99.69	100
6.2.5	Fitted res.	100	72.71	96.04	99.78	99.98	72.56	96.33	99.90	100
6.2.5	Fitted res.res.	64	77.06	96.76	99.78	99.98	78.66	97.34	99.90	100
6.2.6	Fitted SV	100	78.55	97.17	99.78	99.98	81.23	98.01	99.90	100
6.2.6	Fitted SVSV	64	80.35	97.45	99.80	100	83.61	98.16	99.93	100
-	loc. 1500 m	100	76.49	96.51	99.78	99.98	78.33	97.07	99.90	100
-	loc. 1500 m	64	77.92	97.05	99.78	99.98	-	-	-	-
-	loc. 1500 m	49	78.06	97.39	99.80	99.98	-	-	-	-
-	loc. 1500 m	36	77.55	97.43	99.80	99.98	-	-	-	-
6.2.7	loc. 3000 m	100	78.47	97.35	99.80	99.98	81.08	98.07	99.93	100
6.2.7	loc. 3000 m unfit	100	34.38	59.30	85.14	94.21	35.85	60.23	85.32	94.50
-	loc. 4500 m	100	80.06	97.52	99.80	100	83.21	98.38	99.93	100
-	loc. 6000 m	100	79.92	97.31	99.76	100	83.09	98.13	99.87	100

C.1. Estimated source strengths of 2010 for different methods

Table C.3: Groningen estimated source strength values for each well cluster for 2010 measurements with the Gaussian particle filter. Sol.=solution.

Section					6.2.3	6.2.3	6.2.4	6.2.4
Cluster	Region	X RD [m]	Y RD [m]	Depth [m]	Unfitted Step 1-2 [-]	Fitted Step 1-2 [-]	Fitted Subset 12 [-]	Fitted Subset 22 [-]
Amsweer	Oost	256298	591517	3000	-0.6287	-0.7796	-0.6534	-0.8041
Bierum	Oost	254735	599579	3000	-0.7775	-0.5952	-0.5572	-0.5978
Eemskanaal	Eemskanaal	241584	584521	3000	-1.5647	-0.8565	-1.1380	-0.7952
De Eeker 1&2	Oost	259669	577338	3000	-0.5040	-0.6554	-0.6430	-0.6607
Froombosch	Zuidwest	248204	578911	3000	-0.7035	-0.6594	-0.5106	-0.6959
Kooipolder	Zuidwest	246704	580929	3000	-0.3051	-0.3912	-0.41307	-0.3841
Leermens	Loppersum	250083	596956	3000	-1.1082	-1.1485	-1.1051	-1.1595
Overschild	Loppersum	250508	590804	3000	-0.9994	-1.0798	-1.2223	-1.0465
Oudeweg	Oost	256082	585760	3000	-0.1543	-0.6526	-0.4410	-0.6890
De Paauwen	Loppersum	245933	588294	3000	-0.9469	-0.7099	-0.6437	-0.7236
Ten Post	Loppersum	245664	591275	3000	-1.1428	-1.2887	-1.1244	-1.3224
Sappemeer	Zuidwest	249482	575413	3000	-0.8037	-0.2262	-0.4046	-0.1922
Schaapbulten	Oost	257449	588371	3000	-1.0851	-1.3382	-1.4322	-1.3089
Siddeburen	Oost	253213	587431	3000	-0.4744	-0.7020	-0.6447	-0.7159
Slochteren	Zuidwest	246381	579259	3000	-0.9173	-1.2594	-1.1318	-1.2792
Spitsbergen 1&2	Zuidwest	252398	577196	3000	-0.4839	-0.2555	-0.3772	-0.2325
Scheemder-zwaag 1&2	Oost	257318	578169	3000	-0.0931	-0.4831	-0.1262	-0.5536
Tjuchem	Oost	254955	588269	3000	-0.8409	-0.2291	-0.4237	-0.2028
Tusschenklappen	Zuidwest	254366	575209	3000	-0.6720	-0.3745	-0.8310	-0.2846
‘t Zandt	Loppersum	248035	600511	3000	-1.1579	-1.0608	-1.0583	-1.0632
Zuiderpolder	Oost	261906	580858	3000	-1.0309	-0.8696	-0.8087	-0.8820
Zuiderveen	Zuidwest	253141	579267	3000	-0.4957	-0.2623	-0.3039	-0.2583
Veendam	Salt	251633	571181	1833	-0.7532	-0.8871	-0.8088	-0.8991
Winschoten	Salt	263410	574362	1624	-0.0584	-0.0485	-0.0714	-0.0429
Zuidwending	Salt	258560	567561	1506	-0.1141	-0.2962	-0.3734	-0.2781

Table C.4: Groningen estimated source strength values for each well cluster for 2010 measurements with the Gaussian particle filter. Sol.=solution and loc.=localisation

Section					6.2.5	6.2.6	6.2.7	6.2.7
Cluster	Region	X RD [m]	Y RD [m]	Depth [m]	Fitted Sol.I [-]	Fitted Sol.II [-]	Fitted Sol.III loc.1500 m [-]	Fitted Sol.III loc.3000 m [-]
Amsweer	Oost	256298	591517	3000	-0.5231	-0.7173	-0.4945	-0.4018
Bierum	Oost	254735	599579	3000	-0.5886	-0.8124	-0.7440	-0.7767
Eemskanaal	Eemskanaal	241584	584521	3000	-1.2577	-1.1970	-1.0561	-1.1258
De Eeker 1&2	Oost	259669	577338	3000	-0.5430	0.3200	0.2208	0.0231
Froombosch	Zuidwest	248204	578911	3000	-0.3348	-0.3959	-0.5657	-0.3258
Kooipolder	Zuidwest	246704	580929	3000	-0.3644	-0.1891	-0.8325	-0.5466
Leermens	Loppersum	250083	596956	3000	-1.0358	-0.7519	-0.9356	-0.9228
Overschild	Loppersum	250508	590804	3000	-1.2031	-0.9243	-0.9758	-0.8539
Oudeweg	Oost	256082	585760	3000	-0.3398	-0.4073	-0.3396	-0.2206
De Paauwen	Loppersum	245933	588294	3000	-0.5132	-1.0594	-0.9875	-0.9868
Ten Post	Loppersum	245664	591275	3000	-1.0339	-1.1494	-1.1421	-1.1946
Sappemeer	Zuidwest	249482	575413	3000	-0.3527	0.0394	-0.2264	-0.2132
Schaapbulten	Oost	257449	588371	3000	-1.3471	-0.7864	-0.8818	-0.4473
Siddeburen	Oost	253213	587431	3000	-0.5620	-0.4164	-0.6118	-0.2297
Slochteren	Zuidwest	246381	579259	3000	-0.9897	-0.7561	-0.5135	-0.5680
Spitsbergen 1&2	Zuidwest	252398	577196	3000	-0.3152	-0.1872	-0.0415	-0.1235
Scheemder-zwaag 1&2	Oost	257318	578169	3000	0.1513	-0.4952	-0.6082	-0.1787
Tjuchem	Oost	254955	588269	3000	-0.2582	-0.4334	-0.6976	-0.3975
Tusschenklappen	Zuidwest	254366	575209	3000	-1.0502	-0.0982	-0.3161	-0.2457
‘t Zandt	Loppersum	248035	600511	3000	-1.1410	-1.1559	-0.9956	-1.1622
Zuiderpolder	Oost	261906	580858	3000	-0.5492	-0.7186	-0.3827	0.0613
Zuiderveen	Zuidwest	253141	579267	3000	-0.1317	-0.2976	-0.2216	-0.1044
Veendam	Salt	251633	571181	1833	-0.7820	-0.9072	-0.5701	-0.5984
Winschoten	Salt	263410	574362	1624	-0.0664	-0.0875	-0.0321	-0.0532
Zuidwending	Salt	258560	567561	1506	-0.3354	-0.1295	-0.0663	-0.0633

C.2. Particle filter results source strength

Table C.5: RMSE [mm] 2010-2016, Total field, res.=residuals, SV=start value, loc.=localisation

Section		2010	2011	2012	2013	2014	2015	2016
-	Unfitted loc. 3000 m	5.90	4.98	4.88	4.86	4.51	4.96	4.61
-	Fitted loc. 3000 m	1.74	1.95	2.04	2.32	2.66	3.04	3.21

Table C.6: Groningen estimated source strength values for each well cluster for 2010-2013 data with the Gaussian localisation radius 3000 m particle filter applied to unfitted measurements.

Section					6.2.9	6.2.9	6.2.9	6.2.9
Cluster	Region	X RD [m]	Y RD [m]	Depth [m]	2010 [-]	2011 [-]	2012 [-]	2013 [-]
Amsweer	Oost	256298	591517	3000	-0.1624	-0.4093	-0.5805	-0.2975
Bierum	Oost	254735	599579	3000	-0.9416	-0.9106	-0.4775	-0.9217
Eemskanaal	Eemskanaal	241584	584521	3000	-1.3784	-1.3503	-1.0532	-1.3168
De Eeker 1&2	Oost	259669	577338	3000	0.1477	0.1831	0.5372	-0.1087
Froombosch	Zuidwest	248204	578911	3000	-0.3987	-0.5204	-0.2610	-0.5761
Kooipolder	Zuidwest	246704	580929	3000	-0.6855	-0.5808	-0.4848	-0.7248
Leermens	Loppersum	250083	596956	3000	-0.8797	-1.0041	-0.8476	-1.0154
Overschild	Loppersum	250508	590804	3000	-1.0227	-0.7354	-0.9802	-0.6197
Oudeweg	Oost	256082	585760	3000	-0.3705	-0.3340	-0.0941	-0.1955
De Paauwen	Loppersum	245933	588294	3000	-1.1224	-1.1548	-0.9393	-1.0071
Ten Post	Loppersum	245664	591275	3000	-1.1256	-1.3349	-1.1190	-1.3655
Sappemeer	Zuidwest	249482	575413	3000	-0.4328	-0.1221	-0.0922	-0.4830
Schaapbulten	Oost	257449	588371	3000	-0.4758	-0.4890	-0.4369	-0.5248
Siddeburen	Oost	253213	587431	3000	-0.2539	-0.3727	-0.2978	-0.4172
Slochteren	Zuidwest	246381	579259	3000	-0.4918	-0.8365	-0.5437	-1.0105
Spitsbergen 1&2	Zuidwest	252398	577196	3000	-0.2248	-0.1327	-0.1491	-0.0929
Scheemder-zwaag 1&2	Oost	257318	578169	3000	0.0263	-0.3943	-0.3329	-0.4062
Tjuchem	Oost	254955	588269	3000	-0.6091	-0.3949	-0.2837	-0.5220
Tusschenklappen	Zuidwest	254366	575209	3000	-0.3036	-0.4795	-0.3746	-0.4746
‘t Zandt	Loppersum	248035	600511	3000	-1.5074	-1.3932	-0.9628	-1.4950
Zuiderpolder	Oost	261906	580858	3000	-0.1941	0.0431	-0.0833	-0.0349
Zuiderveen	Zuidwest	253141	579267	3000	-0.1585	-0.4502	0.0613	-0.3612
Veendam	Salt	251633	571181	1833	-0.5593	-0.6227	-0.6000	-0.6081
Winschoten	Salt	263410	574362	1624	0.0395	-0.1402	-0.0217	-0.1835
Zuidwending	Salt	258560	567561	1506	0.0412	-0.1055	-0.1028	-0.1703

Table C.7: Groningen estimated source strength values for each well cluster for 2014-2016 data with the Gaussian localisation radius 3000 m particle filter applied to unfitted measurements.

Section Cluster	Region	X RD [m]	Y RD [m]	Depth [m]	6.2.9 2014 [-]	6.2.9 2015 [-]	6.2.9 2016 [-]
Amsweer	Oost	256298	591517	3000	-0.4360	-0.2372	-0.1893
Bierum	Oost	254735	599579	3000	-0.9037	-0.6432	-0.8785
Eemskanaal	Eemskanaal	241584	584521	3000	-1.2405	-1.5713	-1.6052
De Eeker 1&2	Oost	259669	577338	3000	0.4402	-0.3864	0.0319
Froombosch	Zuidwest	248204	578911	3000	-0.5531	-0.5627	-0.6263
Kooipolder	Zuidwest	246704	580929	3000	-0.7816	-0.6245	-0.8047
Leermens	Loppersum	250083	596956	3000	-0.8622	-0.7618	-0.9099
Overschild	Loppersum	250508	590804	3000	-0.7523	-0.7787	-0.5802
Oudeweg	Oost	256082	585760	3000	-0.3069	-0.3511	-0.4450
De Paauwen	Loppersum	245933	588294	3000	-1.1440	-1.0287	-1.1058
Ten Post	Loppersum	245664	591275	3000	-1.2556	-1.2214	-1.2554
Sappemeer	Zuidwest	249482	575413	3000	-0.4512	-0.3305	-0.3434
Schaapbulten	Oost	257449	588371	3000	-0.5749	-0.6193	-0.7078
Siddeburen	Oost	253213	587431	3000	-0.3207	-0.4363	-0.4651
Slochteren	Zuidwest	246381	579259	3000	-0.8633	-1.0856	-0.9357
Spitsbergen 1&2	Zuidwest	252398	577196	3000	-0.1358	-0.1300	-0.4775
Scheemder-zwaag 1&2	Oost	257318	578169	3000	-0.3822	-0.3844	-0.4256
Tjuchem	Oost	254955	588269	3000	-0.2489	-0.3605	-0.4134
Tusschenklappen	Zuidwest	254366	575209	3000	-0.4866	-0.6506	-0.4954
‘t Zandt	Loppersum	248035	600511	3000	-1.5361	-1.4209	-1.3276
Zuiderpolder	Oost	261906	580858	3000	-0.3143	-0.4251	-0.3190
Zuiderveen	Zuidwest	253141	579267	3000	-0.1454	-0.5282	-0.3910
Veendam	Salt	251633	571181	1833	-0.4309	-0.6768	-0.4175
Winschoten	Salt	263410	574362	1624	-0.0076	-0.1753	-0.1732
Zuidwending	Salt	258560	567561	1506	-0.0790	-0.0166	-0.0723

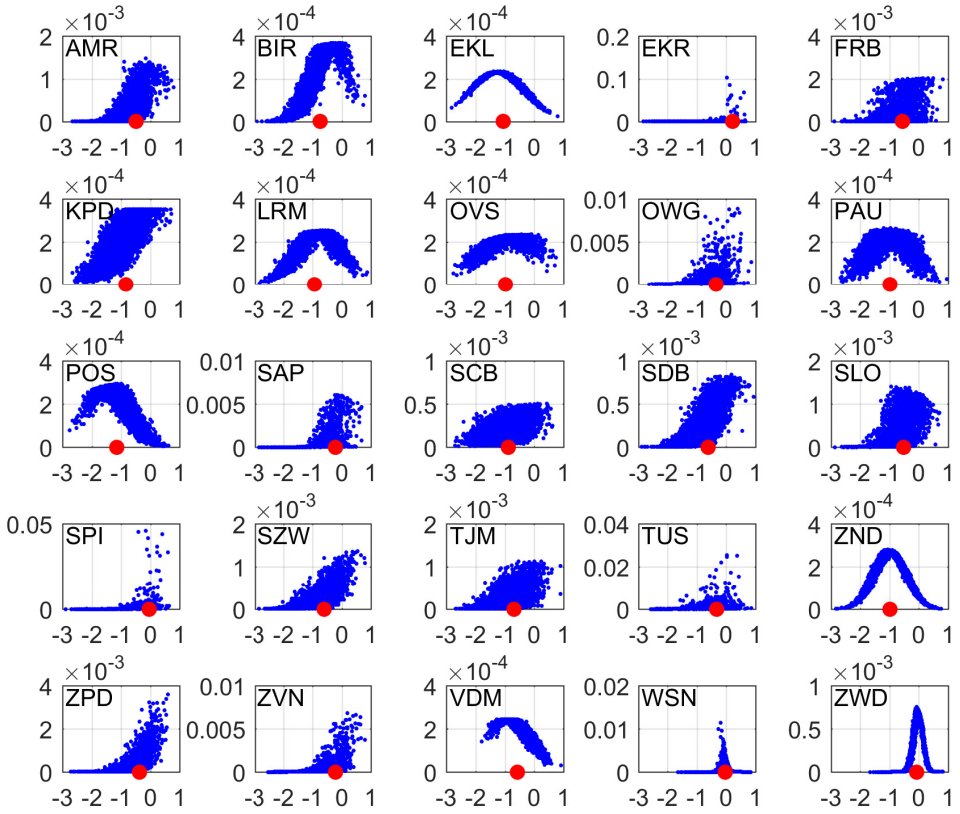

Figure C.1: Particles vs. particle filter weight for well each well, localisation of radius=1500 m. Blue=prior particles and red=estimated posterior source strength.

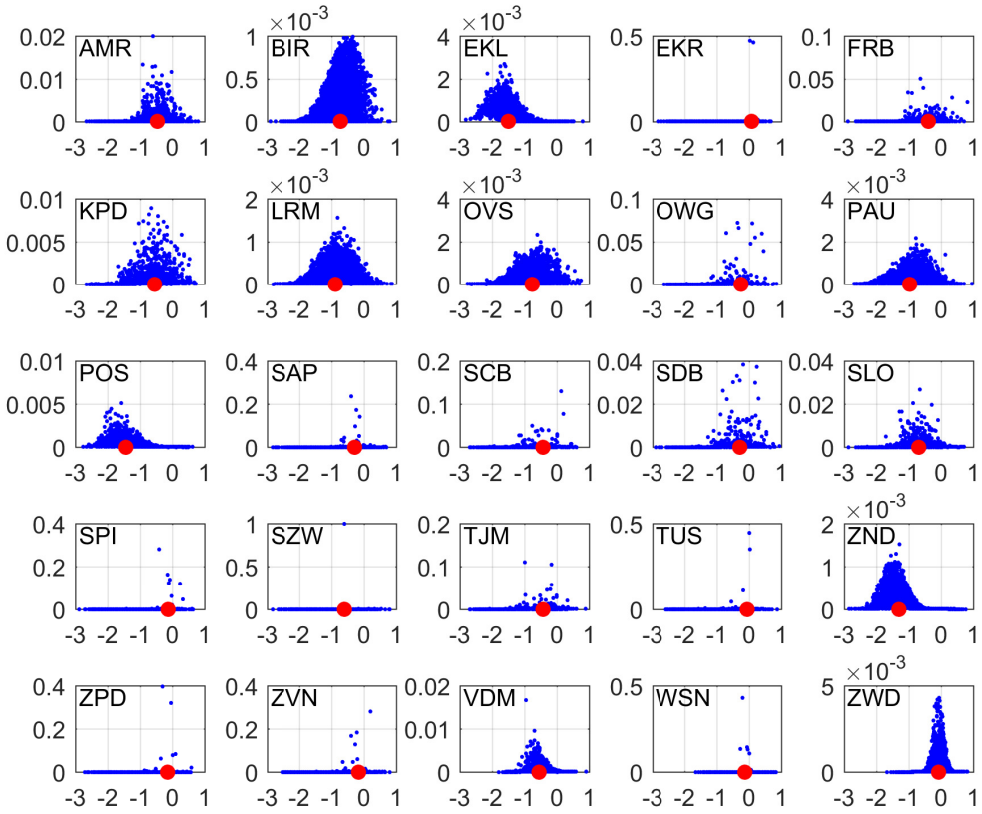

Figure C.2: Particles vs. particle filter weight for well each well, localisation of radius=4500 m. Blue=prior particles and red=estimated posterior source strength.

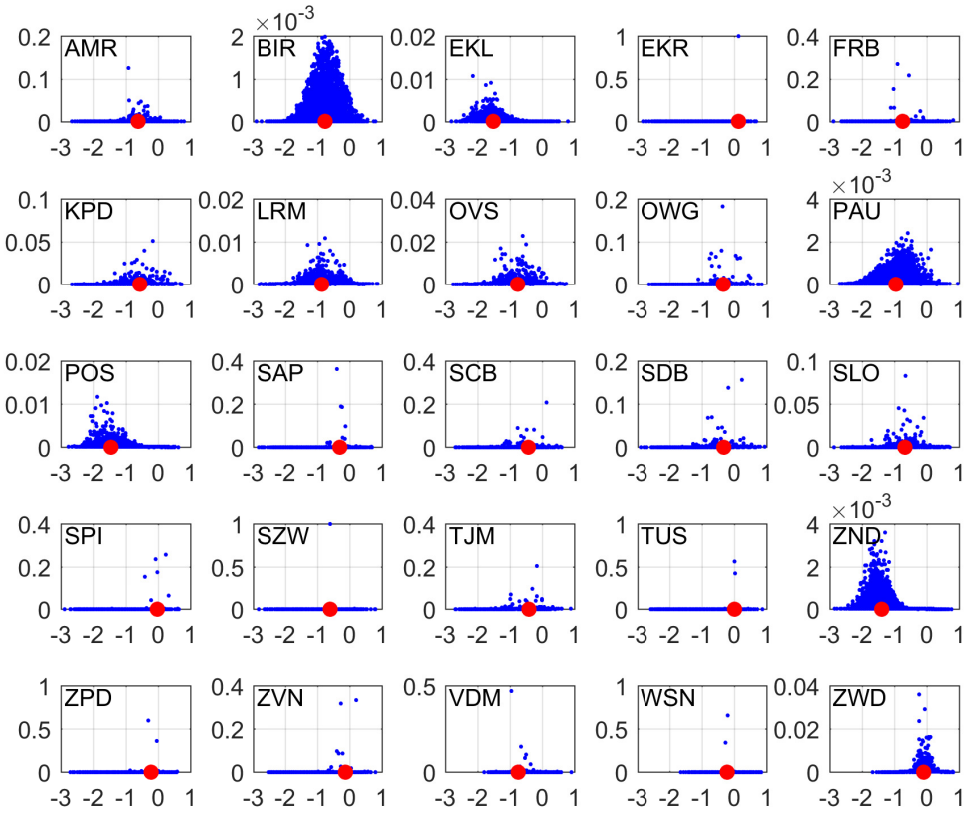

Figure C.3: Particles vs. particle filter weight for well each well, localisation of radius=6000 m. Blue=prior particles and red=estimated posterior source strength.

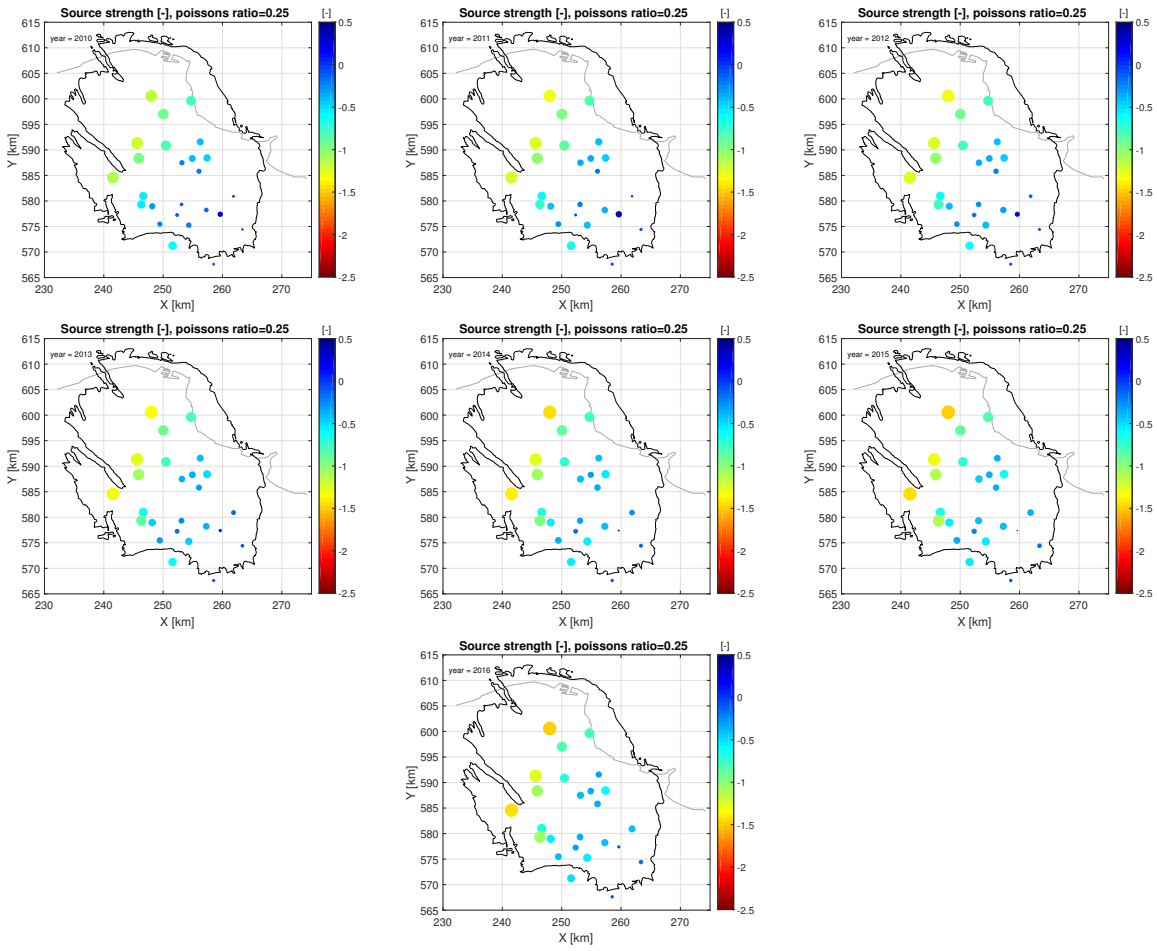

Figure C.4: Estimated source strengths of 2010 to 2016 for a particle filter localisation radius=3000 m. **Top** : fitted PS-InSAR measurements estimated source strengths of years 2010, 2011 and 2012. **Middle**: fitted PS-InSAR measurments estimated source strengths of years 2013, 2014 and 2015. **Bottom**: fitted PS-InSAR measurements estimated source strengths of year 2016. Note: the salt wells are at different depths, 1500 to 1800 m.

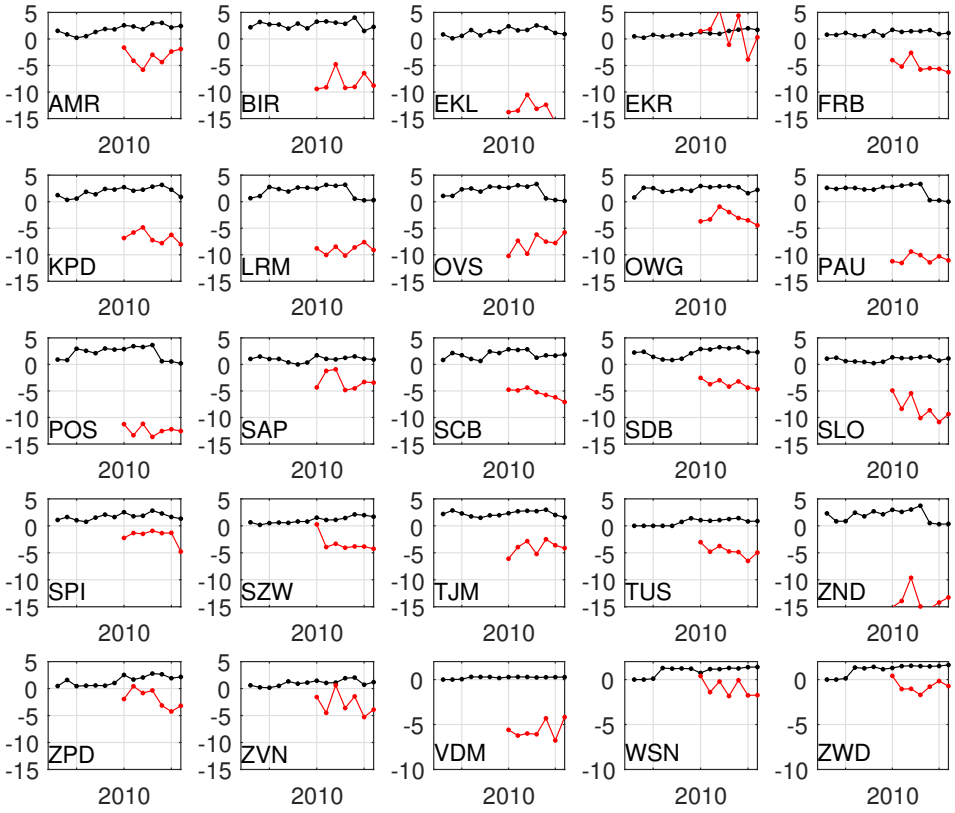

Figure C.5: Source strength and gas production over the period 2010-2016. Note: look only at the shape of the trend, not at the values, because I exaggerated the source strength values.

D

Particle filter experiments extra results

D.1. Experiments resampling

D.1.1. Setup 1: Mogi sources = at deformation locations, k=1500 m

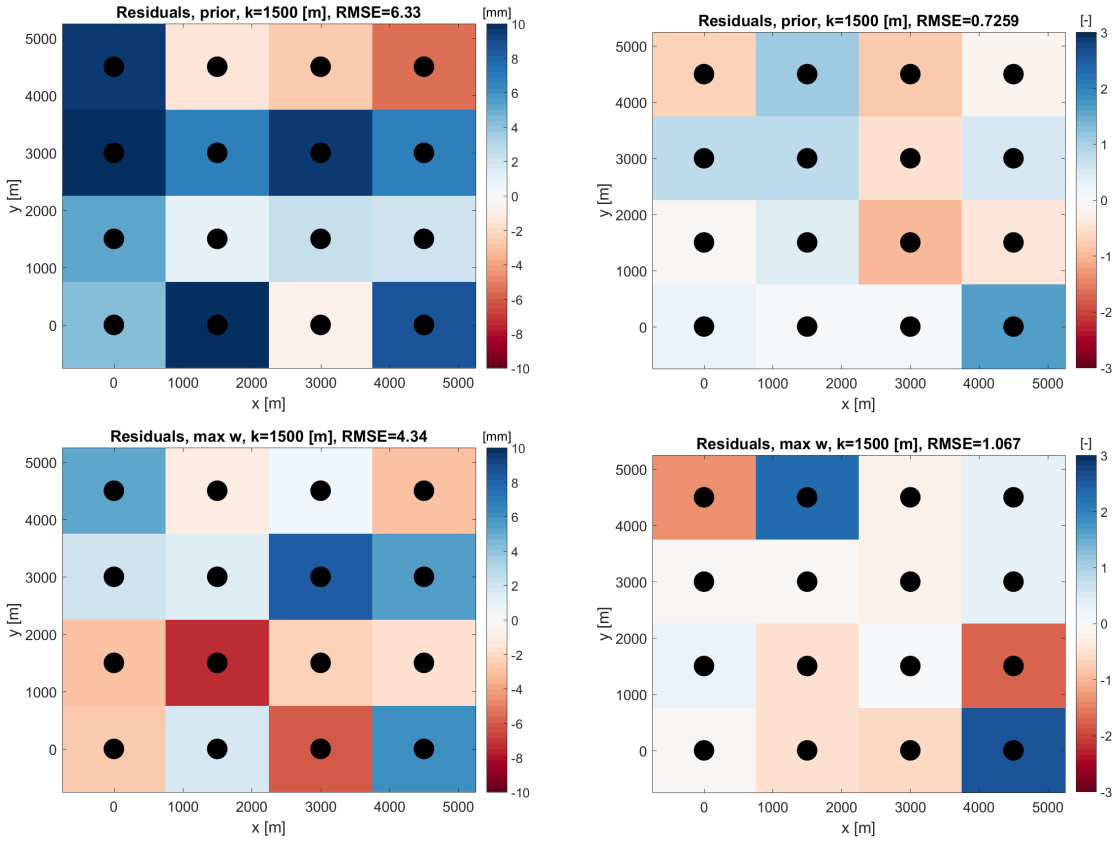

Figure D.1: Residuals maps of deformations and source strengths for k=1500 m, Gaussian pdf σ^2=25 mm. **Left column**: deformation prior residuals [mm], maximum weighted ensemble **Right column**: source strength prior residuals [-], maximum weighted ensemble

D.1.2. Setup 1: Mogi sources = at deformation locations, k=3000 m

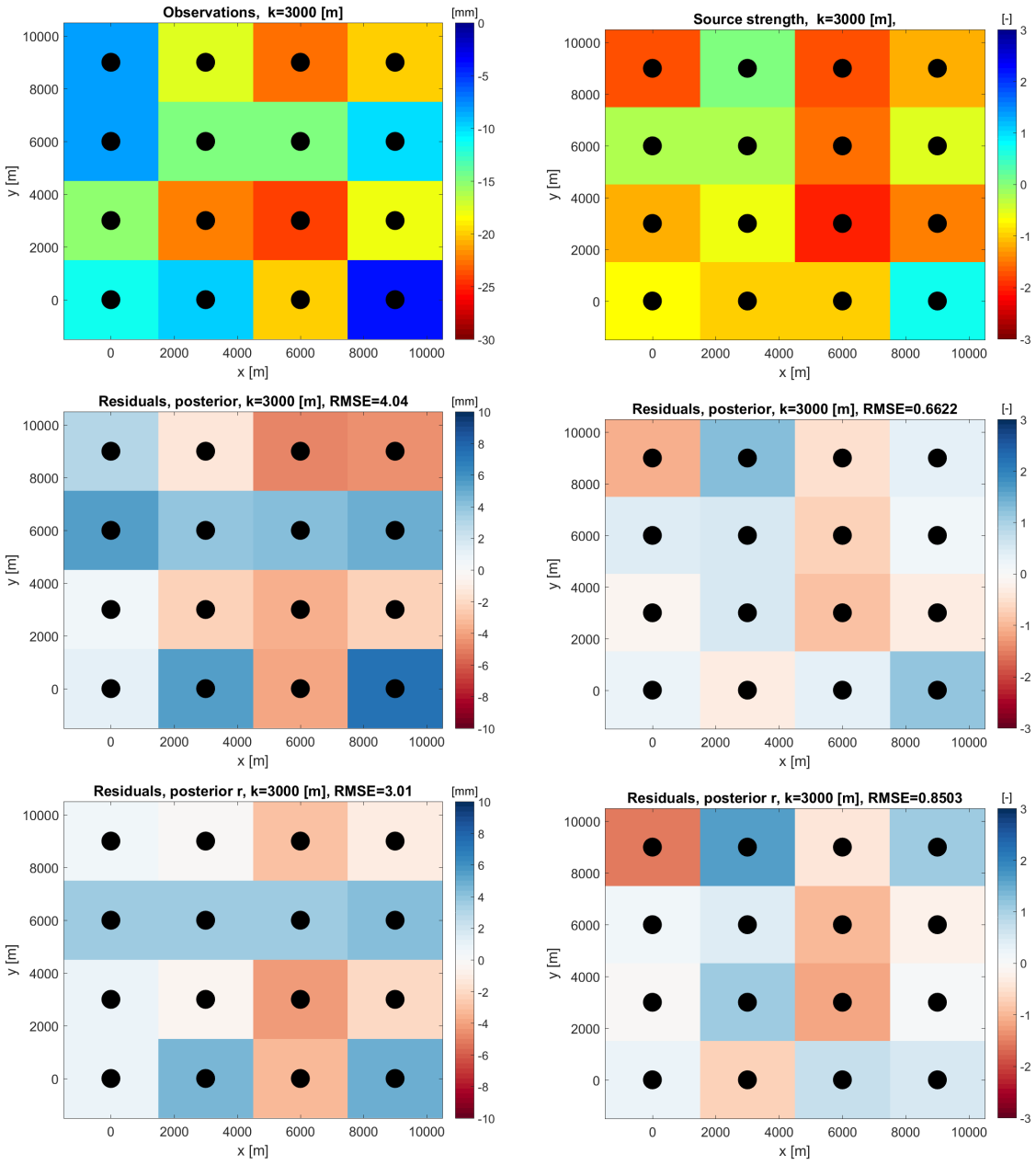

Figure D.2: Deformation map and residuals maps (observed deformation minus estimated deformation, blue/red coloured) for k=3000 m, Gaussian pdf σ^2=25 mm. **Left column**: deformations map [mm], posterior deformation, posterior resampled deformation **Right column**: source strength truth map [-], posterior source strengths, posterior resampled source strengths.

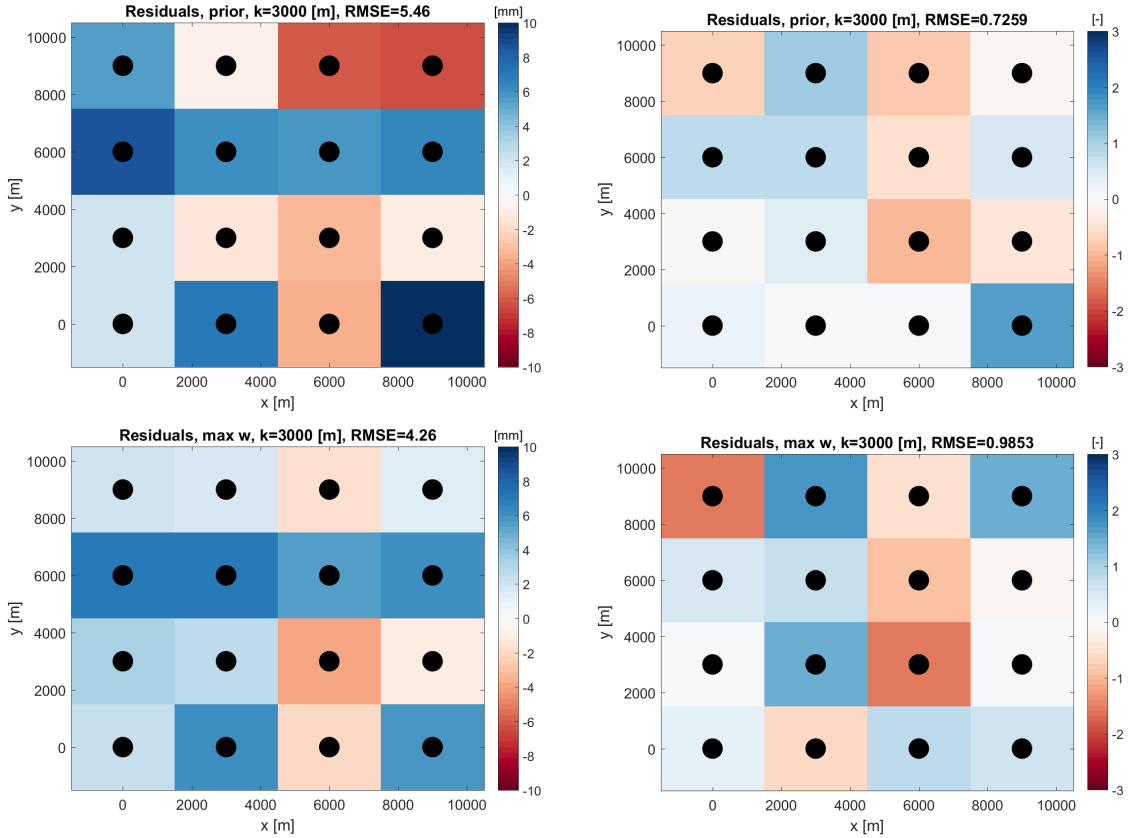

Figure D.3: Residuals maps of deformations and source strengths for k=3000 m, Gaussian pdf σ^2=25 mm. **Left column**: deformation prior residuals [mm], maximum weighted ensemble **Right column**: source strength prior residuals [-] of all particle ensembles, maximum weighted ensemble

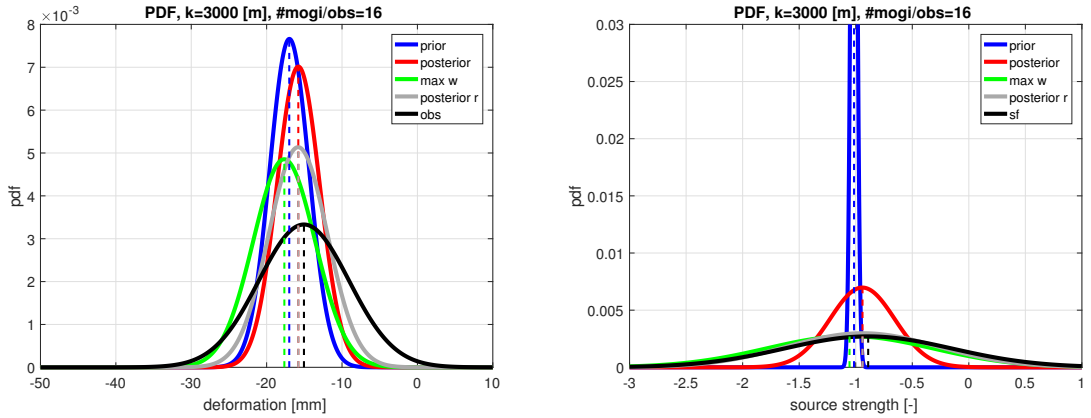

Figure D.4: **Left**: the probability density functions of the deformation and estimated deformations. **Right**: source strength pdf and the estimated source strength values.

D.1.3. Setup 1: Mogi sources = at deformation locations, k=6000 m

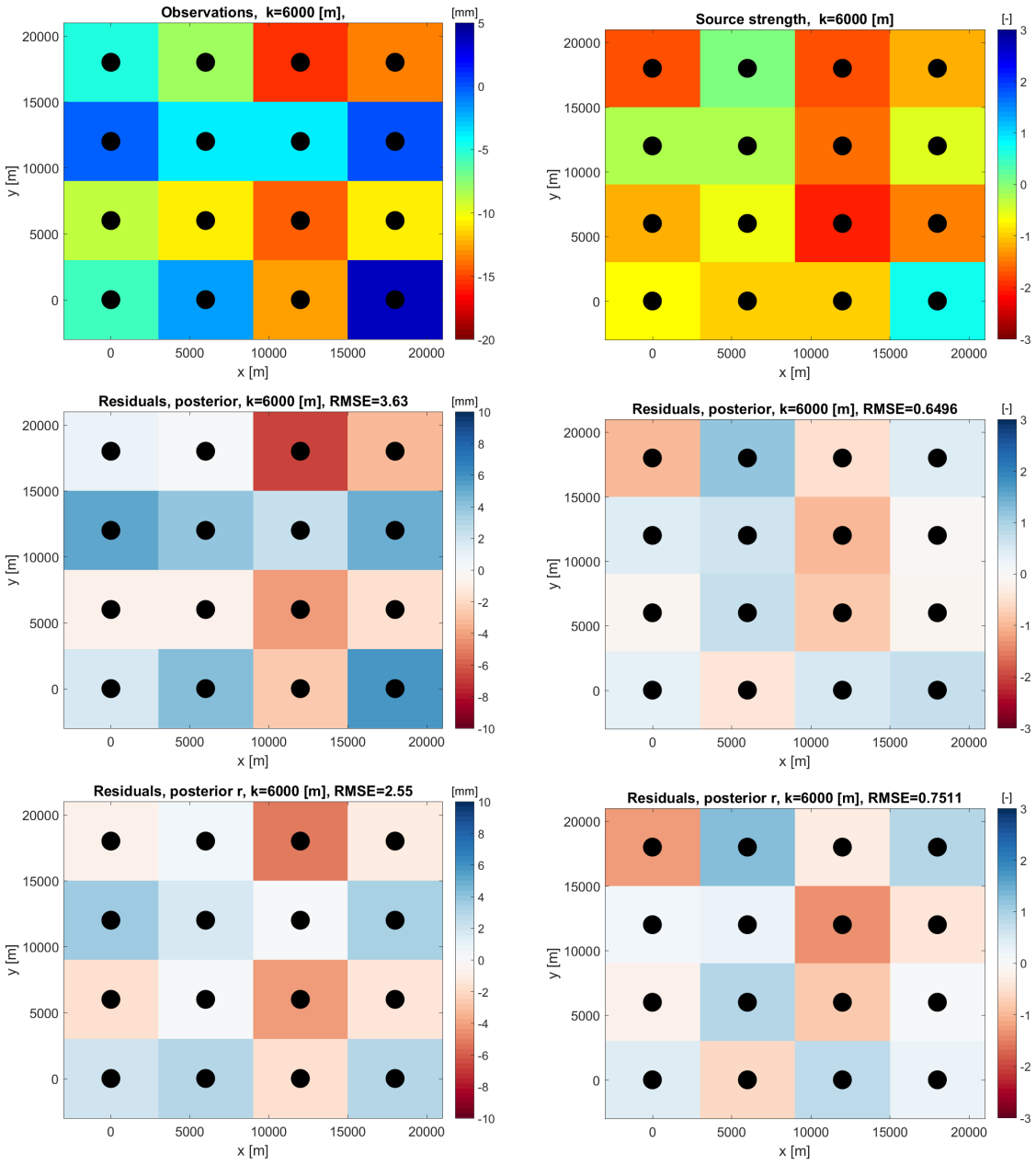

Figure D.5: Deformation map and residuals maps (observed deformation minus estimated deformation, blue/red coloured) for k=6000 m, Gaussian pdf σ^2=25 mm. **Left column**: deformations map [mm], posterior deformation residuals, posterior resampled deformation **Right column**: source strength truth map [-], posterior source strength residuals, posterior resampled source strengths.

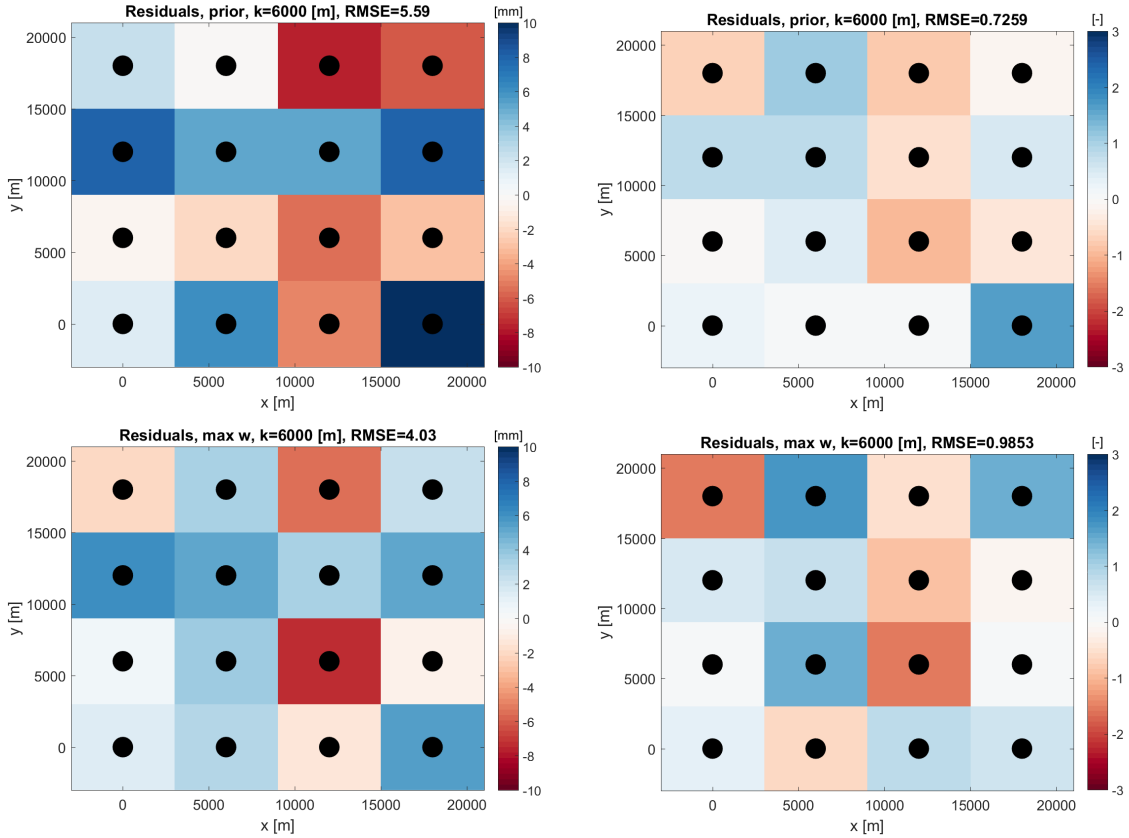

Figure D.6: Residuals maps of deformations and source strengths for k=6000 m, Gaussian pdf σ^2=25 mm. **Left column**: deformation prior residuals mm], maximum weighted ensemble **Right column**: source strength prior residuals [-], maximum weighted ensemble

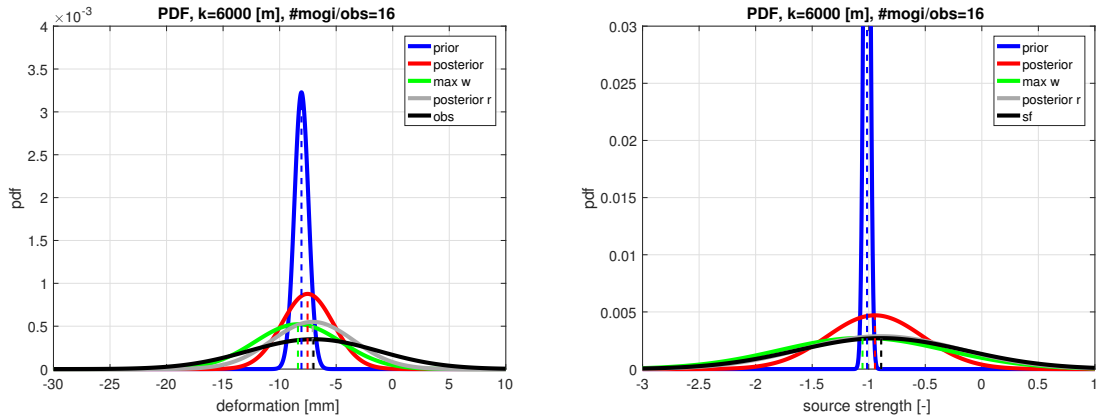

Figure D.7: **Left**: the probability density functions of the deformation and estimated deformations. **Right**: source strength pdf and the estimated source strength values.

D.1.4. Setup 2: 1 Mogi source ≠ at deformation locations, k=1500 m

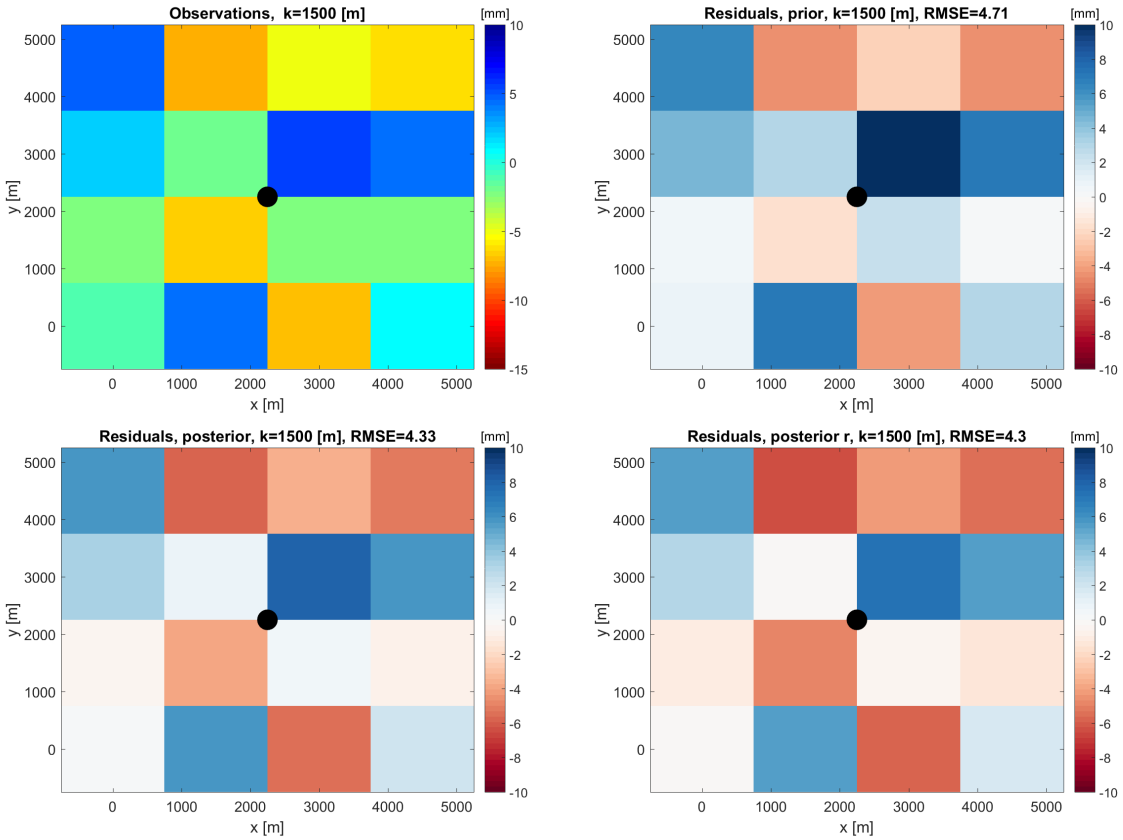

Figure D.8: Deformation map and residuals maps (observed deformation minus estimated deformation) for k=1500 m, Gaussian particle filter σ^2=25 mm. **Top**: left deformations map, deformation prior residuals. **Bottom**: left posterior deformation, right posterior resampled deformation.

D.1.5. Setup 2: 1 Mogi source ≠ at deformation locations, k=300 m

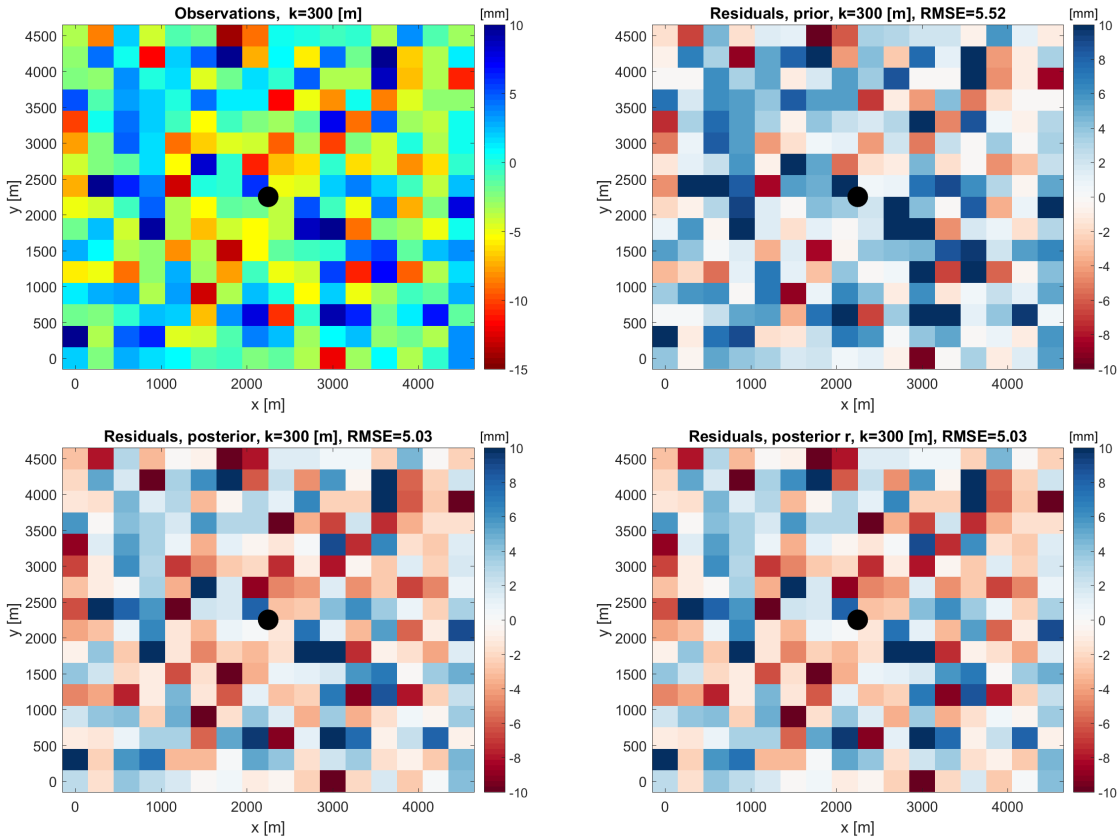

Figure D.9: Deformation map and residuals maps (observed deformation minus estimated deformation) for k=300 m, Gaussian particle filter σ^2=25 mm. **Top**: left deformations map, right residuals prior deformation. **Bottom**: left posterior deformation residuals, right posterior resampled deformation.

D.2. Experiments start value and 'jitter' variance variability

D.2.1. Setup 1: Mogi sources = deformation locations, k=1500 m

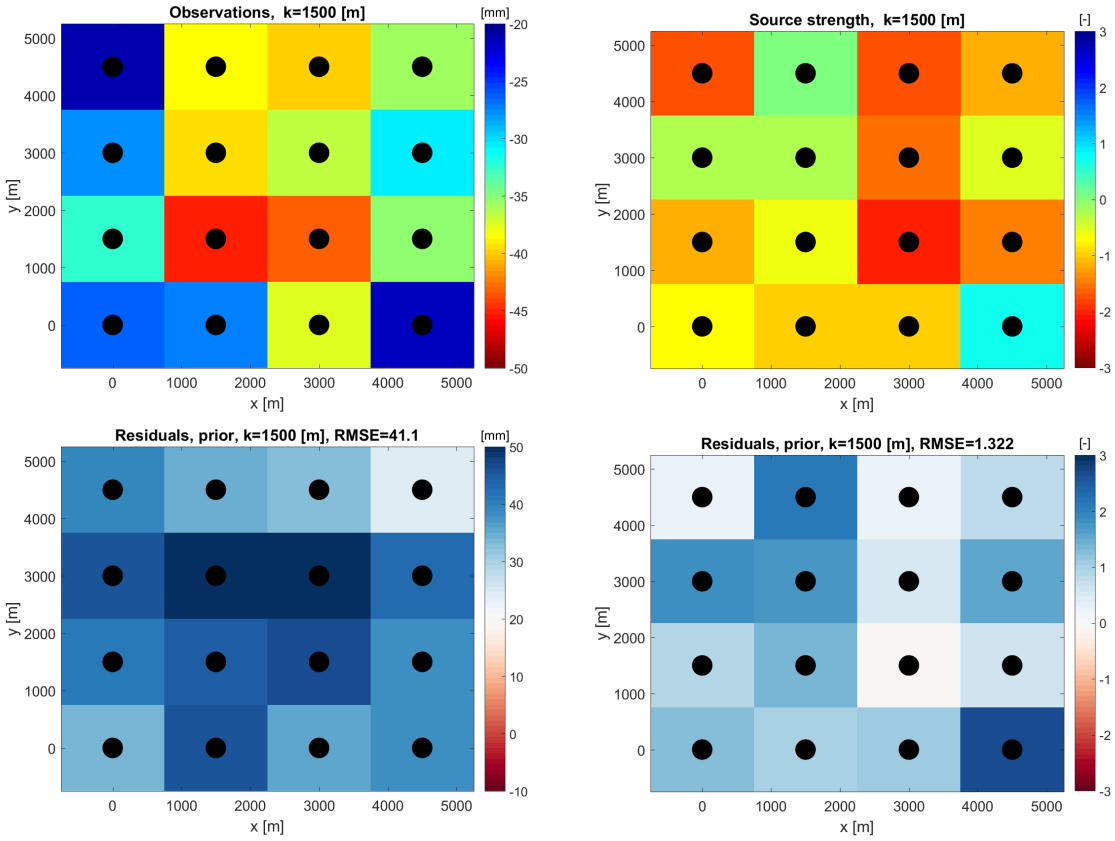

Figure D.10: Deformation / source strength map and residuals maps (observed deformations minus estimated deformation) for k=1500 m, Gaussian particle filter σ^2=25 mm. **Left column**: deformations map [mm], prior deformation residuals. **Right column**: source strength truth map [-], prior source strength residuals.

D.2.2. Setup 1: Mogi sources = deformation locations, k=3000 m

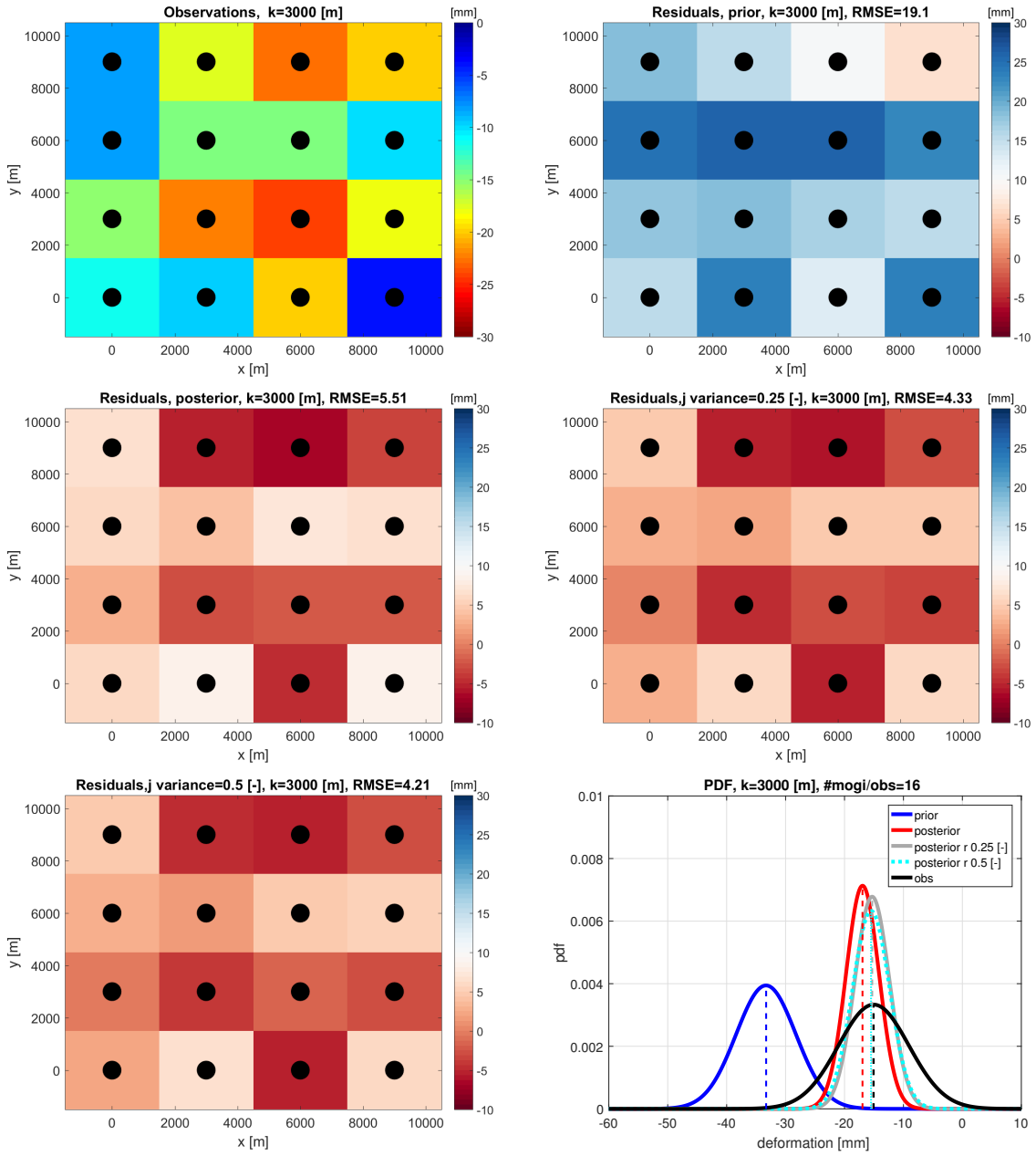

Figure D.11: Deformation map and residuals maps (observed deformation minus estimated deformation) for k=3000 m, Gaussian particle filter σ^2=25 mm. **Top**: left deformations map, right prior deformation residuals. **Middle**: left posterior deformation residuals, right posterior resampled deformation residuals with 'jitter' σ^2=0.25 [-]. **Bottom**: left posterior resampled deformation residuals with 'jitter' σ^2=0.5 [-], right the probability density functions of the deformation and estimated deformations.

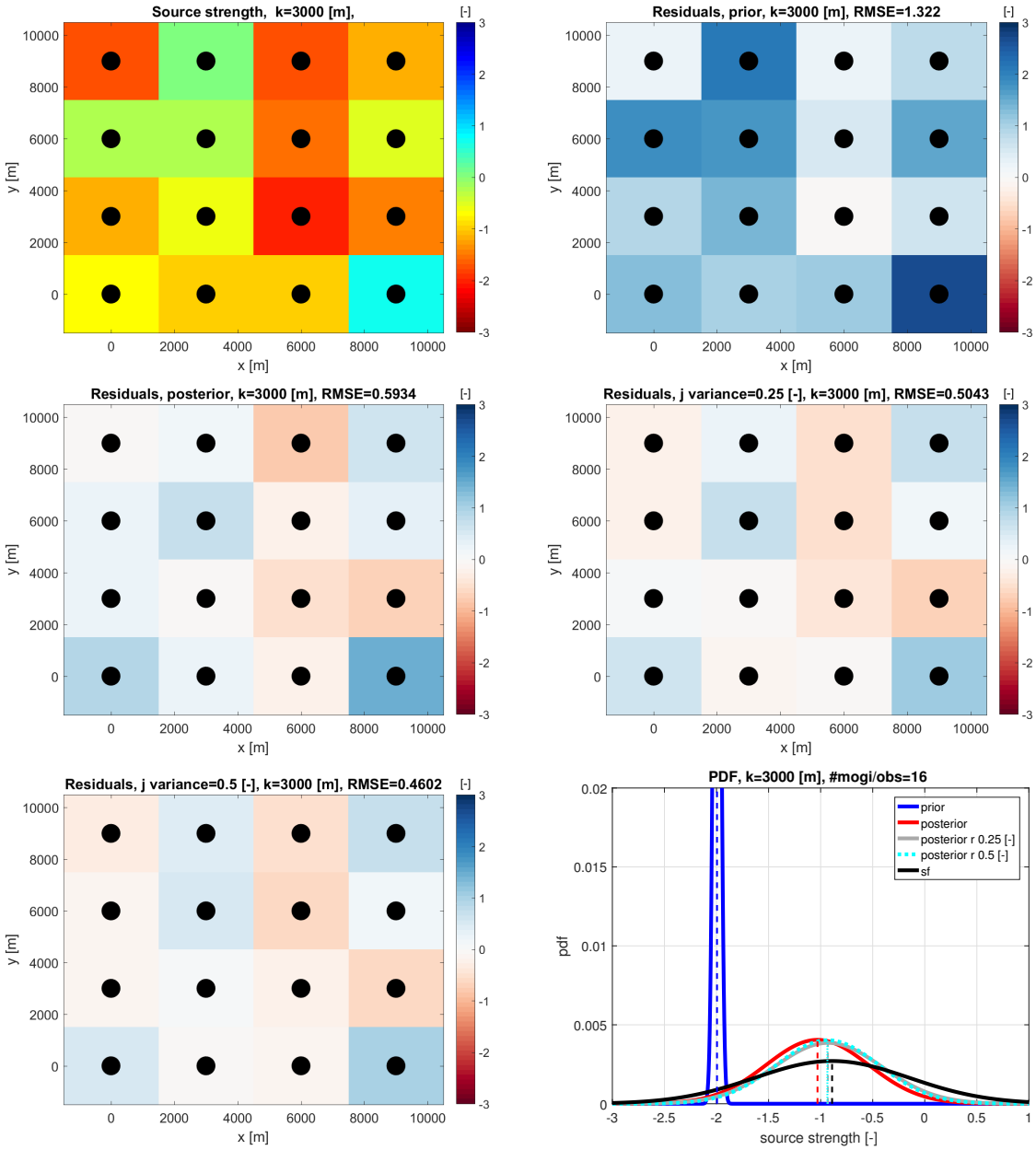

Figure D.12: Source strength map and residuals maps ('truth' source strength minus estimated source strenght) for k=3000 m, Gaussian particle filter σ^2=25 mm. **Top**: left source strength truth map, right prior residuals. **Middle**: left posterior resampled source strength, right posterior resampled source strength with 'jitter' σ^2=0.25 [-]. **Bottom**: left posterior resampled source strength with 'jitter' σ^2=0.5 [-], right the probability density functions of the source strength (sf=scale factor= source strength) and estimated source strength.

D.2.3. Setup 1: Mogi sources = deformation locations, k=6000 m

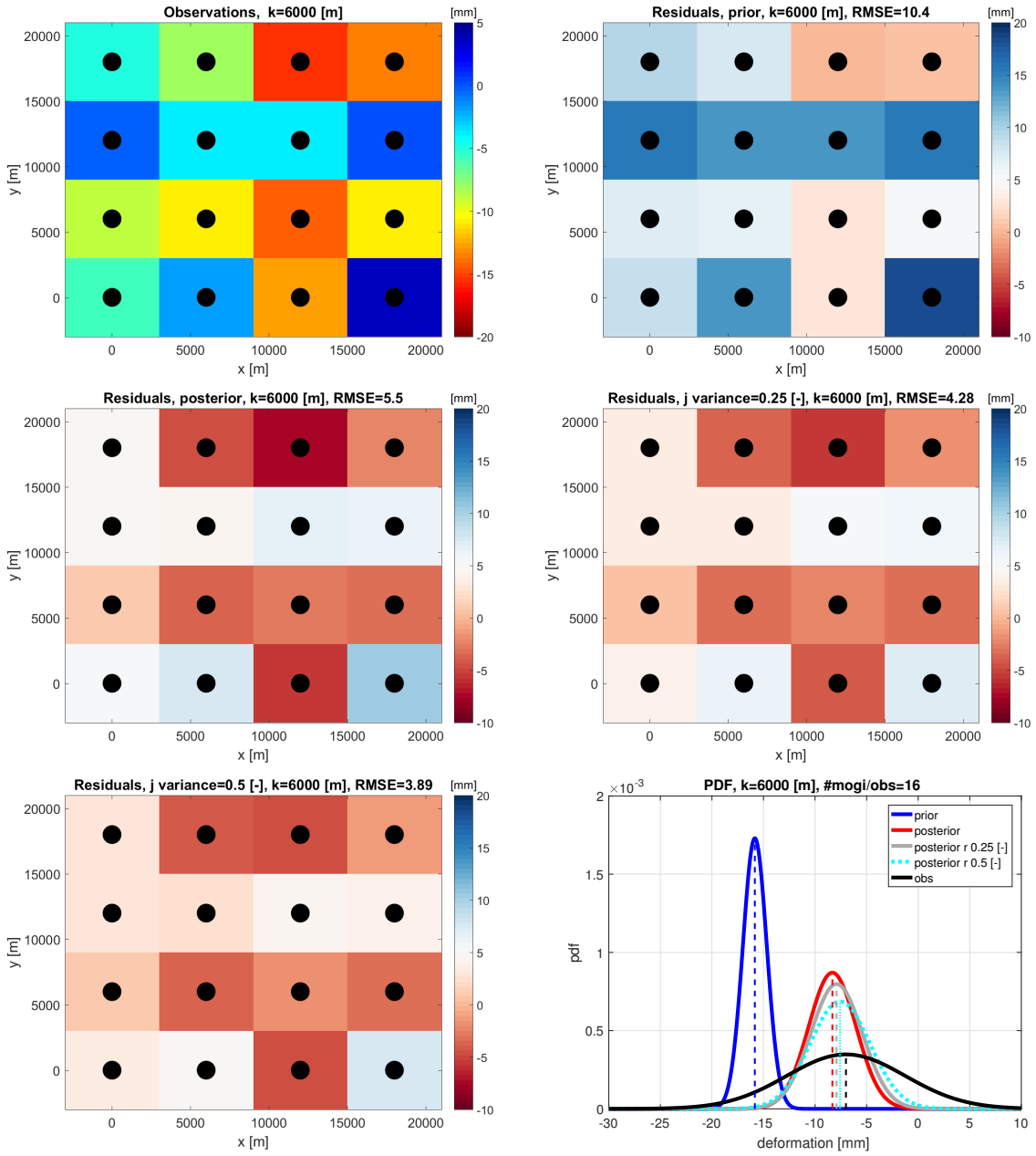

Figure D.13: Deformation map and residuals maps (observed deformation minus estimated deformation) for k=6000 m, Gaussian particle filter σ^2=25 mm. **Top**: left deformations map, right prior deformation. **Middle**: left posterior deformation residuals, right posterior resampled deformation with 'jitter' σ^2=0.25 [-]. **Bottom**: left posterior resampled deformation with 'jitter' σ^2=0.5 [-], right the probability density functions of the deformation and estimated deformations.

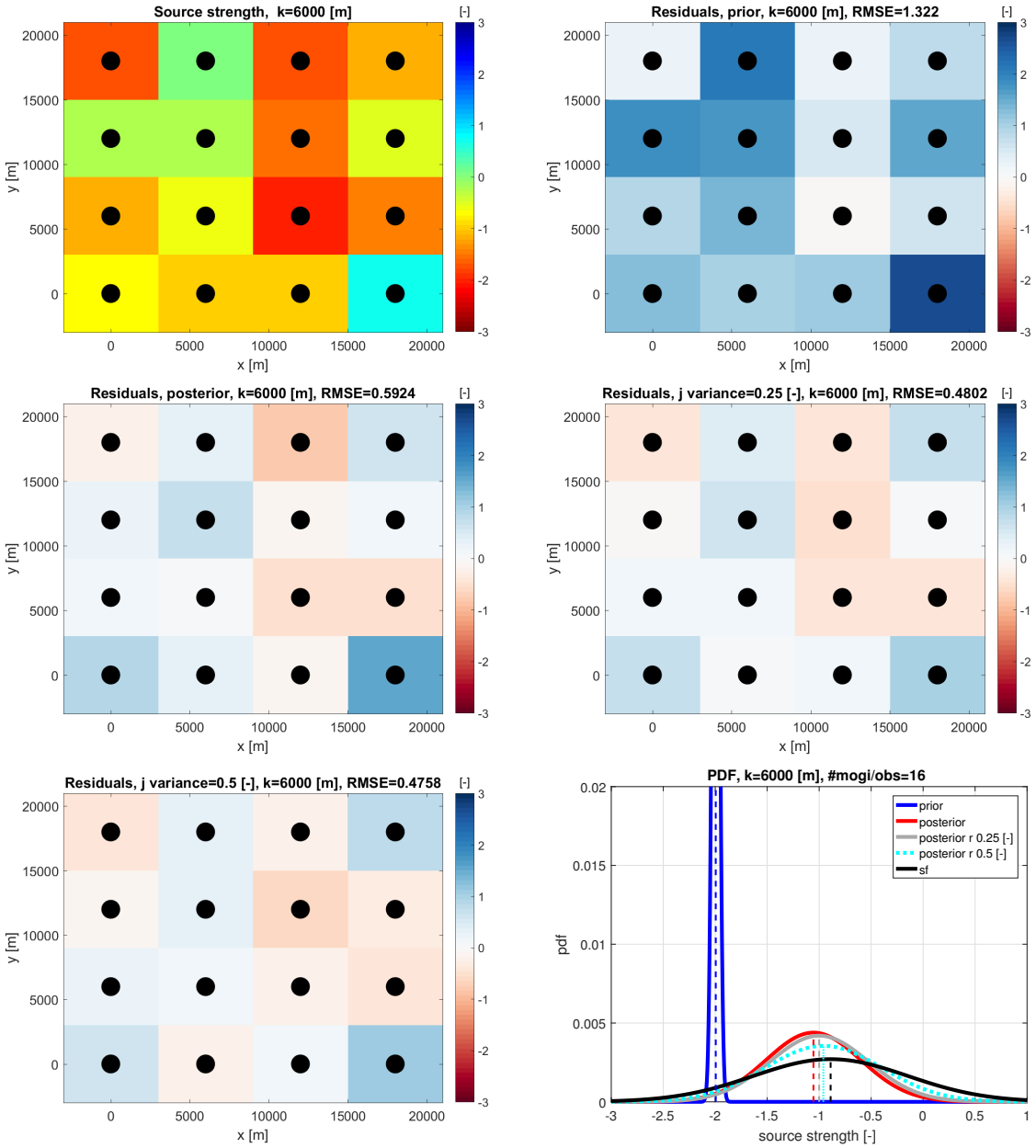

Figure D.14: Source strength map and residuals maps ('truth' source strength minus estimated source strenght) for k=6000 m, Gaussian particle filter σ^2=25 mm. **Top**: left source strength truth, right prior residuals. **Middle**: left posterior source strength residuals, right posterior resampled source strength with 'jitter' σ^2=0.25 [-]. **Bottom**: left posterior resampled source strength with 'jitter' σ^2=0.5 [-], right the probability density functions of the source strength (sf=scale factor= source strength) and estimated source strength.

D.2.4. Setup 2: 1 Mogi source ≠ at deformation locations, k=1500 m and k=300 m

Table D.1: Start value and jitter variance variation, deformation RMSE results of the particle filter.

Distance k [m]	Particle filter σ^2 [mm]	Jitter σ^2 [-]	Residual prior [mm]	Residual posterior [mm]	Residual posterior resampled [mm]
1500	25	0.25	6.52	4.35	4.03
1500	25	0.5	6.52	4.35	4.03
300	25	0.25	7.6	5.03	5.03
300	25	0.5	7.6	5.03	5.03

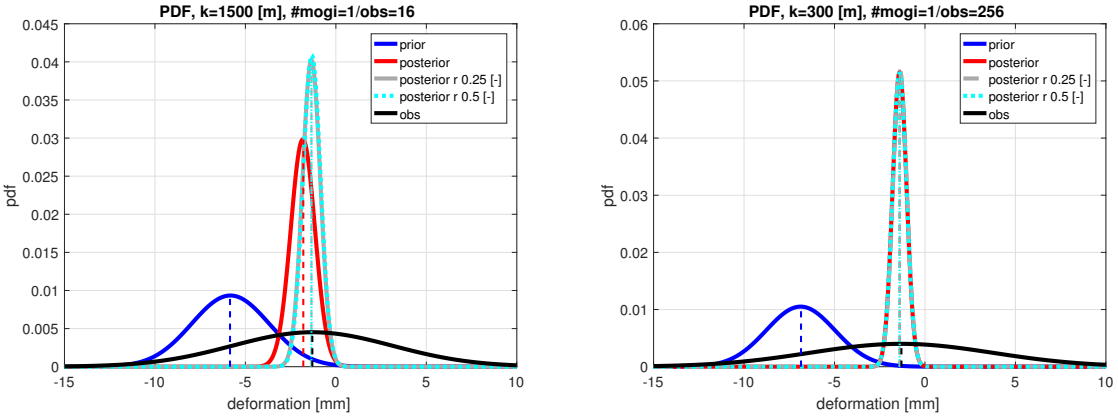

Figure D.15: Deformation pdf's, Gaussian particle filter σ^2=25 mm. **Left**: deformation, prior, posterior and resampled posterior distribution of 1 Mogi source and 16 deformations with grid distance of k=1500 m. **Right**: deformations, prior, posterior and resampled posterior distribution of 1 Mogi source and 256 deformations with grid distance of k=300 m.

Table D.2: Start value and jitter variance variation, source strength RMSE results of the particle filter. The last three columns shows the residual values.

Distance k [m]	Particle filter σ^2 [mm]	Jitter σ^2 [-]	Source strength 'truth' [-]	Residual prior [-]	Residual posterior [-]	Residual posterior resampled [-]
1500	25	0.25	-0.4871	1.486	-0.131	-0.029
1500	25	0.5	-0.4871	1.486	-0.131	-0.036
300	25	0.25	-0.4871	1.486	-0.085	1.586
300	25	0.5	-0.4871	1.486	-0.085	-0.084

D.2.5. Setup 3: 4 Mogi sources ≠ at deformation locations, k=1500 m and k=300 m

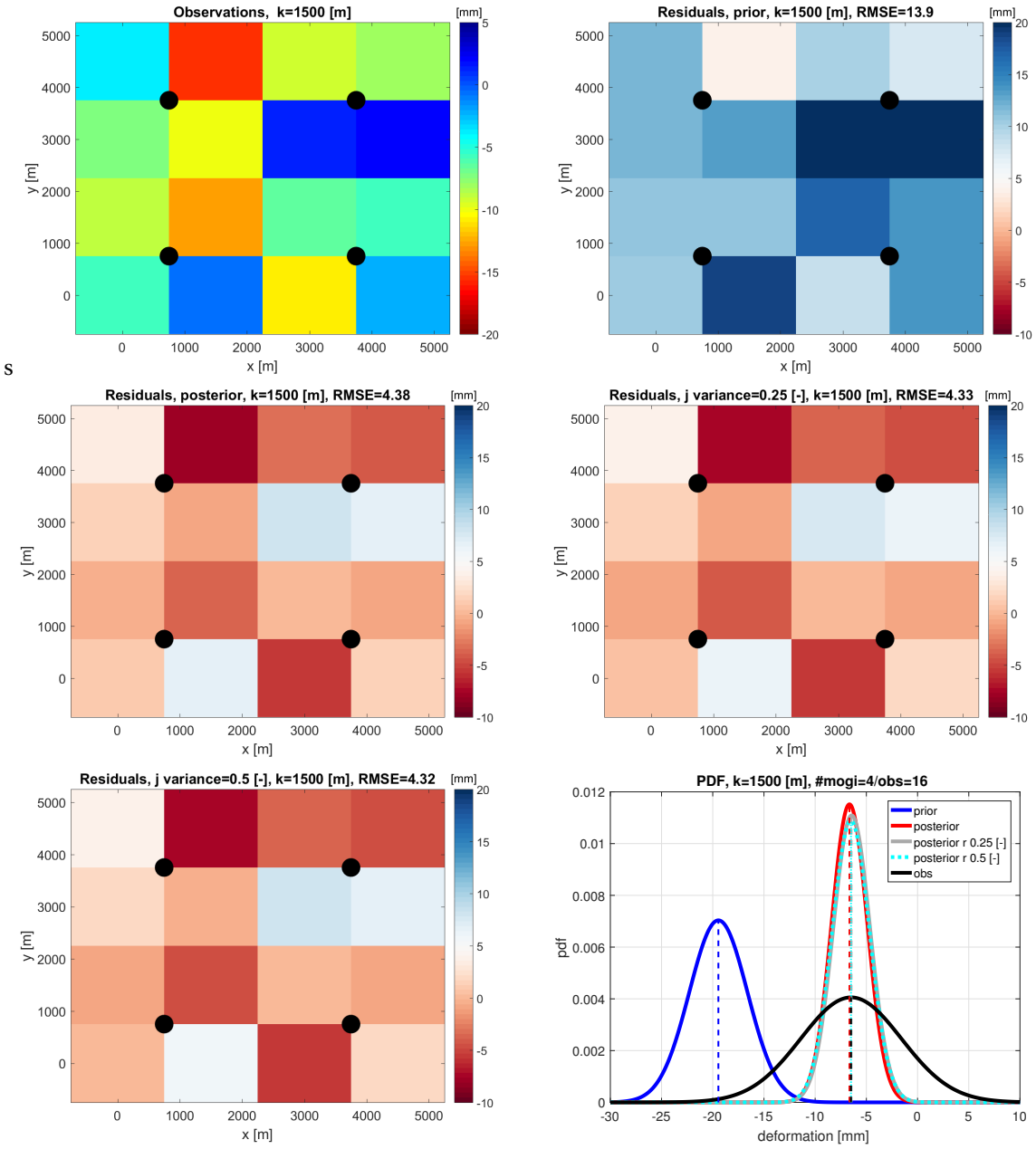

Figure D.16: Deformation map and residuals maps (observed deformation minus estimated deformation) for k=1500 [m] and 4 Mogi sources, Gaussian particle filter σ^2=25 mm. **Top**: left deformations map, right prior residuals. **Middle**: left posterior deformation residuals, right posterior resampled deformation with 'jitter' σ^2=0.25 [-]. **Bottom**: left posterior resampled deformation with 'jitter' σ^2=0.5 [-], right the probability density functions of the deformation and estimated deformations.

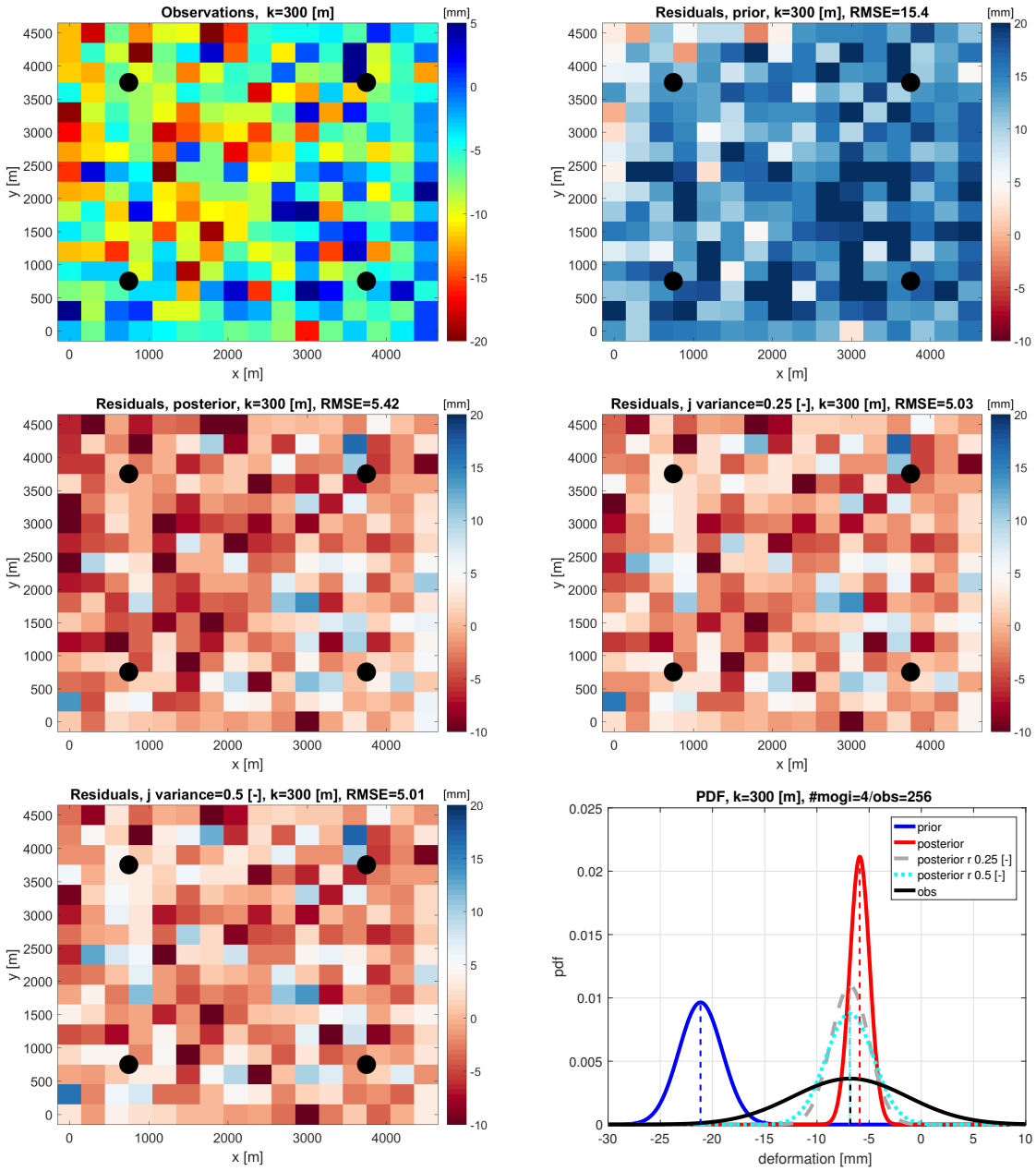

Figure D.17: Deformation map and residuals maps (observed deformation minus estimated deformation) for k=300 m, Gaussian particle filter σ^2=25 mm. **Top**: left deformations map, right prior residuals. **Middle**: left posterior deformation residuals, right right posterior resampled deformation with 'jitter' σ^2=0.25 [-]. **Bottom**: eft posterior resampled deformation with 'jitter' σ^2=0.5 [-], right the probability density functions of the deformation and estimated deformations.

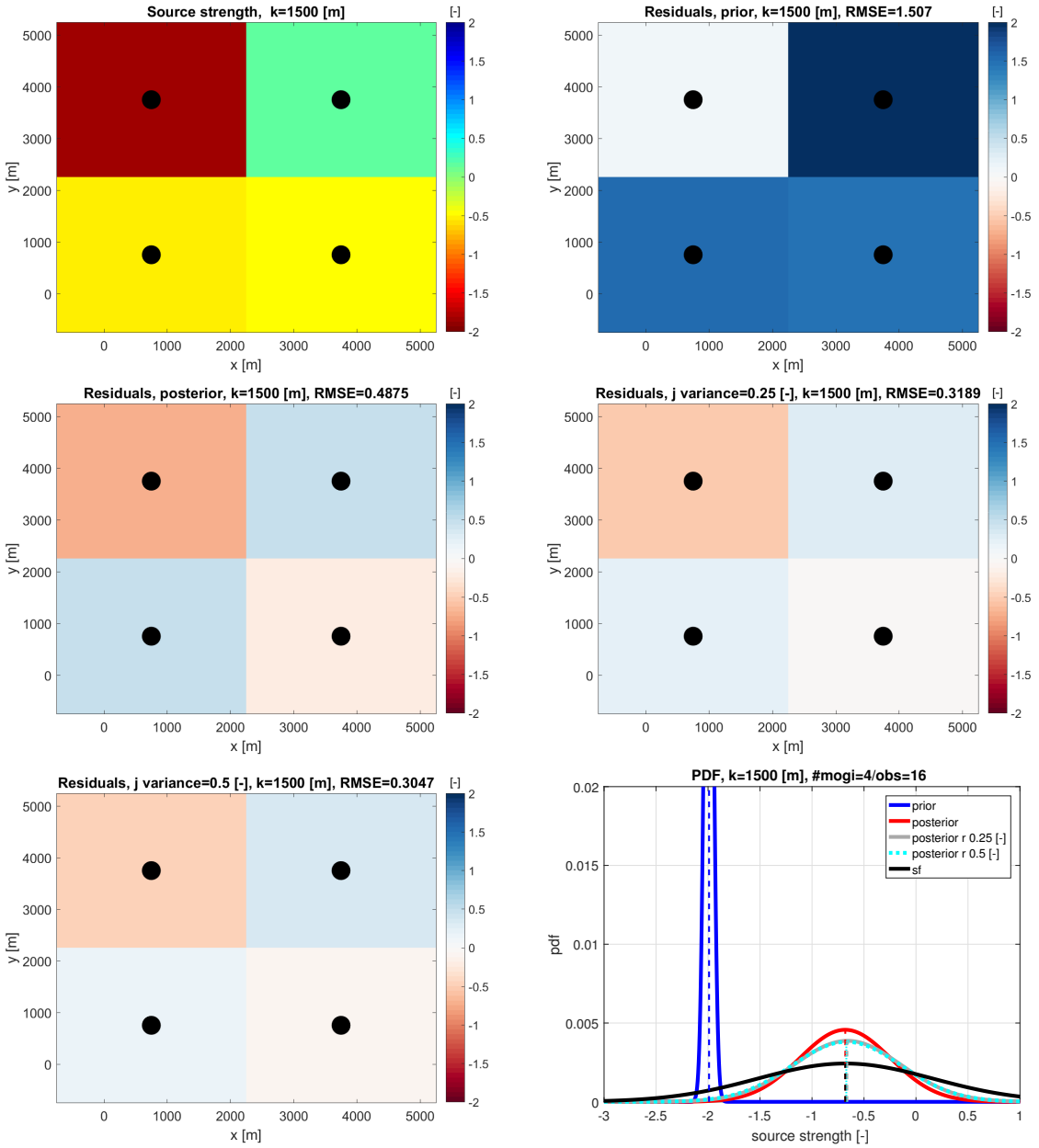

Figure D.18: Source strength map and residuals maps (source strength truth minus estimated source strength) for k=1500 m, Gaussian particle filter σ^2=25 mm. **Top**: left source strength truth, right prior residuals. **Middle**: left posterior source strength residuals, right posterior resampled source strength with 'jitter' σ^2=0.25 [-]. **Bottom**: left posterior resampled source strength with 'jitter' σ^2=0.5 [-], right the probability density functions of the source strength (sf=scale factor= source strength) and estimated source strength.

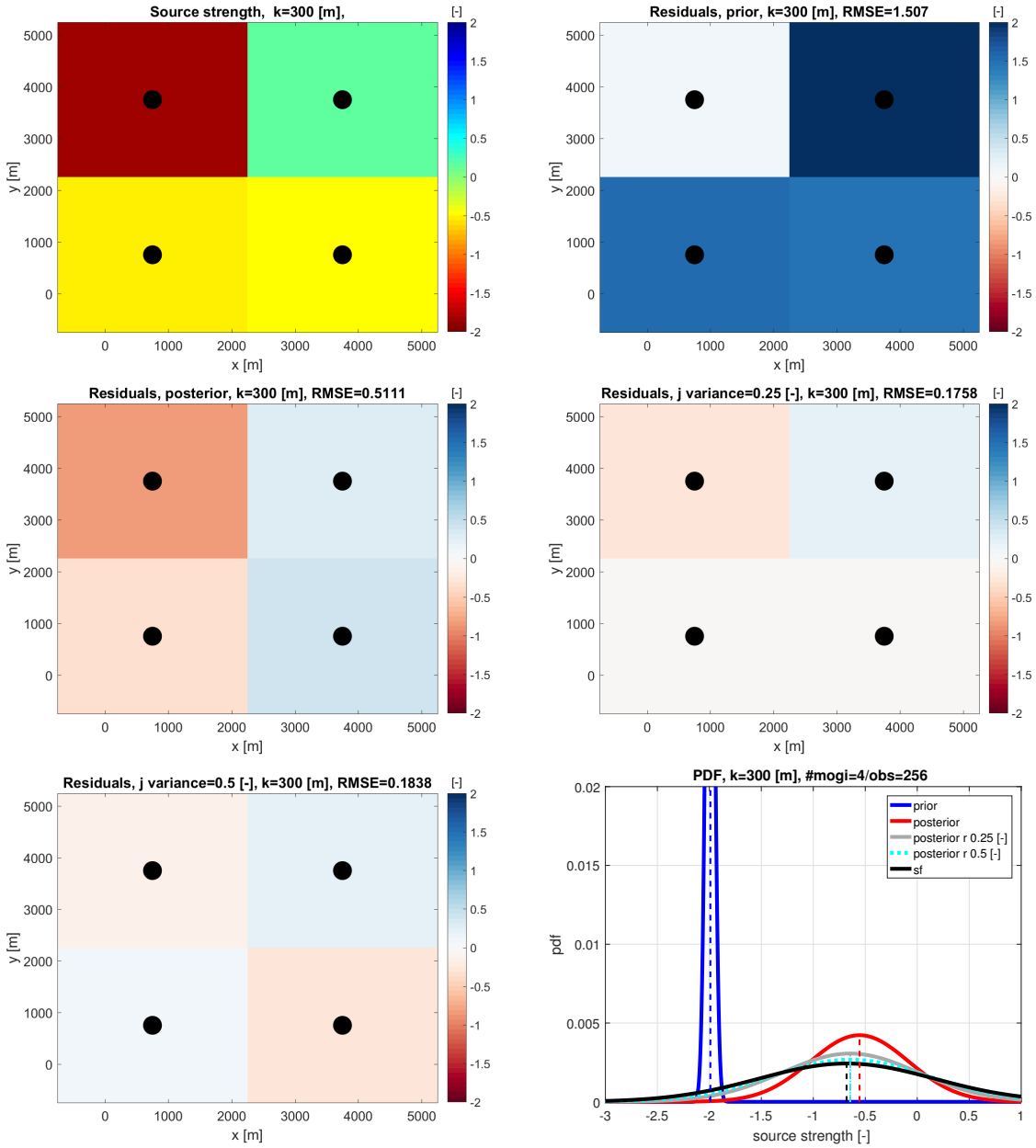

Figure D.19: Source strength map and residuals maps (source strength truth minus estimated source strength) for k=300 m, Gaussian particle filter σ^2=25 mm. **Top**: left source strength truth, right prior residuals. **Middle**: left posterior source strength residuals, right posterior resampled source strength with 'jitter' σ^2=0.25 [-]. **Bottom**: left posterior resampled source strength with 'jitter' σ^2=0.5 [-], right the probability density functions of the source strength (sf=scale factor= source strength) and estimated source strength.

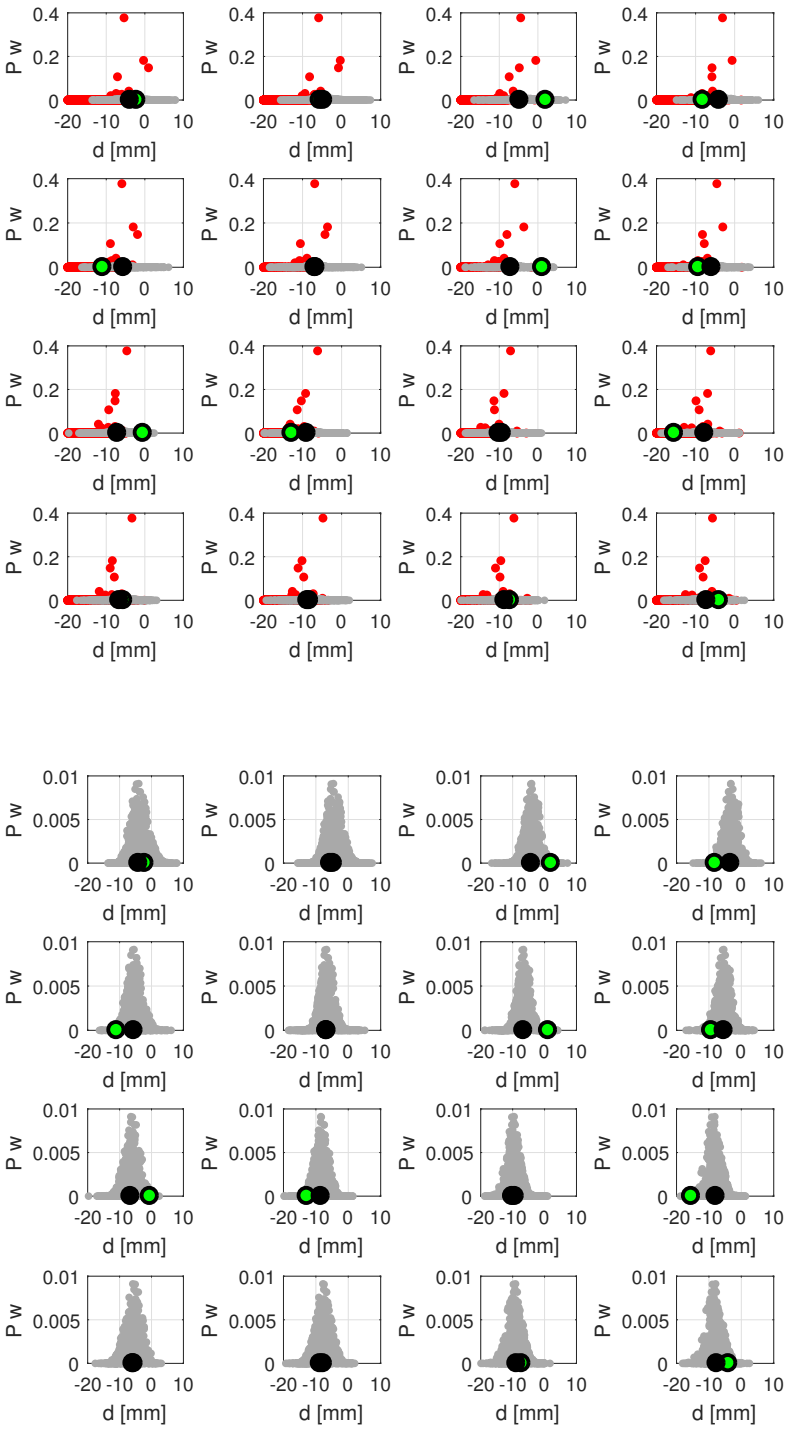

Figure D.20: Deformation vs. particle filter weight generated with a Gaussian particle filter σ^2=25 mm. The subplots are ordered the same as in figure D.16, where the top left subplot is the top left point in that figure. **Top**: red= ensemble members, cyan= resampled ensemble members with a jitter variance of σ^2=0.25 [-], black dot= estimated deformation and green dot=observation truth. **Bottom**: cyan= resampled ensemble members with a jitter variance of σ^2=0.25 [-], black dot= estimated resampled deformation and green dot=observation truth, (different y-axis scale for a better view)

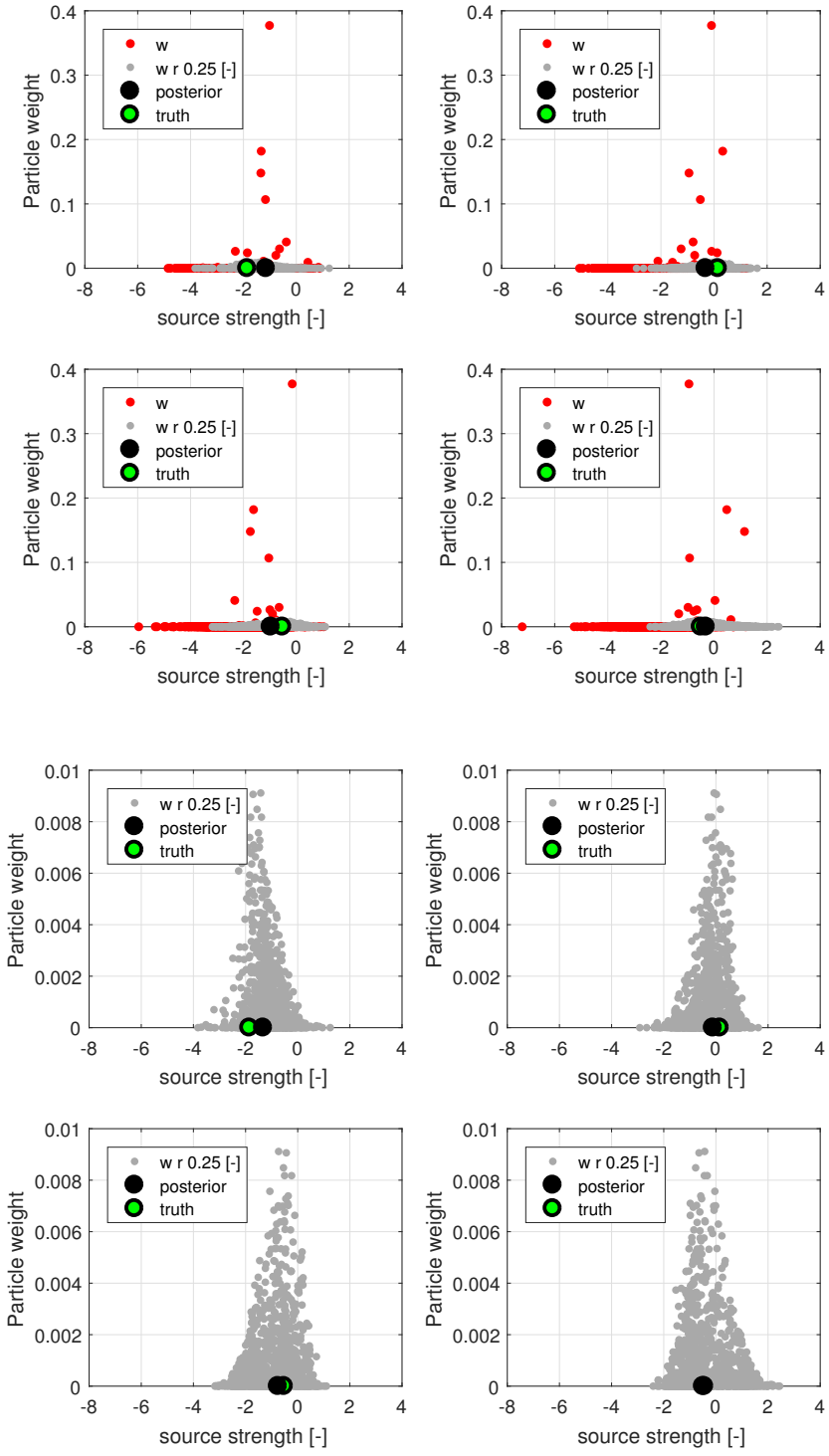

Figure D.21: Source strength (16 deformations) vs. particle filter weight generated with a Gaussian particle filter σ^2=25 mm. The subplots are ordered the same as in figure D.18, where the top left subplot is the top left point in that figure. **Top**: red= ensemble members, cyan= resampled ensemble members with a jitter variance of σ^2=0.25 [-], black dot=estimated source strength and green dot= source strength truth. **Bottom**: cyan= resampled ensemble members with a jitter variance of σ^2=0.25 [-], black dot=source strength truth, (different y-scale)

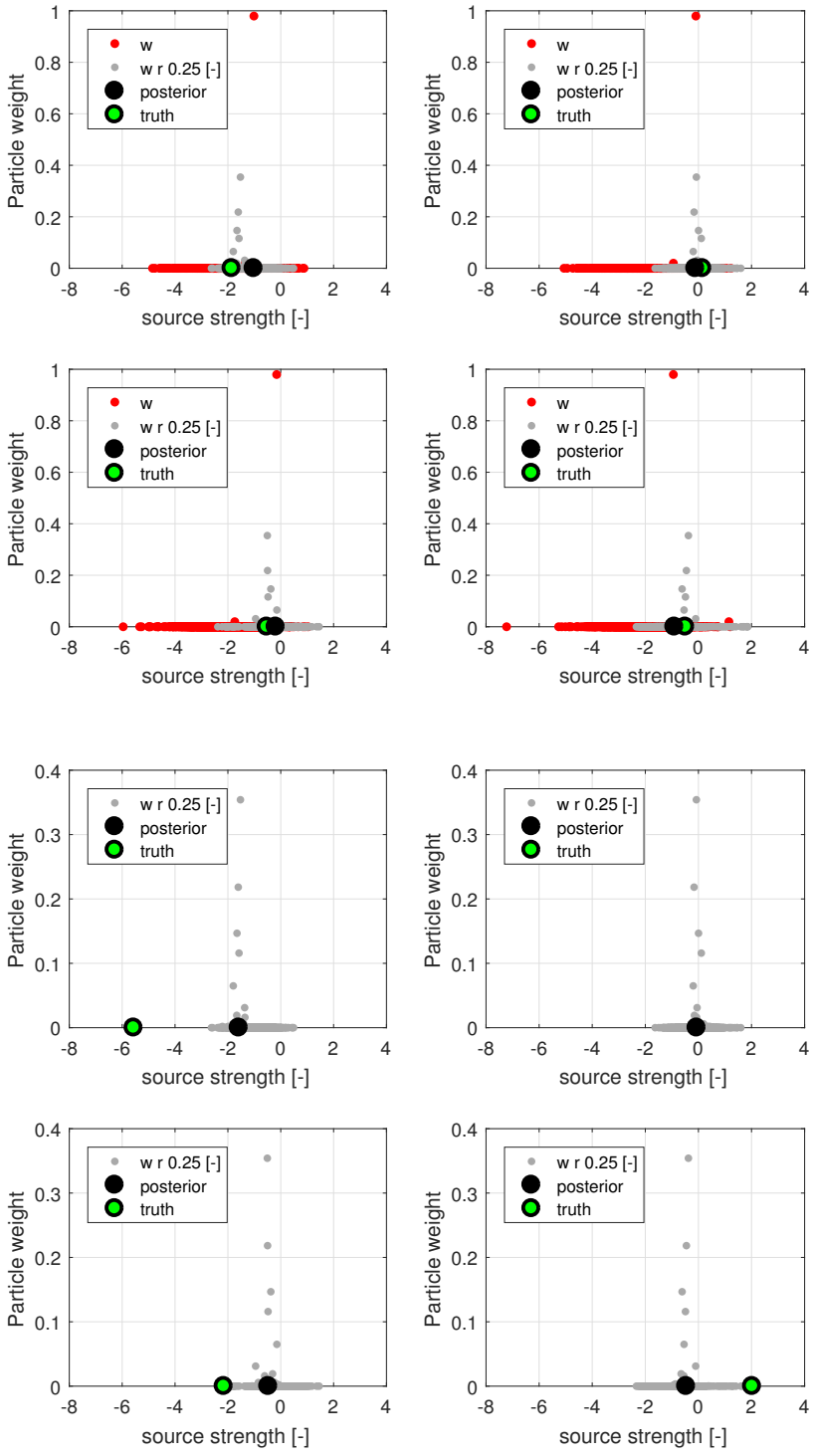

Figure D.22: Source strength (256 deformations) vs. particle filter weight generated with a Gaussian particle filter σ^2=25 mm. The subplots are ordered the same as in figure D.19, where the top left subplot is the top left point in that figure. **Top**: red= ensemble members, cyan= resampled ensemble members with a jitter variance of σ^2=0.25 [-], black dot=estimated source strength and green dot= source strength truth. **Bottom**: cyan= resampled ensemble members with a jitter variance of σ^2=0.25 [-], black dot=source strength truth, (different y-scale)

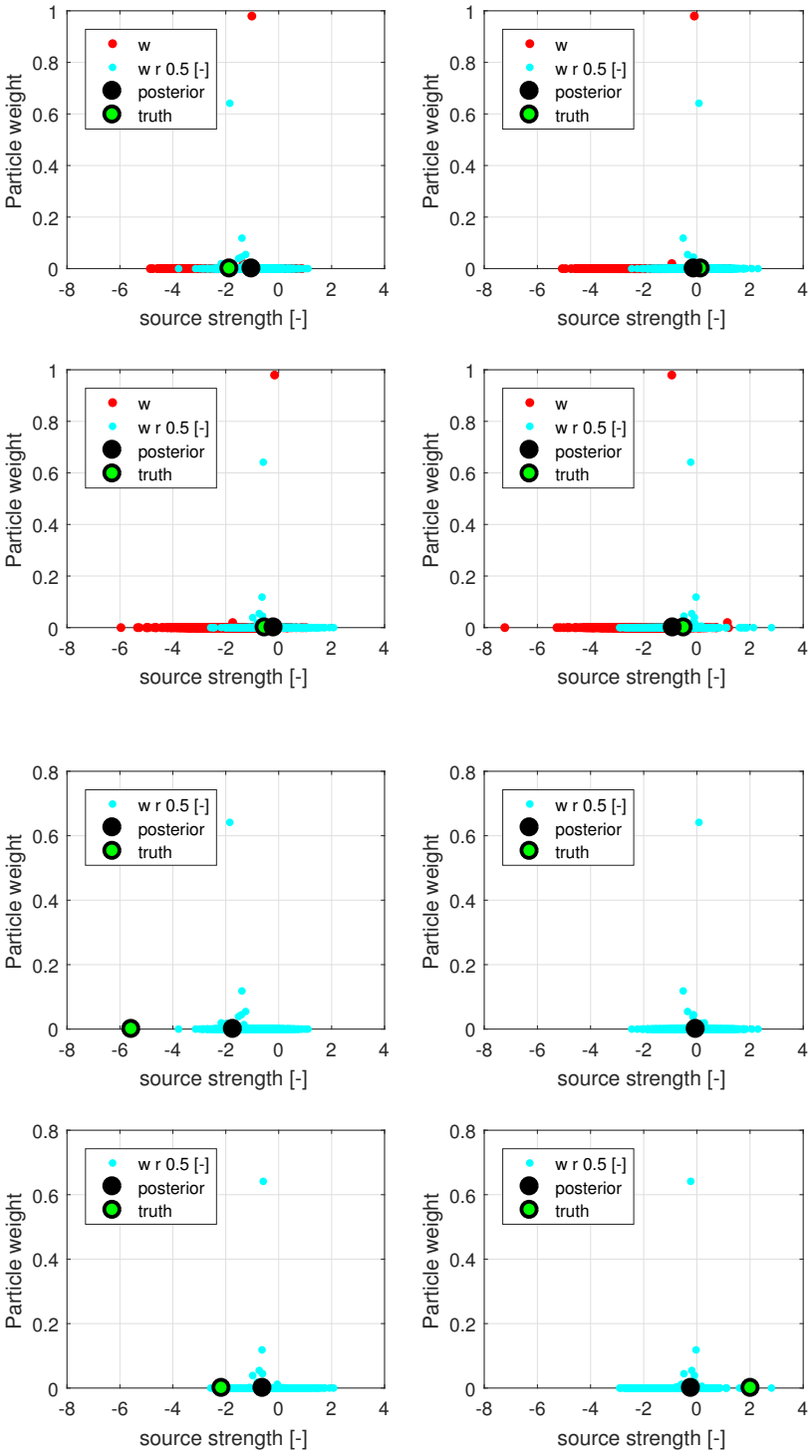

Figure D.23: Source strength (256 deformations) vs. particle filter weight generated with a Gaussian particle filter σ^2=25 mm. The subplots are ordered the same as in figure D.19, where the top left subplot is the top left point in that figure. **Top**: red= ensemble members, cyan= resampled ensemble members with a jitter variance of σ^2=0.5 [-], black dot=estimated source strength and green dot= source strength truth. **Bottom**: cyan= resampled ensemble members with a jitter variance of σ^2=0.5 [-], black dot=source strength truth, (different y-scale)